THE UNIVERSITY *of* EDINBURGH

Representativeness and application of long-term trace gas and photolysis measurements for evaluating local air quality

THE UNIVERSITY
of EDINBURGH

Hannah Walker

Thesis submitted in fulfilment of the requirements

for the degree of Doctor of Philosophy

The University of Edinburgh

2021

Declaration

I declare that this thesis was composed by myself, that the work contained herein is my own except where explicitly stated otherwise in the text, and that this work has not been submitted for any other degree or professional qualification except as specified.

Chapter 2 has been published in
Walker, H. L., Heal, M. R., Braban, C. F., Ritchie, S., Conolly, C., Sanocka, A., Dragosits, U. and Twigg, M. M.: Changing supersites: assessing the impact of the southern UK EMEP supersite relocation on measured atmospheric composition, *Environ. Res. Commun.*, **1**, 041001, https://doi.org/10.1088/2515-7620/ab1a6f, 2019.

Hannah Walker

July 2021

Lay summary

Concentrations of air pollutants are measured in hundreds of locations across the UK and Europe, often as frequently as once an hour. Measurements are actively managed in a series of monitoring networks, which have been running for decades. These measurements constitute an extensive archive of air pollutant concentrations across Europe which provides the data to identify trends in air pollution. In order to see the impact of policy changes made to improve air quality, such as low emission zones in city centres, it is important to identify long-term trends in pollutant concentrations that result from a change in emissions rather than from short-term differences that can be strongly influenced by weather. Monitoring networks can cover large geographical areas using many sites, and therefore reveal how pollutants react and move away from where they are first released into the atmosphere. It is important that all measurements of pollutants across a monitoring network use the same methods, so concentrations can be directly compared. Otherwise differences between concentrations recorded by different measurement methods can be confused with differences between site types (e.g. urban and rural).

Atmospheric chemistry models take estimates of the amount of air pollutants released into the atmosphere, and then using extensive knowledge of reactions taking place in the atmosphere, predict what pollutant concentrations would be in different scenarios. This practice is particularly useful to determine how effective a potential future change in policy could be in reducing public exposure to harmful air pollutants. Confidence in the model results is increased by predicting concentrations of pollutants in known scenarios, which are directly compared against the relevant measurements, in a step

referred to as validation. When the concentrations compared are close, it indicates that the model is working well. Where concentrations are very different, it can signpost potential problems in the model set-up.

Reactions of light with air pollutants are extremely important for driving atmospheric chemistry. These so-called photolysis reactions often produce very reactive species called radicals, which drive the formation of pollutants which are harmful to human health and the environment. Changes in light levels are largely dependent on local conditions, such as the weather. For example, lots of overcast clouds lead to overall lower light levels. In turn, these conditions directly influence the speed at which these reactions take place in the atmosphere. This is measured through a variable known as a photolysis rate constant, or "j-value". As local weather conditions change a lot, j-values can be very difficult to accurately predict in models. Model inaccuracies in j-values can have a big impact on predicted concentrations. Currently, j-values are not yet validated against measurements in the same way pollutant concentrations are, despite their variability and importance.

This PhD study focusses on UK-based monitoring network sites. Chapter 2 used numerical averaging methods, removing the influence of weather to investigate how the relocation of a multi-pollutant monitoring site in England has affected the long-term time series of pollutant concentrations. It was found that for some pollutants the move of the site did not affect the long-term trend, but that for two pollutants a step-change in trend was noted, due to the proximity of sources of pollution at the new site. Chapters 3 and 4 explore how measurements of j-values can be used to validate or adjust model estimations, to account for local conditions. These chapters also discuss how these adjustments change across the UK, and between different pollutants which react with light. 12 important photolysis reactions were separated into 3 groups based on their interaction with different wavelengths of light. The impact of using local measured j-values decreased modelled j-values by an average of 45% across the UK sites. Chapter 5 uses a novel monitoring method at a Scottish site aimed to identify and quantify pollutants not previously measured at the site, to improve our understanding of potential interferences in the pollutant concentrations reported from the UK monitoring networks.

Abstract

Networks of long-term measurements of trace gases are critical for understanding spatio-temporal trends in air pollutants. This data is used to assess long-range and trans-boundary transport of emissions, quantify effects on public health, develop mitigation strategies and examine the impact of implemented policy changes. As part of the European Monitoring and Evaluation Programme (EMEP), the UK operates two "super-sites" which have provided a suite of co-located measurements for this purpose. These supersites have been running for decades, and are located in rural background conditions, with the intention of being representative of the north and south of the country.

A Monitor for AeRosols and Gases in ambient Air (MARGA; Metrohm Applikon, NL) has been included in these sites' measurements for over a decade. However its gaseous measurements of nitric acid (HNO_3) have been demonstrated to include potential artefacts from other oxidised reactive nitrogen species (NO_y), such as dinitrogen pentoxide (N_2O_5). This interference has not yet been formally quantified. Other NO_y measurements at either site are infrequent. Nitryl chloride ($ClNO_2$) in particular was first measured in the UK in 2012, and has been measured only sporadically since.

Meteorological variables are similarly measured in networks to provide locally representative data, which are utilised in atmospheric chemistry and chemical transport models. Photolysis reactions are key drivers of atmospheric chemistry, initiating many reaction routes via the production of reactive radical species. As such, accurate estimation of photolysis rate constants (or photolysis frequencies; j-values) are imperative for understanding subsequent reactions and predicting accurate pollutant concentrations. Photolysis rate constants are highly influenced by local meteorology (e.g. clouds,

aerosols), but capturing the spatio-temporal variability of these changing conditions is challenging, and often computationally costly. Consequently, modelled j-values are often parameterised or determined for unrepresentative local conditions, and results are not validated beyond model conception. Some studies apply adjustment factors to these model results to account for local conditions, but these have not yet been standardised nor explored.

Part of this PhD research presents a systematic analysis of a measurement-driven adjustment factor (MDAF) to adjust clear-sky or cloud-free modelled j-values to capture changes in the local meteorology. MDAFs were derived from the ratios of j-values from both filter- and spectral radiometer measurements and clear-sky estimates from the Tropospheric Ultraviolet and Visible radiative transfer model (TUV). MDAFs were examined in terms of space (3 UK sites), time resolution (hourly to annual averages), photolysis reactions (12 studied), optical inlet used (4-π sr and 2-π sr) and qualitative impact on model chemical schemes. MDAFs derived from $j(NO_2)$ were found to be seasonally similar around the UK, but specific to local environments at higher time resolutions, demonstrating the importance of local j-value measurements. Downwelling (2-π) MDAFs demonstrated a slight increase with solar zenith angle (SZA), which was amplified when measurements of upwelling $j(NO_2)$ were considered (4-π). Increased surface albedo (snow cover) resulted in approximately 36% lower downwelling compared with 4-π MDAF, but the difference was negligible at other times. Derivations of MDAF for the 12 different atmospheric photolysis reactions were grouped using hierarchical cluster analysis (HCA). The groupings of the photolysis reactions were found to be driven by the extent to which a species photodissociates at longer (UVA) wavelengths. MDAFs derived from $j(NO_2)$ measurements were deemed an applicable reference for local adjustment of the j-values for other photodissociations at wavelengths >350 nm. For j-values of photodissociations at shorter wavelengths, adjustment using MDAFs based on a reference of $j(O^1D)$ resulted in lower total error. The presence of clouds had a greater influence on reducing cloud-free model results of $j(NO_2)$ (approx. 45%). Shorter wavelengths, such as those required for the photolysis rate constant $j(O^1D)$, are scattered more readily in clear skies, and thus resulted in a lower magnitude

difference (20%).

The other part of this PhD investigated atmospheric composition at the two UK supersites, by assessing the impact of the relocation of the southern EMEP supersite from Harwell to Chilbolton Observatory, and deploying an iodide chemical ionisation mass spectrometer (I^- CIMS) to measure NO_y species at the northern supersite (Auchencorth Moss). Meteorological normalisation was used on a concatenated time series of pollutant concentrations pre- and post-relocation from Harwell to Chilbolton Observatory, to identify any resulting effects of the move on these time series. Of all the species considered, only nitrogen oxides (NO_x) and ammonia (NH_3) had a step change in concentration, both increasing. The additional contributing sources at Chilbolton Observatory were identified. As a consequence, the long-term time series of NO_x and NH_3 should be considered to be restarted following the relocation, and the new site not strictly representative of the wider area it is intended to be. The aim of the CIMS study at Auchencorth Moss was to measure HNO_3 and N_2O_5 to quantify the interference in co-located MARGA measurements, as well as to contribute the first Scottish $ClNO_2$ measurements. The challenges of this study, and future work required is discussed.

This PhD research has demonstrated a new potential application of meteorological normalisation for air quality site relocations, which will become more pertinent in future years where background sites will on occasion need to be relocated due to local development. Furthermore, this study has emphasised the importance of measuring local photolysis rate constants to account for highly variable local conditions. It provides discussion around making existing measurements standardised and accessible, so as to make more frequent model validation or implementation of MDAF-like metrics easier, and to improve modelled estimations of local photolysis rate constants without significantly increasing computational cost. This PhD research explores the ongoing need to measure both atmospheric chemical components and photolysis rate constants to understand changes in the atmosphere as pollutant emission abatement policies are implemented under real local conditions.

Acknowledgements

First and foremost, I'd like to thank my supervisors for their support, advice and encouragement from my interview to my submission. Dr Marsailidh Twigg allowed me to feel like I always had someone in my corner, and kept me focussed on the technical details of everything I did. Dr Christine Braban has never let me feel like a problem was insurmountable, and encouraged me to be more ambitious with my work goals. Professor Mathew Heal has been a consistent source of help and guidance in all areas of my PhD, and never failed to give me fast feedback on my written work. Through our regular meetings, they have helped guide me through this PhD research, offering me access to their extensive knowledge and experience through invaluable discussions about the work I have presented here, and the work that didn't make it. They never made me feel like I was wasting their time, and believed in me when I didn't believe in myself. I consider myself incredibly lucky to have worked with and learned from them all, and to them I am truly grateful.

I want to thank the UKCEH field team for their support with my field studies at Auchencorth Moss, particularly Ivan Simmons, Sarah Leeson, Duncan Harvevy, Dr Matthew Jones, Karen Yeung and Neil Mullinger. Similarly, I am grateful for the help of Darcy Ladd (STFC) for the remote support at Chilbolton Observatory, when the Covid-19 pandemic prevented me from travelling there myself.

I'd like to thank Dr Richard Kift (University of Manchester) and Dr Lisa Whalley (Univeristy of Leeds) for providing instrument support and data from the spectral radiometers used in Chapters 3 and 4, respectively. I am incredibly grateful for the contribution of data to this work, generously provided by staff at Ricardo Energy & Environ-

ment (Stuart Ritchie, Chris Conolly and Agnieszka Sanocka), the Met Office (Dr Paul Agnew and James McGregor), the University of Manchester (Dr Nicholas Marsden) and Chilbolton Observatory (Judith Jeffery, STFC). This work would not exist without them.

I also thank the members of the MacAQUE (Modelling and measuring atmospheric chemistry and air quality at Edinburgh) for creating a great working atmosphere at UKCEH and the University of Edinburgh, through enjoyable group meetings, thoughtful discussions and some great company in the office.

I have been lucky enough to appreciate the support of so many friends and family members that have helped me to reach this point. Special mentions must go to my parents, who always believe in me and have shown me time and time again what determination looks like. To Jake, for being a great sounding board, a helpful proof-reader, and for keeping me in great company through multiple lockdowns. To Laura, for coxing me through life and never once letting me doubt myself. To my rowing teammates (at ULBC and SABC) for providing me with an outlet, and some amazing memories. And finally, thank you to Siôn, for everything.

Contents

List of Tables

List of Figures

List of Acronyms

Acronym, abbreviation or symbol	Definition
θ	Solar zenith angle (and SZA)
λ	Wavelength
σ	Absorption cross-section
ϕ	Quantum yield
ADMS	Atmospheric Dispersion Modelling System
AERMOD	American Meteorological Society and US Environmental Protection Agency Regulatory Model
AERONET	AErosol RObotic NETwork
AGANet	UK Acid Gases and Aerosols Monitoring Network
AOD	Aerosol Optical Depth
AU	Auchencorth Moss
AURN	Automatic Urban and Rural Network
ACTRIS	Aerosols, Clouds and Trace gases Research Infrastructure
AQMA	Air Quality Monitoring Areas
CA	Cardington
CAPS	Cavity Attenuated Phase Shift
CAO	Chilbolton Atmospheric Observatory
CCD	Charge-coupled device
CDC	Collisional dissociation chamber
CIMS	Chemical ionisation mass spectrometer
CLRTAP	Convention on Long-Range Transboundary Air Pollution
CMAQ	Community Multiscale Air Quality modelling system
CTM	Chemical transport model
Defra	UK Department for Environment, Food & Rural Affairs
DELTA	DEnuder for Long-Term Atmospheric sampling
DOAS	Differential Optical Absorption Spectroscopy
DU	Dobson Unit
$E(\lambda)$	Spectral global irradiance
EMEP	European Monitoring and Evaluation Programme
EMEP-CCC	EMEP Chemical Coordinating Centre
EMEP MSC-W	EMEP Meteorological Synthesizing Centre - West
FCA	Fractionally cloudy atmosphere
$F(\lambda)$	Spectral actinic flux
FR	Filter radiometer
GC-ECD	Gas chromatography with electron capture detection
GRAEGOR	GRadient of AErosol and Gases On-line Registrator
GRS	Generic Reaction Set
HCA	Hierarchical Cluster Analysis

ICA	Independent column atmosphere
IMR	Ion molecule region
IUPAC	International Union of Pure and Applied Chemistry
j	Photolysis rate constant, photolysis frequency or j-value
L	Radiance
LOD	Limit of detection
LOPAP	LOng Path liquid Absorption Photometer
MA	Manchester
MARGA	Monitor for AeRosols and Gases in ambient Air
MAQS	Manchester Air Quality Supersite
MCM	Master Chemical Mechanism
MDAF	Measurement-driven adjustment factor
MGLY	Methy glyoxal
m/z	Mass-to-charge ratio
NAEI	National Atmospheric Emissions Inventory
NOAA	National Oceanic and Atmospheric Administration
OMI	Ozone Monitoring Instrument
PA	Peroxyacetyl (radical)
PAA	Peroxyacetic acid
PAN	Peroxyacetyl nitrate
PM	Particulate matter
ppm	Parts per billion
ppm	Parts per million
ppt	Parts per trillion
PSS	Photostationary state
RACM	Regional Atmospheric Chemistry Mechanism
RADM	Regional Acid Dispersion Model
RSD	Relative standard deviation
SIA	Secondary inorganic aerosol
SOA	Secondary organic aerosol
SR	Spectral radiometer
sr	Steradian
SSA	Single scattering albedo
SZA	Solar zenith angle (and θ)
TUV	Tropospheric Ultraviolet & Visible (model)
UKEAP	UK Eutrophying and Acidifying atmospheric Pollutants
UNECE	United Nations Economic Commission for Europe
UTC	Coordinated Universal Time
VOC	Volatile Organic Compound
WRD	Wet rotating denuder

Chapter 1

Introduction

The bulk composition of the Earth's dry atmosphere is 78% nitrogen (N_2), 21% oxygen (O_2) and 0.93% argon (Prinn, 2003). The remaining 0.1% contains a wide variety of reactive species which drive chemistry within the atmosphere (Jacob, 1999), despite being present in small mixing ratios (i.e. in parts per million, billion or trillion by volume; ppm, ppb and ppt, respectively). These species are predominantly located in the troposphere, the layer of the atmosphere closest to the Earth's surface. The troposphere can be further divided into two layers: the "free troposphere" above, and the "boundary layer" below. The boundary layer is closest to, and therefore most influenced by, the surface. Concentrations of atmospheric pollutants in this layer are affected by the quantity of sources and sinks present (such as emission and deposition, respectively), surface topography (like valleys or urban street canyons), and local meteorological conditions (e.g. wind speed and direction or solar radiation affecting long-range transport and photolysis, respectively). Primary pollutants are emitted directly into the atmosphere, from both natural and anthropogenic sources. Secondary pollutants are formed in the atmosphere by reactions between atmospheric species, including those driven by the presence of sunlight.

Many of these pollutants have detrimental effects on human and environmental health. In order to investigate these effects and formulate effective mitigation actions, it is es-

sential to monitor their local concentrations, and meteorological variables which could affect them (such as the amount of solar radiation, which drives photolysis reactions). The work presented in this thesis focuses on the monitoring aspects for reactive oxidised nitrogen species (NO_y), but also for other pollutants of concern. The specific aims of this thesis are outlined in Section 1.7. This chapter provides an introduction to the thesis work overall, but further introduction and methods material are presented in individual results chapters.

1.1 Tropospheric chemistry and local air quality

Across Europe, atmospheric pollutants including nitrogen dioxide (NO_2), ammonia (NH_3), particulate matter (PM_{10} and $PM_{2.5}$), sulphur dioxide (SO_2) and ozone (O_3) are monitored with fairly high spatio-temporal resolution, to identify long-term trends in pollutant concentrations, and transboundary transport of pollution (see Section 1.2). Nitrogen oxides (NO_x; the collective term for nitric oxide (NO) and NO_2) are released into the atmosphere from combustion reactions, such as in vehicle exhausts (AQEG, 2004). The rate and proximity of NO_x emissions affect local measured concentrations of NO_2, as does the rate of pollutant dispersion, amount of exposure to solar radiation, and potential for subsequent chemical reactions. For these reasons, concentrations of NO_2 demonstrate high spatial variability, with largest concentrations found closest to the source (Cyrys et al., 2012; Kenagy et al., 2016). Short- and long-term exposure to NO_2 can have significant implications for human health (Brunekreef & Holgate, 2002; COMEAP, 2018). NO_2 is a key precursor to many atmospheric NO_y species (the collective term for all gaseous and particulate oxidised N species), demonstrated by the simplified schematic (Figure 1.1) and discussion in Section 1.4.

Photolysis of NO_2 is the main source of tropospheric ozone (O_3):

$$NO_2 + h\nu \longrightarrow NO + O(^3P) \tag{R1.1}$$

$$O(^3P) + O_2 + M \longrightarrow O_3 + M \tag{R1.2}$$

Short-term exposure to tropospheric ozone has been shown to be particularly harmful to human health (Orellano et al., 2020; Vicedo-Cabrera et al., 2020) and vegetation (RoTAP, 2012). Concentrations of O_3 are lowest near to NO_x sources, due to titration from the excess NO present (R1.3).

$$NO + O_3 \longrightarrow NO_2 + O_2 \tag{R1.3}$$

As a result, O_3 concentrations increase further from these sources, with concentrations typically higher in rural locations compared with urban (AQEG, 2009). During daylight hours, NO_x and O_3 concentrations are in steady state, referred to as the photostationary state (PSS), shown in R1.1-R1.3. Deviations from the PSS occur in the presence of volatile organic compounds (VOCs), peroxy radicals from the oxidation of which convert NO back to NO_2 (R1.4 and R1.5), resulting in increased concentrations of O_3.

$$NO + HO_2 \longrightarrow NO_2 + OH \tag{R1.4}$$

$$NO + RO_2 \longrightarrow NO_2 + RO \tag{R1.5}$$

The hydroperoxyl (HO_2) and organic peroxy (RO_2) radicals are the products of analogous oxidation reactions between the hydroxyl radical (OH) and carbon monoxide (CO) or VOCs. The rapid cycling of HO_2 radicals with NO (R1.4) or O_3 (R1.6) reforms OH radicals.

$$O_3 + HO_2 \longrightarrow OH + 2\,O_2 \tag{R1.6}$$

The close coupling of OH and HO_2 radicals means they are collectively termed HO_x (= OH and HO_2), and are known to be important species in local in-situ chemistry, initiating and propagating chain reactions which lead to further formation of tropospheric O_3 (Stone et al., 2012).

Ammonia (NH_3) is primarily emitted from agricultural sources (Misselbrook et al., 2000), typically in rural environments. NH_3 is the main base for the neutralisation of atmospheric acidic gases, such as HNO_3 and SO_2, by forming secondary inorganic aerosols (SIA) such as ammonium nitrate (NH_4NO_3; R1.7) and ammonium sulphate ($(NH_4)_2SO_4$; R1.8), i.e. ammonium-containing particulate matter (PM).

$$\mathrm{HNO_3 + NH_3 \rightleftharpoons NH_4NO_3} \tag{R1.7}$$

$$\mathrm{H_2SO_4 + 2\,NH_3 \rightleftharpoons (NH_4)_2SO_4} \tag{R1.8}$$

Ammonia has a relatively short atmospheric lifetime as it can rapidly deposit resulting in significant environmental risks on a local scale (Vogt et al., 2013), but its conversion to ammonium (NH_4^+) in SIA lengthens its atmospheric lifetime up to several days (Vieno et al., 2014), expanding the area impacted. Deposition of NH_x (= NH_3 and NH_4^+) can cause soil acidification, as well as terrestrial and freshwater habitat and biodiversity loss due to eutrophication, i.e. to excess nutrient loading (Sutton & Fowler, 2002; Sutton et al., 2009).

In northwest Europe, pollution events are frequently dominated by NH_4NO_3 (Vieno et al., 2014). Similarly to primary PM emitted from anthropogenic sources (e.g. vehicle exhausts), this secondary ammonium-containing PM is predominantly in the "fine" mode, less than 2.5 μm in diameter ($PM_{2.5}$). Larger PM fractions such as PM_{coarse} (PM_{10} – $PM_{2.5}$, where PM_{10} is <10 μm in diameter) tend to be formed naturally, from sources such as sea spray (Twigg et al., 2015). Smaller size fractions of PM pose a greater health risk, as these can be transported further into the respiratory system (Brunekreef & Hol-

gate, 2002). This can lead to cardiovascular problems (WHO, 2013a) and premature mortality from long-term exposure (Chen & Hoek, 2020).

Sulphur dioxide (SO_2) is largely generated from combustion of fuels containing sulphur. However biogenic sources which include volcanoes and oxidation of sulphur-containing gases, such as dimethyl sulphide (DMS), can make important contributions to background concentrations in rural locations, or perturbation events of increased SO_2 (Twigg et al., 2016). SO_2 contributes to secondary PM pollution by acting as a precursor for sulphuric acid (H_2SO_4), which is neutralised by NH_3 to form $(NH_4)_2SO_4$ (R1.8).

The UNECE Convention on Long-range Transboundary Air Pollution (CLRTAP) concluded that European SO_2 emissions fell by 73% between 1980 and 2004, in part a result of policy regulation and successful implementation of mitigation measures (Vestreng et al., 2007). The decline in SO_2 emissions is reflected in long-term SO_2 observations across the UK (Tang et al., 2018b), while the impact of step-changes in regulations in the sulphur content of marine fuels can be visualised using meteorological normalisation of time series of SO_2 measurements close to shipping lanes (Grange & Carslaw, 2019). A decreasing trend is also observed in deposition of sulphur to terrestrial and aquatic ecosystems (RoTAP, 2012). SO_2 demonstrates that policy regulations in primary emissions can have a marked impact on ambient concentrations.

1.2 Monitoring networks

In order to determine compliance with air quality standards, help establish achievable mitigation strategies and track these implemented measures, reliable networks measuring pollutant concentrations are critical (Pope & Wu, 2014). In the UK the Automatic Urban and Rural Network (AURN; Defra, 2021e) provides accurate and comprehensive air quality monitoring data for particulate matter ($PM_{2.5}$, PM_{10}), SO_2, NO_x, O_3 and carbon monoxide (CO) to fulfil the UK Government's statutory reporting obligations un-

der the EU Air Quality Directive 2008/50/EC (European Council, 2008) to demonstrate compliance with limit values set. The European Monitoring and Evaluation Programme (EMEP; www.emep.int) network operates under the Gothenburg Protocol (part of the Convention for Long-Range Transmission of Air Pollutants; CLRTAP; UNECE, 2012). EMEP aims to quantify and assess long-term trends in measured pollutants which are used to inform policy, as well as quantify the significance of long-range transmission of air pollutants and their fluxes across boundaries (Tørseth et al., 2012).

Distribution of monitoring sites within a network across a wide area allows for the identification of spatial patterns and transboundary movement of pollution, while long-term measurements provide the opportunity to characterise emission patterns, and separate long-term trends in concentration from interannual variability (Tørseth et al., 2012). It is important that measurements made across the network use a standardised methodology, in order for data to be comparable between sites (Malley et al., 2016b). The advantage of established spatio-temporal measurements is that it provides an extensive dataset from which to evaluate the performance of atmospheric models, which are used to assess health and environmental impacts (Fagerli & Aas, 2008; Cape, 2009) and forecast potential future scenarios (AQEG, 2015). Establishing monitoring networks in new areas (from local to regional) are dependent on financial constraints of the managing body, environmental priorities of the area, and political decisions. As such, new networks are often focussed on urbanised areas where population density, and therefore risk of exposure, is highest (Joly & Peuch, 2012) and where exceedances of air quality objectives are most likely to occur (Kuhlbusch et al., 2014).

Site locations within monitoring networks are an important feature, and are selected based on the overarching aim of the network. This can include the assessment of public exposure to air pollution, where measurements would be made in populated locations, as well as: long-term trend analysis, requiring sites in rural locations unaffected by any single source; model validation, sites well distributed within the model domain in a va-

riety of site types; for scientific objectives, such as where sites require co-location with other instrumentation; or reporting compliance to limit values, where sites need to measure pollution "hotspots" (Spangl et al., 2007). Since measurements within networks are generally collected at a limited number of sites, each is assumed to be representative of its surrounding area. This concept of representativeness of a monitoring site has not yet been quantitatively, or unambiguously, defined (Spangl et al., 2007; Martín et al., 2015; Kracht et al., 2017). This can be an issue as concentrations may vary significantly between two neighbouring sites, which is particularly important in urban locations where local concentrations are likely to be affected by multiple sources of pollution. It is also important at rural sites, as these are usually assumed to be representative of a much wider area (explored further in Chapter 2), but can vary over time as a result of changes in local development (Latif et al., 2014).

The AURN is the largest UK monitoring network used for compliance reporting against the UK and EU Limit Values and for public information (Defra, 2021e). However the number of site types within the network that have measurements available for public information, allow the network to contribute towards tackling a number of air quality aims. Representativeness of each monitoring station within the AURN is identified by a site-type label based on specific recorded criteria (Telling et al., 2009). The general classification of each site is separated into either "remote", "rural", "suburban" or "urban" locations. Within suburban or urban areas, monitoring stations can have additional classification labels based on the proximity and type of specific individual sources. These include "background", which should not be unduly influenced by any one specific source; "industrial", measuring at the point of maximum impact of a specific point source; and traffic, which are located within 1 m ("kerbside") or 1–5 m ("roadside") of the kerb (Telling et al., 2009).

The EMEP network is an example of a network aimed to evaluate large-scale trends and variability in pollutants and assess regional air quality models. As such, the require-

ment is for measurements of rural background air composition that is not significantly influenced by any individual emission source. The EMEP network is comprised of >130 monitoring sites throughout Europe (EMEP, 2020a,b). Each monitoring station within the network is selected to be a rural representative of the surrounding area (approx. 50 km^2), with standardised siting criteria and sampling methodologies to ensure comparability (EMEP, 2014). Within the UK there are currently two operational level II/III EMEP sites, Auchencorth Moss (southeast Scotland) and Chilbolton Observatory (Hampshire, south England), to represent the north and south of the country, respectively. These are referred to as "supersites" due to the quantity of instrumentation and variety of co-located measurements (UNECE, 2004b). The two sites host a number of UK air quality monitoring networks including the AURN.

Across the AURN network, NO_2 is monitored at 159 sites (Defra, 2018c) using a chemiluminescence methodology. In contrast, other NO_y species are not monitored with much spatial frequency. Nitrous acid (HONO) and nitric acid (HNO_3) are only measured at hourly resolution at the two UK supersites with a Monitor for AeRosols and Gases (MARGA; Metrohm Applikon, NL). Monthly low-cost measurements of HNO_3 are contributed by 30 sites in the UK Acid Gases and Aerosols Monitoring Network (AGANet). These measurements are made using a low-cost DEnuder for Long-Term Air sampling (DELTA; Tang et al., 2018b). Each of these measurement methods has been demonstrated to be subject to interference (discussed in Section 1.5).

Similarly, the UK land observation network run by the UK Met Office makes observations of ambient meteorological variables to determine the present state of the atmosphere, and provide standardised measurements on which to base future weather forecasts (Met Office, 2021). Since meteorological variables, like atmospheric concentrations, can be highly influenced by local effects, sites are intended to be representative of a wider area, such as far enough away from buildings, trees and topographical features that could affect measurement of temperature, wind and solar radiation.

1.3 Photolysis overview

1.3.1 HO_x radicals

Solar radiation is an important driver of tropospheric chemistry. This is largely due to photodissociation reactions releasing highly reactive radical species, which initiate and propagate many chain reactions within the troposphere. The hydroxyl radical (OH) is one of the primary oxidants in the atmosphere (Levy, 1972). OH initiates the oxidation of many trace gases, including VOCs, thus controlling their atmospheric lifetimes. This reactivity means OH has a very short atmospheric lifetime (<1 s; Monks, 2005) but can reach maximum daytime concentrations of ca. 10^6 cm^{-3} in the midlatitudes (Holland et al., 2003; Lew et al., 2020). The hydroxyl radical is ubiquitous through the troposphere, owing to the abundance of ozone, water vapour and solar radiation (R1.9 and R1.10):

$$\mathrm{O_3} + h\nu \longrightarrow \mathrm{O(^1D)} + \mathrm{O_2} \tag{R1.9}$$

$$\mathrm{O(^1D)} + \mathrm{H_2O} \longrightarrow 2\,\mathrm{OH} \tag{R1.10}$$

The fraction of O(^{1}D) atoms that form OH, rather than proceeding via a collisional quenching reaction to O(^{3}P) with either N_2 or O_2, depends on the concentration of H_2O present. This fraction is typically around 10% in the boundary layer (Monks, 2005). HO_2 radicals are produced by a two-stage process, initiated by the photolysis of formaldehyde (HCHO; R1.11 to R1.13) by UV radiation.

$$\mathrm{HCHO} + h\nu \longrightarrow \mathrm{H} + \mathrm{HCO} \tag{R1.11}$$

$$\mathrm{H} + \mathrm{O_2} + \mathrm{M} \longrightarrow \mathrm{HO_2} + \mathrm{M} \tag{R1.12}$$

$$\mathrm{HCO} + \mathrm{O_2} \longrightarrow \mathrm{HO_2} + \mathrm{CO} \tag{R1.13}$$

Sources of formaldehyde include the oxidation of non-methane VOCs, fuel combustion, biomass burning and vegetation. HO_x radicals can also be formed from a number of other photolytic sources, such as nitrous acid (HONO), hydrogen peroxide (H_2O_2), other VOCs, and VOC oxidation intermediates such as acetaldehyde (CH_3CHO), discussed further in Sections (Section 1.4.1 and Chapter 4). Maximum midday concentrations of HO_2 are also relatively small, but can be $\geq$100 times greater than OH concentrations (Holland et al., 2003; Monks, 2005; Lew et al., 2020).

1.3.2 Measurement of solar radiation

Solar radiation can be quantified using a number of different methods. The majority of existing measurements occur in the form of solar irradiance, the radiation incident of a flat surface, typically horizontal. The spectral global irradiance as a function of wavelength, $E(\lambda)$, can be broken down into the radiance (L) weighted by the cosine of the angle between the incident direction and the zenith, directly above the point of observation and vertically opposite to the Earth's gravitational pull (known as the solar zenith angle; θ or SZA), integrated over a hemisphere:

$$E(\lambda) = \int_0^{2\pi} \int_0^{\frac{\pi}{2}} L(\lambda, \theta, \phi) \cos(\theta) \sin(\theta) \, \mathrm{d}\theta \mathrm{d}\phi \tag{1.1}$$

Alternatively, the spectral actinic flux, $F(\lambda)$, describes the number of photons incident at a point in the atmosphere (Madronich, 1987) from all possible directions, i.e. the unweighted radiance integrated over a sphere:

$$F(\lambda = \int_0^{2\pi} \int_{-\frac{\pi}{2}}^{\frac{\pi}{2}} L(\lambda, \theta, \phi) \sin(\theta) \, \mathrm{d}\theta \mathrm{d}\phi \tag{1.2}$$

In both equations (Eq. 1.1 and 1.2), θ is the solar zenith angle (discussed above), and ϕ is the azimuth angle (horizontal angle between the centre of the suns disc and true North). $L(\lambda, \theta, \phi)$ is the radiance distribution, and is dependent on scattering throughout the atmosphere before reaching the point of measurement. In turn, this is dependent on the

atmospheric composition and surface properties (Webb et al., 2002b).

1.3.3 Scattering and absorption of radiation

Atmospheric attenuation of UV radiation occurs from a combination of absorption and scattering. When absorbed, the energy of a photon is usually lost to breakage of chemical bonds or heat, and is removed from the radiation field (Madronich, 1987). For example, wavelengths of light <290 nm are absorbed by stratospheric ozone and oxygen before reaching the troposphere, limiting the range of wavelengths reaching ground level. The total ozone column (the amount of ozone between the top of the atmosphere and ground level) is therefore an important variable in determining the amount of radiation at ground level. Conversely, scattering changes the direction and propagation of radiation.

Both solar irradiance and actinic flux represent a total comprised of direct and diffuse radiation. For example, the total actinic flux can be broken down into the constituent parts of $F = F_0 + F_\downarrow + F_\uparrow$, where F_0 is the direct beam, and $F_\downarrow$ and $F_\uparrow$ indicate the diffuse components of down- and upwelling actinic flux (respectively) which have been scattered before reaching the surface. Similarly for solar irradiance, $E = E_0 + E_\downarrow$ when measuring across a horizontal surface (Kylling et al., 2003).

The direct-diffuse partitioning of radiation depends on the altitude, wavelength, solar zenith angle (i.e. on the effective path length of light), and the number of scatterers along the given path length (Webb et al., 2002b). More scatterers (e.g. cloud particles, aerosols) along the path length increase the likelihood of actinic flux scattering before it reaches the point of observation. This is important when considering actinic flux available at lower altitudes, and higher solar zenith angles. In the stratosphere, actinic flux is typically dominated by direct radiation, but in the lower troposphere, more than 50% of actinic flux is contributed by diffuse radiation (Heard, 2006).

Diffuse radiation, by nature, is dispersed in many directions. Scattering properties of particles depend primarily on their size, as the direction of scattering is dependent on their circumference (Wild et al., 2000). In a clean atmosphere, Rayleigh scattering dominates. This occurs with particles which have a circumference much less than the wavelength of light (e.g. air molecules), and tend to scatter isotropically with an efficiency of λ^{-4} (Webb et al., 2002b). For larger particles (e.g. cloud and aerosol), scattering efficiency is less dependent on wavelength, but propagates mainly in the forward direction (Mie scattering; Wallace & Hobbs, 2006). Cloud layers can prevent direct radiation from reaching the surface, leading to low light levels observed beneath. However broken clouds, and other local scatterers, can lead to enhancements in downwelling radiation at the surface point of observation, compared with a clear sky (Schade et al., 2007).

Surface albedo, the fraction of incident light reflected from the surface, can contribute a significant quantity to upwelling radiation. For example, in the UK seasonal changes in weather can lead to large variations in surface albedo throughout the year. Grassy ground cover, such as that in summer, has a surface albedo of around 0.2, but when covered with snow in the winter months, the surface albedo can increase to 0.9 (Lee-Taylor & Madronich, 2002).

1.3.4 Molecule-specific radiation absorption and photolysis

For models of chemical mechanisms, it is essential to know the rate of each reaction. For photolysis reactions, quantifying the rate of photodissociation for each species is heavily dependent on the availability of actinic flux. For an example molecule AB, the rate of the photodissociation reaction (R1.14), is defined with Eq. 1.3.

$$\mathrm{AB} + h\nu \longrightarrow \mathrm{A} + \mathrm{B} \tag{R1.14}$$

$$-\frac{d[\mathrm{AB}]}{dt} = j_{\mathrm{AB}}[\mathrm{AB}] \tag{1.3}$$

Photodissociation reactions are characterised by *j*, the photolysis frequency, which is dependent on local actinic flux and molecular-specific parameters, such as the absorption cross-section (σ) and quantum yield (ϕ). In turn, these molecular parameters are a function of temperature, pressure and wavelength. As such, the photolysis frequency (*j*) is represented by the integral of the product of actinic flux (F), absorption cross-section (σ) and quantum yield (ϕ), in Eq. 1.4.

$$j = \int_{\lambda_1}^{\lambda_2} \sigma(\lambda, T, p)\ \phi(\lambda, T, p)\ F(\lambda)\ \mathrm{d}\lambda \tag{1.4}$$

In this equation, λ_2 and λ_1 are the wavelength limits of photolysis. Reactions at ground level are driven by wavelengths of light >290 nm, a result of the absorption of shorter-wave UV radiation by stratospheric O_3 molecules. The upper limit for this wavelength range depends on the absorption band of the molecule for which *j* is being calculated. These molecule-specific parameters are fundamental properties of a molecule, which can be derived in a laboratory setting, and applied to a wide variety of ambient atmospheric data without being determined on-site. However, as discussed earlier, actinic flux is highly variable at a given site, making predictions of this component of Eq. 1.4 more difficult.

1.3.5 Radiative transfer models

Radiative transfer models use the position of the Earth in relation to the sun (w.r.t. time and date), site location and altitude to predict the paths of photons from the top of the atmosphere to the point of observation. Accuracy can be improved by including knowledge of the atmospheric column above the site, including various measured meteorological and physical variables that could affect the light path (e.g. aerosol optical depth, ozone column, single scattering albedo, surface albedo, cloud height etc.).

The model domain is usually split into atmospheric layers, where the propagation of short-wave radiation can be sequentially calculated separately within each. Each layer

is homogeneous in its distribution of absorbers (e.g. O_2, O_3, SO_2, NO_2, cloud and aerosol particles) and scatterers (Rayleigh for air; Mie for particles). This approach allows for vertical distributions in absorbers and scatterers to more closely replicate atmospheric distribution (Lee-Taylor & Madronich, 2002).

Some models are based upon faster two-stream methods, e.g., Madronich (1987), which reduce the computational cost required to integrate the radiative transfer equation, as only radiation propagating along two discrete directions are considered. However, this restriction leads to a lack of accuracy (Wild et al., 2000). More detailed multi-stream approaches can provide a higher level of accuracy, particularly for an anisotropic medium (van Oss & Spurr, 2002), but result in an increased computational cost. Similarly, in lieu of a complex and resource-consuming full-spherical radiative transfer model, a pseudo-spherical correction can provide good accuracy at high solar elevations, approximately <75° SZA (Kylling et al., 1995; Caudill et al., 1997).

1.4 Importance of NO_y species

Total oxidised reactive nitrogen (NO_y) includes NO_x and its subsequent oxidation products, such as nitrous acid (HONO), nitric acid (HNO_3), dinitrogen pentoxide (N_2O_5), nitryl chloride ($ClNO_2$), sum of all alkyl nitrates (ΣANs or $RONO_2$), peroxy nitrates (ΣPNs or RO_2NO_2) and acyl peroxy nitrates (ΣAPNs or $RC(O)O_2NO_2$), etc. These species are of great importance to overall tropospheric chemistry in both urban and remote areas, on local and regional scales. Knowledge of each species sources, sinks and interactions with other species are critical to understanding this chemistry. A schematic overview of their interlinked chemistry is presented in Figure 1.1, while discussion of the importance of HONO, HNO_3, N_2O_5, $ClNO_2$ and peroxyacetyl nitrate (PAN; $CH_3C(O)O_2NO_2$) are detailed in this section.

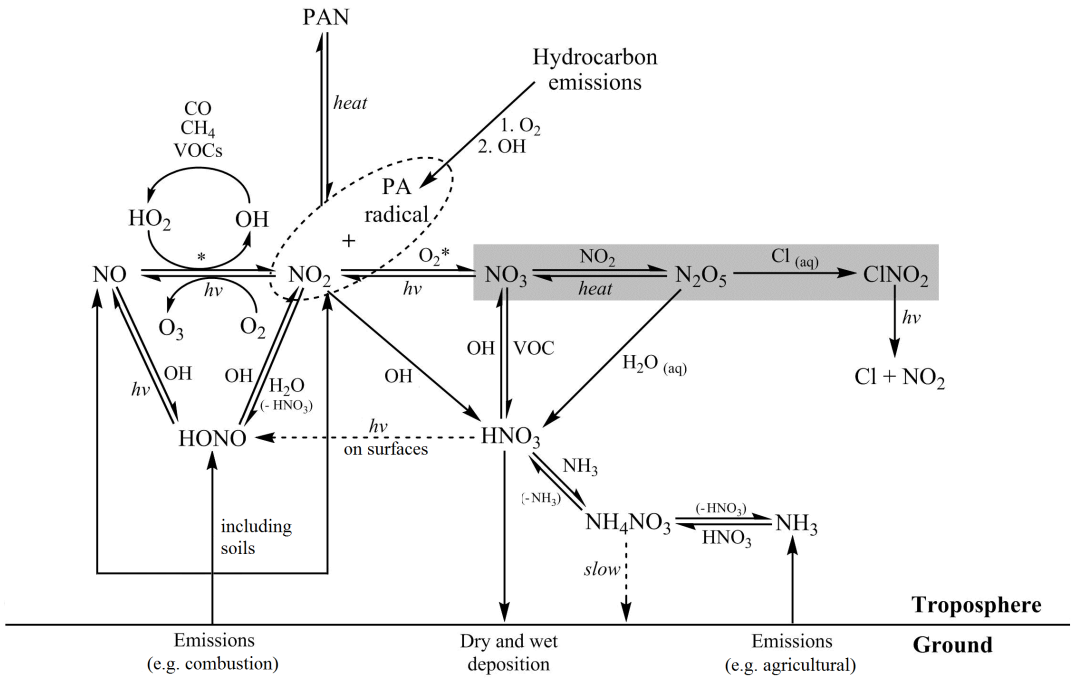

Figure 1.1: A simplified schematic of the atmospheric NO_y cycle, created from references cited in this chapter. The forward reactions in the grey box predominantly occur nocturnally. The two reactions labelled with an asterisk (*) occur diurnally, but at night are sinks of tropospheric ozone by: $NO + O_3 \longrightarrow NO_2 + O_2$ (R1.3) and $NO_2 + O_3 \longrightarrow NO_3 + O_2$. PA = peroxyacetyl.

1.4.1 Nitrous acid (HONO)

Nitrous acid (HONO) is an important atmospheric species in the boundary layer, as its photolysis leads to the formation of OH radicals (R1.15). This is of particular importance in urban areas where its concentrations are higher ($\sim$ppb), and can lead to HONO being the dominant local HO_x source (Kleffmann, 2007; Elshorbany et al., 2009; Villena et al., 2011; Lee et al., 2016; Ryan et al., 2018).

$$\mathrm{HONO} + h\nu \longrightarrow \mathrm{NO} + \mathrm{OH} \qquad \text{(R1.15)}$$

HONO can be produced by direct emission from anthropogenic sources such as vehicle emissions (Kramer et al., 2020) or from biogenic sources, like microbial activity in soil (Su et al., 2011). Secondary sources of HONO include the homogeneous reaction

between NO and OH during the day (R1.16; Kleffmann, 2007) or the predominant nocturnal heterogeneous reaction of NO_2 on humid surfaces (R1.17; Harrison et al., 1996; Spataro & Ianniello, 2014; Ren et al., 2020).

$$\mathrm{NO + OH + M \longrightarrow HONO + M} \tag{R1.16}$$

$$\mathrm{2\,NO_{2\,(g)} + H_2O_{\,(aq)} \longrightarrow HONO_{\,(g)} + HNO_{3\,(ads)}} \tag{R1.17}$$

The dependence on the presence of water for R1.17 was confirmed by the positive correlation between HONO/NO_2 and relative humidity (Bernard et al., 2016; Wang et al., 2017b). Further reaction of HONO with OH can result in a sink of both species during the day:

$$\mathrm{HONO + OH \longrightarrow H_2O + NO_2} \tag{R1.18}$$

However this is a minor sink of HONO compared to its photodissociation. Due to the strength of these diurnal sinks, HONO has a diurnal lifetime of <1 hour (Levy, 1972). Consequently, larger concentrations of HONO are observed during the night. Nocturnal accumulation of HONO results in a diurnal cycle which peaks in the early morning hours, and falls in the late afternoon (Bernard et al., 2016; Wang et al., 2017b).

The major photolytic sink of HONO (R1.15) leads to a shift in the oxidation capacity of the atmosphere in the morning hours, due to the production of OH radicals (Acker & Möller, 2007; Wang et al., 2017a; Stieger et al., 2018). It would follow that concentrations of HONO would be negligible during the daylight hours. However models have frequently been unable to account for all measured HONO without including unknown sources (Sörgel et al., 2011; Li et al., 2012; Michoud et al., 2014; Lee et al., 2016).

Suggestions for the missing source have included direct emissions from biomass burning, traffic (Kramer et al., 2020) and domestic heating (Kleffmann, 2007). In urban and other polluted areas, high concentrations of HONO were found to correlate well with

low wind speeds (Bernard et al., 2016), and scaled well with increased NO_2 mixing ratios (Acker & Möller, 2007). However at a rural forested site in Finland, concentrations were consistently greater than could be attributed to only road traffic (Makkonen et al., 2014). Su et al. (2011) report diurnal emissions of HONO from soil nitrate on fertilized agricultural land where soil pH is low, and Oswald et al. (2013) present laboratory studies that show HONO emission from neutral-basic soils in comparable quantities to NO. Vertically resolved HONO mixing ratios support this hypothesis, finding them to be strongly enhanced near the ground and decreasing further aloft (Young et al., 2012).

Stemmler et al. (2007) show that HONO is produced from the light-induced reduction of NO_2 on humic acid aerosols, in a laboratory study, but suggest this may only be a minor contributor. Other studies propose similar sources, such as photo-enhanced heterogeneous conversion of nitric acid and nitrate (HNO_3/NO_3^-) produced HONO when occurring on plant material in a laboratory study (Ye et al., 2016) and on particulate nitrate at a Chinese urban background site (Shi et al., 2020). Measured HONO could not be fully accounted for by Shi et al. (2020) in their box model simulation of the site, without including this daytime nitrate photolysis (R1.19).

$$\mathrm{HNO_3}\,/\mathrm{NO_3^-} + h\nu \longrightarrow \mathrm{HONO}/\mathrm{NO_2^-} + \mathrm{O} \qquad \text{(R1.19)}$$

1.4.2 Nitric acid (HNO_3)

Deposition is believed to be the dominant sink of HNO_3 from the atmosphere (Hanke et al., 2003), through rain-out and surface deposition (wet and dry, respectively). Due to the relatively high deposition velocity and "sticky" nature of HNO_3, this sink is considered an end-point for the atmospheric processing of NO_x (Hanke et al., 2003; Phillips et al., 2013a). In comparison, the photolysis of HNO_3 is a minor sink (R1.20), and produces significantly smaller quantities of OH radicals in the troposphere than does

the photolysis of HONO (R1.15).

$$\mathrm{HNO_3} + h\nu \longrightarrow \mathrm{OH} + \mathrm{NO_2} \tag{R1.20}$$

The products of this photodissociation can react homogeneously to produce HNO_3 (R1.21), forming a null cycle with R1.20.

$$\mathrm{NO_2} + \mathrm{OH} + \mathrm{M} \longrightarrow \mathrm{HNO_3} + \mathrm{M} \tag{R1.21}$$

Nocturnal reactions between the nitrate radical (NO_3) and VOCs, as well as the heterogeneous hydrolysis of N_2O_5 on water-containing aerosol particles and surfaces (R1.22), constitute sources of HNO_3 (Jacob, 2000; Phillips et al., 2013a).

$$\mathrm{N_2O_5} + \mathrm{H_2O}_{\,\text{(het)}} \longrightarrow 2\,\mathrm{HNO_3} \tag{R1.22}$$

The heterogeneous hydrolysis of N_2O_5 has been attributed to measurement interference of both HNO_3 and N_2O_5 (see Section 1.5 and Chapter 5). Neither of these processes occur diurnally, due to the efficient photolysis of NO_3 (R1.23 and R1.24; Brown & Stutz, 2012).

$$\mathrm{NO_3} + \mathrm{hv} \longrightarrow \mathrm{NO} + \mathrm{O_2} \tag{R1.23}$$

$$\mathrm{NO_3} + \mathrm{hv} \longrightarrow \mathrm{NO_2} + \mathrm{O} \tag{R1.24}$$

Although photochemically unstable during the day, NO_3 is one of the most important species in the nocturnal atmosphere (Brown & Stutz, 2012), as it reacts with biogenic VOCs (BVOCs) leading to the formation of secondary organic aerosols (SOA).

1.4.3 Dinitrogen pentoxide (N_2O_5)

NO_3 is formed through the oxidation of NO_2 with O_3 (R1.25), which can then form an equilibrium with NO_2 to form the reservoir species N_2O_5 (R1.26; Jacob, 2000; Ayers & Simpson, 2006; Brown & Stutz, 2012; Le Breton et al., 2014a). Since NO_3 is involved in its formation, N_2O_5 is also a night-time species.

$$NO_2 + O_3 \longrightarrow NO_3 + O_2 \tag{R1.25}$$

$$NO_2 + NO_3 + M \rightleftharpoons N_2O_5 + M \tag{R1.26}$$

The equilibrium between N_2O_5 and NO_3 is established within a few minutes in the atmosphere (Brown et al., 2003), but is strongly dependent on temperature. As such, the atmospheric lifetime of N_2O_5 covers a range from near 40 s at 290 K to more than 10 minutes at 270 K (Brown & Stutz, 2012). Formation of N_2O_5 is an important process in the removal of NO_x from the atmosphere, as its ease of hydrolysis to HNO_3 (R1.22) and subsequent fast deposition provides an efficient sink.

1.4.4 Nitryl chloride ($ClNO_2$)

Heterogeneous reactions of N_2O_5 on chloride-containing aerosols (R1.27) form a source of nitryl chloride ($ClNO_2$; Phillips et al., 2012).

$$N_2O_{5\,(g)} + Cl^-_{(aq)} \longrightarrow ClNO_{2\,(g)} + {NO_3}^-{}_{(aq)} \tag{R1.27}$$

Sources of Cl-containing aerosols can be both natural and anthropogenic in origin. Natural aerosols deliver the majority of chloride ions from sea salt, which is of particular importance on islands such as the UK, where the distance to the nearest coastline is often short. More land-locked continental sites have a greater contribution of particulate chloride from anthropogenic sources like fossil fuel combustion, biomass burning (Ahern et al., 2018) and application of road salt in winter for deicing purposes (McNamara

et al., 2020).

$ClNO_2$ is an important nocturnal reservoir of NO_2, which is regenerated following the photolysis of $ClNO_2$ after sunrise.

$$ClNO_2 + h\nu \longrightarrow Cl + NO_2 \quad \text{(R1.28)}$$

This photodissociation reaction also releases chlorine (Cl) atom radicals, which are a powerful tropospheric oxidant (Osthoff et al., 2008; Phillips et al., 2012; Young et al., 2012; Sarwar et al., 2014). Cl atoms alter the oxidising capacity of the atmosphere where produced, and increase the potential for tropospheric O_3 formation (Finlayson-Pitts et al., 1989), particularly near coastal areas (Osthoff et al., 2008; Sarwar et al., 2014).

In comparison to the OH radical, reactions between Cl atoms and some VOCs are established to be up to 200 times faster than the equivalent reaction with OH, as based on a comparison of rate constants between like-reactions (Young et al., 2014; Bannan et al., 2015). As most $ClNO_2$ photolysis takes place in the early hours of the day, when other oxidants such as NO_3 and OH are at their lowest abundances, $ClNO_2$ is recognised as increasingly important in early morning atmospheric chemistry (Osthoff et al., 2008).

1.4.5 Peroxyacetyl nitrate (PAN)

Peroxyacetyl nitrate (PAN) is an acyl peroxy nitrate (APN; $RC(O)O_2NO_2$) with the simplest structure, where R is a methyl group (CH_3; Slusher et al., 2004). These are secondary species, often formed alongside O_3 in polluted air masses (Singh & Hanst, 1981). PAN acts as a diurnal reservoir species of NO_2, governed by its stability at low temperatures, and demonstrated by its atmospheric lifetime of a few hours in the lower troposphere, and up to 6 months in the lower stratosphere (Khan et al., 2017). In forming PAN, VOCs such as acetaldehyde (R1.29) or methyl glyoxal (R1.30) are

oxidised to form the peroxyacetyl (PA) radical intermediate (Fischer et al., 2014), which then enters a thermal equilibrium reaction with NO_2 (R1.31).

$$CH_3CHO + OH \xrightarrow{O_2} CH_3C(O)OO + H_2O \quad \text{(R1.29)}$$

$$CH_3C(O)CHO + h\nu \xrightarrow{O_2} CH_3C(O)OO + HCO \quad \text{(R1.30)}$$

$$CH_3C(O)OO + NO_2 + M \rightleftharpoons PAN + M \quad \text{(R1.31)}$$

The formation of PAN (R1.31, forward) acts as a NO_x sink in the location in which it occurs, but does not result in long-term removal from the atmosphere (Brown et al., 2004). Instead it is mixed into the upper troposphere, becoming more stable as the air cools. The longer lifetime at these altitudes allows PAN to carry NO_2 substantial distances downwind of the emission source until it thermally decomposes, becoming a source of NO_x in the new location (Singh & Hanst, 1981). Where this dissociation occurs in rural atmospheres, PAN is a strong source of NO_x (Moxim et al., 1996) and consequently promotes the production of tropospheric ozone (LaFranchi et al., 2009).

1.5 Interference in monitoring measurements

1.5.1 Chemiluminescence measurements of NO_2

Trace gas monitoring networks are reliant on standardised measurements in order to make comparisons across the network, and as discussed earlier, provide evidence for compliance to EU and government-set air quality objectives (European Council, 2008). Therefore, monitoring networks must evaluate each individual measurement method employed for potential artefacts or chemical interferences that could result in reporting artificially higher or lower concentrations. Each measurement technique can be systematically assessed for interferences, but the overall potential for interference will vary between sites in a network due to differences in atmospheric composition and local meteorological conditions.

It is well established that NO_2 measurements made by chemiluminescence instruments which employ a molybdenum catalyst converter are subject to significant interferences. The principle of this measurement technique involves the detection of the chemiluminescence emitted from electronically excited NO_2 (NO_2^*; R1.33), formed from the reaction between ambient NO and excess O_3 (R1.32).

$$NO + O_3 \longrightarrow NO_2^* + O_2 \quad \text{(R1.32)}$$

$$NO_2^* \longrightarrow NO_2 + h\nu \quad (\text{peak} \quad \lambda{\sim}1200\,\text{nm}) \quad \text{(R1.33)}$$

These instruments alternate between two measurement modes. The first measures the concentration of NO in ambient air, and the second measures NO_x, the sum total of NO and NO_2, following a conversion of ambient NO_2 to NO. The difference in NO detected between these two modes determines the concentration of NO_2 present. Most frequently this conversion is carried out using a heated (300–350 °C) molybdenum catalyst, including at all AURN sites across the UK (AQEG, 2004; Telling et al., 2009). However, efficient thermal reduction of other NO_y species to NO (such as PAN and HNO_3) results in a significant amount of positive interference in the NO_2 measurement mode (Heard, 2006). Gerboles et al. (2003) report that where these chemiluminescence analysers are used to assess compliance to air quality objectives in rural areas, interference from NO_y (specifically PAN) and humidity is the largest source of error. Other studies confirm the importance of assessing interference in NO_2 measurements at rural sites, as this can be high, particularly in the summer months or when measuring photochemically-aged air masses (Steinbacher et al., 2007; Xu et al., 2013; Jung et al., 2017).

Converters with greater specificity for NO_2 were developed to use blue light to initiate the photolysis of NO_2 to NO (R1.1), based upon the weaker absorption of other NO_y species in the 300–400 nm range. Despite this, interferences have been demonstrated with blue light converters in both polluted and rural conditions. Positive interference

has been attributed to the photochemical production of NO_y species leading to an overestimation of NO_2, while negative interference has been demonstrated via the photolysis of VOCs generating peroxy radicals which react with ambient NO (Villena et al., 2012; Reed et al., 2016), and the incomplete conversion of NO_2 to NO (conversion efficiency <100%; Jung et al., 2017).

Interferences are not limited to the converter type. Other demonstrated sources occur within the reaction chamber, including negative interference from the quenching of excited NO_2*, and chemiluminescence emitted from ozonolysis reactions of alkenes during the instruments background cycle (Alam et al., 2020).

1.5.2 Denuder measurements of HONO and HNO_3

As mentioned in Section 1.2, continuous measurements of HONO and HNO_3 are very infrequent across the UK, being restricted to those using a MARGA instrument at the two UK EMEP supersites. This instrument is an online chromatography system that measures a large number of water-soluble gases and aerosols at an hourly resolution (Rumsey et al., 2014). Sampled air flows in a laminar fashion through a horizontal annular wet rotating denuder (WRD), a device which separates gases from aerosols with a thin film coating of a specifically chosen solution (Twigg et al., 2016).

Evidence of overestimations in HONO measurements made by a MARGA and a GRAEGOR (Gradient of Aerosols and Gases Online Registrator; utilising the same analytical method) have been demonstrated against a Long Path Absorption Photometer (LOPAP) in northern Europe (Ramsay et al., 2018; Ren et al., 2020). LOPAPs are designed to minimise chemical interference and artefacts that impact other wet-chemistry detection methods, showing good agreement with other measurement techniques, such as Differential Optical Absorption Spectroscopy (DOAS; Kleffmann et al., 2006). The MARGA interferences are attributed to a number of sources, including heterogeneous formation of HONO on inlet walls and the denuder coating, and photolytic artefacts introduced

in the sampling line. For these reasons, the length of the inlet, and thus the available surface area for heterogeneous reactions to occur, plays a large role in the potential for these interferences.

MARGA HNO_3 measurements demonstrate negative artefacts, reporting approximately half the concentrations as standard filter methods (Makkonen et al., 2014) as a result of loss on inlet walls. These loses will vary between individual instruments as inlet length is not standardised. Potential for positive artefacts has been briefly discussed in Section 1.4.2, as a consequence of N_2O_5 hydrolysis on alkaline or aqueous denuder coatings (R1.22). Phillips et al. (2013a) present this route as evidence for a considerable bias of up to 90% in nocturnal MARGA measurements.

Similarly, interferences resulting from denuder coatings in DELTA systems, which report monthly measurements at 30 UK sites as part of AGANet (see Section 1.2), were investigated at 5 sites in the UK. Denuders coated with a non-specific carbonate solution (K_2CO_3-glycerol) only measured 44% of the HNO_3 concentration reported from those using an NaCl coating (HNO_3-specific) at non-urban sites (UKEAP, 2015), giving DELTAs a correction factor of 0.45. The interferences in the K_2CO_3-glycerol coating arise through simultaneous collection of NO_y that forms nitrate ions (NO_3^-) on aqueous extracts of exposed denuders (Tang et al., 2018b). Potential interfering species include HONO, NO_2, N_2O_5 and PAN.

Where these interferences are not yet quantified (e.g. for MARGA at long-term monitoring sites), this provides a notable caveat to reported measurements, and considerable uncertainty where this data is used. This can have impacts on measurements used to validate atmospheric chemistry model outputs, reported to demonstrate compliance with national air quality objectives, and those used to underpin policy and mitigation strategies.

1.6 Missing validation in atmospheric chemistry modelling

Atmospheric chemistry and chemical transport models are used for a myriad of applications. Box models (simple model where the atmospheric domain is represented by one box) can be used to assess the detail of atmospheric chemistry in support of measurement campaigns (Dusanter et al., 2009; Young et al., 2014; Wang et al., 2017a; Tan et al., 2018; Whalley et al., 2018). Regional air quality can be assessed in terms of long-term trends in pollutant concentrations (Fagerli & Aas, 2008) and transboundary transport of emissions (Iversen, 1993; Vieno et al., 2014), including that for specific pollution events (Twigg et al., 2016; Vieno et al., 2016a). They can also be used to model future scenarios, and the impact of reducing emissions on ambient concentrations (Makar et al., 2009; Vieno et al., 2016b). The latter is often used by policy-makers to understand current public health, test the potential of mitigation strategies, and monitor the success of those implemented.

Models used to satisfy these objectives range from those with highly parameterised chemistry (e.g. ADMS or AERMOD), to explicit chemical transport models with full chemical mechanisms, such as the Master Chemical Mechanism (MCM, http://mcm.york.ac.uk; Saunders et al., 2003), Regional Atmospheric Chemistry Mechanism (RACM; Stockwell et al., 1997; Goliff et al., 2013) or Regional Acid Deposition Model (RADM) chemical mechanism (Stockwell et al., 1990).

All models require validation and improvement before they can be utilised for any form of air quality assessment. The procedure of model validation is to check whether predictions from the model are consistent with measured observations. It is critical to evaluate air quality and atmospheric chemistry models in this way, to ensure that model results are reasonable, reliable and an appropriate basis from which to make regulatory decisions and use as evidence in support of policy. For atmospheric pollutant concen-

trations, validation is an important step in the model development. The spatio-temporal frequency of measurements within monitoring networks provide a high likelihood of available measurements within the model domain, and provide frequent opportunities for validation (e.g. see monitoring stations presented by the Air Quality Index Project; https://aqicn.org/map/world/).

However, despite the importance of ensuring photolysis rate constants (also known as photolysis frequencies) are accurate in chemical mechanisms, including their impact on modelled concentrations (e.g. O_3; Chen et al., 2021), predicted j-values do not include this validation step, with the exception of specific measurement campaigns which target photolytic products (e.g. radical concentrations). Furthermore, calculations of photolysis rate constants within even highly detailed chemical mechanisms remain parameterised.

Within the MCM, j-values are estimated as a function of solar zenith angle (SZA), with parameterisations derived from clear-sky model estimations. RADM and RACM precalculate actinic flux for clear-sky atmospheres, based on evenly-spaced increments in latitude, altitude and time. This is used with Eq. 1.4 and selected absorption cross-section (σ) and quantum yields (ϕ) to determine j-values and construct a look-up table. Models interpolate the j-values within this look-up table to estimate j-values for the latitude, altitude and time required (Roselle et al., 1999). To account for the high variability in local conditions, photolysis schemes often utilise a cloud cover correction as an alternative to computing local cloud cover. The latter is computationally expensive, particularly for models at high time resolutions. This is discussed further in Chapter 3.

In the UK, the Department for Environment Food and Rural Affairs (Defra) use a combination of model approaches to achieve their objectives (Defra, 2021d). This includes the Community Multiscale Air Quality (CMAQ) modelling system, and the EMEP model, which use photolysis schemes derived from RADM (Roselle et al., 1999) and MCM (Simpson et al., 2012), respectively.

Part of this PhD research discusses the data availability of photolysis rate constant measurements for the purpose of model validation, as well as illustrating an alternative method which could be utilised by models to accurately account for local meteorology, while limiting the increase in computational cost (Chapters 3 and 4).

1.7 Aims and structure of the thesis

The preceding sections have outlined tropospheric chemistry of NO_y species and other pollutants of concern, potential measurement interferences and the current state of monitoring networks, as well as the fundamentals of photolysis processes and current model estimations. As stressed in Section 1.6, model determination of photolysis rate constants are often parameterised, and not routinely validated against measurements as are pollutant concentrations. This is despite the considerable variability of photolysis rate constants with local meteorological conditions, and the impact this has on subsequent reactions in the chemical mechanism and on the important applications of the model results. Similarly, interference in trace gas measurement methods are not often quantified across the monitoring networks in which they are employed, despite the large potential uncertainty at rural sites.

This PhD research explores aspects of the ongoing need to make long-term measurements of both atmospheric chemical components and photolysis rate constant measurements, such as are needed to understand changes in the atmosphere as pollutant emission abatement policies are formulated and implemented under real local conditions. The specific aims of each chapter are as follows:

Chapter 2: Identify the impact of the relocation of the southern UK EMEP supersite on the long-term time series of its pollutant measurements, and determine whether such measurements remain representative of the wider area of the south of the UK, as intended in the network.

Chapter 3: Explore the application of accessible long-term $j(NO_2)$ measurements for verifying modelled photolysis rate constants, to account for variation in local meteorological conditions, using data from 3 sites across the UK. This is examined through the systematic analysis of a $j(NO_2)$-derived measurement-driven adjustment factor (MDAF), which is similar to techniques accepted and employed in existing model approaches without scrutiny.

Chapter 4: Determine whether the MDAF values derived from reference measurements of $j(O^1D)$ and $j(NO_2)$ (examined in Chapter 3) are applicable for adjusting other important photolysis rate constants in chemical mechanisms and the uncertainty levels that this approach may introduce for different photolysis reactions. This is presented through a systematic comparison of hourly MDAF derivations for 12 photolysis rate constants in a variety of local meteorological conditions.

Chapter 5: Design and test an inlet switching system for a quadrupole iodide chemical ionisation mass spectrometer (I^- CIMS) to simultaneously measure multiple NO_y species at the remote northern UK EMEP supersite, where concentrations were expected to be small. If successful, the deployment measurements would be used to quantify potential N_2O_5 interference in long-term MARGA measurements of HNO_3, and assess the current state of NO_y chemistry at the site.

The studies included in this thesis were developed to fill a gap in verification of atmospheric chemistry and air quality modelling using local long-term measurements. Further relevant introduction and methods material is presented in each results chapter.

Chapter 2

Changing supersites: assessing the impact of the southern UK EMEP supersite relocation on measured atmospheric composition

The work presented in this chapter has been published in Environmental Research Communications (Walker, H. L. *et. al.* (2019), *Environ. Res. Commun.*, **1**, 041001., https://doi.org/10.1088/2515-7620/ab1a6f). *I ran the deweather model and interpretted results with help from my supervisors Dr M.M. Twigg, Dr C.F. Braban and Professor M.R. Heal. The majority of data was publicly available from the Department for Environment Food and Rural Affairs UK-AIR resource. MARGA and co-located meteorological measurements at both sites were contributed by staff at Ricardo Energy and Environment (S. Ritchie, C. Conolly and A. Sanocka). Dr U. Dragosits provided help with NH_3 emissions and agricultural regulations. The manuscript was written by me, with contributions from all co-authors. Supplementary information for this chapter is presented in the Appendices.*

2.1 Introduction

Atmospheric pollution has a significant influence on human and ecosystem health. Inhalation of ozone (O_3) and particulate matter has been linked to cardiovascular and respiratory diseases (WHO, 2006, 2013b). Deposition of acidic gases causes acidification of terrestrial and aquatic ecosystems, and nitrogen deposition (e.g. from nitrogen oxides, NO_x, or ammonia, NH_3) leads to eutrophication (Sutton et al., 2011; RoTAP, 2012).

Monitoring of air pollutant concentrations is important for quantifying these effects and their spatio-temporal trends (Fagerli & Aas, 2008; Malley et al., 2014). In Europe, the Cooperative Programme for Monitoring and Evaluation of the Long-Range Transmission of Air Pollutants in Europe (EMEP) has the aim of providing member states with this quantitative information (Tørseth et al., 2012). Measurements within EMEP are made at rural sites representative of the surrounding area (Spangl et al., 2007; Joly & Peuch, 2012) and adhere to prescribed sampling methods and siting criteria detailed by the Chemical Coordinating Centre (EMEP-CCC) to ensure comparability (Kuhlbusch et al., 2014). Spatially distributed sites provide data for evaluation of regional models (Fagerli & Aas, 2008; Cape, 2009; Malley et al., 2014), whilst hourly measurements for 40+ years allow characterisation of emission patterns and separation of long-term trends from interannual variability (Tørseth et al., 2012). Such data help establish achievable mitigation strategies (Pope & Wu, 2014) and track impacts of implemented measures.

The UK has been a member of EMEP since its inception in 1979, and currently operates two level-2 "supersites" (UNECE, 2004a, 2004b) at Auchencorth Moss in southern Scotland, and Chilbolton Observatory in southern England (Defra, 2018a, 2021c; Figure 2.1) measuring a wide range of pollutants. The southern supersite, Chilbolton Observatory, opened in January 2016 following the closure of the previous site (Harwell; Figure 2.1) in December 2015, which had been active for several decades. The

aim of this study is to investigate whether the move from Harwell to Chilbolton led to a temporal change in the chemical climate recorded by the southern rural UK supersite. Given the extensive instrumentation, duplicate measurements could not be run for any overlap period. An analysis is presented of measurements in the years directly pre- and post- relocation (2014-15 and 2016-17 respectively), focussing on nitrogen oxides (NO_x), ammonia (NH_3), sulphur dioxide (SO_2), particulate matter <10 and 2.5 µm in diameter (PM_{10} and $PM_{2.5}$, respectively) and ozone (O_3).

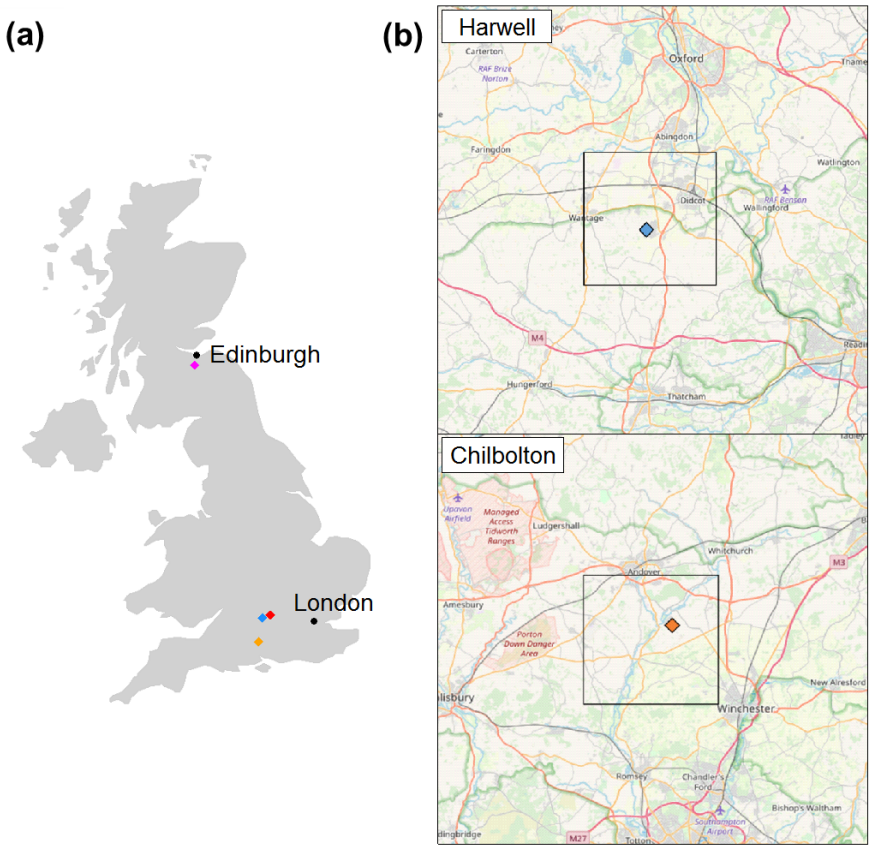

Figure 2.1: **(a)** Locations of the UK EMEP "supersites" at Auchencorth Moss (pink), Harwell (blue), Chilbolton Observatory (orange) and the meteorological station at Benson (red). **(b)** Maps of the 50 km × 50 km area surrounding Harwell (top, blue diamond) and Chilbolton (bottom, orange diamond) from OpenStreetMap. The boxes surrounding each site show the 15 km × 15 km area used for comparisons with the UK National Atmospheric Emissions Inventory (NAEI) based upon the 5 km × 5 km resolution of the agricultural NH_3 emissions.

2.2 Method

2.2.1 Site details

The Harwell supersite is predominantly surrounded by agricultural land near Didcot, Oxfordshire (lat: 51°34'N, lon: 1°19'W, altitude: 126 m), 70 km west of London and 20 km south of Oxford (Figure 2.1). The closest minor road was approx. 400 m to the west and a dual-carriageway (A34) ran 2 km to the east. The town of Didcot was 6.4 km to the north-east, and the Great Western Railway line ran in the east-west direction ∼5.7 km north of the site. Approximately 8 km in the same direction was a coal and oil fired power station ("Didcot A"), formerly a nearby major point source of NO_x and SO_2 (Abdalmogith & Harrison, 2006; Vieno et al., 2010), that closed on 22 March 2013 and was demolished in 2016. "Didcot B", a natural gas power plant on the same site, remains operational. Measurement of atmospheric pollutants at Harwell started in 1976 (UKEAP, 2015) prior to its incorporation as an EMEP level-2 supersite (UNECE, 2004b). Operations ceased on 31 December 2015.

The Chilbolton Observatory site is located 50 km south of Harwell in an agricultural (mainly arable) landscape, ∼200 m south-east of the edge of Chilbolton village, Hampshire (lat: 51°08'N, lon: 1°26'W, altitude: 78 m) and 100 km south-west of London (Defra, 2021c). Two single-carriageway main roads run ∼1 km to the west (A3057), and ∼3 km to the south (A30) (Figure 2.1). The site began monitoring as an EMEP level-2 supersite on 11 January 2016, after instrument relocation from Harwell.

2.2.2 Measurement data

The full suite of measurements at the two sites is summarised in UK Eutrophying and Acidifying Pollutants (UKEAP) network reports (Defra, 2018), a subset of which are investigated in this work (Table 2.1 and Figure S1). Concentration data were downloaded from the UK Department for Environment, Food and Rural Affairs (Defra) online data

repository (Defra, 2021b).

Data are evaluated here for the two years either side of site relocation (Harwell in 2014-15 and Chilbolton in 2016-17, respectively). Data capture statistics are given in Table 2.1. O_3, NO_x, SO_2, PM_{10} and $PM_{2.5}$ measurements derive from the UK Automatic Urban and Rural Network (AURN). Instrumentation selection, calibration and data ratification follow EU Air Quality Directives (European Council, 2008), and data are archived as hourly averages (Defra, 2018). Hourly measurements of NH_3 and other trace gases, together with water-soluble ions within $PM_{2.5}$ and PM_{10}, are provided by the Monitor for AeRosols and Gases in Air (MARGA) instrument (EMEP, 2007; Stieger et al., 2018) with data quality assurance processes as described in Twigg et al. (2015).

Hourly meteorological data comprise on-site measurements at Harwell and Chilbolton (CFARR, 2003). Data were also downloaded for the meteorological station at Benson, Oxfordshire (lat: 51°36'N, lon: 1°05'W, altitude: 57 m), marked on Figure 2.1a, from the NOAA Integrated Surface Database using the *worldmet* package (Carslaw, 2017; NOAA, 2020) for the full time period being considered. These data were used to validate use of concatenated meteorological time series from the two supersites (see Supplementary Information; Section S1 and Figure S2).

2.2.3 Meteorological detrending

To examine for evidence of a step-change in concentration coincident with site relocation, the *deweather* function (Carslaw, 2015) used in RStudio (R Core Team, 2020) was applied to concatenated Harwell and Chilbolton Observatory datasets (2014-17) in a technique known as "meteorological normalisation" (Grange et al., 2018). This accounts for non-linear and complex relationships between predictors, including wind direction and speed, ambient temperature, relative humidity, time of year, weekday and time of day (Carslaw & Taylor, 2009), allowing changes in time series not directly caused by these predictors to be identified. The *deweather* function uses a boosted re-

gression trees approach to build a predictive model for air pollutant concentrations from the predictor variables. Models are built using a stochastic process, selecting a random subset of data from which to build regression trees. In each new model, trees are built sequentially, with each new tree reducing the overall predictive error of the model (all trees built until this point). This process results in reduced variance in the final model (Friedman, 2002), but a consequence is that a slightly different model is produced with each run (Elith et al., 2008). To ensure repeatability in this work, a set of 10 models were built using the same input data for each pollutant time series "deweathered". Each of the meteorological predictor variables used were measured at the same site as the pollutants. A comparison using meteorological measurements made at a reference site is given in the Supplementary Information (Figure S3).

2.2.4 Emission inventories

Annual emission estimates for NH_3, NO_x, SO_2, $PM_{2.5}$ and PM_{10} were obtained from the UK National Atmospheric Emission Inventory (NAEI; http://naei.beis.gov.uk/) for both locations. Individual species emissions were taken from the 2015 inventory and were aggregated over the 15 km $\times$ 15 km area surrounding each site shown in Figure 2.1. The areas were defined according to the gridded agricultural sector NH_3 emissions which have a spatial resolution of 5 km $\times$ 5 km, but for all other pollutants the underlying resolution was 1 km $\times$ 1 km.

2.3 Results and discussion

2.3.1 Overview

Table 2.1 summarises the annual mean concentration and corresponding 95% confidence interval for each pollutant for each year. Chilbolton Observatory MARGA measurements have the lowest data capture in 2016 (54-58%) since these measurements did not commence until 11 February 2016, and instrument issues led to missing data

between 9 July and 1 September 2016. The MARGA data capture improved in 2017 (79-82%). Between August and September 2014 a plume from the volcanic eruption at Holuhraun, Iceland, passed over the UK and is observed in the SO_2 time series (Figure S1). Similarly in spring 2014, elevated PM concentrations were caused by a combination of Saharan dust and ammonium nitrate formed from European emissions (Vieno et al. 2016a; Figure S1). Other PM episodes are also apparent between 2014 and 2017 (Figure S1), typically accumulating in low wind speeds and lasting no more than a few days (Defra, 2015, 2016, 2017).

2.3.2 Nitrogen oxides (NO_x)

The average 2016 and 2017 concentration of NO_x at Chilbolton was approximately 1.6 times greater than the average 2014 and 2015 concentration at Harwell (annual means of 18.5 and 13.8 µg m^{-3} compared with 10.5 and 9.20 µg m^{-3} respectively; Table 2.1). The NO_x *deweather* time series also shows an abrupt increase coincident in timing with the relocation of the measurement site (Figure 2.2a).

In contrast to the greater average NO_x concentrations at Chilbolton, the total local NO_x emissions integrated over the 15 km × 15 km area around Harwell are more than 5 times greater than from the same-size area around Chilbolton (Figure 2.3). The NO_x emissions close to Harwell are dominated by specific sources including Didcot town, Didcot B power station in the north-east, and a high traffic flow on the dual-carriageway (A34) running north-south 2 km to the east. Across the 225 individual 1 km × 1 km grid squares within the area surrounding Harwell, 47% of total local emissions are contributed by the grid square with the highest emissions, whilst the 25 highest emission grid squares contribute 84%. Similar analysis at Chilbolton show less dominance of local emissions from the single highest (6%) and 25 highest (61%, including part of the A303, ∼8 km north) grid squares.

These differences in NO_x source configurations are illustrated by pollution wind roses

Table 2.1: Annual mean concentrations (with 95% confidence intervals) and annual percentage data capture of measurements for the investigated species at Harwell (2014-15), and Chilbolton Observatory (2016-17).

		Annual mean concentrations ±95% confidence intervals / μg m^{-3} (Data capture / %)			
Species	Instrument	Harwell 2014	Harwell 2015	Chilbolton 2016	Chilbolton 2017
SO_2	Monitor for AeRosols and Gases in Air (MARGA)	0.245 ± 0.028 (94%)	0.150 ± 0.0027 (70%)	0.157 ± 0.0044 (58%)	0.131 ± 0.0032 (79%)
HONO		0.464 ± 0.0068 (94%)	0.340 ± 0.0049 (70%)	0.494 ± 0.011 (58%)	0.454 ± 0.008 (79%)
HNO_3		0.159 ± 0.0029 (94%)	0.138 ± 0.0032 (68%)	0.159 ± 0.0050 (57%)	0.162 ± 0.0037 (80%)
NH_3		1.96 ± 0.049 (95%)	2.05 ± 0.044 (70%)	5.88 ± 0.22 (54%)	6.23 ± 0.18 (82%)
		Automatic Urban and Rural Network (AURN)			
O_3	UV absorption	56.0 ± 0.45 (99%)	57.1 ± 0.42 (98%)	48.9 ± 0.53 (97%)	51.5 ± 0.48 (98%)
NO_x	Chemiluminescence	10.5 ± 0.30 (97%)	9.20 ± 0.22 (97%)	18.5 ± 0.49 (91%)	13.8 ± 0.35 (97%)
NO_2		7.99 ± 0.20 (97%)	7.68 ± 0.16 (97%)	14.3 ± 0.25 (91%)	11.2 ± 0.19 (97%)
PM_{10}	TEOM-FDMS	14.3 ± 0.27 (74%)	15.1 ± 0.21 (89%)	14.9 ± 0.25 (85%)	13.3 ± 0.19 (98%)
$PM_{2.5}$		9.06 ± 0.19 (96%)	8.55 ± 0.17 (96%)	9.45 ± 0.19 (93%)	7.38 ± 0.17 (98%)
SO_2	UV fluorescence	1.01 ± 0.054 (98%)	0.939 ± 0.013 (93%)	0.876 ± 0.017 (64%)	0.763 ± 0.013 (89%)

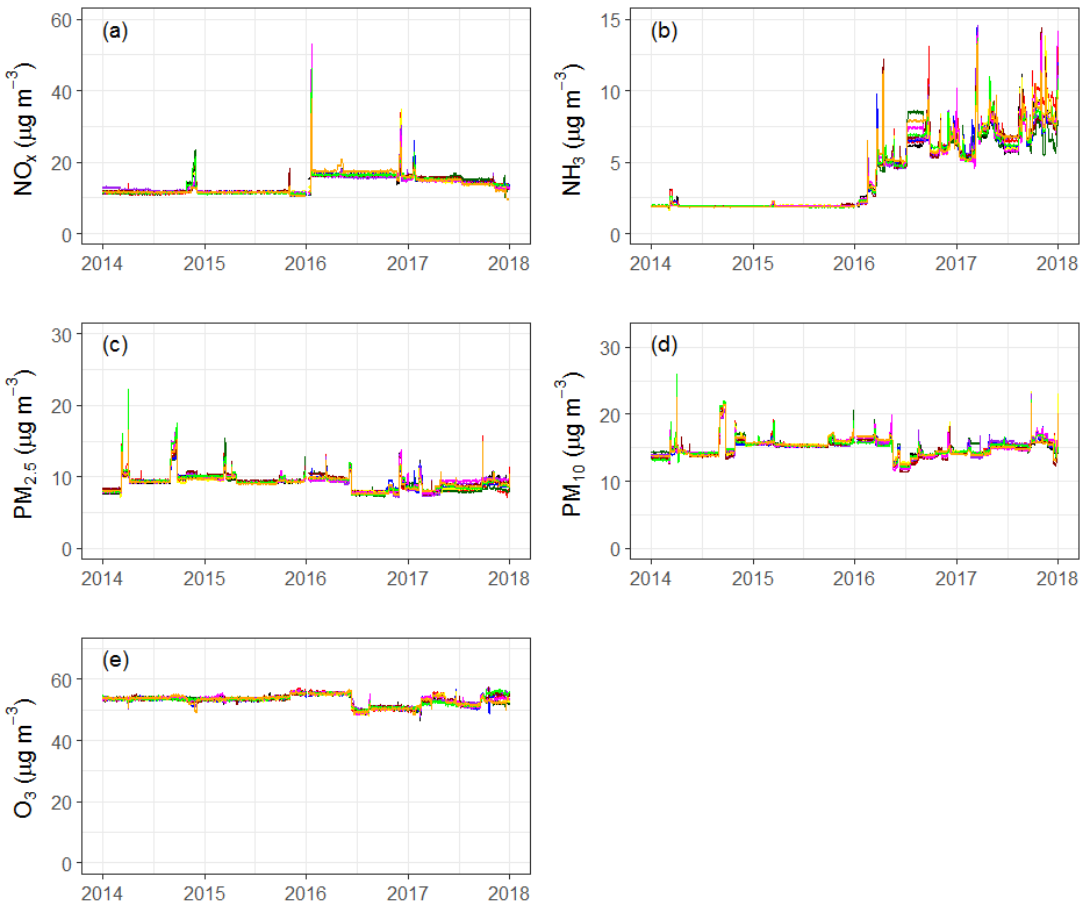

Figure 2.2: Modelled pollutant concentrations of (a) NO_x, (b) NH_3, (c) $PM_{2.5}$, (d) PM_{10} and (e) O_3 predicted using the *deweather* function for R (Carslaw, 2015) applied to concatenated time series of hourly measurements at Harwell until 31 December 2015 and at Chilbolton Observatory from 11 January 2016. Modelled data have been smoothed by plotting the daily mean predicted concentration. The different coloured lines distinguish the individual results of the 10 models built to predict each pollutants concentrations.

(Figure 2.4). The aforementioned sources north of Harwell generate the most polluted air transported to the site, but do not contribute significantly more to the annual average than other directions. Considering NO_x to have an atmospheric lifetime of ∼4-6 h in the mid-latitudes (Beirle et al., 2011) and an average wind speed of around 15 km h^{-1} for southern England (Figure S2; CFARR, 2003; NOAA, 2020), the London pollution plume could plausibly be observed at both sites. It appears Harwell is less influenced by London (∼100° bearing) than Chilbolton (∼70°), for which this wind direction provides a dominant contribution to the annual average. However the M3 motorway also contributes NO_x to this wind direction, stretching for ∼56 km between Chilbolton and London. Traffic along the length of the M3 (∼95 km) and other major roads are the probable reason why a larger average concentration of NO_x (>2.2 times higher) is observed in easterly (0-180°) than in westerly winds (181-360°; Table 2.2). More frequent westerly winds during 2017 led to a reduced annual average compared with 2016 (13.8 compared to 18.5 µg m^{-3}; Table 2.1).

The importance of wind direction to NO_x concentrations at both sites is reflected in the relative importance of variables used in the *deweather* models (Table S2). Wind direction had the largest mean relative importance of 19.1%, closely followed by ambient temperature (18.7%) and (long-term) trend (18.4%). Unsurprisingly, predicted concentrations of NO_x are elevated at lower ambient temperatures ($\leq$10 °C) and during colder months (October to February), as these conditions limit the dispersion of emissions (AQEG, 2004), and there is a higher demand for domestic heating. The importance of the trend variable is a consequence of the abrupt increase in NO_x at the time of site relocation in the concatenated *deweather* time series (Figure 2.2a). This supports the interpretation of a real difference in annual mean NO_x concentration between Harwell and Chilbolton.

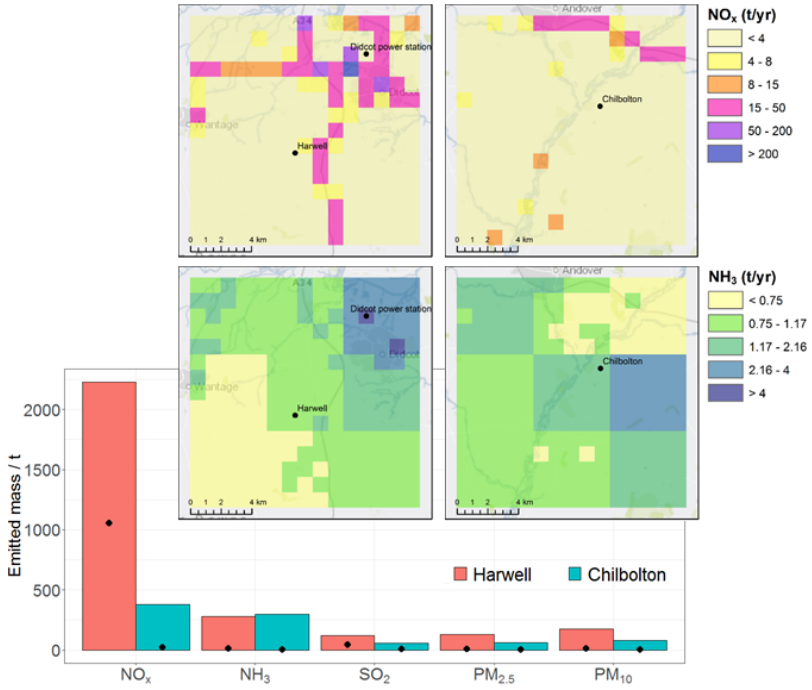

Figure 2.3: **(Top)** Annual emissions maps of NO_x and NH_3 from the National Atmospheric Emissions Inventory database (NAEI, http://naei.beis.gov.uk/) for the 15 km × 15 km area surrounding the Harwell and Chilbolton Observatory sites. Underlying data area at 5 km × 5 km grid resolution for agricultural NH_3, displayed at 1 km × 1 km resolution. **(Bottom)** Bar plot in the lower panel displays the total emissions of NO_x, NH_3, SO_2, $PM_{2.5}$ and PM_{10} for the same area around both sites, whilst the black point indicates the emission from the component grid square with the maximum emission across the contributing grid squares.

Table 2.2: Annual mean concentrations of hourly NO_x measurements for easterly (0-180°) and westerly (181-360°) wind directions. The remaining percentage of data (% NA) includes hours where NO_x concentration or wind direction were not recorded.

	Mean NO_x concentration / µg m^{-3}		Percentage of annual wind / %		
Site and year	Westerly	Easterly	Westerly	Easterly	NA
Harwell 2014	11.1	10.0	39	59	2
Harwell 2015	10.5	8.60	34	55	11
Chilbolton 2016	12.0	28.6	54	35	11
Chilbolton 2017	10.2	22.6	69	28	3

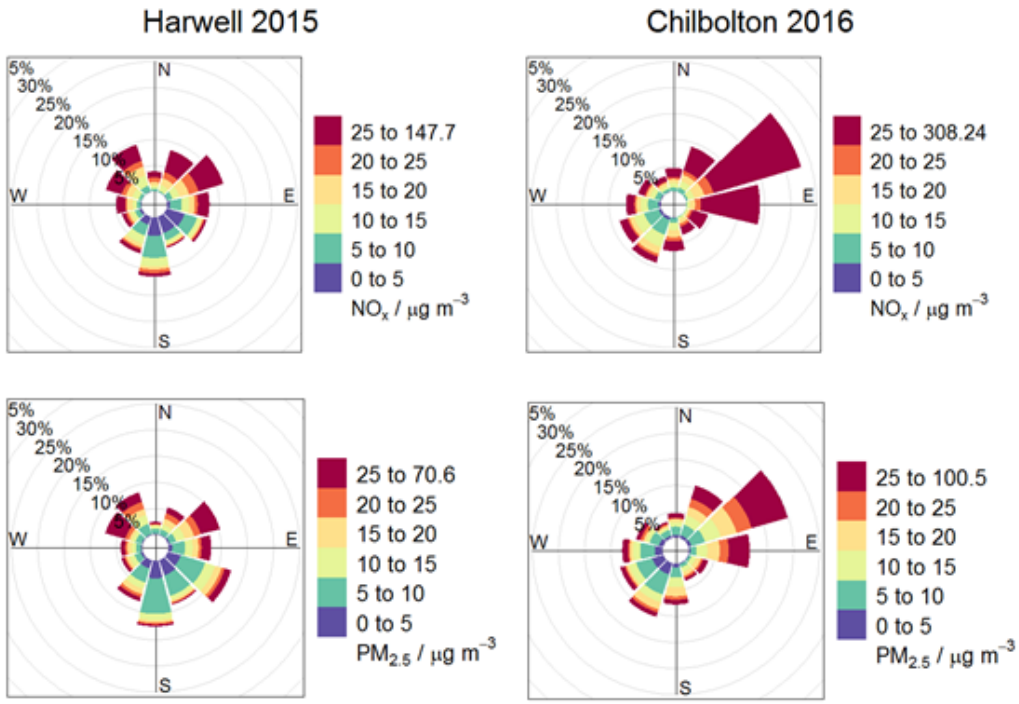

Figure 2.4: Pollution wind roses for NO_x and $PM_{2.5}$ concentrations at Harwell in 2015 and at Chilbolton in 2016, depicting the contribution of 5 µg m^{-3} contribution bins in each sector to the annual mean concentration. Wind and pollutant concentration measurements were co-located and the underlying time resolution was hourly for both. The last bin in each sector (red) includes concentrations between 25 µg m^{-3}, and the maximum hourly concentration measured in each year.

2.3.3 Ammonia (NH_3)

The annual mean NH_3 concentrations at Chilbolton Observatory in 2016 and 2017 (5.88 and 6.23 $\mu g\, m^{-3}$, respectively, Table 2.1) are about 3 times higher than at Harwell in 2014 and 2015 (1.96 and 2.05 $\mu g\, m^{-3}$, respectively), the greatest difference of all pollutants investigated. Data capture at Chilbolton in 2016 was rather low (54%), and most missing data occurred during the summer (Figure S1) when NH_3 concentrations are typically larger (Tang et al., 2018a). Therefore, the annual average in 2016 is likely biased low by the missing data.

Application of the *deweather* model to the concatenated time series of NH_3 concentrations (Figure 2.2b) confirms a distinct increase in mid-February 2016, coincident with commissioning of the MARGA at Chilbolton. Trend is the dominant variable in the *deweather* model (45.5±0.6%, Figure S4 and Table S2). The raw time series shows moderately elevated springtime concentrations at Harwell (Figure S1), consistent with typical livestock manure and synthetic fertiliser applications observed in NW European springtime (Vieno et al., 2016a). These springtime peaks are mirrored in the predicted concentrations of NH_3 during 2014 and 2015, and reflected by the partial dependency of the week-of-year variable predicting increased concentrations during Julian weeks 5-20 (Figure S4). Following site relocation the *deweather* time series showed NH_3 concentrations remaining high, with large and infrequent peaks that demonstrate little seasonality. Despite this, maximum hourly NH_3 at Chilbolton in 2016 and 2017 were during spring (126 $\mu g\, m^{-3}$ on 22 March 2016 and 94.4 $\mu g\, m^{-3}$ on 24 May 2017).

Ammonia has a short atmospheric lifetime and high spatial heterogeneity in its sources (Vogt et al., 2013; Dammers et al., 2017), so receptor concentrations are significantly influenced by local emissions. The contrasting concentrations at Harwell and Chilbolton are not reflected in the total NAEI estimates of local NH_3 emissions, which show similar averages over the 15 km × 15 km area surrounding each site (Figure 2.3). However, the total at Harwell includes contribution from a disproportionately large 1 km × 1 km

grid square over the site of Didcot B power station, over 3.4 times greater than any other grid square surrounding either site. When emissions from only the agricultural sector are considered, the greatest emissions are associated with the 5 km $\times$ 5 km grid square also containing the site, suggesting the presence of a nearby agricultural source or sources.

Polar plots of NH_3 concentration as a function of wind speed and direction for both sites (Figure 2.5) reveal an obvious dominant local source to the south-west of Chilbolton. Figure 2.6 demonstrates the difference in concentration between this source and background NH_3 at Chilbolton in 2016, by dividing prevailing wind into four direction sectors: east (E, 30-180°), south-west (SW, 180-250°), north-west (NW, 250-350°) and north (N, 350-30°). The N sector appears to reflect background NH_3 levels, with a mean concentration of 2.2 μg m^{-3}, comparable to average NH_3 concentrations measured at Harwell across all wind directions (Figure 2.5). Mean concentrations in E, NW and SW sectors are higher (3.1, 3.4 and 7.1 μg m^{-3}, respectively) and demonstrate an inverse relationship with wind speed, suggesting nearby sources at Chilbolton. Approximately 1.5 km from the site in the SW sector is the centre of a cattle farm, whilst a further 1.5 km in the same direction is a mushroom farm, likely to release NH_3 at regular intervals coinciding with mushroom growth cycles (Sather et al., 2008). For the remaining E and NW sectors, NH_3 concentrations presumably reflect levels associated with the surrounding intensively managed arable land, which in general are larger emitters than agricultural activities near Harwell.

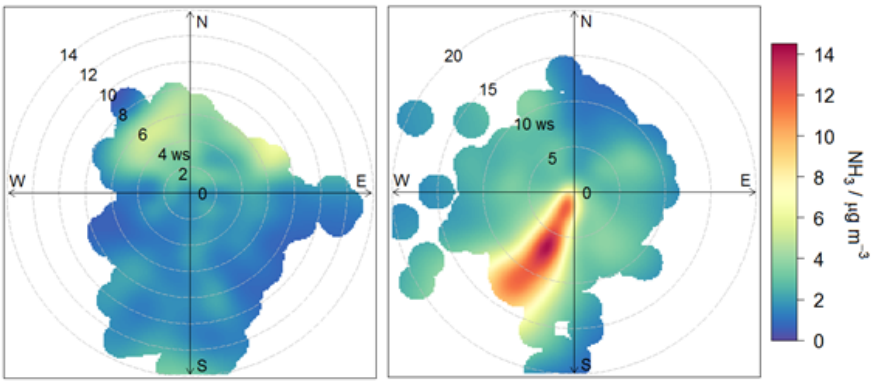

Figure 2.5: Polar plots of hourly NH_3 concentration (MARGA) as a function of hourly wind speed and direction at Harwell 2015 (left) and Chilbolton Observatory 2016 (right). Wind and NH_3 concentration measurements were co-located.

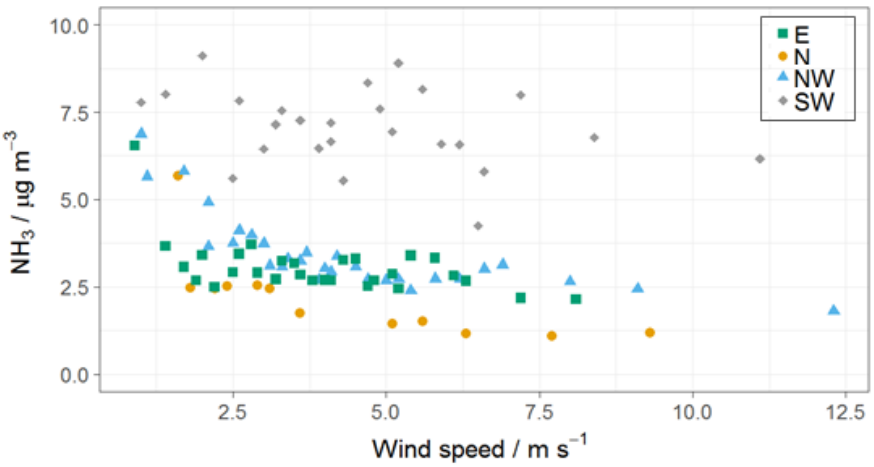

Figure 2.6: Hourly NH_3 concentrations (MARGA) as a function of wind speed at Chilbolton in 2016, for the four wind direction sectors: north (350-30°), south-west (180-250°), east (30-180°) and north-west (250-350°). Data points are medians of 50 hourly measurements sorted by ascending wind direction, following Flechard & Fowler (1998).

2.3.4 Sulphur dioxide (SO_2)

Hourly SO_2 concentrations at both sites are determined by two different measurement methodologies (Table 2.1) but there was poor agreement between them (Figure S5). This is anticipated, as the limit of detection (LOD) of the AURN UV fluorescence analyser (1.5 ppb, $\sim$4 $\mu g\,m^{-3}$) is approximately two orders of magnitude greater than that of the MARGA (0.04 $\mu g\,m^{-3}$; Makkonen et al., 2012). The aim of the AURN SO_2 analysers is to detect pollution events (Twigg et al., 2016) where concentrations could exceed national and EU limit values (hourly and daily means of 350 and 125 $\mu g\,m^{-3}$), whereas the MARGA is designed to monitor changes in background concentrations of SO_2. Extending the time series of SO_2 measurements at Harwell back to 2012 shows that there was a large reduction in concentrations in early 2013 (Figure 2.7), coincident with the closure of Didcot A coal and oil power station, which whilst operational was one of the largest SO_2 emission sources in the UK (Vieno et al., 2010). Following this event there are no discernible changes in SO_2 concentration, including through the site relocation, apart from a singular peak in August 2014 which can be attributed to an Icelandic volcanic eruption (Twigg et al., 2016). Whilst the emission inventory estimates greater local SO_2 emissions around Harwell than around Chilbolton (Figure 2.3), these are overwhelmingly dominated at Harwell by Didcot B power station. The relative infrequency of north-easterly wind to the site, coupled with the elevated source of these emissions, resulted in little influence of Didcot B on ambient measured concentrations. Consequently, there is effectively no change in measured SO_2 arising from the site relocation.

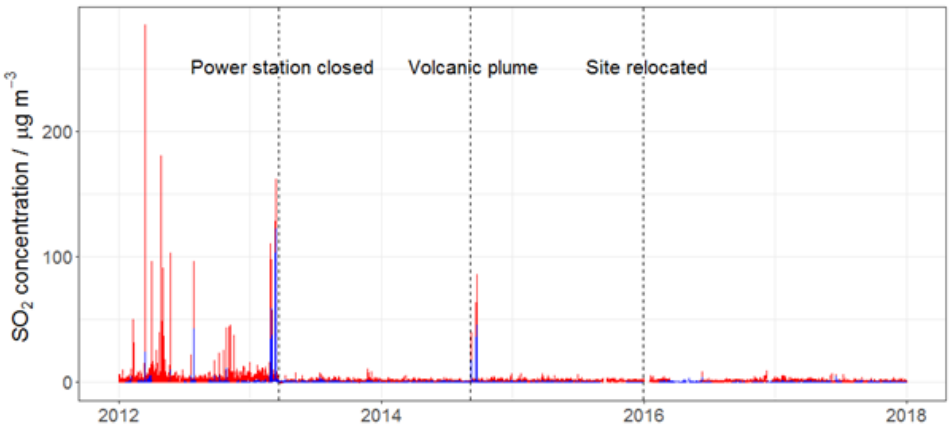

Figure 2.7: Time series from 1 January 2012 to 30 September 2017 of hourly SO_2 concentrations measured using UV fluorescence in the AURN (red), and by the MARGA (blue). Vertical dotted lines show the closure of Didcot A power station (22 March 2013), the volcanic eruption plume from Holuhraun, Iceland passing over the UK (September 2014) and the site relocation from Harwell to Chilbolton in early January 2016.

2.3.5 Particulate matter (PM_{10} and $PM_{2.5}$)

Data capture was high for total PM_{10} and $PM_{2.5}$ (Table 2.1), but poorer for the individual species concentrations. Annual mean concentrations of PM_{10} and $PM_{2.5}$ were similar at Harwell and Chilbolton (2014 & 2015 average PM_{10} = 14.7 µg m^{-3}, 2016 & 2017 average PM_{10} = 14.1 µg m^{-3}; equivalent data for $PM_{2.5}$ = 8.8 and 8.4 µg m^{-3}), indicating no substantive change in long-term mean PM concentration at the time of site relocation. There was also no significant difference in the number of PM_{10} daily mean exceedances of 50 µg m^{-3} before and after site relocation: twice each year at Harwell, 3 times at Chilbolton in 2016 and once in 2017.

The *deweather* models for both $PM_{2.5}$ and PM_{10} (Figures 2.2c and 2.2d) show temporal variability, but no evidence of a significant step-change in concentration at the time of site relocation. The model predicted lower concentrations of PM_{10} in June 2016 because measured values in this period 12 June – 31 July 2016 (mean of 7.6 µg m^{-3}) were substantially lower than the mean for the rest of the time series (14.4 µg m^{-3}). There is a similar effect in the modelled $PM_{2.5}$ time series. Disagreement between

models in the latter part of the $PM_{2.5}$ *deweather* time series is presumed to be due to the presence of a large measurement value (186.8 µg m^{-3}, 27 April 2017), almost twice any other hourly $PM_{2.5}$ concentration. The stochastic nature of the *deweather* function resulted in some models being built using this data point, while others were not.

The annual NAEI emissions integrated over the 15 km × 15 km area surrounding each site are substantially greater around Harwell than Chilbolton for both PM_{10} and $PM_{2.5}$ (Figure 2.3). Locations of high $PM_{2.5}$ emissions within the area surrounding Harwell include those with substantial NO_x emissions (Didcot town, Didcot B power station and the A34). The 25 1 km^2 grid squares with highest PM emissions around Harwell contribute 63% to the total, whereas the equivalent at Chilbolton contribute 54%. As with NO_x, an increase in $PM_{2.5}$ concentrations is observed in the prevailing easterly wind at Chilbolton as compared to Harwell (13.2 µg m^{-3} in 2016 compared with 8.1 µg m^{-3} in 2015; Table S3), however westerly winds have lower concentrations (6.8 compared with 9.6 µg m^{-3}), which accounts for the comparable annual averages pre- and post-relocation. The same conclusions apply for PM_{10} (Figure S6).

Annual data capture (%) for MARGA measurements were poorer than for TEOM-FDMS measurements (Table 2.1). Nevertheless for all secondary inorganic aerosol (SIA) ions analysed, the data capture rate was sufficient for comparisons of annual measurements (all years >58%). Anthropogenically derived NH_4^+, NO_3^- and SO_4^{2-} dominate $PM_{2.5}$ at both sites, contributing an average of 58% to total measured mass at Harwell (2014-15) and 59% at Chilbolton (2016-17). Annual mean concentrations of these ions in both $PM_{2.5}$ and PM_{10} are presented in Table 2.3. The calculated SIA ion balance for $PM_{2.5}$ (Figure 2.8) shows good correlation for all years, despite a few events of exception. More acidic aerosols are observed in 2014, due to more NO_3^- and SO_4^{2-} ions compared to NH_4^+. The greatest excess occurs in September where concentrations of SO_4^{2-} were significantly elevated from the Holuhraun eruption plume passing over the UK (Twigg et al., 2016). Both years at Chilbolton exhibit a large excess of

basic aerosol on days reaching high NH_4^+ concentrations (8.64 and 22.6 µg m^{-3} on 22 March 2016 and 11 March 2017, respectively). In general, all years appear to have a slight bias towards basic aerosol, and are comparable to observations at the northern UK EMEP supersite (Auchencorth Moss; Twigg et al., 2015). Similar observations apply to the coarse fraction (PM_{coarse} = PM_{10} – $PM_{2.5}$), where SIA contributes 15% to total aerosol mass at both Harwell (2014-15) and Chilbolton (2016-17). Annual average black carbon measurements (Aethalometer, Black Carbon Network; Defra, 2018b) are comparable at ~0.40 µg m^{-3} between Harwell (2014-15) and Chilbolton (2016-17). Given the comparable total PM at both sites, this indicates that there is also a similar contribution of secondary organic aerosols (SOA) in both fractions.

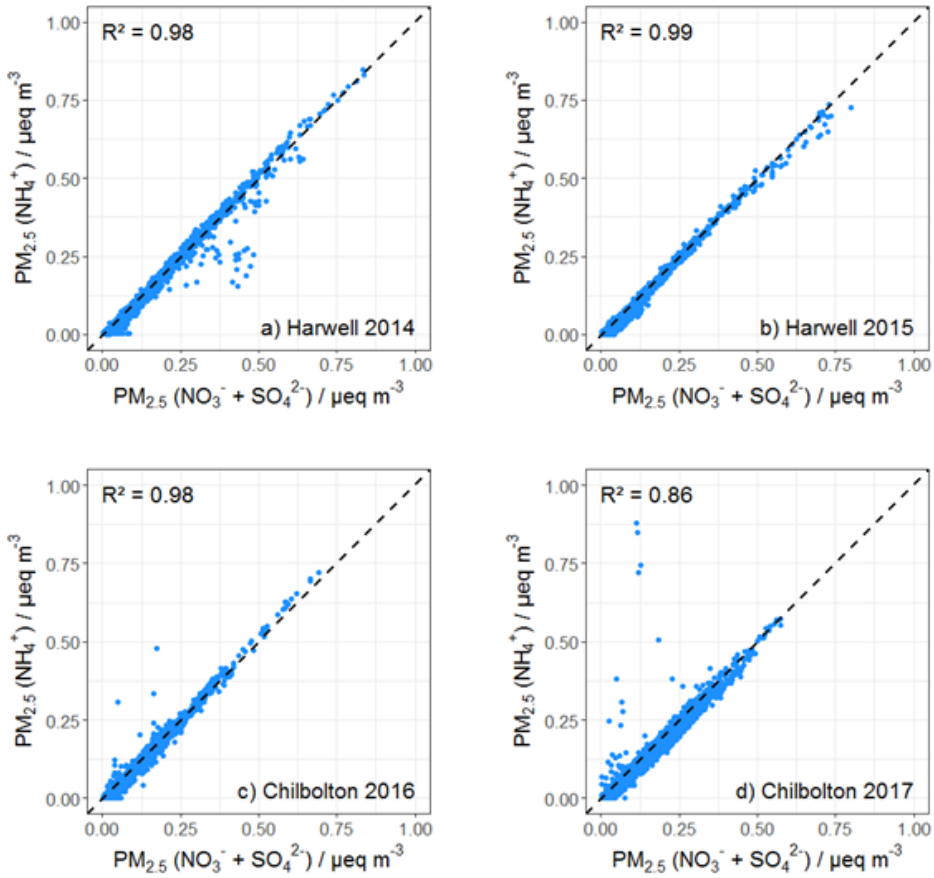

Figure 2.8: Measured ion balance (in µeq m^{-3}) between NH_4^+ and the sum of NO_3^- and SO_4^{2-} in $PM_{2.5}$ during the two years at Harwell (2014 and 2015) and Chilbolton Observatory (2016 and 2017). Black dotted line illustrates 1:1 ratio.

Table 2.3: Annual mean particulate NH_4^+, NO_3^- and SO_4^{2-} concentrations measured by MARGA in $PM_{2.5}$ and PM_{10}. Key: max = maximum hourly measurement of the year, μ_A = arithmetic annual mean and σ_A = arithmetic standard deviation across the year.

	2014 / μg m^{-3}			2015 / μg m^{-3}			2016 / μg m^{-3}			2017 / μg m^{-3}		
$PM_{2.5}$	NH_4^+	NO_3^-	SO_4^{2-}	NH_4^+	NO_3^-	SO_4^{2-}	NH_4^+	NO_3^-	SO_4^{2-}	NH_4^+	NO_3^-	SO_4^{2-}
max	15.2	47.4	29.9	13.2	38.0	13.3	13.0	33.7	9.98	22.6	29.0	13.5
μ_A	1.25	2.62	1.87	0.94	2.33	1.87	1.28	2.98	1.43	1.05	2.87	1.38
σ_A	1.75	4.17	2.20	1.46	3.95	1.04	1.51	3.78	1.04	1.49	3.69	1.23
PM_{10}												
max	16.0	50.9	31.4	13.8	41.2	13.9	12.8	34.0	9,7	21.6	35.9	15.8
μ_A	1.31	2.97	2.02	0.98	2.65	1.48	1.35	3.50	1.55	1.17	3.37	1.61
σ_A	1.82	4.42	2.32	1.51	4.17	1.09	1.53	4.04	1.05	1.61	4.15	1.33

2.3.6 Ozone (O_3)

Data capture for hourly O_3 concentrations was high ($\geq$97% for each year; Table 2.1). Annual mean concentrations of O_3 were somewhat lower after the site relocation, 48.9 and 51.5 µg m^{-3} for 2016 and 2017 respectively at Chilbolton, compared with 56.0 and 57.1 µg m^{-3} for 2014 and 2015 at Harwell (Table 2.1). However, the *deweather* model time series for O_3 data (Figure 2.2e) does not show evidence of a step-change associated with the site relocation (the modelled decrease in mid-2016 is coincident with the similar observation for PM). The slightly lower annual mean background O_3 at Chilbolton than at Harwell may be due to interannual variability in O_3, but the lower background concentration is also consistent with an inverse concentration relationship with the unambiguously higher background NO_x at Chilbolton. Since NO and NO_2 have different chemical impacts on ambient O_3 concentrations (Section 1.1), the large step change in modelled NO_x, and lack thereof in O_3, could be further explored by separately considering measurements NO and NO_2. Unfortunately, this was not possible in this work due to a lack of available measurements.

2.4 Conclusions

The relocation of the southern UK EMEP supersite from Harwell to Chilbolton in January 2016 has not resulted in discontinuities in average measured concentrations of $PM_{2.5}$, PM_{10}, SO_2 and O_3 (based on two-year pre- and post-relocation time comparisons), but has led to substantial increases in average concentrations of NO_x and NH_3, by a factor of $\sim$1.6 and $\sim$3, respectively.

Concentrations of NO_x and PM in easterly wind arriving at Chilbolton are approximately 2.7 and 1.5 times larger than at Harwell, from common sources including the M3 motorway and Greater London. Prevailing winds from the west contribute similar NO_x concentrations at both sites, therefore despite a higher frequency of westerly wind at Chilbolton, the larger easterly concentrations result in larger annual means. Westerly

winds carry lower concentrations of PM to Chilbolton than Harwell, thereby resulting in similar annual averages. Measurements show no substantive difference in the contribution of secondary inorganic aerosols (SIA) and black carbon to the total PM mass between the two site locations, although more NH_4^+ events are observed in the SIA at Chilbolton Observatory. Background concentrations of NH_3 at both sites reflect the presence of mixed farmland; however the contribution of very strong local sources to the south-west of Chilbolton cause the large increase in annual average between sites.

In conclusion, when considering long-term regional trends based on the southern UK supersite data, the increase in NO_x and NH_3 at Chilbolton must be taken into account and the Harwell and Chilbolton datasets should be treated separately.

Chapter 3

Analysis of a measurement-driven adjustment factor as a method to capture local meteorological variability in modelled $j(NO_2)$

The work presented in this chapter is based on a research paper currently in preparation for submission to the journal Atmospheric Measurement Techniques. I took the Auchencorth Moss filter radiometer measurements, processed the data, and interpreted the results with help from my supervisors, Dr M.M. Twigg, Dr C.F. Braban and Professor M.R. Heal. Field work at Auchencorth Moss was assisted by I. Simmons, S.R. Leeson and Dr M.R. Jones (UK Centre for Ecology & Hydrology). Operation and data provision of measurements made by the Bentham DTM300 spectroradiometer during the calibration at the University of Manchester was undertaken by Dr R. Kift (U. Manchester). The rest of the data processing for the calibration was managed by me. Measurements of $j(NO_2)$ and air temperature were provided by Dr N. Marsden (U. Manchester) for Manchester Air Quality Supersite, and by J. McGregor and Dr P. Agnew (Met Office) for Cardington. I wrote the manuscript with subsequent contributions from my supervisors.

3.1 Introduction

Atmospheric chemistry is largely driven by solar radiation. Therefore, in atmospheric chemistry models, accurately calculating photolysis rate constants (*j*-values) is essential for improving model estimates of subsequent reactions and quantifying the production rate and concentration of secondary pollutants. This is particularly important when assessing local air quality, i.e. for evaluation of public exposure to air pollution, or derivation of local mitigation measures to reduce local pollutant concentrations. Predicting accurate local *j*-values is quite challenging as *j*-values can be largely affected by the variability in local meteorological conditions, such as clouds (Thiel et al., 2008) and aerosols (Wang et al., 2019; Zhao et al., 2021). Validation of modelled pollutant concentrations by comparison to local measurements is typical for evaluating model performance. However, despite the importance of *j*-values and difficulty of accurate estimation, these values are not often validated in the same manner. Less accurate *j*-values can have important implications on model outputs, like pollutant concentrations (Chen et al., 2021).

An important photolysis reaction in the lower atmosphere is the photolysis of nitrogen dioxide (NO_2), as it contributes to the formation of harmful pollutants like tropospheric ozone (O_3; Reactions R3.1 and R3.2).

$$\mathrm{NO_2} + h\nu\,(\lambda \leq 420\,\mathrm{nm}) \longrightarrow \mathrm{NO} + \mathrm{O}(^3\mathrm{P}) \tag{R3.1}$$

$$\mathrm{O}(^3\mathrm{P}) + \mathrm{O_2} + \mathrm{M} \longrightarrow \mathrm{O_3} + \mathrm{M} \tag{R3.2}$$

Hence, the photolysis rate constant for the photolysis of NO_2, $j(NO_2)$, is an important variable for modelling local atmospheric chemical reactions. Its value at any given location and time is given by the equation,

$$j(\mathrm{NO_2}) = \int_{\lambda_1}^{\lambda_2} \sigma_{\mathrm{NO_2}}(\lambda)\,\phi_{\mathrm{O}(^3\mathrm{P})}(\lambda)\,F(\lambda)\,\mathrm{d}\lambda \tag{3.1}$$

where F is the actinic flux over the relevant wavelength range ($\lambda_2 - \lambda_1$), and σ_{NO_2} and $\phi_{O(^3P)}$ are respectively the molecule-specific absorption cross-section and quantum yield parameters for this photolysis reaction. The latter two parameters can vary with both temperature and pressure but for NO_2 in ambient conditions this is considered small (Shetter et al., 1988; Burkholder et al., 2019). The actinic flux (F) is the spherically integrated radiation available to a molecule in the atmosphere, which upon absorption results in photodissociation (Madronich, 1987). Actinic flux can be directly measured as a function of wavelength, independent of the angle of incidence (2-π sr field of view), using a spectroradiometer. These measurements are then used to calculate the integral in Eq. 3.1 to determine the photolysis rate constant (Edwards & Monks, 2003). Alternatively, a filter radiometer provides a simpler approach to determine a photolysis rate constant, by using bandpass filters to measure broadband actinic flux between the two wavelength limits ($\lambda_2 - \lambda_1$; Eq. 3.1). The instrument response is designed to simulate the $\sigma \times \phi$ product of the desired photolysis reaction in its strongest absorbing region (Junkermann et al., 1989; Volz-Thomas et al., 1996). For $j(NO_2)$ this relationship is linear; however for other photolysis rate constants, such as $j(O^1D)$ (the rate constant for the photolysis of O_3 to reactive $O(^1D)$ oxygen atoms), more processing of the instrument response is required to account for influences of solar zenith angle (SZA) and total ozone column (Bohn et al., 2004, 2016). The value of $j(NO_2)$ can also be measured directly in absolute terms using a chemical actinometer to detect the change in concentration of nitric oxide (NO) when a known concentration of NO_2 in a chamber is exposed to ambient light (Bahe et al., 1980; Shetter et al., 1992; Lantz et al., 1996; Bohn et al., 2005).

Chemical mechanisms, such as the Master Chemical Mechanism (MCM) are used to provide extensive chemical schemes for atmospheric chemistry and chemical transport models (CTMs). However, these photochemical schemes often use parameterisations to estimate *j*-values as a function of SZA (Saunders et al., 2003; Sommariva et al., 2020). Such expressions are derived by optimising empirical parameters in a generic expres-

sion to fit clear-sky estimates from a two-stream isotropic scattering model (Jenkin et al., 1997). These schemes only account for the solar position and the relevant molecular parameters (σ and ϕ), while ignoring the influence of other variables that can affect the magnitude of j-values, such as cloud cover, aerosol optical depth (AOD), ozone column and surface albedo.

For the photolysis of NO_2, the impact of the ozone column is small due to only small overlaps between wavelengths required for photodissociation of NO_2 (290-420 nm) and those absorbed by stratospheric O_3 (200-330 nm). The presence of clouds can both reduce (Kylling et al., 1995) and enhance (Schade et al., 2007) radiation and consequently increase or decrease the value of $j(NO_2)$ at ground level compared with that under clear-sky conditions. Similarly, increased AOD has been demonstrated to reduce observed $j(NO_2)$ compared to clear-sky conditions (Kanaya et al., 2003; Gerasopoulos et al., 2012; Hollaway et al., 2019; Zhao et al., 2021).

In atmospheric chemistry models, fractionally cloudy atmospheres (FCAs) can be accounted for, provided there is knowledge of how the clouds in each layer overlap. Photolysis rate constants are calculated in FCAs by solving the radiative transfer equation in a plane-parallel atmosphere, where vertical distribution can be highly variable but horizontal layers are uniform (Stamnes et al., 1988; Wild et al., 2000). These assumptions do not reflect realistic environments, such as the huge spatio-temporal variability of clouds in north-west Europe. To allow for this, vertical layers can be separated into appropriately sized independent column atmospheres (ICAs), which describe unique cloud profiles (Prather, 2015). Each ICA is either 100% clear or cloudy in each vertical layer. The Fast-JX algorithm (Neu et al., 2007) uses this technique, allowing for multiple layers of overlapping cloud within a model grid, based on the cloud overlap scheme selected (Feng et al., 2004). It uses a few representative sub-grid ICAs to approximate a larger number of ICAs, with each weighted by the frequency of ICAs with similar cloud distribution (Neu et al., 2007). However, this does not account for scattering out-

side of each specific column, and assumes fully overcast cloud (100%) when cloud is present in the ICA, limiting prediction of broken clouds at higher time resolutions (e.g. hourly).

Other methods to derive local j-values use measurements to estimate realistic cloud cover, including satellite (Ryu et al., 2017) and ground-based radiometer measurements (Kraus & Hofzumahaus, 1998; Cantrell et al., 2003; Topaloglou et al., 2005; Bohn et al., 2008; Trebs et al., 2009). For the latter, the ratio of spectroradiometer measurements to modelled estimates of actinic flux have been used to verify model calculations of radiation integrated over the UVB and UVA regions (300-315 and 315-405 nm, respectively) with altitude (Balis et al., 2002). Model estimates of $j(NO_2)$ have also been used as a reference for a radiometer measurement intercomparison (Bohn et al., 2008).

The ratio of measured to modelled $j(NO_2)$ has been used as a scaling factor to adjust modelled j-values and account for cloud and aerosol conditions at a local site at high time resolution (hourly). For example, this has been undertaken using MCM for atmospheric chemistry simulations. Bannan et al. (2017) only scale modelled $j(ClNO_2)$, while Elshorbany et al. (2012) and Xue et al. (2020) scale all photolysis rate constants in the MCM within their respective box model schemes. Sommariva et al. (2020) state that within AtChem, a box model specifically designed for use with the MCM, the j-values can be corrected to account for environmental factors by either constraining them to measured values, or scaling them based on the reference ratio discussed here. Where this is not done, the j-values will default to the MCM determined j-values, calculated as a function of SZA. Since these default values are derived for clear-sky estimations at a specific time and location (45°N, 500 m altitude, 1 July), the percentage differences between measured and model results for Boulder, Colorado (USA) were between 25-30% on average across all seasons. These large discrepancies emphasise the importance of using local measurements to scale j-values to local conditions. Sommariva et al. (2021) subsequently used local measurements of photolysis rate constants in Leices-

ter, UK, to constrain $j(NO_2)$, $j(HONO)$ and $j(ClNO_2)$ to their average diurnal cycles. Other photolysis rate constants were determined by AtChem (as above, initialised using measurements from Leicester), and were scaled by the diurnal cycle of $j(NO_2)$. This improves the accuracy of the clear-sky j-values for the local area, but does not reflect the highly changeable local conditions such as broken clouds, expected during winter in Leicester. The uncertainty introduced from applying a reference j-value scaling factor to other modelled photolysis rate constants is discussed in Chapter 4.

This study reports a systematic analysis of the derivation and potential application of an approach to adjust $j(NO_2)$ to capture the hourly variability in local meteorological and column conditions. A measurement-driven adjustment factor (MDAF) is derived and explored for three sites across the UK during 2019–2020: the EMEP rural supersite at Auchencorth Moss in south-east Scotland, the Met Office research site at Cardington in southern England, and the Manchester urban background air quality supersite. The characteristics and uncertainties of these $j(NO_2)$-derived MDAF values are discussed for each site, and the variation between them is compared. A case study on the influence of surface albedo on MDAF is also presented for 2 years of data at the Auchencorth Moss site. The implications of these findings, including the potential accessibility of relevant measurements in the future, are discussed.

3.2 Methods

3.2.1 Site descriptions and instrumentation

Radiometer measurements were made at three locations spread across the UK: the EMEP rural supersite at Auchencorth Moss in south-east Scotland, the Met Office research site at Cardington in southern England, and the Manchester urban background air quality supersite. Figure 3.1 shows the locations of these sites within the UK and satellite images of the area surrounding each one.

Figure 3.1: **(a)** The locations of the three measurement sites in the UK included in this study. **(b)-(d)** Satellite images of the area surrounding each measurement site to approx. 1 km in all directions, for Auchencorth Moss, Manchester Air Quality Supersite and Cardington, respectively. Satellite imagery was obtained from Google Earth (Google Earth, 2021).

Auchencorth Moss (AU)

Auchencorth Moss is a rural air quality monitoring station located in south-east Scotland, approximately 18 km SSW of Edinburgh (lat: 55°47'N, lon: 3°14'W, altitude: 260 m). It is a low-lying peatland, with an extensive fetch of open moorland in most directions (Figure 3.1b) and further described in Twigg et al. (2015) and Coyle et al. (2019). The site operates as a Level II/III European Monitoring and Evaluation Programme (EMEP) "supersite", representative of the northern UK background atmosphere (Malley et al., 2014) with atmospheric components measured using standardised methodology (Tørseth et al., 2012). Collectively, EMEP monitoring sites are used to understand long-range transport of air pollution around Europe, verify regional modelling approaches and advise governmental bodies on concentration and deposition of pollutants (UNECE, 2004b; Aas et al., 2012). Auchencorth Moss is also a site for a number of national and local monitoring networks (see Twigg et al., 2015), hosting an extensive array of instrumentation to measure trace gas and aerosol concentrations as well as meteorological parameters (Coyle et al., 2019).

A $j(NO_2)$ 4-π filter radiometer (Metcon, Meteorologie Consult GmbH, DE) is mounted at Auchencorth Moss on a mast approx. 3 m above ground level (from here on referred to as **AU-FR**). Measurements are recorded at 1-second resolution, and 2 years of data are analysed here (1 January 2019 – 31 December 2020), excluding a period when the instrument was removed from the site for calibration (5–26 June 2019; described in the next section). The deployment position of the filter radiometer was carefully considered to minimise potential sources of interference from the site. It is situated at the outskirts of the site and directed away from all other physical features at the site (e.g. cabins, trees, other instruments). Its supporting mast has a matte black coating to reduce any reflection that would not otherwise occur. The ground cover beneath the instrument is largely long grasses, where features that could increase surface albedo (e.g. snow) are quite evenly distributed. The closest change in these features (approx. 5 m behind the

supporting mast) is a wooden slatted path covered in black non-slip mats. This could contribute some uncertainty to upwelling measurements, but as it is often obscured by vegetation growth, this is expected to be negligible.

The 4-π sr filter radiometer provides a 360° field-of-view of the surrounding environment, by utilising two identical optical inlets facing in opposite directions (↓, downwelling, facing zenith; and ↑, upwelling, facing nadir). The inlet optic of each dome is designed to have a near-uniform angular response through use of a quartz diffusor (Bohn et al., 2004), and is surrounded by a light shield to provide an "artificial horizon", restricting the field-of-view for each dome to one hemisphere (Volz-Thomas et al., 1996). This allows total measured actinic flux, and therefore $j(NO_2)$, to be separated into its down- and upwelling components. This separation is not perfect as increased sensitivity can be observed near the horizon in a 4-π system due to contribution from the opposite dome. Hofzumahaus et al. (2002) show that this bias is partially compensated by the reduced sensitivity in individual 2-π inlets, resulting in a maximum overestimation of their actinic flux of 4% (between 0-12 km altitude). Transmitted light is guided through a set of optical filters (2-mm UG3, 1-mm UG5; Schott GmbH, DE) that restricts transmitted photons to the wavelengths of interest (310–420 nm) prior to their detection by a Hamamatsu photodiode, which proportionally converts incident radiation into an output voltage.

AU-FR calibration

Output signals from the filter radiometer were calibrated at the University of Manchester against a Bentham DTM300 scanning spectroradiometer (Webb et al., 2002a; Thiel et al., 2008) between 13-25 June 2019. This mid-summer period was selected to provide calibration over the maximum possible range of ambient incident radiation for the UK, between solar zenith angles (SZA) of 30–90°. The direction of the filter radiometer was turned 180° mid-way through this period, in order to calibrate each dome separately. Overall uncertainty in the spectroradiometer was ±5%, the sum in

quadrature of uncertainties in instrumental parameters (including cosine and actinic head responses), measured wavelength and general setup. Values of $j(NO_2)$ were calculated from the actinic flux spectra collected by using $\sigma(NO_2)$ from Mérienne et al. (1995) and $\phi(NO_2)$ from Troe (2000). Calibration factors for each dome were quantified using data presented in Figure 3.2.

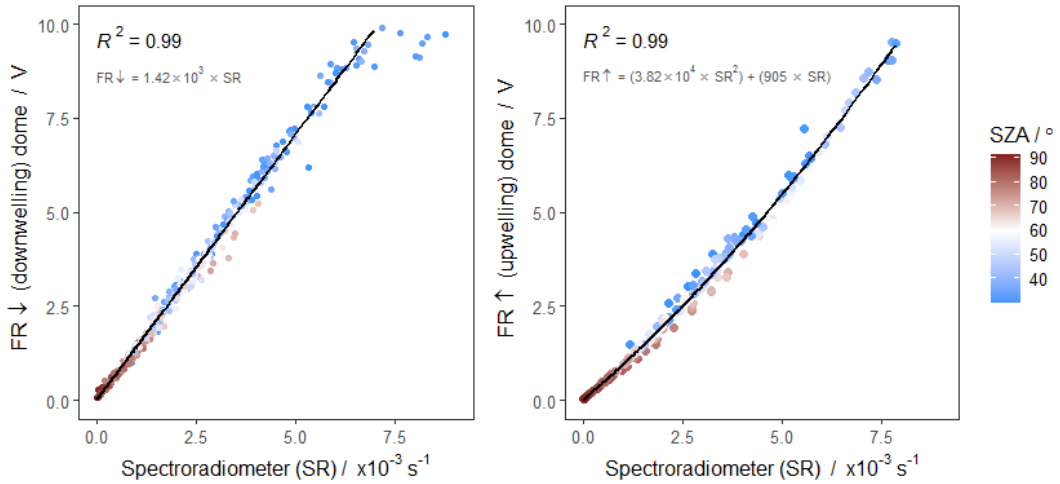

Figure 3.2: Calibration of the two Auchencorth Moss filter radiometer optical inlet domes against a Bentham DTM300 spectroradiometer at the University of Manchester from 13-25 June 2019. Filter radiometer measurements (1 s) are averaged to equal the scan duration of the spectroradiometer (approx. 3 min), and data where conditions were highly variable for this period (e.g. intermittent cloud cover), have been excluded. Points are coloured by the solar zenith angle (SZA) measured by the spectroradiometer (30–90°). Black lines indicate the calibration relationship for each dome, which is presented on its respective figure panel.

The limits of detection (LOD; 3σ of background signal) for the down- and upwelling domes were 9.40×10^{-6} s^{-1} and 1.15×10^{-5} s^{-1}, respectively. Background signals were determined from averaged measurements made after sunset and before sunrise (SZA $\geq$96°) and removed prior to data analysis. Broadband measurements made by the filter radiometer (1 s) during each spectroradiometer scan (actinic flux measured in each narrow λ band ($\sim$0.8 nm) sequentially; 3 min total) were averaged to obtain a calibration comparison point. Large standard deviations associated with these mean values were used to remove calibration points where actinic flux was highly variable during a single scan (e.g. rapidly changing cloud cover), which would result in inconsistent conditions

between λ intervals and yield an unrepresentative comparison to the filter radiometer. This range was primarily within $\pm$5% of the mean calculated.

On a few occasions of peak solar irradiance (noon in summer), recorded voltage of the downwelling dome exceeded the range of the detector and was reported as just over 9.6 V, observed during the calibration in Figure 3.2. These incidences of high $j(NO_2)\downarrow$ (here defined as signal >9.5 V) comprised 1% of all raw data collected, and were excluded from further analysis. An hourly average was only calculated if the 1 s data remaining within that hour met or exceeded 75% data capture. As a consequence, maximum $j(NO_2)\downarrow$ presented in this study is an underestimate, estimated as 7–22% based on extrapolation of the calibrated relationship to the spectroradiometer. The upper limit is quantified at solar noon on the clearest day that was close to the summer solstice (21 June 2019). It is possible that the curvature of the upwelling dome calibration (Figure 3.2) would be replicated by the downwelling dome, if the detector had not "topped out" at measurements exceeding 9.6 V.

Ratio plots of $j(NO_2)$ measured by the spectroradiometer and each dome of the filter radiometer are presented in Figure 3.3 as a function of SZA. Deviations from unity are observed predominantly at higher SZA, particularly during the “golden hour”, a colloquial term defined here as SZAs between the sun being 5° above the horizon, and sunrise or sunset (SZA = 90°). During this time measured values of $j(NO_2)$ are close to the LOD, and observed deviations in this ratio are larger in magnitude. Using the same criteria as Bohn et al. (2008) in their intercomparsion of filter- and spectroradiometers, these low-light conditions are grouped where $j(NO_2)$ is less than 5% of the observed maximum. In this dataset, Figure 3.3 shows that this grouping broadly corresponds with measurements at SZA >85°.

The deviation from unity and the larger spread of data at the higher values of SZA (>80°), shown in Figure 3.3, can be attributed to synchronisation issues between the two measurement methods when conditions are not constant. This includes periods of

intermittent cloud cover resulting in shading or enhancements in solar radiation during a single spectroradiometer scan (Schade et al., 2007). The extreme occurrences of this are removed via use of the standard deviation of averaged filter radiometer measurements (see above), but some minor occurrences remain. Consequently, the spread of data is generally larger for the downwelling dome because there were more overcast conditions during its calibration than for the upwelling dome. However, on the clearest day, the topping out of this dome at high solar intensities is expected to result in an increased ratio due to an underestimation of the filter radiometer compared to the spectroradiometer.

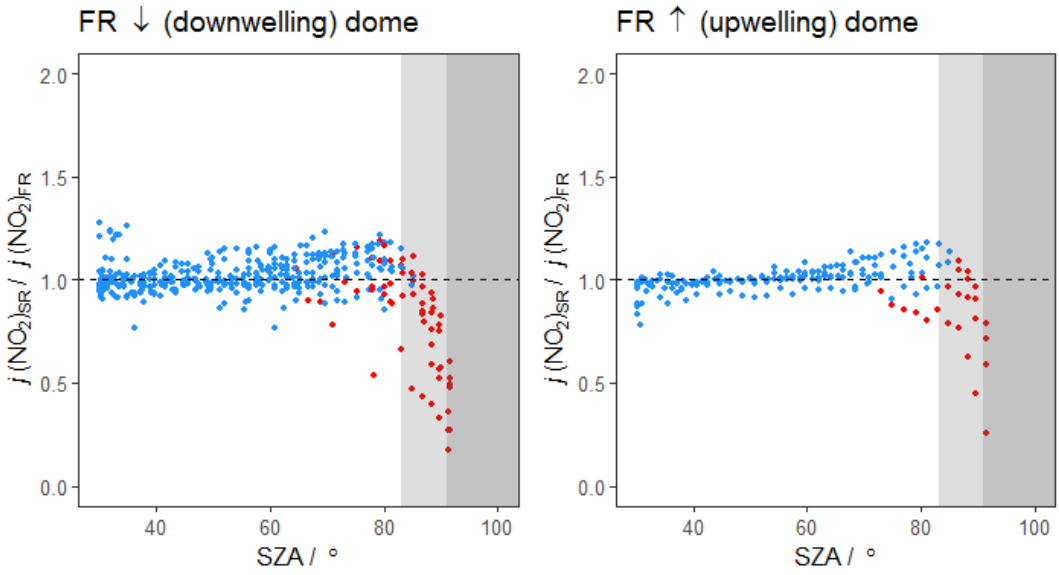

Figure 3.3: Ratios of spectroradiometer to filter radiometer photolysis frequencies measured during the co-location calibration period as a function of solar zenith angle. Left and right panels are for the FR downwelling and upwelling domes, respectively. Black dashed lines show the 1:1 ratio. Red points indicate values less than 5% of the maximum value for $j(NO_2)$ observed during the calibration. The lighter shading on both plots indicate the SZA at the start of "golden hour" (defined here as 5° above the horizon; 85°), while the darker shading show the SZA of sunrise/sunset (90°).

Overall, the uncertainty of the filter radiometer measurements were calculated as a combination of instrumental error (e.g. Larason & Cromer, 2001), error from the calibration to this spectroradiometer, and errors due to external factors (e.g. temperature stability of the instrument). For six of the same filter radiometers, Shetter et al. (2003) quoted

overall error as 9.6–11%, the range dependent on whether conditions were clear or cloudy. Laboratory assessments of instrumental error in this study were not feasible, so to provide a benchmark estimate of error for both domes of the filter radiometer used here, the upper bound (11%; cloudy conditions) was combined with the calibration error of each dome. This yields an overall error for both the down- and upwelling domes of 13% for SZAs between 30 and 85°. For SZAs >85° the error increases to 32% and 25%, respectively.

Manchester (MA)

The Manchester Air Quality Supersite (MAQS) is an urban background site located on the University of Manchester's Fallowfield Campus (lat: 53°26'N, lon: 2°12'W, altitude: 43 m); Figure 3.1c). The site is one of the most instrumented urban background sites in the UK, aiming to use a range of trace gas, aerosol and meteorology measurements to assess air quality and exposure in a typical high population area, to create better policy interventions to improve public health. The actinic flux that is measured at the site with an Ocean Optics spectrometer (FLMS12526) coupled to a 2-π actinic flux optical inlet is used to calculate downwelling $j(NO_2)$. This instrument is referred to from here on as **MA-SR**. The optical inlet is attached to black painted railings on top of the site hut, $\sim$7.2 m above an asphalt car park. The nearest obstruction is some deciduous trees south of the site, reaching up to 1.5 m above the height of the optical inlet, approx. 5 m away. This is anticipated to result in brief and intermittent shielding of radiation at SZA $\geq$73°. Measurements are recorded with a 1-min integration time and data for the period 6 September 2019 to 31 May 2020 are used here. The limit of detection (LOD), quantified as 3σ of the measured background signal, where SZA $\geq$96°, was 1.92×10^{-6} s^{-1}.

Cardington (CA)

The Met Office Meteorological Research Unit is located in Cardington, Bedfordshire (lat: 52°06'N, lon: 0°25'W, altitude: 29 m; Figure 3.1d). A $j(NO_2)$ 2-π filter radiometer from the same manufacturer as used at Auchencorth Moss (Metcon, Meteorologie Consult GmbH, DE) is secured to an instrument cabin roof approx. 4 m above ground level. The instrument is referred to from here on as **CA-FR**. The immediate area surrounding the cabin is a mostly grass-covered arable field, with buildings of a similar height approx. 20 m to the west, and scattered trees around 60 m away to the north-east. The site is situated in a wide shallow valley on the south side of Bedford. Other instrumentation at the site is used to monitor and study boundary-layer meteorological and surface processes to aid development of Met Office weather prediction methods (McGregor & Price, 2018).

Measurements are recorded at 1-min resolution and data for the period 6 March 2019 to 14 June 2020 are used here. Measured voltages are converted to $j(NO_2)$ values using the instrument's Metcon factory calibration against a chemical actinometer. The LOD for $j(NO_2)$ during this period was calculated using the same method as at Manchester, and determined to be 3.25×10^{-5} s^{-1}. This is the largest LOD of the instruments in this study. In addition, the $j(NO_2)$ values derived from the CA-FR measurements frequently exceed the cloud-free model estimates of $j(NO_2)$ for the site (see Figures 3.4 and 3.5, discussed in Section 3.3.1). Compared to the relationships between measured and modelled $j(NO_2)$ at the Auchencorth Moss and Manchester sites, the bias in measured $j(NO_2)$ at Cardington (irrespective of day/night and summer/winter) suggests that the calibration of the instrument response requires further investigation. This was not possible within this study, and in fact the measurements and MDAF ratios for this site are presented as a real example of the importance of the need for instrument standardisation and local-derived adjustment of j-values (see Section 3.4).

3.2.2 Radiative Transfer Model

A model estimate for $j(NO_2)$ was calculated using the Tropospheric Ultraviolet and Visible radiation model (TUV v5.3; Madronich, 1987; NCAR, 2019), one of the most widely used radiation models (Lee-Taylor & Madronich, 2002; Bais et al., 2003; Wilson, 2015; Bohn et al., 2016; Ghosh & Sarkar, 2016; Wang et al., 2017b; Xu et al., 2019). The model was set up to match the location and height of the radiometer at each site. The time resolution of the model output was hourly.

The TUV results used in this study were intended to provide reasonable estimates of cloud-free conditions, as an example of typical model estimations of $j(NO_2)$. Daily average ozone column and air temperature data used in the model were obtained from the OMI satellite (NOAA ESRL, 2021) and measurements made at each site, respectively. Days with missing O_3 column measurements were filled with that from the following day. TUV default values for surface albedo (0.1) and aerosol optical depth (AOD) at 550 nm (Elterman, 1968) were used in all model calculations. The surface albedos of grass (Auchencorth Moss and Cardington) and asphalt (Manchester) are expected to be similar to the default value. At Auchencorth Moss, where there is occasional snow cover, the upwelling radiation is also measured to capture this change in local conditions (see snow case study; Section 3.3.2). Variation in AOD within and between sites is assumed be small, and therefore have minor impact on modelled $j(NO_2)$. Any periods of larger variation are assumed to be captured by the local measurements of $j(NO_2)$ (demonstrated by a spike in AOD during early March 2021 in Chapter 4). The aerosol single scattering albedo (SSA) was set to 0.99. High values of SSA denote a highly scattering atmosphere in the model (1 = purely scattering, 0 = purely absorbing), and small changes can lead to a larger difference in transmission of diffuse radiation (e.g. 300–360 nm region reported by Michalsky & Kiedron, 2008). In this model set-up, a decrease in SSA of 0.1 resulted in approx. 6% decrease in $j(NO_2)\downarrow$. It is expected that the SSA will be >0.8 for aerosols (Madronich, 1993), resulting in a maximum potential

uncertainty of <12%. The NO_2 column was assumed to be zero. This is unlikely to be the case at any of the sites, but to be between 6.75 and 15 $\times$ 10^{15} molecules cm^{-2} (approx. 0.25-0.5 DU; Pope et al., 2018). However, inclusion of even this upper limit in NO_2 column resulted in a maximum change in $j(NO_2)\downarrow$ of less than 2%.

Since the radiometers at all sites are zenith-pointing, the TUV model domain replicates this 2-π sr field-of-view by including only direct light and downward propagating diffuse radiation. However, as the AU-FR instrument has a 4-π sr field-of-view and includes a separate measurement of upwelling radiation, TUV was run a second time for Auchencorth Moss including upward propagating diffuse radiation. These model results are referred to as $j(NO_2)$-down and $j(NO_2)$-total, respectively.

3.2.3 Measurement-driven adjustment factor

Hourly mean $j(NO_2)$ measurements from each radiometer were ratioed with that site's calculated $j(NO_2)$ values to yield a measurement-driven adjustment factor (MDAF) for each hour at each site:

$$NO_2\text{-MDAF} = \frac{\text{measured } j(\mathrm{NO_2})}{\text{modelled } j(\mathrm{NO_2})} \tag{3.2}$$

Two sets of MDAF values were calculated for the Auchencorth Moss site: one using the total signal measured by both domes of the AU-FR, and the $j(NO_2)$-total model results; and one using the AU-FR downwelling dome measurements, and the $j(NO_2)$-down TUV output. It should be noted that in this study the quantum yield for NO_2 photodissociation used by the TUV model is the same as that used in the calibration of the AU-FR and MA-SR calculations (Troe, 2000), but the absorption cross-sections differ. The TUV model uses the absorption cross-sections measured by Vandaele et al. (1998), which differ from values used in the AU-FR calibration and MA-SR calculations (Mérienne et al., 1995) by 2-3% at room temperature (Burkholder et al., 2019).

This $j(NO_2)$-derived MDAF metric (henceforth only referred to as MDAF) is only applicable for model validation where the radiometer measurements can be obtained at the same location as the model domain. In this study, MDAF values were excluded from all sites if they were calculated at SZA >90° (defined as between sunset and sunrise), as these conditions are likely to result in more significant uncertainty in measurements, and were not observed during the AU-FR calibration.

3.3 Results and discussion

3.3.1 Overview of measurements, model results and MDAF values

Overall, measurements of $j(NO_2)$ exhibit the seasonal variation expected in the northern hemisphere (Figure 3.4), with the smallest solar noon values observed in the winter (approximately 2.5×10^{-3} s^{-1}; December to February), increasing through the spring (March to May) to a solar noon maximum of approximately 8×10^{-3} s^{-1} in the summer (June to August). There are no summer measurements in the MA-SR dataset, but there is 97% data capture for the time period presented. Values of $j(NO_2)$ derived from the CA-FR are larger than from both the AU-FR and MA-SR on clear days throughout the year (Figure 3.4). Monthly mean measurements of $j(NO_2)$ at Cardington are approximately 1.5–2 times larger than at Manchester, potentially attributed to a drift in the instrument response from the calibration supplied by the manufacturer. The data which remain in this analysis demonstrates the importance of properly calibrated $j(NO_2)$ measurements for this application.

Sites demonstrate broadly similar temporal variation in $j(NO_2)$ measurements at finer time resolutions (e.g. hourly and daily). For example, the largest $j(NO_2)$ measurements are associated with high pressure, and the smallest with overcast conditions across the UK, respectively. However for the majority of $j(NO_2)$ measurements, the variation in local conditions at each site led to differences in measured $j(NO_2)$ values at the same time, and on the same day. Observed measurements at higher time resolution show

little correlation between each radiometer (discussed at the end of this section), as local meteorology (e.g. cloud cover and aerosol profile) is unique to each site.

At Auchencorth Moss, large peaks in the time series of total (4-π) measurements can be observed in the winter, because of an increased contribution of upwelling radiation (discussed in Section 3.3.2). The topping out of the AU-FR downwelling dome is less evident in the overall time series, but is clear in Figure 3.5 where the expected larger measurements of $j(NO_2)$ at lowest SZAs (30-40°) are missing. Based on diurnal cycles on clear days where raw AU-FR (and co-located pyronameter; UKCEH, 2017) measurements show smooth profiles, seasonal mean $j(NO_2)\downarrow$ values at Auchencorth are estimated to be up to $\sim$12% lower in spring, and $\sim$20% lower in summer. These relative uncertainties lie within the bounds of those estimated during calibration (7-22%; see Section 3.2). However, considering these uncertainties, there is still a sizable discrepancy with the TUV cloud-free model estimations of $j(NO_2)$ at the same SZA. The $j(NO_2)$ values measured by the MA-SR shows a similar magnitude difference (up to approx. 20%) at low SZA. As no summer period is included in the MA-SR comparison, the quantity of data at SZA <35° at this site is lower than for the AU-FR comparison, but overall the commonality in discrepancies at these two sites suggests an overestimation by the TUV model. This is possible, as the model input uses a number of assumptions detailed in Section 3.2.2. Despite this, the TUV model results provide a good estimate of $j(NO_2)$ from which to evaluate the MDAF metric.

At large SZAs, the AU-FR measurements exceed the TUV estimates. The occasions with more substantial differences between the measured total $j(NO_2)$ and the TUV estimate are due to the contribution of upwelling radiation, as demonstrated by their absence in the corresponding AU-FR downwelling plot (Figure 3.5). The AU-FR measured values of $j(NO_2)$ that only exceed the modelled estimates by a small amount (presented on the downwelling plot) are at SZAs between 64–90°. The exceedances between SZA of 64–85° occur predominantly on occasions where the surface albedo

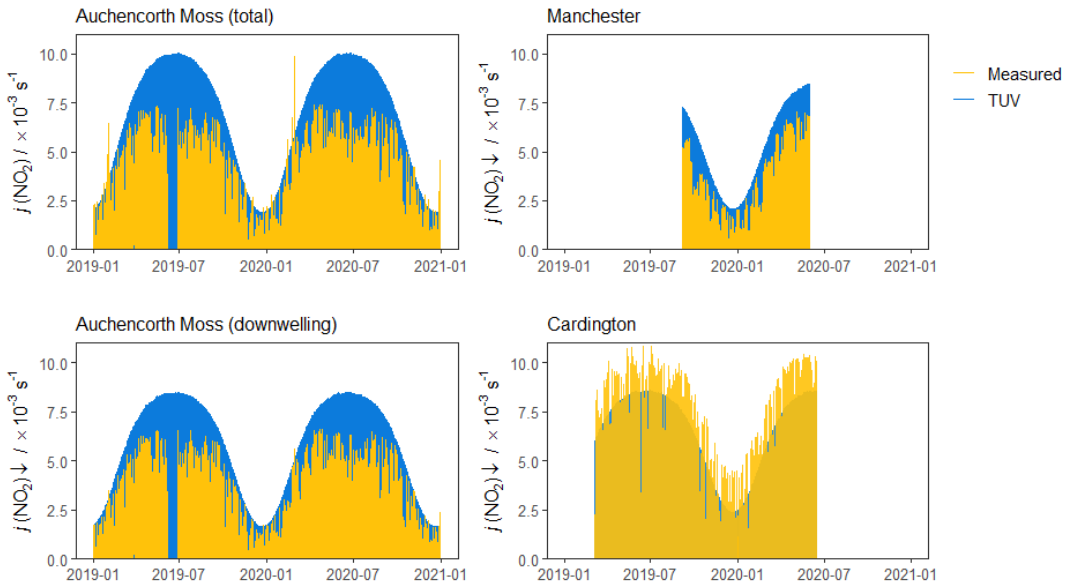

Figure 3.4: Time series of hourly measured (yellow) and modelled (blue) $j(NO_2)$ at the Auchencorth Moss, Manchester and Cardington sites. Auchencorth data are provided for total $j(NO_2)$ ($\downarrow + \uparrow$; top-left) and only downwelling $j(NO_2)$ ($\downarrow$; bottom-left).

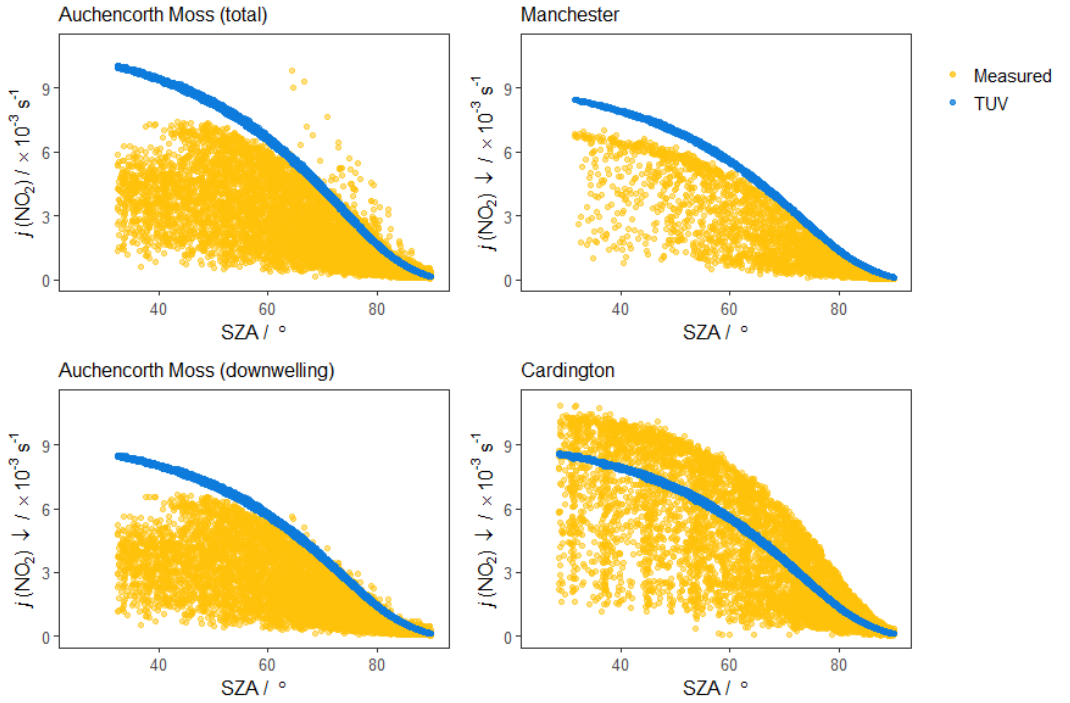

Figure 3.5: Hourly measured (yellow) and modelled (blue) $j(NO_2)$ as a function of solar zenith angle, at the Auchencorth Moss, Manchester and Cardington sites. Auchencorth data are provided for total $j(NO_2)$ ($\downarrow + \uparrow$; top-left) and only downwelling $j(NO_2)$ ($\downarrow$; bottom-left).

is larger, shown by $j(NO_2)\uparrow$ values >1 $\times$ 10^{-3} s^{-1}. This strongly implies that some diffuse radiation is also being detected by the downwelling dome of the AU-FR. Exceedances at SZA >85° are more heavily influenced by the increased uncertainty in the AU-FR measurements (32% and 25% for down- and upwelling domes, respectively). Measured $j(NO_2)$ does not exceed the modelled estimates at Manchester, showing good agreement for SZAs >65°.

The hourly $j(NO_2)$ MDAF values derived for each site are shown in Figure 3.6 both as time series and as scatter plots with respect to SZA. The time series of MDAF values suggest no substantial seasonal variation, aside from total $j(NO_2)$ at Auchencorth Moss, where increased contribution of upwelling radiation leads to peaks in the time series during winter and spring (see the case study in Section 3.3.2). As the TUV clear-sky estimate is larger than almost all measurements made at Auchencorth Moss and Manchester, MDAF values at these sites are mostly below unity, scaling the corresponding model estimates down. The largest values of MDAF increase slightly with the SZA in a generally linear trend (Figure 3.6, right), surpassing unity at a SZA of 68° at Auchencorth Moss (for both 4-π and 2-π derivations) and 74° at Manchester. More scatter is observed in MDAF derivations at larger SZAs at Auchencorth Moss, caused by the measurement uncertainties discussed earlier.

The magnitude of the influence of local meteorology is illustrated by the impact of the MDAF approach on the $j(NO_2)$ values. For example, application of the hourly total AU-MDAF and downwelling AU-MDAF resulted in a reduction of the annual mean cloud-free modelled $j(NO_2)$ at Auchencorth Moss by approximately 44% and 45%, respectively.

Seasonally averaged MDAF values derived at each site are presented in Figure 3.7, as well as the measured and modelled $j(NO_2)$ from which they are derived. While the MDAF measurements are broadly similar between seasons, there are small discrepancies to note for each site which are explored here. The MA-MDAF values show that, of

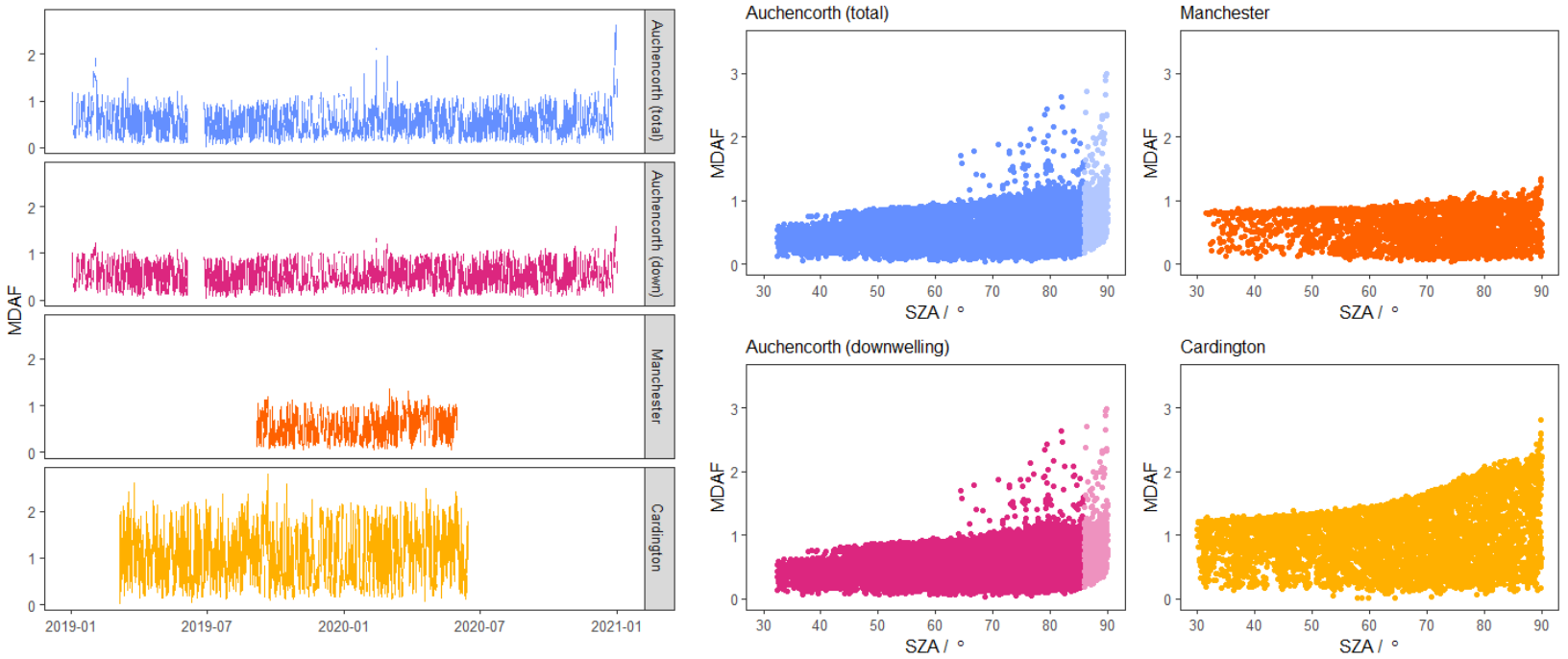

Figure 3.6: Hourly derived $j(NO_2)$ measurement driven adjustment factors (MDAF) for: blue, Auchencorth Moss (total); pink, Auchencorth Moss (downwelling); orange, Manchester Air Quality Supersite; and yellow, Cardington. **(Left)** time series of all hourly MDAF values. **(Right)** the MDAF values plotted as a function of SZA. AU-FR measurements of higher uncertainty (>85°) have been filtered out of the time series, but are presented on the scatter plots in a lighter colour.

the autumn to spring data available, the largest average reductions in modelled $j(NO_2)$ (shown by the smallest MDAF values in Figure 3.7) occur during autumn and winter (51% and 53% reductions in $j(NO_2)$, respectively). These are seasons in which local meteorological conditions are characteristically more overcast. The largest observed seasonal average MA-MDAF values are in spring, leading to the smallest reduction in modelled $j(NO_2)$ (36%), when the weather is typically clearer. No summer measurements were available at Manchester, but it is assumed these MA-MDAF values would be similar to those in spring.

Total AU-MDAF estimates have an almost opposite relationship, with the largest seasonal MDAF values (and therefore smallest reduction in modelled $j(NO_2)$ values) in winter (31%) compared with summer (52%). The larger magnitude reduction of $j(NO_2)$ in summer is likely a consequence of the removal of topped-out measurements on clear days, leaving only conditions of intermittent and heavy cloud to be considered in the average.

The larger mean of AU-MDAF in winter, compared to MA-MDAF, is contributed by the more prevalent diurnal cycle in Figure 3.7. Greater values of AU-MDAF occur at higher SZA, and bias the subsequent reduction in modelled $j(NO_2)$ to the lower value of 31%. If only periods of higher solar intensity (with more direct light at larger SZAs) are considered, the wintertime reduction in modelled $j(NO_2)$ increases to 45%. The contribution of enhanced upwelling radiation (discussed in Section 3.3.2) also contributes to the lower reduction of modelled $j(NO_2)$ in winter. When only downwelling is considered this increases from 31% to 39%. This reduction in modelled $j(NO_2)$ is less than is observed for Manchester (51%), however both sites are still subject to a substantial decrease in modelled $j(NO_2)$ as a result of the local conditions. This difference in winter averaged MDAF is attributed to interference from beyond the 2-π sr view of the inlet optic being more prevalent at Auchencorth Moss, due to differences in the radiometer position at each site. The AU-FR is fixed to a mast approximately 3 m above ground

level (a.g.l.), while the MA-SR is attached to a cabin roof almost twice as high a.g.l. (approx. 7.2 m). The difference in height is not reflected in the TUV model input, which considers only the output altitude. During periods of increased surface albedo, more diffuse upwelling radiation will be collected by the downwelling dome of the AU-FR as it is closer to ground level, than by the MA-SR. These occasions were also more frequent at Auchencorth Moss, during the period of each deployment.

MDAF values derived for Cardington show a similar increase of maximum values with SZA as Auchencorth Moss and Manchester (Figure 3.6 and Figure 3.7), but at a greater magnitude due to larger measurements of $j(NO_2)$ compared to both other sites. This trend appears linear until SZA of 63° where it surpasses 1.5, then curving slightly upwards at higher SZA. This rise in MDAF is the result of a) the reduced sensitivity of the employed optical inlet of the filter radiometer (>75° SZA; Volz-Thomas et al., 1996; Hofzumahaus et al., 2002), and b) the increased relative difference between measured and modelled estimations of $j(NO_2)$ at high magnitudes of SZA. Similarly, the lower light levels in winter result in a wider confidence interval around mean estimations of MDAF in Figure 3.7. Between seasons there is little difference in the average reduction of $j(NO_2)$ (<10% between all seasons), and this value is mostly contributed by the larger magnitude of MDAF values at higher SZAs.

Within the UK context of this study, some spatial trends in $j(NO_2)$ can be identified in the downwelling TUV model results (Figure 3.7). Similar values of $j(NO_2)\downarrow$ are predicted for all UK sites in the spring and summer (within 2%). In autumn and winter months the magnitude of solar noon predictions of $j(NO_2)$ have an inverse relationship with site latitude, as simultaneous measurements will be at greater SZAs (and thus increased air mass factor $\approx 1/\cos(\mathrm{SZA})$) when collected at higher latitudes. At higher SZA and air mass factors, there is more opportunity for scattering and absorption of actinic flux prior to reaching the site, thus a reduced estimate of $j(NO_2)\downarrow$. The magnitude of such differences in $j(NO_2)\downarrow$ range between 22–40% at Auchencorth Moss (56°N) and

Cardington (52°N) in autumn and winter, respectively. Results at Manchester (53.5°N) lie between these two sites, approximately 17–28% more than Auchencorth Moss and 4–10% less than Cardington.

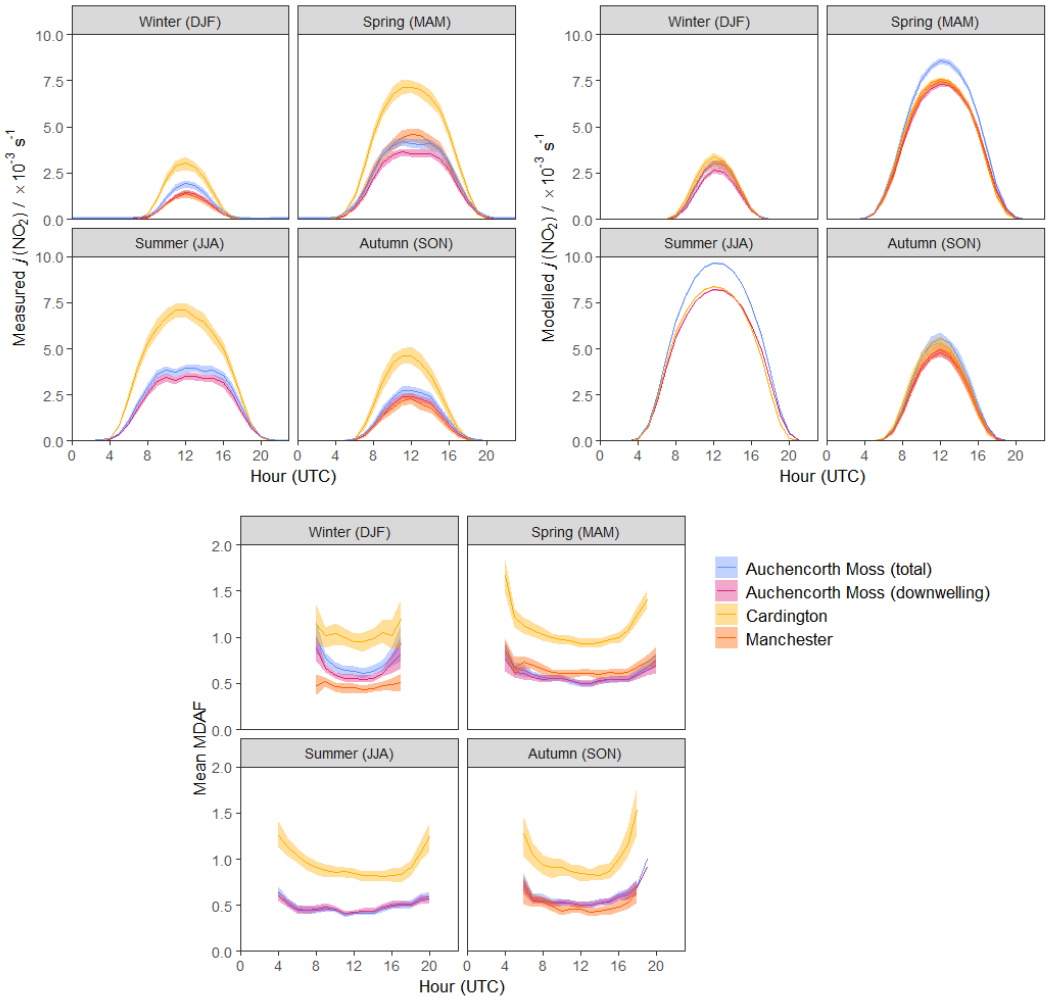

Figure 3.7: Seasonal mean diurnal profiles of measured $j(NO_2)$, modelled $j(NO_2)$ and MDAF values at the Auchencorth Moss, Manchester and Cardington sites. The shaded areas represent the 95% confidence interval. There is no summer season data for Manchester.

Figure 3.8 demonstrates the lack of correlation between hourly MDAF derivations at Auchencorth Moss, and those at Manchester or Cardington. Due to the similarity of temporal variability in the cloud-free model results, this is a result of the difference in measurements between each site. MDAF values are driven by local conditions, and at an hourly resolution, they are not applicable beyond this area. Further comparisons are more difficult to make with measured data when measurement intercomparison be-

tween instruments is lacking. Consequently, spatial MDAF trends are more difficult to conclude, beyond the comparisons presented in this Section. This illustrates the importance of using standardised $j(NO_2)$ measurements, or instruments that have been subject to co-located intercomparison, where more spatial information is required (e.g. national or regional model domains).

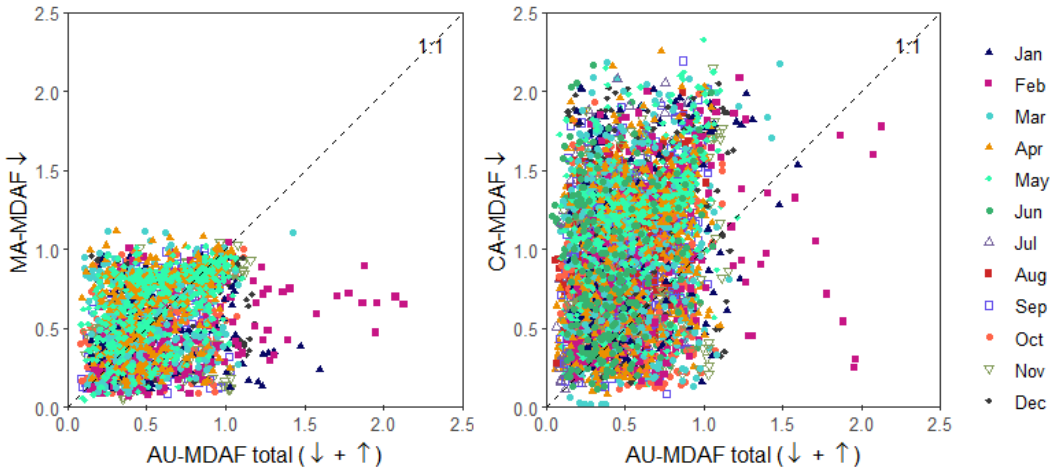

Figure 3.8: Comparison of hourly Auchencorth Moss MDAF values using total $j(NO_2)$ (↓ + ↑) with **(left)** Manchester MDAF values (6 September 2019 to 31 May 2020) and **(right)** Cardington MDAF values (6 March 2019 to 14 June 2020). Colour and shape of points indicates month of measurement. Black dashed line indicates 1:1 relationship.

3.3.2 2-π vs. 4-π derived MDAF

Measurements from the 4-π AU-FR can be separated into down- and upwelling components. The sensitivity of each dome reduces close to the horizon, but the total signal (sum of down- and upwelling components) is partially compensated by interference from the opposite facing dome (Hofzumahaus et al., 2002), which can lead to positively biased measurements during occasions of high surface albedo (see previous Section and Figure 3.4). Both downwelling (zenith-facing; ↓) and total (sum of zenith- and nadir-facing; ↓ + ↑) are visualised in Figure 3.9. The first plot presents the ratio of hourly mean upwelling $j(NO_2)$ measurements to the total, as a function of SZA. The second presents a direct comparison of the hourly MDAF values derived for both down-

welling and total $j(NO_2)$, for the full 2 years. When considering diffuse radiation from both zenith and nadir-facing directions, the TUV model consistently estimated $j(NO_2)$ values that were 15-17% larger than the 2-π counterpart year-round, indicating that the seasonal difference in the AU-MDAF values are driven by measured $j(NO_2)$.

The majority of $j(NO_2)\uparrow$ to total $j(NO_2)$ ratios (Figure 3.9) are near-independent of SZA between 32° (minimum observed) and 60°, but shows a curved increase with SZA (>60°), where overall light levels are lower. This is expected, as at larger SZA there is an increased partitioning of diffuse to direct radiation in the total available at the point of observation. Less direct radiation is collected by the downwelling dome, while more diffuse radiation reaches the upwelling dome (compared to the middle of the day). This results in the percentage contribution of the upwelling dome to total $j(NO_2)$ to increase to around half. Points above the main trend in the data represent irregular environmental changes that drive increased measurement of upwelling $j(NO_2)$, such as changes in surface albedo increasing the daytime contribution of upwelling radiation compared to the rest of the year. These occurrences were predominantly in January-March of both years, a short period at the end of December 2020, and a single day in April 2019.

For most of the year, derived AU-MDAF values for total and downwelling-only $j(NO_2)$ agree very well, lying close to the 1:1 line (Figure 3.9, right). There is a second well-correlated trend where the downwelling derived AU-MDAF is approximately 60% of the total derived AU-MDAF, which correspond with the identified days of increased upwelling radiation. This group has a slightly wider spread of data, due to larger variations in surface albedo. In the TUV model, the surface albedo was left constant at 0.1, however where snow is present, it is likely to be nearer to unity (0.8–0.9; Lee-Taylor & Madronich, 2002; Lin et al., 2008).

The impact of the change in surface albedo is demonstrated through a case study of measurements made during February 2020, presented in Figure 3.10. For the start of the

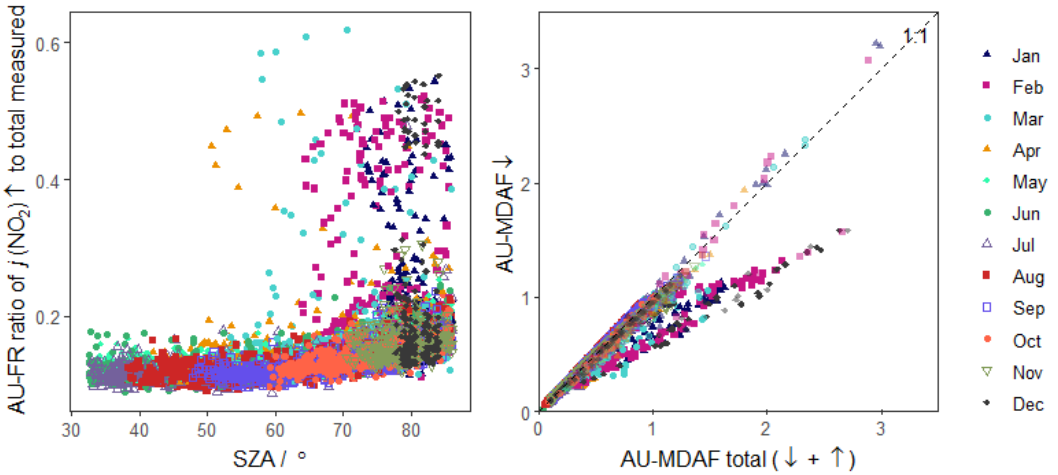

Figure 3.9: **(Left)** Ratio plot of hourly mean $j(NO_2)$ upwelling (2-π; $\uparrow$) measurements compared to total (4-π; $\downarrow + \uparrow$), as a function of solar zenith angle. **(Right)** Comparison of hourly average AU-MDAF values using total $j(NO_2)$ ($\downarrow + \uparrow$) against only downwelling $j(NO_2)$. Colour and shape of points indicates month of measurement. All AU-FR measurements are included in this plot, but measurements of higher uncertainty (>85°), which were removed from the AU-FR time series for analysis (in Section 3.3.1) are shown in a lighter colour. Black dashed line indicates 1:1 relationship.

case study (2–9 February), measurements were made when ground cover (and therefore surface albedo) was typical for Auchencorth Moss. The last few days measurements (10–13 February) were collected during and following moderate snowfall (for the site). These two contrasting ground cover conditions represent the largest change in surface albedo observed at Auchencorth Moss during this study, corresponding with a rise in the contribution of measured $j(NO_2)\uparrow$ to total $j(NO_2)$, from 16% to 48%. The increased contribution of upwelling $j(NO_2)$ translated to a 36% increase in the total MDAF, compared to the MDAF derived for only downwelling measurements. This therefore demonstrates the importance of considering upwelling radiation on derived MDAF values, which can have significant implications when used for adjusting modelled values of $j(NO_2)$.

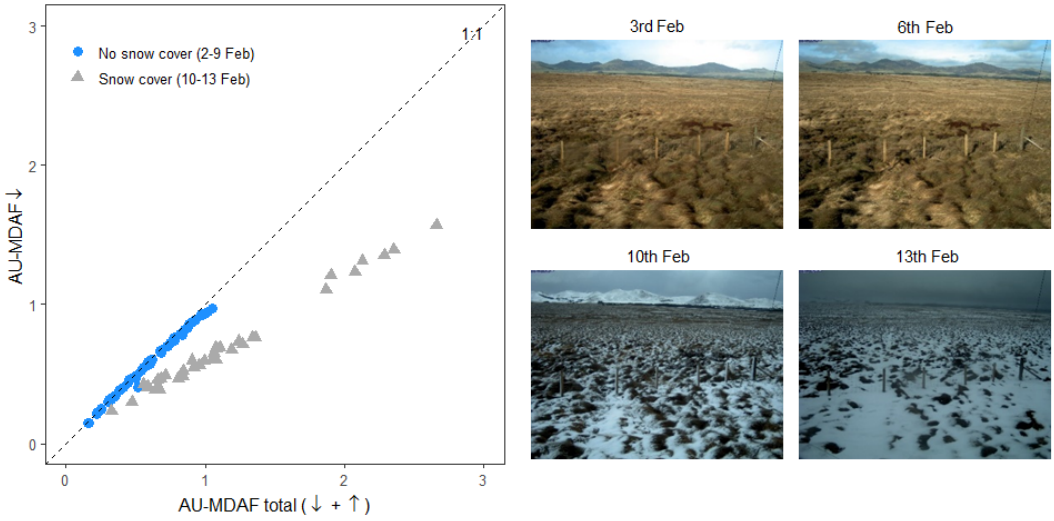

Figure 3.10: Comparison of hourly average AU-MDAF values using total $j(NO_2)$ (↓ + ↑) against only downwelling $j(NO_2)$ for 2–13 February 2020. Days with typical ground cover for Auchencorth Moss (2–9 February 2020) are shown by blue circles, while days during and following snowfall (10–13 February 2020) are presented as grey triangles. Example photos of the site, taken by an automatic Phenocam (EuroPhen, 2020), are presented for 3, 6 February (no snow) and 10, 13 February (with snow) at 12:00 (UTC).

3.4 Conclusions and implications of NO_2-MDAF

Modelled trace gas concentrations are frequently validated against measurements to ensure a model's performance is accurate, but the same is rarely performed for photolysis rate constants, despite the known variability in meteorological conditions at a local site and the importance of photolysis to atmospheric chemistry processes. This is often a consequence of the lack of data outside of specific campaigns. This study has demonstrated the use of local radiometer measurements for capturing this variability at a high temporal resolution, to both validate model predictions and to adjust clear-sky or cloud-free model estimates, to account for local conditions affecting $j(NO_2)$.

Prior discussions describe how the MDAF metric demonstrated that TUV (v5.3) model estimates of $j(NO_2)\downarrow$ in cloud-free conditions were, on average, approximately 45% larger than $j(NO_2)\downarrow$ measured across the UK (Figure 3.7), which would lead to the same level of bias if model results were not adjusted to account for local conditions.

The TUV modelling conducted for this study was limited by some assumptions in input parameters (e.g. SSA and O_3 column, see Section 3.2.2). However, the modelled $j(NO_2)$ values in this study provide a typical estimate of cloud-free modelled $j(NO_2)$, and therefore a good baseline for comparison and demonstration of MDAF application at different sites.

At Auchencorth Moss, MDAF values calculated considering 4-π and 2-π sr fields of view demonstrate good agreement (<6% difference, on average) for most conditions. However, conditions of particularly high surface albedo (such as snow cover) increase the upwelling component of the local diffuse radiation. As a result, under these conditions the AU-MDAF based on total radiation (considering both $j(NO_2)\downarrow$ and $j(NO_2)\uparrow$) is around 40% larger than the AU-MDAF when only downwelling $j(NO_2)\downarrow$ is considered. Annual average MDAF values are similar at Auchencorth Moss and Manchester, but at higher time resolutions site-specific variations in conditions lead to more differences in MDAF values at each site (Figure 3.8). Cardington measurements of $j(NO_2)$ demonstrate similar trends, both temporally and with SZA, but are approximately 1.5–2 times larger than at Manchester. As a result, CA-MDAF values are greater by a similar amount than both AU-MDAF and MA-MDAF values. This larger magnitude of measured $j(NO_2)$ at Cardington, and hence in CA-MDAF values, is attributed to a drift in the calibration of the Cardington FR instrument.

Accurate calculations of photolysis rate constants are integral to accurately assessing air quality. In particular, these values are important drivers for the production of secondary pollutants that negatively affect both human and environmental health (e.g. O_3 and particulate matter), via the production of radicals. Local atmospheric chemistry and air quality modelling, such as those used to assess public health and the effectiveness of implemented mitigation measures, often include only simple chemical schemes with highly parameterised photochemistry (e.g. the ADMS model). The Master Chemical Mechanism (MCM) is a widely used advanced chemistry scheme for atmospheric

chemistry and chemistry transport models, but still uses simplified photochemistry. In MCM the photolysis rate constants are determined as a function of solar zenith angle, based on the fitting of a generalised equation to clear-sky model results for a single site (Jenkin et al., 1997; Saunders et al., 2003). To improve j-values determined within the model domain, models can be coupled with dedicated radiative transfer models, such as the TUV model used here, Fast-JX or less explicit photolysis schemes like the Generic Reaction Set (GRS). However, within these schemes estimates of the extent of cloud cover is frequently neglected, oversimplified, or computationally intensive when calculating j-values for a local site, leading to considerable potential uncertainty.

The radiometer measurements analysed in this study are being made in a long-term capacity in the UK, alongside similar occurrences across Europe (at least 4 ACTRIS sites; *personal communication*). If these existing long-term multi-site measurements could be standardised and archived for use, it would consequently have immense value in supporting atmospheric chemistry measurement and modelling. Such measurements of $j(NO_2)$ could be used directly within models to constrain $j(NO_2)$, or derive a metric like MDAF to scale modelled j-values of other photodissociation reactions, as has been done in previous studies (e.g. Elshorbany et al., 2012; Bannan et al., 2017; Xue et al., 2020; Sommariva et al., 2021). This use of MDAF expands the application of $j(NO_2)$ measurements to a number of important radical producing photodissociation reactions, such as the HO_x sources of HONO and HCHO, and Cl atom sources like $ClNO_2$. These methods of using $j(NO_2)$ measurements to account for changes in local conditions in model predictions of photolysis rate constants provide invaluable data for understanding tropospheric chemistry and radical production rates. An analysis of applying an MDAF value derived from a reference species, like $j(NO_2)$, to other modelled photolysis rate constants is detailed in Chapter 4.

These uses of $j(NO_2)$ measurements could provide advantages in urban environments. Such measurements would be hyper-specific to individual locations, as even small dif-

ferences in location could provide very different light levels due to the high variability in the local environment. A wide array of nearby materials may provide very different surface albedos that alter the measured actinic flux, and the lack of uniformity in local features (e.g. buildings and trees) can result in unique temporal patterns of shadows at each site. Urban radiometer measurements would therefore be most applicable for investigating photolytic interference in pollutant concentrations measured at a specific site, or to improve photolysis schemes in urban model domains. Therefore, radiometer measurements in urban settings have implications for public health policy assessments, and monitoring local Air Quality Management Areas (AQMAs; Defra, 2021a) where it is predicted that target air quality concentrations will not be achieved.

Chapter 4

Investigation of reaction-specific measurement-driven adjustment factors on the derivation of atmospheric photolysis rate coefficients which account for local meteorology

The work presented in this chapter is based on a research paper currently in preparation for submission to the journal Atmospheric Measurement Techniques. The Ocean Optics QE65000 spectral radiometer and 2-π optical inlet were provided and calibrated by Dr L.K. Whalley (U. Leeds). Due to Covid-19 related travel and access restrictions, the spectral radiometer was set-up at Chilbolton Observatory by D. Ladd (Science and Technology Facilities Council; STFC), and operated by me through remote access. Data was processed by me, with help from Dr L.K. Whalley. Air temperature and relative humity measurements on site were provided by J. Jeffery (STFC). I interpretted the results and wrote the manuscript, with subsequent contributions from my supervisors, Dr M.M. Twigg, Dr C.F. Braban and Professor M.R. Heal. Supplementary information for this chapter is presented in the Appendices.

4.1 Introduction

Photolysis is a driving force of tropospheric chemistry. Interactions of atmospheric species with light often release highly reactive radicals, reactions of which lead to production of secondary pollutants (Monks, 2005). Secondary pollutants (as well as primary) can be harmful to human health and the environment. They can also act as a reservoir species that can transport pollution long distances from its source. As such, improper quantification of the rate of photolysis reactions can have significant impacts on subsequent chemistry in mechanisms and models, which can lead to uncertainty in model estimates of both primary and secondary pollutant concentrations (Chen et al., 2021).

The rate of photodissociation is characterised by a photolysis rate constant (*j*-value), calculated using Eq. 4.1.

$$j = \int_{\lambda_1}^{\lambda_2} \sigma(\lambda, T, p)\ \phi(\lambda, T, p)\ F(\lambda)\ \mathrm{d}\lambda \tag{4.1}$$

Absorption cross-section (σ) and quantum yield (ϕ) are wavelength-dependent molecule-specific parameters that respectively quantify the ability of the molecule to absorb radiation and to dissociate into the specified products. For some species, σ and ϕ are more sensitive to changes in temperature and pressure than others (Heard, 2006), which can lead to differences in *j*-values compared to standard conditions. Actinic flux (F) represents the quantity of radiation available at the given wavelength. The *j*-values are most often measured by molecule-specific filter radiometers (Bohn et al., 2008; Gerasopoulos et al., 2012; Crowley et al., 2018), or calculated from spectroradiometer scans of actinic flux by wavelength (Edwards & Monks, 2003; Topaloglou et al., 2005; Sommariva et al., 2021).

Photolysis of NO_2 is the driver of tropospheric ozone (O_3) production (R4.1 and R4.2). As such, its photolysis rate constant is an important quantity that is consequently mea-

sured in some measurement campaigns (Brown et al., 2013; Bohnenstengel et al., 2015; Shi et al., 2019).

$$\mathrm{NO_2} + h\nu\,(\lambda \leq 420\,\mathrm{nm}) \longrightarrow \mathrm{NO} + \mathrm{O(^3P)} \tag{R4.1}$$

$$\mathrm{O(^3P)} + \mathrm{O_2} + \mathrm{M} \longrightarrow \mathrm{O_3} + \mathrm{M} \tag{R4.2}$$

In turn, photolysis of tropospheric ozone is an important source of the hydroxyl radical (OH, R4.3 and R4.4; Levy, 1972). OH is often referred to as the "detergent" of the atmosphere due to its reactivity, initiating many reactions in the troposphere.

$$\mathrm{O_3} + h\nu\,(\lambda \leq 330\,\mathrm{nm}) \longrightarrow \mathrm{O(^1D)} + \mathrm{O_2} \tag{R4.3}$$

$$\mathrm{O(^1D)} + \mathrm{H_2O} \longrightarrow 2\,\mathrm{OH} \tag{R4.4}$$

Approximately 10% of the excited oxygen atoms, $O(^1D)$, directly produced from O_3 photolysis react with H_2O (Finlayson-Pitts & Pitts Jr., 1999). The rest are quenched to ground state atoms, $O(^3P)$, via collisions with molecular nitrogen or oxygen. Recent field studies have also demonstrated that photolysis of nitrous acid (HONO) is an important source of primary OH radicals (R4.5) in the boundary layer (Young et al., 2012), contributing up to 30-60% in both urban and rural areas (Alicke et al., 2003; Kleffmann, 2005; Elshorbany et al., 2009).

$$\mathrm{HONO} + h\nu\,(\lambda \leq 405\,\mathrm{nm}) \longrightarrow \mathrm{OH} + \mathrm{NO} \tag{R4.5}$$

Oxidation reactions initiated with the OH radical can lead to a wide range of intermediate species, with a range of atmospheric lifetimes and impacts (Monks, 2005). This is important for local air quality, as these reactions with OH, for example for volatile organic compounds (VOCs), can lead to the formation of tropospheric ozone, photochemical smog (Lu et al., 2019), secondary organic aerosols (Claeys et al., 2004) and secondary hydroperoxy and peroxy radicals (HO_2 and RO_2, respectively). These are

closely coupled with OH (OH and HO_2 are collectively known as HO_x), and regenerate OH in the presence of nitric oxide (NO; R4.6), increasing the oxidising capacity of the troposphere.

$$HO_2 + NO \longrightarrow OH + NO_2 \tag{R4.6}$$

HO_2 is also produced through another important class of photolysis reactions, that of aldehydes (R4.7 to R4.10; Table 4.1).

$$HCHO + h\nu\,(\lambda \leq 335\,\mathrm{nm}) \longrightarrow H + HCO \tag{R4.7}$$

$$HCHO + h\nu\,(\lambda \leq 361\,\mathrm{nm}) \longrightarrow H_2 + CO \tag{R4.8}$$

$$H + O_2 + M \longrightarrow HO_2 + M \tag{R4.9}$$

$$HCO + O_2 \longrightarrow HO_2 + CO \tag{R4.10}$$

The aldehydes in the atmosphere are dominated by formaldehyde (HCHO; Dusanter et al., 2009; Elshorbany et al., 2009), but also include species such as acetaldehyde (CH_3CHO; R4.11) and methylglyoxal (CH_3COCHO; R4.12). Values of j(HCHO) can be difficult to quantify from spectroradiometer measurements, due to the narrow absorption bands of HCHO which require a high resolution wavelength measurement (Bohn et al., 2008).

$$CH_3CHO + h\nu\,(\lambda \leq 330\,\mathrm{nm}) \longrightarrow CH_3 + HCO \tag{R4.11}$$

$$CH_3COCHO + h\nu\,(\lambda \leq 475\,\mathrm{nm}) \longrightarrow CH_3CO + HCO \tag{R4.12}$$

Photolysis and oxidation of acetaldehyde and methyl glyoxal are two of the dominant sources of the peroxyacetyl (PA) radical, $CH_3C(O)O_2$ (LaFranchi et al., 2009; Fischer et al., 2014; Yuan et al., 2018). This radical reversibly combines with NO_2 to produce peroxyacetyl nitrate (PAN), which acts as a reservoir for long-distance transport of NO_x (= NO + NO_2).

Photolysis of hydrogen peroxide (H_2O_2; R4.13) is a minor source of OH (compared with O_3, HONO and HCHO), but acts as a temporary reservoir of HO_2, forming from the self-reaction of two HO_2 radicals (Dollard et al., 1991).

$$\mathrm{H_2O_2} + h\nu\,(\lambda \leq 400\,\mathrm{nm}) \longrightarrow 2\,\mathrm{OH} \tag{R4.13}$$

Nitryl chloride ($ClNO_2$) acts as a nocturnal reservoir of chlorine atom radicals (Cl), which are released in the early morning hours following its photodissociation (R4.14; Osthoff et al., 2008; Young et al., 2014). Cl atoms are extremely reactive with VOCs, and the resulting alkyl radicals contribute to the production of RO_2 (Riedel et al., 2014).

$$\mathrm{ClNO_2} + h\nu\,(\lambda \leq 475\,\mathrm{nm}) \longrightarrow \mathrm{Cl} + \mathrm{NO_2} \tag{R4.14}$$

Chlorine nitrate ($ClONO_2$) is more important in the stratosphere than the troposphere. Compared to $ClNO_2$, it is a very small source of Cl radicals in the boundary layer (Riedel et al., 2014). In the lower stratosphere, its photolysis leads to the production of both Cl atom and chlorine monoxide (ClO) radicals (R4.15 and R4.16, respectively), which when released can contribute to the destruction of stratospheric ozone (von Clarmann & Johansson, 2018). $ClONO_2$ also acts as a reservoir for these reactive chlorine species, contributing to the long-range transport of their effects.

$$\mathrm{ClONO_2} + h\nu\,(\lambda \leq 432\,\mathrm{nm}) \longrightarrow \mathrm{Cl} + \mathrm{NO_3} \tag{R4.15}$$

$$\longrightarrow \mathrm{ClO} + \mathrm{NO_2} \tag{R4.16}$$

Atmospheric chemistry mechanisms, that utilise the photolysis reactions above, among others, play an essential role in all forms of air quality models, from box models and dispersion models to chemical transport models (CTMs). The Master Chemical Mechanism (MCM) parameterises *j*-values of all species within the model as a function of solar zenith angle (SZA; Saunders et al., 2003; Sommariva et al., 2020). CTMs can

be coupled with radiative transfer models like the Tropospheric Ultraviolet and Visible radiation model (TUV; Madronich, 1987), or the Fast-J subroutine (Wild et al., 2000), which resolve the path of radiation from the top of the atmosphere, accounting for absorption and scattering of radiation by atmospheric components including clouds, aerosols and stratospheric ozone (Tie et al., 2003; Voulgarakis et al., 2009; Søvde et al., 2012). Different cloud conditions can both reduce (Hall et al., 2018) and enhance (Schade et al., 2007) the magnitude of shortwave radiation and hence the *j*-values at the surface. However, it is challenging to create model representations of these conditions with high accuracy without becoming computationally demanding, due to the inhomogeneity and variability in meteorological conditions with respect to location and time (e.g. Chapter 3; Mao et al., 2003).

For example, the EMEP CTM uses the two-stream PHODIS routine (Kylling et al., 1995) to calculate photolysis rate constants, which are then compiled into look-up tables (of 10° latitude and 1° SZA resolution at each model height; EMEP MSC-W, 2020) for 3 predefined separate conditions: clear sky, light cloud and dense cloud (differing by cloud depth, water content and mean droplet radius). All properties for each cloud condition are constant and evenly distributed throughout the cloud layer (Simpson et al., 2012). This set-up limits the computational cost required to determine the quantity of actinic flux at the output location by only propagating radiation along two discrete directions through the atmosphere. It is possible to incorporate Fast-J into global CTMs to determine hourly *j*-values, and account for the range of spatial and temporal variation in cloud and aerosol cover captured by the model. However this is still limited by model representation of conditions, and the uniformity throughout a given model grid.

Photolysis rate constants predicted by long-term or frequently-run models are often not verified beyond an initial intercomparison with measurements. Although these can perform well (Bais et al., 2003; Barnard et al., 2004), these validation steps should be repeated with further use of each model, particularly where such models are used to

support policy-makers in formulating mitigations.

Specific campaigns or short-term studies have constrained model j-values based on spectral radiometer measurements (Whalley et al., 2018), or adjusted for local conditions using some form of scaling factor. Kanaya et al. (2003) suggested that a single transmission factor, defined as the ratio of actinic flux in cloudy vs clear conditions at the same wavelength, could be used as a linear scaling factor to calculate any j-value under cloudy conditions at the same SZA, within 15%. Ratios of measured to modelled photolysis rate constants for reference species have been used more often in subsequent years. The usual reference rate constant is $j(NO_2)$ (Elshorbany et al., 2012; Bannan et al., 2017; Xue et al., 2020), due to the simplicity and long-term stability of its measurement with a filter radiometer (Bohn et al., 2008).

Measurements of $j(O^1D)$ (R4.3) have been used where this reaction pathway is studied specifically (Heard et al., 2004; Whalley et al., 2018). Measurement of $j(O^1D)$ can be made by spectral or filter radiometer, however the latter is more difficult since instrument outputs require corrections to account for SZA, total ozone column, and temperature (Bohn et al., 2004, 2016).

Studies such as Sörgel et al. (2011) and Lew et al. (2020) used ratios derived from $j(NO_2)$ measurements to scale modelled $j(O^1D)$, despite the lack of overlap in wavelengths of actinic flux contributing to photolysis. The use of a single reference species assumes that all wavelengths of actinic flux respond linearly to changes in meteorological conditions (e.g. clouds and aerosols; referred to as the "collinear assumption"), which has been demonstrated to be invalid for the photolysis of NO_2 and O_3 (Monks et al., 2004). Therefore how the j-value of a reference species changes with meteorological conditions and other factors may not represent how it changes for another species.

Individual species j-values have different dependencies on SZA and total ozone column,

driven by the different spectral distributions in cross-sections and actinic flux contributing to the photolysis. In clear-sky conditions Rayleigh scattering is dominant (which is proportional to λ^{-4}), resulting in more efficient scattering of shorter wavelengths and more diffuse solar radiation at the surface relative to direct radiation. Because of this, the quantity of diffuse light is greater at higher SZA, due to the longer radiation path length and greater columnar content (e.g. the number of scatterers in the path). As a result, in clear skies, shorter wavelengths of light are more likely to be scattered prior to reaching the surface. The presence of clouds and aerosols produce a comparatively lower dependence on wavelength (Webb et al., 2002a) and consequently affect $j(NO_2)$ at the surface to a greater extent than $j(O^1D)$ (McKenzie et al., 2002), since the difference with clear skies is greater.

Studies such as Dusanter et al. (2009) and Stone et al. (2010) have recognised this and used a mixture of $j(NO_2)$- and $j(O^1D)$-derived adjustment factors, where each photolysis rate constant is scaled based on the wavelengths relevant to the photolysis reaction under consideration. Photolysis rate constants for reactions which take place more in the UVB region (280–315 nm) use a $j(O^1D)$-derived adjustment factor, and vice versa. However the impact of this mixed approach for deriving adjustment factors for other species has not yet been explored.

This study investigates the use of reaction-specific measurement-driven adjustment factors (MDAFs) compared to that of reference species, and the implications of this choice on accurately modelling locally relevant j-values, and therefore on understanding local air quality. This is conducted through the systematic assessment of MDAFs derived for 12 major atmospheric photodissociation reactions, using spectral radiometer measurements at Chilbolton Observatory. Chilbolton is the UK's southern EMEP level II supersite and has intensive long-term air quality measurements. Hierarchical cluster analysis is used to cluster these photolysis reactions into groups, and investigate the applicability of $j(NO_2)$- and $j(O^1D)$-derived reference MDAF values on the j-values of

other species. The difference in these scaling factors is demonstrated through calculations of the production rate of OH radicals from the photolysis of O_3 ($p(\mathrm{OH})_{\mathrm{O_3}}$), and the implications for use of MDAF for understanding local air quality are discussed.

4.2 Method

4.2.1 Site description

Chilbolton Observatory is a rural background air quality monitoring station located in Hampshire, south England (lat: 51°09'N, lon: 1°26'W, altitude: 78 m; Figure 4.1), ∼10 km south of Andover and ∼100 km south-west of London. It is located in the grounds of Chilbolton Atmospheric Observatory (CAO), which operates long-term meteorological observations that provides national capability for the study of clouds, rainfall, boundary-layer processes and aerosols (CEDA, 2021). At the start of 2016, it replaced Harwell as the UK's southern EMEP level II supersite (Walker et al., 2019 and Chapter 2), operating instruments for a variety of different pollutant monitoring networks including the UK's Automatic Urban and Rural Monitoring Network (AURN; Defra, 2021c, 2021e).

The spectral radiometer was deployed at the site between 17 December 2020 and 19 March 2021. It was located on the north side of the site, mounted ∼6.5 m above ground level on black-painted railings of a cabin roof. The ground beneath the cabin is predominantly short grasses, surrounded by homogeneous arable farmland. The immediate area within the view of the 2-π sr optical inlet is clear, and the majority of the CAO site, including the 25 m radar antenna, is approximately 500 m south of the cabin.

Figure 4.1: **(a)** The locations of Chilbolton Observatory in the UK. **(b)** Satellite images of the area surrounding Chilbolton Observatory to approximately 1 km in all directions. Satellite imagery was obtained from Google Earth (Google Earth, 2021).

4.2.2 Instrumentation

Spectral actinic flux was measured between 280–750 nm ($\sim$1 nm resolution) using a spectrometer with a back-thinned CCD detector (Ocean Optics QE65000, USA) coupled with a fibre-optic cable to a 2-π quartz receiver optic (Meteorologie Consult GmbH, DE). Photolysis rate constants for the photodissociation of each molecule considered were derived using IUPAC-recommended literature values of wavelength-dependant absorption cross-sections and quantum yields (Table 4.1), interpolated to the wavelength resolution of measurements made. Time resolution of estimated photolysis rate constants was 1 min.

Raw signals measured by the spectrometer were corrected by subtracting both the dark signal, and the estimated contribution of stray light. The dark signal was acquired from spectra measured during the night, and stray light was determined by extrapolating a curve fit where no solar light is observed, to all measured wavelengths where solar and stray light both contribute. The instrument was calibrated between 280–750 nm against a 1000 W tungsten-halogen lamp of standard spectral irradiance (OL FEL-A;

Gooch & Housego, USA) prior to being deployed at Chilbolton. The solar zenith angle (SZA) was determined for each scan from latitude, longitude, date and time in UTC (Madronich, 1993), and measurements at SZA >86° were excluded from further analysis.

The clearest day in the dataset was identified to be 9 March 2021 from the smoothest curves of 1-minute measurements of each species (collectively covering the whole UVA and UVB wavelength ranges; see Figure S7). All spectra of photodissociation rate coefficients, and corresponding hierarchical clustering, utilise data collected at solar noon on this day.

4.2.3 Radiative transfer model

Photolysis frequencies for each molecule were determined for cloud-free conditions using the Tropospheric Ultraviolet and Visible radiative transfer model (TUV v5.3; Madronich, 1987; NCAR, 2019), and use the σ and ϕ values detailed in Table 4.1. The model domain was set to replicate the location and altitude of the optical inlet, and considered only downwelling radiation (direct and diffuse). The TUV default wavelength grid between 250 and 700 nm was used, and model outputs were calculated for SZAs in the range 40–90°, in intervals of 0.5°.

The O_3 column, air temperature and aerosol optical depth (AOD) measurements used as model input were daily averages, and linearly interpolated between existing measurements where data was missing. O_3 column measurements were obtained from the OMI instrument on NASA's Earth Observing System's (EOS) Aura satellite (NOAA ESRL, 2021). Air temperature and AOD were measured on-site at Chilbolton Observatory. The former was measured by a Vaisala HMP155A humidity and temperature probe, and the latter retrieved from a Cimel Sunphotometer, reported to the AERONET (AErosol RObotic NETwork) project (Ladd & Rumi, 2021). AOD at 550 nm was obtained from a linear interpolation of AOD at measured wavelengths (340, 380, 440,

Table 4.1: Photolysis reactions included in this study, their associated j-value and MDAF labels, and references for the associated absorption cross-section (σ) and quantum yield (ϕ) values used in calculations with the spectral radiometer measurement, and with the TUV model.
* Quantum yield used is unity at all wavelengths considered.
** Unpublished evaluation of these references by S. Madronich (1991).
*** $HNO_3 + h\nu \longrightarrow OH + NO_2$

j-value & MDAF name	Photolysis reaction		Molecular-specific parameter references	
			Spectral radiometer	TUV
$j(NO_2)$ NO_2-MDAF	R4.1	σ	Mérienne et al. (1995)	Vandaele et al. (1998)
		ϕ	Gardner et al. (1987)	Roehl et al. (1994), corrected by Troe (2000)
$j(O^1D)$ $O(^1D)$-MDAF	R4.3	σ	Molina & Molina (1986)	Molina & Molina (1981)
		ϕ	Matsumi et al. (2002)	Matsumi et al. (2002)
$j(H_2O_2)$ H_2O_2-MDAF	R4.13	σ	Burkholder et al. (2019)	DeMore et al. (1994, 1997)
		ϕ	Atkinson et al. (2004)*	Assumed to be 1*
j(HONO) HONO-MDAF	R4.5	σ	Bongartz et al. (1991, 1994)	Bongartz et al. (1991)
		ϕ	Burkholder et al. (2019)*	Sander et al. (2011)*
$j(HNO_3)$ HNO_3-MDAF	***	σ	Burkholder et al. (1993)	Molina & Molina (1981)
		ϕ	Atkinson et al. (2004)*	Assumed to be 1*
j(HCHO)-H HCHO-H-MDAF	R4.7	σ	Meller & Moortgat (2000)	Meller & Moortgat (2000)
		ϕ	Smith et al. (2002)	Horowitz & Calvert (1978); Moortgat et al. (1983)**
j(HCHO)-H_2 HCHO-H_2-MDAF	R4.8	σ	Meller & Moortgat (2000)	Meller & Moortgat (2000)
		ϕ	Moortgat et al. (1983)	Horowitz & Calvert (1978); Moortgat et al. (1983)**
$j(CH_3CHO)$ CH_3CHO-MDAF	R4.11	σ	Martinez et al. (1992)	Sander et al. (2011)
		ϕ	Meyrahn et al. (1982)	Horowitz & Calvert (1982)
j(MGLY) MGLY-MDAF	R4.12	σ	Meller et al. (1991); Staffelbach et al. (1995)	Sander et al. (2011)
		ϕ	Chen et al. (2000)	Chen et al. (2000)
$j(ClNO_2)$ $ClNO_2$-MDAF	R4.14	σ	Ghosh et al. (2012)	Illies & Takacs (1976); Furlan et al. (2000)
		ϕ	Assumed to be 1*	Assumed to be 1*
$j(ClONO_2)$-Cl $ClONO_2$-Cl-MDAF	R4.15	σ	Burkholder et al. (1994)	Burkholder et al. (1994)
		ϕ	Atkinson et al. (2007); Sander et al. (2011)	Atkinson et al. (2007); Sander et al. (2011)
$j(ClONO_2)$-ClO $ClONO_2$-ClO-MDAF	R4.16	σ	Burkholder et al. (1994)	Burkholder et al. (1994)
		ϕ	$\phi_{ClONO_2-ClO}(\lambda) = 1 - \phi_{ClONO_2-Cl}(\lambda)$	

500, 675, 870 and 1020 nm) on each day, and scaled in the model by altitude using the US Standard Atmosphere profile (Elterman, 1968). Single scattering albedo of aerosols was set as 0.99 (see Section 3.2.2).

4.2.4 Measurement-driven adjustment factor

The approach used to derive a measurement-driven adjustment factor (MDAF) was the same as that described for the photolysis of NO_2 in Chapter 3. Hourly averaged measured *j*-values for each molecule were used to determine the corresponding MDAF metric via the following generalised equation,

$$\mathrm{X} - MDAF = \frac{\text{measured } j(X)}{\text{modelled } j(X)} \tag{4.2}$$

where *j*(X) and X-MDAF represent the photolysis rate constant, and MDAF metric determined for molecule X, respectively. Where multiple photolysis channels are considered (e.g. for *j*(HCHO) and *j*($ClONO_2$)), the MDAF labels for each one calculated are presented in Table 4.1. The MDAF metric is only applicable where measurement site and model domain are co-located. MDAF values in this study were excluded if the solar zenith angle exceeded 86° as these values were not measured.

4.2.5 Hierarchical cluster analysis

Hierarchical cluster analysis (HCA) has been used in a variety of air quality studies (Govender & Sivakumar, 2020): for example for identifying the representativeness of sites in the context of a monitoring network (Malley et al., 2014), classifying site types (e.g. rural, urban) based on observed air pollutant concentrations (Flemming et al., 2005) and grouping back-trajectories of air masses arriving at a site to provide information about the source regions (Robinson et al., 2011).

In agglomerative algorithms of HCA, each observation initially comprises its own clus-

ter. The distances between clusters are then computed, and the two nearest (most similar) clusters are merged together. Distances are then recomputed to reflect this merging process. The algorithm is iterative, repeating until all clusters are merged into one containing all observations. The hierarchy of results are often visualised using a dendrogram, which provides information on how closely the observations relate to one another.

Here, HCA is used separately on two groups of data associated with each photolysis reaction included in this study: a) the molecular action spectra and b) the time series of MDAF values derived from the measurements. The action spectra selected for this analysis were those measured at solar noon on the clearest day (9 March 2021). This was identified from the smooth curve of raw measurements of both $j(NO_2)$ and $j(O^1D)$ ($\sim$1 min), to ensure conditions were clear in both the UVA ($315 < \lambda < 400$ nm and UVB ($280 < \lambda < 315$ nm) regions (diurnal cycles in Figure S7). The HCA was performed with R statistical software (R Core Team, 2020), and presented using the openair package (Carslaw & Ropkins, 2012).

4.3 Results and discussion

4.3.1 Overview of measured *j*-values, modelled *j*-values and derived MDAFs

Measured *j*-values

Figure 4.2 shows that the *j*-values determined from measured actinic flux follow broadly the same variation across all photolysis reactions over the full time series of measurements, driven by the prevailing meteorology. Mean measured and modelled *j*-values for this period are presented in Table 4.2. Overview statistics of observed daily mean and maximum *j*-values on the clearest day (9 March 2021; Figure S7) are presented in Table 4.3. Example diurnal cycles of *j*-values for each photolysis process in overcast

and intermittent cloud conditions are also presented in Figure S7.

The maximum measurement of $j(NO_2)$ on 9 March (6.4×10^{-3} s^{-1}) compares well to downwelling winter measurements made by a filter radiometer at Auchencorth Moss (5.6×10^{-3} s^{-1}; Chapter 3) and Mainz, Germany ($\sim 6 \times 10^{-3}$ s^{-1}; 50°N; Trebs et al., 2009), as well as a spectral radiometer at Manchester Air Quality Supersite (5.9×10^{-3} s^{-1}; Chapter 3). Gerasopoulos et al. (2012) present filter radiometer measurements of $j(NO_2)$ and $j(O^1D)$ on the island of Crete, Greece. During the same time of year as this study, the upper limits of both measurements were greater than those observed at Chilbolton Observatory (approx. 7.7×10^{-3} s^{-1} and 1.8×10^{-5} s^{-1} for $j(NO_2)$ and $j(O^1D)$, respectively in Crete). However the relative difference in $j(O^1D)$ measurements is more than twice as much (48% compared with 18%). Seasonal average diurnal cycles in winter show similar $j(O^1D)$ values at solar noon in Crete ($\sim 7.5 \times 10^{-6}$ s^{-1}), as are reported in central Tokyo, Japan (approx. 1×10^{-5} s^{-1}; Kanaya et al., 2007), compared to the same metric at Chilbolton ($\sim 2.2 \times 10^{-6}$ s^{-1}).

This large difference in observed $j(O^1D)$ is expected to be due to the variation in both the total O_3 column and the atmospheric path length of incident actinic flux to the site, which is proportional to 1/cos(SZA). Since Chilbolton Observatory is at a higher latitude than the locations of these other two studies (approx. 51°N compared to 35°N) there is both a greater average total O_3 column and greater minimum SZA (53° compared with 43°) at this site. This results in an increased slant O_3 column at Chilbolton compared with the other sites. Slant O_3 column is proportional to total O_3 column divided by cos(SZA) and is effectively the amount of O_3 along the atmospheric path length at each SZA. The slant O_3 column has a negligible impact on $j(NO_2)$ compared to $j(O^1D)$ because the latter involves absorption at shorter wavelengths at which both absorption by O_3 and Rayleigh scattering are more efficient (Figure 4.3). Summer measurements of $j(O^1D)$ reported during the ClearfLo campaign (London, UK; 51°N) using the same instrument as this study were larger (maximum approx. 1.6×10^{-5} s^{-1};

Whalley et al., 2018) than observed in winter at Chilbolton (1.1×10^{-5} s^{-1}). This is an expected seasonal difference driven by smaller observed SZA (minimum 31° compared with 53°), and a reduced atmospheric path length.

Figure 4.2: Time series of hourly averaged photodissociation rate constants at Chilbolton Observatory as **(left)** measured by spectral radiometer with 2-π optic head and **(right)** modelled by TUV v5.3 from 17 December 2020 to 19 March 2021.

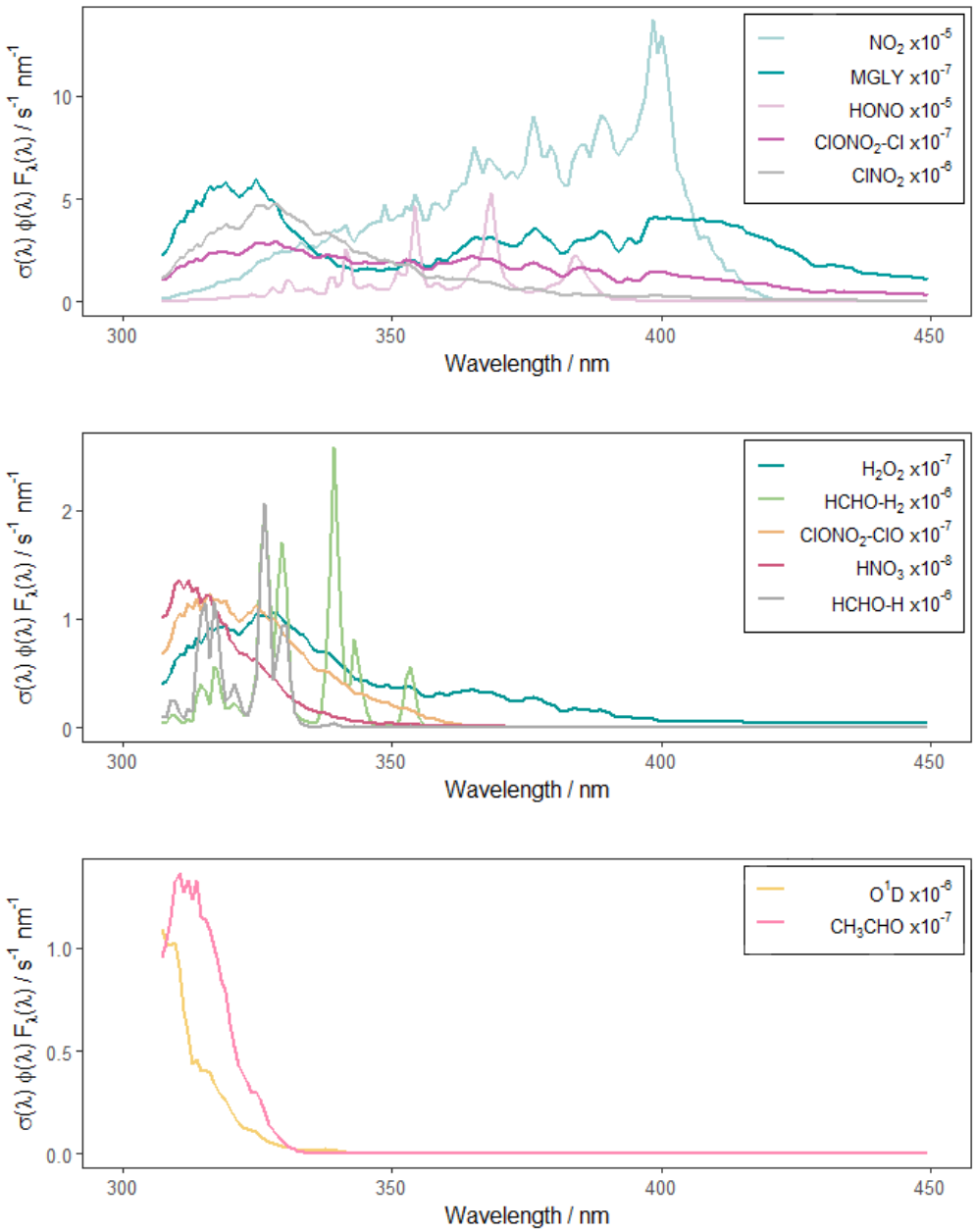

Figure 4.3: Photolysis action spectra (the product of absorption cross section, quantum yield and actinic flux at each wavelength) for each photolysis reaction. Spectra are calculated using actinic flux measured on the clearest day (9 March 2021) at ∼55° SZA, and are grouped according to the hierarchical clustering of the full MDAF time series for each photolysis reaction.

Table 4.2: Summary of hourly mean photolysis rate constants derived from measurements and predicted by the TUV model, during daylight hours (SZA $\leq$86°) for the full duration of the study (17 December 2020 and 19 March 2021), and the percentage difference between them, calculated against the measured value.

Photolysis rate constant	Mean / s^{-1}		Percentage difference / %
	Measured	Modelled	
$j(NO_2)$	1.7×10^{-3}	3.3×10^{-3}	94
$j(O^1D)$	1.8×10^{-6}	2.3×10^{-6}	28
$j(H_2O_2)$	1.5×10^{-6}	1.7×10^{-6}	13
j(HONO)	2.6×10^{-4}	5.1×10^{-4}	96
$j(HNO_3)$	6.2×10^{-8}	7.8×10^{-8}	26
j(HCHO)-H	4.3×10^{-6}	6.0×10^{-6}	33
j(HCHO)-H_2	7.2×10^{-6}	1.2×10^{-5}	66
$j(CH_3CHO)$	4.0×10^{-7}	5.5×10^{-7}	38
j(MGLY)	1.5×10^{-5}	3.9×10^{-5}	160
$j(ClNO_2)$	5.7×10^{-5}	1.3×10^{-4}	128
$j(ClONO_2)$-Cl	7.4×10^{-6}	1.3×10^{-5}	76
$j(ClONO_2)$-ClO	1.0×10^{-6}	1.4×10^{-6}	40

Table 4.3: Summary of 1-min photolysis rate constants derived from measurements collected by the spectral radiometer on the clearest day of the study at Chilbolton Observatory (9 March 2021). The arithmetic mean ($\overline{x}$) is the average of all j-values for SZA $\leq$86° on this day (measurements at greater SZAs are excluded from the data set; see Section 4.2.2), and the maximum is the largest j-value reached at solar noon on this day.

Photolysis rate constant	$\overline{x}$ / s^{-1}	Maximum / s^{-1}
$j(NO_2)$	1.8×10^{-3}	6.4×10^{-3}
$j(O^1D)$	2.2×10^{-6}	1.1×10^{-5}
$j(H_2O_2)$	1.6×10^{-6}	5.9×10^{-6}
j(HONO)	2.7×10^{-4}	9.7×10^{-4}
$j(HNO_3)$	7.0×10^{-8}	3.0×10^{-7}
j(HCHO)-H	4.7×10^{-6}	1.8×10^{-5}
j(HCHO)-H_2	7.4×10^{-6}	2.8×10^{-5}
$j(CH_3CHO)$	4.8×10^{-7}	2.1×10^{-6}
j(MGLY)	1.5×10^{-5}	5.3×10^{-5}
$j(ClNO_2)$	6.0×10^{-5}	2.3×10^{-4}
$j(ClONO_2)$-Cl	7.8×10^{-6}	2.8×10^{-5}
$j(ClONO_2)$-ClO	1.1×10^{-6}	4.3×10^{-6}

Photodissociation rate constants of other species (such as HCHO, HONO, H_2O_2 and CH_3CHO) were measured at two sites in Germany during summer. Bohn et al. (2008) present an intercomparison of a variety of spectroradiometers, and $j(NO_2)$ and $j(O^1D)$ filter radiometers in Julich (51°N), while Kraus & Hofzumahaus (1998) derived these j-values from actinic flux measurements made by a spectroradiometer in Pennewitt, NE Germany (53°N).

As would be expected, the maximum summertime measurements of the photolysis rate constants in these studies were greater than that at Chilbolton (Table 4.3). The measurements of j(HCHO)-H and j(HCHO)-H_2 by Bohn et al. (2008) were greatest (approx. 3.5×10^{-5} and 4.5×10^{-5} s^{-1}, respectively) as these occur at relatively short wavelengths (<361 nm; Figure 4.3), which are influenced more by the lower SZA (near 27° compared with 40° at Julich or 55° at Chilbolton). The relative difference between maximum $j(CH_3CHO)$ measured at Chilbolton and Pennewitt (approx. 32%) was greater than for $j(H_2O_2)$ (approx. 10%), as CH_3CHO photolyses at shorter wavelengths, and, like $j(O^1D)$, is more heavily influenced by atmospheric ozone at greater SZA. For j(HCHO)-H, the difference lies between these two (24%; 2.3×10^{-5} s^{-1}), contributed by the action spectra for HCHO photolysis occurring between that of CH_3CHO and H_2O_2 (Figure 4.3). There is also likely non-negligible influence from the use of different molecule-specific parameters by Kraus & Hofzumahaus (1998) compared to those in this study; for example 7–10% for σ(HCHO) and 6–8% for $\sigma(NO_2)$, as quantified by Burkholder et al., 2019.

Modelled *j*-values

Variations in the modelled cloud-free photolysis rate constants for a given species are driven by changes in aerosol optical depth (AOD; 550 nm) and the ozone column. During this study, daily mean AOD ranges from 0.035-0.43 (mean 0.082), while the total ozone column show a broadly increasing trend between December and March, with an absolute range of 258–424 DU (mean 318 DU; Figure S8). As discussed earlier,

the total ozone column has negligible impact on photodissociation processes at longer wavelengths (e.g. NO_2). The primary influences on these j-values in cloudless conditions are SZA and AOD. This is illustrated during the period of maximum AOD (>0.1; 1–3 March 2021) in the time series of modelled j-values (see Figure 4.2), where modelled j-values decrease from the otherwise upwards trend in time. There are no other factors causing significant variations in j-values for photodissociations that predominantly occur in the UVA region. However, photodissociations that occur further into the UVB region (i.e. at shorter wavelengths, such as the $O(^1D)$ channel of O_3) are affected by SZA, AOD and total ozone column, and therefore have more variation in predicted cloud-free j-values. Since the impact of total ozone column is intrinsically linked to SZA (via the slant ozone column), modelled diurnal variation for the UVB absorbing photolyses are influenced by the measured ozone column used in the input. Where the total ozone column is higher, predicted j-values are smaller, particularly at high SZA (such as sunrise or sunset), resulting in a narrower diurnal cycle than for the predominantly UVA-dependent photodissociations (e.g. see Figure S7).

Temperature can have a large impact on predicted photolysis rate constants, due to the temperature dependence of molecule-specific parameters of absorption cross-section (σ) and quantum yield (ϕ). For example, including this temperature dependence results in a 13% increase in $j(O^1D)$ and a 1% increase in $j(ClNO_2)$, between 273 and 298 K (Matsumi et al., 2002; Bohn et al., 2004, 2016; Ghosh et al., 2012). However in this study, the range of daily average temperatures used as model input is relatively small (14 K; 271-285 K), which led to a difference of approximately 7.5% for $j(O^1D)$, and a negligible effect on $j(ClNO_2)$. Temperature therefore has less impact on j-value estimates than either AOD or total ozone column in this study.

The uncertainty in the molecule-specific σ and ϕ parameters propagates through to the calculated j-values. An assessment was therefore made of the sources of the values of these parameters used in the TUV model and in the spectral actinic flux measurements

(the literature sources are listed in Table 4.1). The latter used the same σ and ϕ values that are contained in the Master Chemical Mechanism (MCM v3.3); except for $ClNO_2$ and $ClONO_2$ which are not included in the current version of the MCM. All values used in calculations from spectral radiometer measurements were those recommended by IUPAC, while those used in the TUV model are mostly from the JPL recommendations.

There is agreement in absolute values of the parameters used in the spectral radiometer and TUV calculations to $\leq$10%, with a few exceptions. The IUPAC recommended $\sigma(HNO_3)$ values used in the spectral radiometer calculations (Burkholder et al., 1993) agree with those used in the TUV model (Molina & Molina, 1981) by $\leq$15% for wavelengths <310 nm (Burkholder et al., 2019), increasing to around 50% at 330 nm. The $\sigma(ClNO_2)$ values used in both approaches demonstrate good agreement for $\lambda \leq 310$ nm, but deviations from the more recent IUPAC recommended values (Ghosh et al., 2012) occur for $\lambda > 320$ nm. Values used in the TUV model are an averaged combination of Illies & Takacs (1976) and Furlan et al. (2000), which reach a maximum difference of 45% and 70% smaller than those of Ghosh et al. (2012), respectively. These largest discrepancies occur at the smallest values of $\sigma(ClNO_2)$ (at 400 nm), and consequently are determined to have little impact on total calculated $j(ClNO_2)$. IUPAC and JPL recommended values are periodically evaluated to reflect more recent literature on gas-phase kinetic and photochemical data. Some values used here have been updated in more recent editions, e.g. values of σ(HCHO) from JPL in 2011 (Sander et al., 2011) have since been scaled up by 8% for JPL recommendations in 2019 (Burkholder et al., 2019). This study proceeded using the values used by TUV v5.3, and MCM v3.3 (as specified in Table 4.1).

MDAF values

Average diurnal cycles of MDAF values for each photolysis reaction are presented in Figure 4.4. The MDAF values for all photolysis reactions are in the range 0–2 across the full time series of measurements (the maximum hourly MDAF value determined was

2.0 for O(^{1}D)-MDAF). The magnitude of mean MDAF values ranges between 0.35 and 0.89 (Table 4.4; and discussed further in Section 4.3.2). Derived MDAF values in Chapter 3 exhibited little seasonal variation, a result of the good agreement in seasonality in $j(NO_2)$ values captured by both the measurements and the model. Based on this evidence it is anticipated that the magnitudes of the MDAF values derived here for a given photolysis reaction would be similar throughout the rest of the year.

For most photolyses, little diurnal variation in MDAF is observed, except for a slightly higher average value at 07:00-08:00, and a slightly lower average value at 16:00 (all UTC; Figure 4.4). Measured data at 07:00 is only present after sunrise from the last week of February; likewise, measurements at 17:00 are only present before sunset from early February. These deviations occur at the highest SZA during lowest light levels observed during the study. As a consequence, MDAF values are more sensitive to differences between measured and modelled j-values. It is of interest to note that there is a peak of varying magnitude at 15:00 for most MDAF derivations, particularly for species whose photolysis action spectra occur predominantly in the UVB region, such as O_3 (to O(^{1}D)). This is hypothesised to be caused by the narrower diurnal cycle of such photolysis rate constants, where the modelled j-values decrease rapidly at higher increasing SZA. Measured results drop more slowly, resulting in the peak close to sunset.

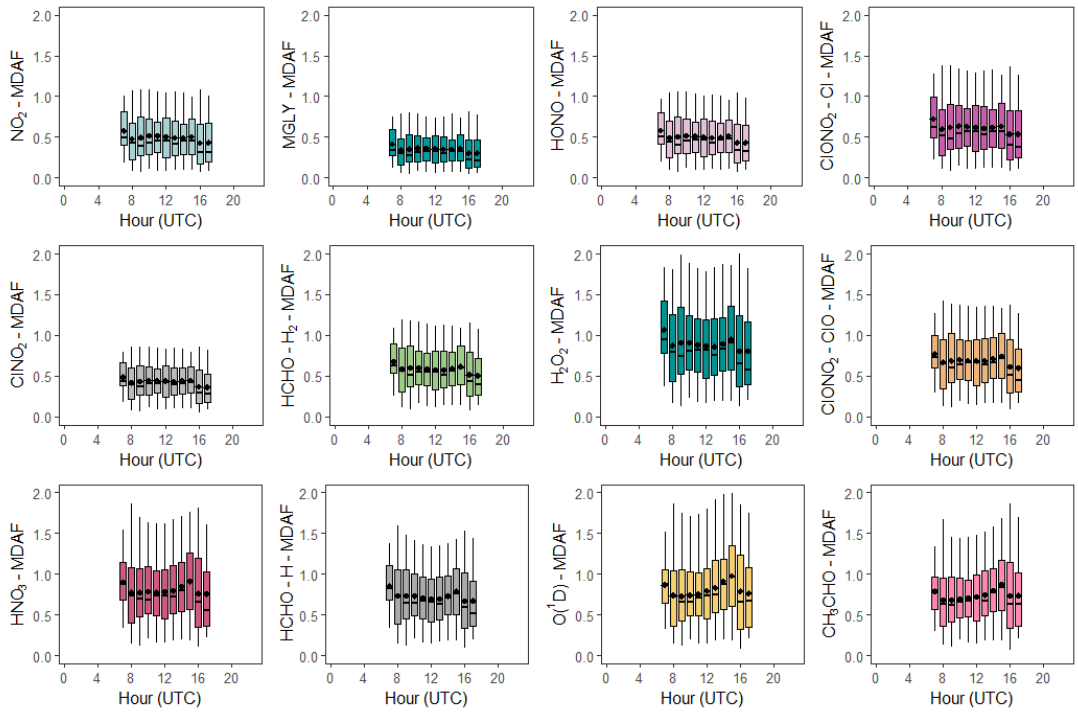

Figure 4.4: Box plots of the diurnal cycles of hourly MDAF values for each photolysis reaction for measurements made between 17 December 2020 and 19 March 2021. The horizontal line shows the median MDAF value each hour whilst the mean values are represented by diamond points. Boxes show the upper and lower quartiles, and the whiskers present the 5-95% range. Hours are expressed in UTC.

4.3.2 Groupings of MDAF derivations

Correlation matrices and the associated agglomerative heirarchical clustering of both the action spectra of each photolysis reaction, and the time series of their respective MDAF values, are presented in Figure 4.5. Correlation is strongest between the action spectra of $j(O^1D)$, $j(CH_3CHO)$, $j(HNO_3)$ and $j(ClONO_2)$–ClO (R^2 = 0.86–0.97) which all have a similar shape within this wavelength range, with a peak at $\lambda < 325$ nm and negligible photodissociation at $\lambda > 350$ nm (Figure 4.3). The larger "tails" in the action spectra of $j(HNO_3)$, and particularly of $j(ClONO_2)$–ClO, demonstrate that the clustering in this analysis is driven by photodissociation at longer wavelengths. Consequently, the action spectrum of $j(ClONO_2)$–ClO has good correlation with those with non-negligible photodissociation rate constants in the range 350–400 nm, such as $j(H_2O_2)$ and $j(ClNO_2)$ (R^2 of 0.93 and 0.88, respectively). These correlate well with $j(ClONO_2)$–Cl (R^2 of 0.87 and 0.85, respectively) for similar reasons.

For the following analysis, the photolysis reactions are divided into the following three groups based on the clustering of the full time series of the hourly MDAF values derived in this study (presented in the dendrogram in Figure 4.5).

- **Group 1**: Nitrogen dioxide (NO_2), methyl glyoxal (MGLY), nitrous acid (HONO), chlorine nitrate (Cl-route, $ClONO_2$-Cl) and nitryl chloride ($ClNO_2$).
- **Group 2**: Hydrogen peroxide (H_2O_2), formaldehyde (molecule route, HCHO-H_2), chlorine nitrate (ClO-route, $ClONO_2$-ClO), nitric acid (HNO_3) and formaldehyde (radical route, HCHO-H).
- **Group 3**: Ozone (O^1D) and acetaldehyde (CH_3CHO).

The hierarchical clustering between the two datasets analysed are broadly similar, with a few notable exceptions. In the action spectra dendrogram, $j(NO_2)$ and $j(HONO)$ are the most distant from all other species included, due to large magnitude peaks at longer

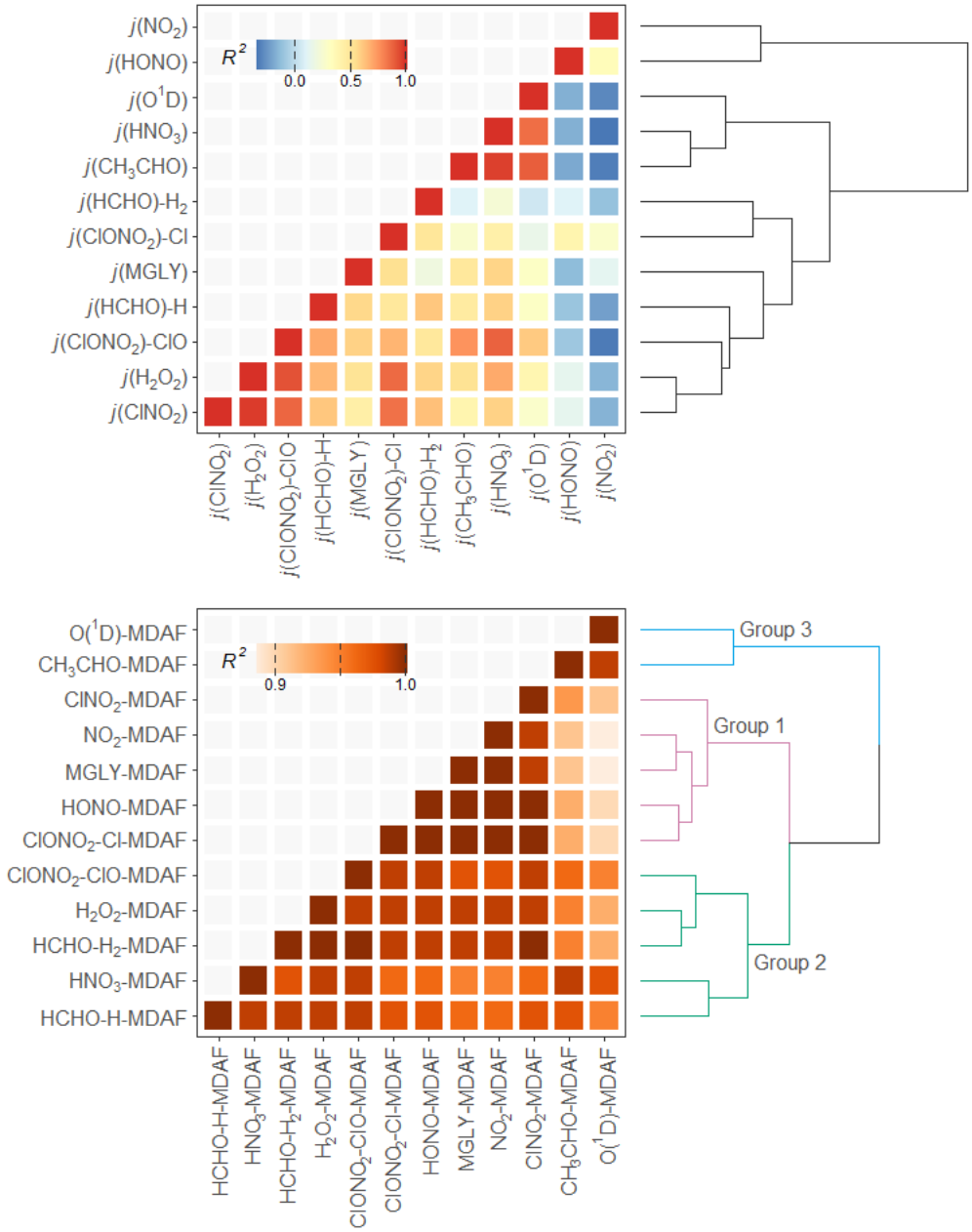

Figure 4.5: **(Top)** Correlation matrices between each of the photolysis action spectra (308 < λ < 450 nm), and the dendrogram visualising the agglomerative hierarchical clustering of variables within this correlation matrix. **(Bottom)** Presents the same for the MDAF time series derived for each photolysis rate constant. Colours on this dendrogram visualise the grouping of photolysis reactions in this study.

wavelengths that are not present in other spectra (see Figure 4.3). However, $j(O^1D)$ and $j(CH_3CHO)$ are clustered separately to the other species in the MDAF dendrogram, suggesting the lack of photodissociation at longer wavelengths is a more significant influence on MDAF than photodissociation at shorter wavelengths. Although the HCA process requires some choices on clustering algorithm to use, exploration of other HCA options (e.g. distance matrix), led to similar clustering driven by the action spectra "tail" at longer wavelengths. This is also demonstrated by the similarity of shape in the action spectra of $j(H_2O_2)$ and $j(ClNO_2)$. This similarity causes these j-values to be the first to cluster based on their action spectra ($R^2 = 0.98$), but they are separated into different groups based on the difference in magnitude of their MDAF values. Since the ϕ for both species is taken as unity, this difference is a result of the greater magnitude of $\sigma(ClNO_2)$ compared with $\sigma(H_2O_2)$ at longer wavelengths ($\lambda > 340$ nm; Molina & Molina, 1981; Ghosh et al., 2012).

MDAF groupings appear to correlate well with the broad features of the photolysis action spectra of the reaction routes included (Figure 4.3), primarily the regions of wavelengths which drive these photodissociation processes. This is expected, as fluctuations in actinic flux within the UVA region as a result of varying optical features (e.g. clouds and aerosols) are not expected to be the same at wavelengths in the UVB region (Monks et al., 2004).

Mean MDAF values for the full time series are presented in Table 4.4, alongside a comparison of each X-MDAF value against the more commonly used reference ratios of NO_2-MDAF and $O(^1D)$-MDAF (discussed in Section 4.3.3). Separated into groups, this demonstrates the relative magnitude of the influence which application of an MDAF metric has on modelled j-values based on the action spectra. These magnitudes agree well with the mean percentage difference between measured and modelled j-values (Table 4.2), as expected.

Molecules within Group 1 photodissociate at the longest wavelengths, predominantly

within the upper limit of the UVA region (>350 nm), with some also photodissociating at wavelengths >400 nm. As such, variation in the j-values for these species behave similarly to $j(NO_2)$, and are primarily affected by SZA and AOD. The MDAF values for these species exhibit a consistent range of values with SZA, with only a small difference for SZA greater or less than 70° (Figure 4.6). Similarly, a constant range of MDAF values are observed with slant ozone column (Figure S9). Absorption by the ozone column of wavelengths relevant to these action spectra is not very great. As a result, the quantity of actinic flux reaching the point of observation has a larger relative decrease when clouds are considered in the measurement (Figure S10). This increased variation between measurements including cloud cover and the cloud-free model estimate give the smallest average values of the MDAF metric (0.35–0.61; see Table 4.4).

By the same principle, average MDAF values are larger for photolysis reactions in Group 3 (mean $O(^1D)$-MDAF = 0.81 and mean CH_3CHO-MDAF = 0.74), which primarily photodissociate in the UVB region (λ < 330 nm). Stronger Rayleigh scattering and greater absorption by the ozone column at larger SZA and longer atmospheric path lengths result in less relative difference in actinic flux between cloudy and cloud-free conditions.

The MDAF values of photolysis reactions within Group 2 lie between these two extremes, since these reactions depend on absorption across both the UVA and UVB regions (mostly <350 nm). The MDAF values demonstrate some dependence on SZA, but show more within-group variation. H_2O_2-MDAF and HNO_3-MDAF have the greatest range of values with SZA, contributed by the considerable absorption at shorter wavelengths, demonstrated by the broad peaks in Figure 4.3.

Table 4.4: Arithmetic mean ($\overline{x}$) and standard deviation (σ) of hourly X-MDAF measurements over the full dataset. The same is presented for the ratio of X-MDAF to NO_2-MDAF and the ratio of X-MDAF to O(^{1}D)-MDAF. Also presented are the relative standard deviation (RSD, %) and the overall error (in %) in the ratios, the latter of which represents the sum in quadrature of the RSD and the absolute percentage difference between the mean X-MDAF/ NO_2-MDAF or X-MDAF/ O(^{1}D)-MDAF and unity.

HCA Group	Photolysis reaction (X)	X-MDAF		X-MDAF / NO_2-MDAF			X-MDAF / O(^{1}D)-MDAF		
		$\overline{x}$	σ	$\overline{x}$	σ (RSD /%)	Overall error (%)	$\overline{x}$	σ (RSD /%)	Overall error (%)
1	NO_2	0.49	0.3	—	—	—	0.60	0.1 (17%)	43
	MGLY	0.35	0.2	0.71	0.02 (3%)	29	0.43	0.09 (21%)	61
	HONO	0.50	0.3	1.0	0.04 (4%)	4	0.61	0.1 (16%)	42
	$ClONO_2$-Cl	0.61	0.3	1.3	0.03 (2%)	30	0.75	0.2 (26%)	36
	$ClNO_2$	0.43	0.2	0.91	0.08 (9%)	13	0.54	0.09 (17%)	49
2	H_2O_2	0.89	0.5	1.9	0.2 (11%)	91	1.1	0.2 (18%)	21
	HCHO-H_2	0.58	0.3	1.3	0.1 (8%)	31	0.74	0.1 (14%)	30
	$ClONO_2$-ClO	0.69	0.3	1.5	0.2 (13%)	52	0.86	0.1 (12%)	18
	HNO_3	0.80	0.4	1.7	0.3 (18%)	72	1.0	0.09 (9%)	9
	HCHO-H	0.72	0.3	1.6	0.2 (13%)	61	0.92	0.1 (11%)	14
3	O(^{1}D)	0.81	0.4	1.7	0.4 (24%)	74	—	—	—
	CH_3CHO	0.74	0.4	1.6	0.3 (19%)	63	0.93	0.07 (8%)	11

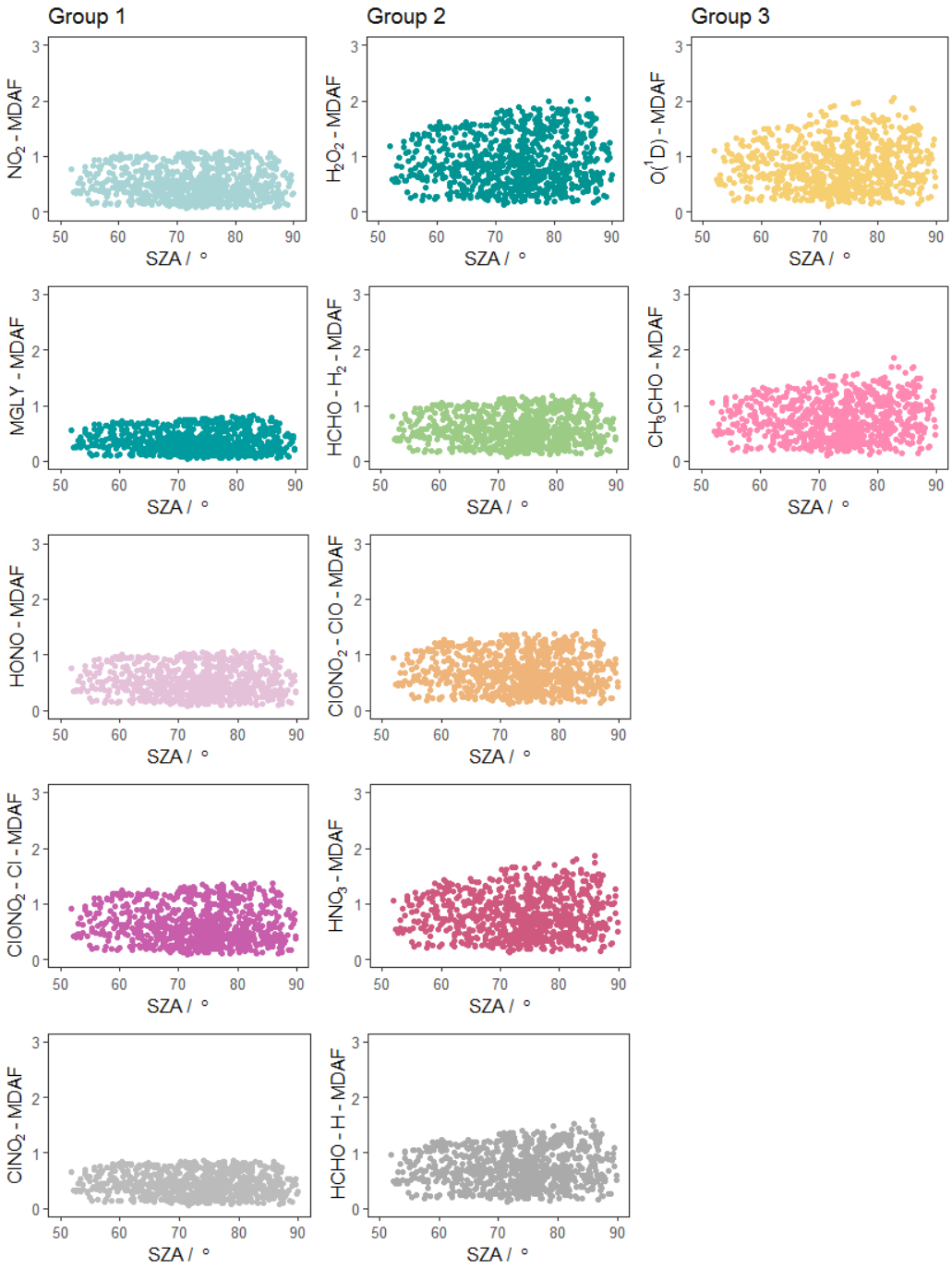

Figure 4.6: Plots of hourly MDAF values against SZA for each photolysis reaction. Plots are presented in columns corresponding to the three hierarchical clustering groups derived from the MDAF time series.

4.3.3 Impact of using a reference species to scale other photodissociation rate constants

NO_2-MDAF

NO_2-MDAF or similar metrics have been used to scale photolysis rate constants for other molecules in local atmospheric chemistry models or chemical mechanisms (Sörgel et al., 2011; Elshorbany et al., 2012; Xue et al., 2020; Lew et al., 2020). All other hourly X-MDAF values in this study were directly compared to NO_2-MDAF to estimate the potential uncertainty this could introduce into chemical schemes involving these photolysis reactions.

The photolysis of NO_2 appears in Group 1. Therefore, as expected, ratios of X-MDAF to NO_2-MDAF have best agreement for the rest of the photolysis reactions in Group 1, due to the significance of longer wavelengths of light in their photolysis reactions. HONO-MDAF has the best agreement with NO_2-MDAF with a mean ratio of 1.0 ± 0.04; (Table 4.4), and little dependence on SZA (Figure 4.7) and on slant ozone column (Figure 4.8). This is consistent with the high correlation observed between $j(NO_2)$ and j(HONO) observed by Kraus & Hofzumahaus (1998). At greater SZA there is more variation in the agreement, which is attributed to larger differences between measurements and model results in low light levels, compared to during the middle of the day. Values of $ClNO_2$-MDAF demonstrate good agreement with NO_2-MDAF, albeit with more uncertainty at all SZAs existing in this dataset (55-86°), leading to a ratio between the two of 0.91 ± 0.08. Therefore using NO_2-MDAF values to represent HONO-MDAF and $ClNO_2$-MDAF values would be a suitable approach to providing locally explicit j-values without significant additional errors. Relying solely on the TUV model predictions of these j-values results in an overestimate by approximately 94-128% (Table 4.2).

The MDAF values of the remainder of the photolysis reactions in Group 1 (MGLY

and $ClONO_2$–Cl) also have very good linearity with NO_2-MDAF for the full range of observed SZA and slant ozone column abundance. However the mean values of the ratios of MGLY-MDAF and $ClONO_2$-Cl-MDAF to NO_2-MDAF are approximately 30% above and below unity, respectively (Table 4.4 and Figure 4.7). Since the *j*-values are calculated with the same molecule-specific parameters for both the measured and modelled data, the difference in ratio to NO_2-MDAF is a consequence of j(MGLY) and $j(ClONO_2)$–Cl being approximately two orders of magnitude smaller than j(NO_2) (Figure 4.2). The absolute differences between the cloud-free modelled and cloud-inclusive measured interpretations of j(MGLY) are larger than $j(NO_2)$, while those of $j(ClONO_2)$-Cl are smaller. Ultimately, this raises the potential uncertainty of applying a NO_2-MDAF metric to these modelled *j*-values to around 30%, but this could be reduced to an uncertainty closer to the RSD estimates (4% and 2%, respectively) by using another adjustment factor to scale the NO_2-MDAF ratio for each photolysis reaction.

Photolysis reactions in Group 2 have more variation in the X-MDAF to NO_2-MDAF ratios (RSD $\geq$8%) than those in Group 1. The X-MDAF/NO_2-MDAF relationships are mostly constant at lower SZA ($\leq$60° and below; Figure 4.7) before increasing in both magnitude and scatter of data at SZA >60°. This observation is also apparent in Figure 4.8, where the ratio of X-MDAF to NO_2-MDAF increases rapidly at similar SZA, demonstrating the importance of the total ozone column abundance when considering species that photolyse at shorter wavelengths. HCHO-H_2-MDAF demonstrates the most similarities to NO_2-MDAF, near unity and constant at the smaller observed SZA (approx. <65°). This could be attributed to a larger peak in the action spectra of HCHO-H_2 at around 340 nm, compared to its smaller peaks in the UVB region (<315 nm), which could be driving the increased scatter at larger SZA. The relative standard deviation (8%) and overall error (31%) of using an NO_2-MDAF reference to adjust j(HCHO)-H_2 is similar to photolysis reactions in Group 1.

HNO_3-MDAF shows the weakest consistency with NO_2-MDAF (RSD = 18%) in Group

2, and is more similar in characteristics to those in Group 3. $O(^1D)$-MDAF and CH_3CHO-MDAF exhibit the most variation in their ratio to NO_2-MDAF across all SZA (Figure 4.7 and the full range of observed slant ozone columns, Figure 4.8). This large deviation from NO_2-MDAF is expected, due to the photolysis reactions of these species occurring at shorter wavelengths.

Of all of the photolysis reactions investigated, the largest overall error (91%; H_2O_2-MDAF) is within a factor of 2 when compared to NO_2-MDAF. The main constituent of this error is the difference in MDAF magnitudes, rather than in the spread (or imprecision) of the values (RSD = 11%). Since the TUV predicts similar values of $j(H_2O_2)$ as those measured, it provides the largest mean MDAF value (0.89). This is likely contributed in part by the temperature dependence of $\sigma(H_2O_2)$ used by the TUV (but not the spectral radiometer) which decreases modelled $j(H_2O_2)$ by around 8% at the ambient temperatures measured during the study.

$O(^1D)$-MDAF

In general, the relationships of X-MDAF values to $O(^1D)$-MDAF values are more constant across all SZA, than they are with NO_2-MDAF values (Figure 4.7). $O(^1D)$-MDAF shows good agreement with CH_3CHO-MDAF (overall error = 11%) across all SZA (RSD = 8%, Figure 4.7). This is consistent with the work of Kraus & Hofzumahaus (1998) who demonstrate high correlation between $j(O^1D)$ and $j(CH_3CHO)$, attributed to the similar wavelength region of the photodissociations. For the same reason, HNO_3-MDAF and HCHO-H-MDAF agree well with $O(^1D)$-MDAF (overall errors of 9 and 14%, respectively), while species with incompatible absorption regions in Group 1 (e.g. NO_2, $ClNO_2$ and MGLY) show the greatest deviations from the 1:1 relationship (overall errors of 43, 49 and 61%, respectively). As such, the HCA groups identified remain mostly applicable here too.

The mean $O(^1D)$-MDAF is larger than that of NO_2-MDAF, in part because measured

changes in ozone column abundance are considered in the model input, and because absorption of short wavelengths (UVB) by the ozone column accounts for a large reduction in actinic flux. Therefore the difference between cloud-free and cloudy conditions (as examined in this study) is not as great as observed for $j(NO_2)$, which photodissociates at longer wavelengths than this region (mostly UVA; see Figure S10). This is also observed in Figure 4.8 where the magnitude of the ratio of X-MDAF to $O(^1D)$-MDAF (where X = Group 1 species) increases at slightly shorter slant ozone columns. This is affected by the variation in measured ozone column abundance at similar SZA driving the variation in modelled $j(O^1D)$ compared to the photolysis rate constants for reactions in Group 1.

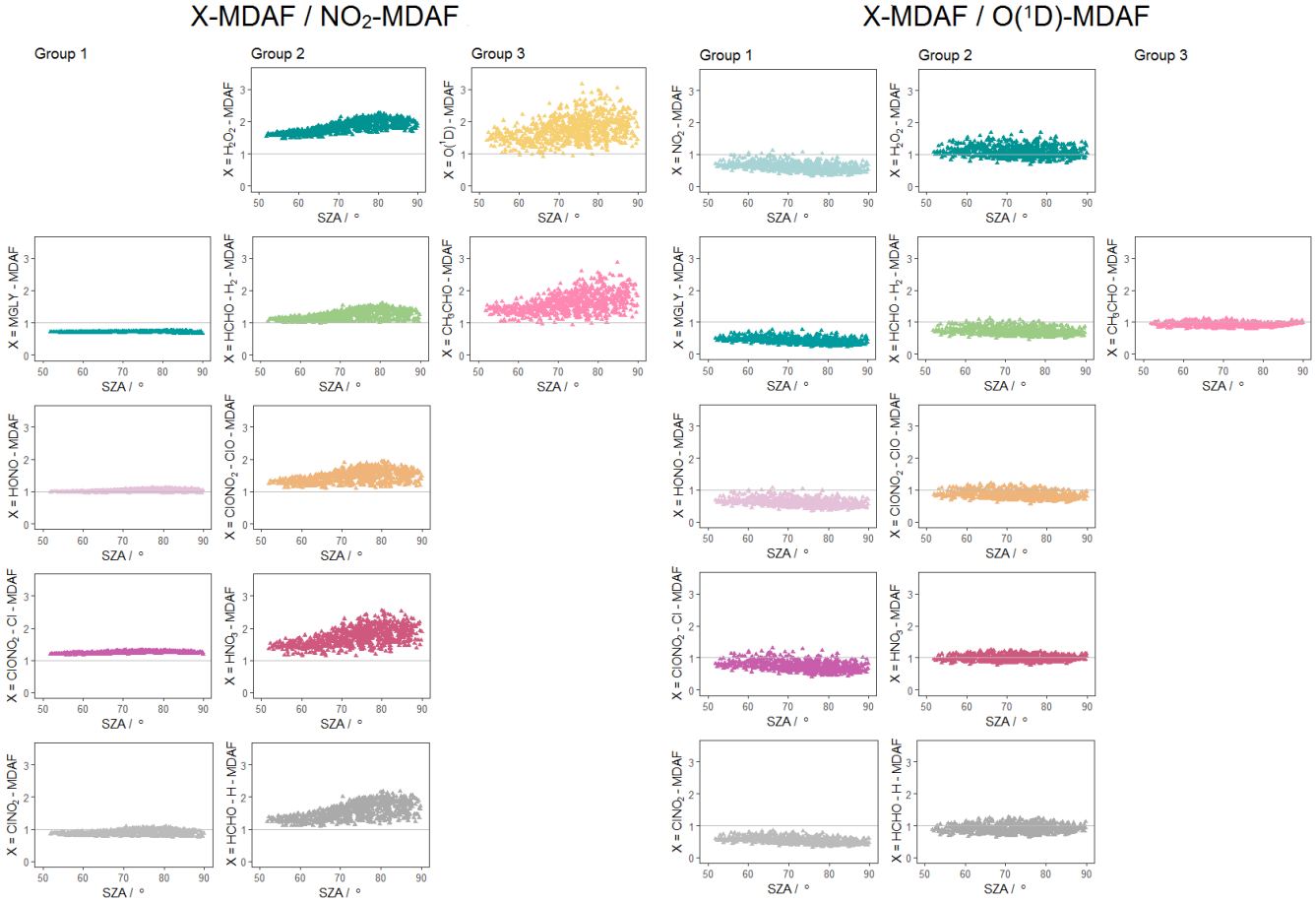

Figure 4.7: Ratios of derived MDAF values for each photolysis reaction relative to an NO_2-MDAF reference **(left)** and an $O(^1D)$-MDAF reference **(right)**, as a function of SZA. Plots are presented in columns corresponding to the three hierarchical clustering groups derived from the MDAF time series, and the same positions as Figure 4.6.

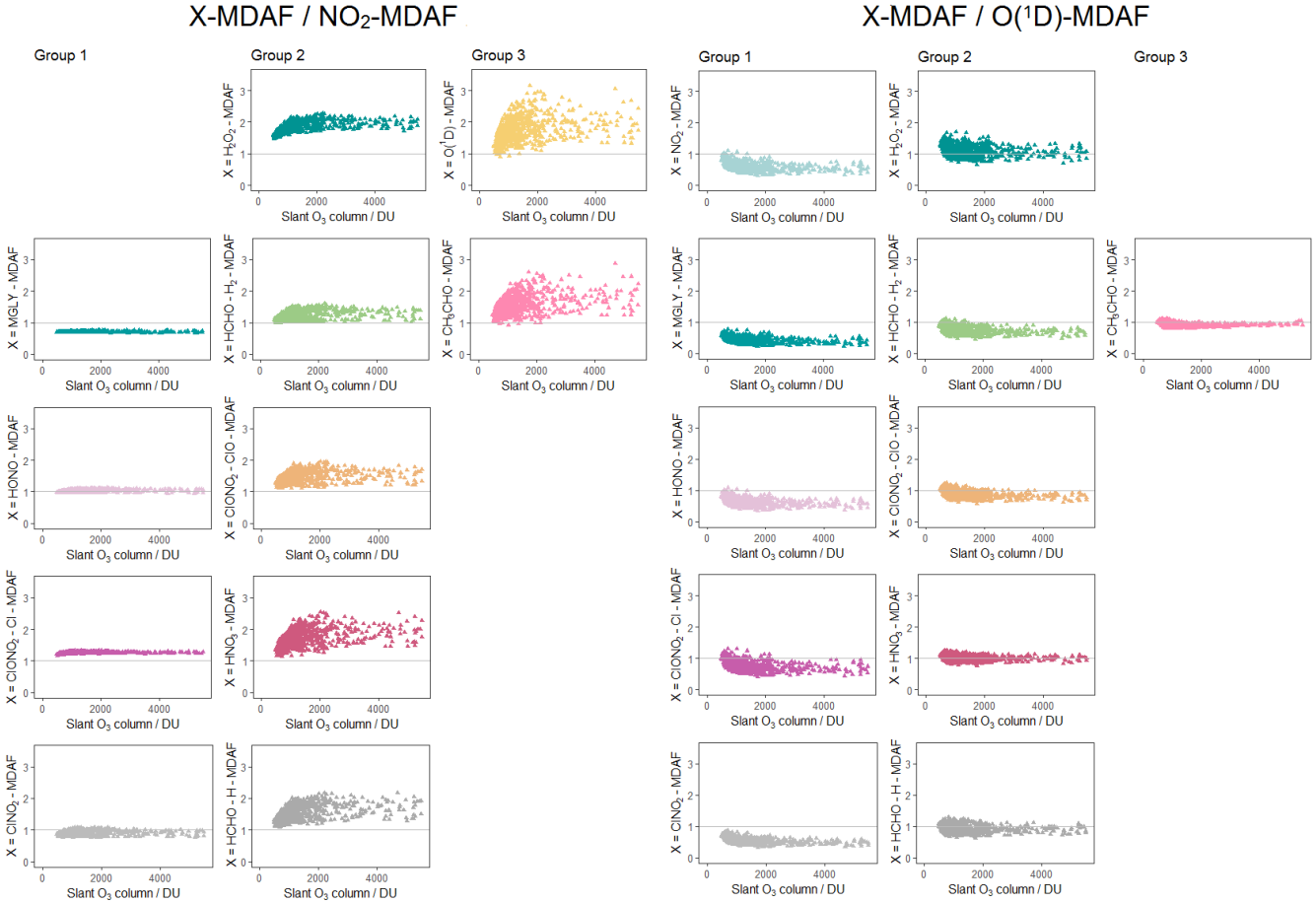

Figure 4.8: Ratios of derived MDAF values for each photolysis reaction to an NO_2-MDAF reference **(left)** and an (O^1D)-MDAF reference **(right)**, as a function of the slant ozone column. Plots are presented in columns corresponding to the three hierarchical clustering groups derived from the MDAF time series, and the same positions as Figure 4.6.

Recommendations for reference species

As well as parameterisations to determine j(HONO) from $j(NO_2)$ and $j(CH_3CHO)$ from $j(O^1D)$, as discussed earlier, Kraus & Hofzumahaus (1998) propose a parameterisation for another photolysis reaction that was grouped in Group 2 in this study: estimating j(HCHO)–H from $j(H_2O_2)$. Similarly to the other two combinations, the ratio in MDAF values between these two species in Group 2 exhibit a constant value with both slant ozone column and SZA (RSD = 7%; Figure 4.9). However, this HCHO-H-MDAF to H_2O_2-MDAF ratio lies below unity due to the larger magnitude of H_2O_2-MDAF.

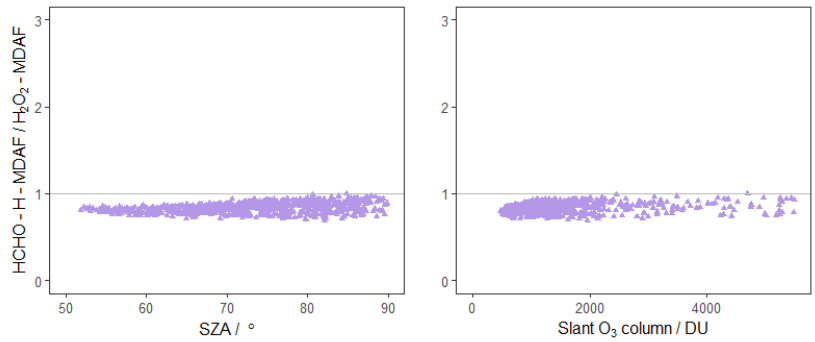

Figure 4.9: Ratio of HCHO-H-MDAF to H_2O_2-MDAF as a function of SZA **(left)** and slant ozone column **(right)**. The combination of j(HCHO)-H and $j(H_2O_2)$ was suggested by Kraus & Hofzumahaus (1998) based on the high correlation of their spectroradiometer measurements. Other pairs of j-values also suggested by these authors were j(HONO) and $j(NO_2)$ as well as $j(CH_3CHO)$ and $j(O^1D)$, which are presented in both Figures 4.7 and 4.8.

The magnitude of MDAF values are consistent within the groups derived from the hierarchical cluster analysis, due to the wavelength regions that are relevant for each photodissociation. MDAF values in Group 1 are smallest (0.35–0.61) because the photolysis reactions in this group are dependent on absorption at longer wavelengths which are most influenced by the presence of local clouds, as discussed earlier. It is concluded that NO_2-MDAF values are sufficient to be used to adjust any of this group's members, or another photolysis reaction that is significantly dependent on wavelengths >350 nm.

The magnitude of the $O(^1D)$-MDAF is consistently one of the largest of the MDAFs (Table 4.4 and Figure 4.6), signifying that cloud-free model estimates require little ad-

justment for local conditions. Application of an NO_2-MDAF to the $O(^1D)$ photolysis channel of O_3 (e.g. Sörgel et al., 2011) results in a bias of approximately 55%. This can propagate through model calculations, as illustrated via the calculation using Eq. 4.3, of the rate of production of OH from the photolysis of O_3 (Figure 4.10; R4.3 and R4.4).

$$p(\mathrm{OH})_{\mathrm{O_3}} = 2 \times f \times j(\mathrm{O^1D}) \times [\mathrm{O_3}] \tag{4.3}$$

In this equation, f is the fraction of $O(^1D)$ atoms which react with water vapour to form OH, as opposed to their quenched removal by N_2 or O_2 molecules, which for this period was 4.7±1% (based on hourly values). More detail for this calculation is given in the Supplementary Information (Section S4). By adjusting cloud-free model estimations of $j(O^1D)$ to account for local changes in meteorology using NO_2-MDAF, the mean $p(\mathrm{OH})_{\mathrm{O_3}}$ production rate at solar noon for the full time series is approximately 7×10^4 radicals cm^{-3} s^{-1} less (32%) than if using $O(^1D)$-MDAF. Using only the cloud-free TUV model output results in $p(\mathrm{OH})_{\mathrm{O_3}}$ estimations approx. 1.3×10^5 radicals cm^{-3} s^{-1} (86%) and approx. 6×10^4 radicals cm^{-3} s^{-1} (26%) larger than using NO_2-MDAF or $O(^1D)$-MDAF, respectively.

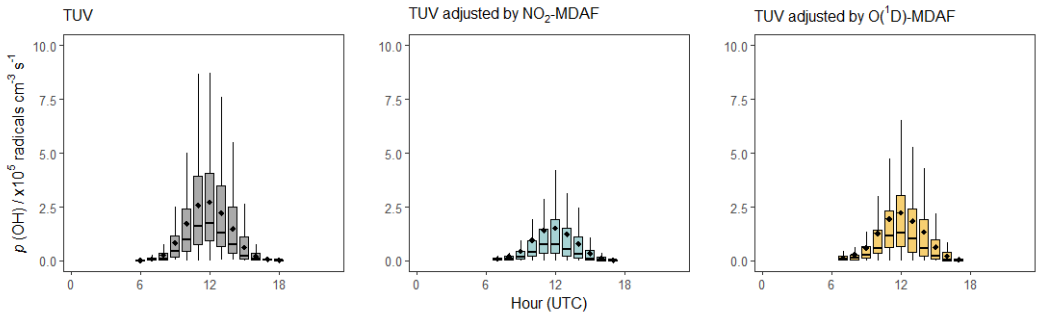

Figure 4.10: Box plot of diel cycles for the production rate of OH from the photolysis of O_3 at Chilbolton Observatory between 17 December 2020 and 19 March 2021, calculated using Eq. 4.3. Plots show data calculated using cloud-free TUV-modelled $j(O^1D)$ values **(left, grey)**, using TUV-modelled $j(O^1D)$ values adjusted using NO_2-MDAF **(middle, blue)** and using TUV-modelled $j(O^1D)$ values adjusted using $O(^1D)$-MDAF **(right, yellow)**. The horizontal line shows the median radical production rates each hour whilst mean values are represented by diamond points. Boxes show the upper and lower quartiles, and the whiskers indicate the 5-95% range.

This uncertainty in the production rate of OH radicals from the photolysis of O_3 due to the choice of photolysis rate demonstrates how this can propagate through chemical mechanisms in atmospheric chemistry and chemical transport models. Ultimately this can lead to uncertainty in estimated pollutant concentrations predicted by the model, as demonstrated by Chen et al. (2021). Chen et al. show that after updating j-values (via σ and ϕ) in RADM2 and RACM, daily maximum O_3 concentrations increased by up to 25% in East Asia. This demonstrates the importance of accurate j-values, and the potential impact that accounting for local meteorology can have on modelled pollutant concentrations.

Groups 2 and 3 both include photodissociation regions at shorter wavelengths ($\leq$325 nm), and are more closely related to each other than to Group 1. As demonstrated in Section 4.3.3, MDAF values derived from $j(O^1D)$ can be applied with relatively little error (less than 15%) to the photolysis of CH_3CHO (in Group 3), as well as to the photolysis of HNO_3 and to the radical-producing photolysis of HCHO (HCHO-H). For photolysis reactions whose action spectra align with those in Group 2 (photolysing at $\lambda < 350$ nm), this study demonstrates that a lower propagated error for local j(X) will be achieved when using an O(^{1}D)-MDAF rather than an NO_2-MDAF to correct the cloud-free j(X) value for local meteorological conditions.

Whilst the most accurate estimates for photolysis rate constants will be achieved by constraining them to calibrated measurements at the local site, this is not practical for the suite of atmospherically-relevant photolysis reactions. This work has shown that in the absence of local calibration then deployment of locally measured of $j(O^1D)$ and application of O(^{1}D)-MDAF to modelled j-values results in less overall error than application of NO_2-MDAF, as earlier studies have used (Sörgel et al., 2011; Elshorbany et al., 2012; Lew et al., 2020; Xue et al., 2020). A full intercomparison of all MDAF derivations is presented in Figure S11, which supports the HCA groupings and the discussed suitability (or lack) of reference MDAF values to correct the cloud-free j(X) of

other photolysis reactions.

4.4 Conclusions

Using data from Chilbolton Observatory, southern England, measurement-driven adjustment factors (MDAF) that adjust model-derived clear-sky j-values according to local meteorology are investigated for a suite of 12 photodissociation reactions important in air quality and chemical transport models. The local j-values were measured by a spectral radiometer for the period 17 December 2020 – 19 March 2021 and clear-sky values calculated with the TUV model. Good correlations in hourly MDAF values are observed across all photolysis reactions ($R^2 > 0.90$). This is because the broad patterns of variation in observed j-values are based on changes in local meteorology and therefore similar. However evidence presented demonstrates that despite the temporal correlations in MDAF values across the photolysis reactions the absolute MDAF values span a wide range (mean MDAF values for the whole time series span 0.35–0.89), which indicates varying influences of different aspects of local meteorological conditions on the j-values of different photolysis reactions.

On the basis of the time series of hourly MDAF values derived in this study, the 12 photolysis reactions were allocated into the following 3 groups by agglomerative hierarchical clustering analysis (HCA).

- **Group 1**: NO_2, MGLY, HONO, $ClONO_2$-Cl and $ClNO_2$.
- **Group 2**: H_2O_2, HCHO-H_2, HCHO-H, $ClONO_2$-ClO and HNO_3.
- **Group 3**: O^1D (O_3 photolysis) and CH_3CHO.

The groupings strongly reflect similar characteristics in the photodissociation action spectra of the photolysis reactions, as well as similar responses to relevant parameters such as solar zenith angle (SZA) and slant ozone column.

Group 1 includes NO_2, whose photolysis rate constant is often used as a reference where scaling factors to account for local variations in actinic flux are applied. The other photolysis reactions that cluster in this group also photolyse mostly in the UVA region, at the longest wavelengths examined in this study (>350 nm). The ratios of the MDAF for each of the other photolysis reactions in this group to NO_2-MDAF are near independent of both SZA and slant ozone column. Consequently NO_2-MDAF estimates can be applied to cloud-free modelled j-values for these species with the least overall error (4–30%). There is potential to reduce biases for the photolysis reactions at the higher end of this uncertainty range (MGLY and $ClONO_2$–Cl) by scaling the site's derived NO_2-MDAF to that derived for these species.

Species that predominantly photodissociate in the UVB region (Group 3; <325 nm), as well as those at photodissociate at slightly longer wavelengths (Group 2; mostly <350 nm), are subject to more variation in derived MDAF values due to stronger scattering and absorption of radiation prior to reaching ground level, in all local meteorological conditions. For this reason, the most scatter is observed at both higher SZA and greater ozone column abundances, due to the increased atmospheric slant path length.

The more efficient scattering and absorption of UVB radiation demonstrates that between the measurements at Chilbolton Observatory and the cloud-free model approach, there is a larger change in available actinic flux at longer wavelengths as a result of the variation in local conditions. Consequently, MDAF values derived for photolysis reactions in Groups 2 and 3 are of larger magnitude (i.e. closer to unity) than for Group 1, as these are less heavily dependent on unaccounted for changes in local meteorology (e.g. cloud cover). Overall, whether a photolysis reaction includes absorptions at longer wavelengths has more of an influence on the magnitude of MDAF and the HCA clustering, than any absorptions in the UVB region.

For these reasons, use of an NO_2-MDAF value for the j-values of reactions in Groups 2 and 3 result in much larger magnitudes of error (31–91%) due to a) the difference

in magnitude of MDAF values, and b) the spread of results, particularly at high SZA. Conversely, use of an O(^{1}D)-MDAF for Groups 2 and 3 result in considerably less error (9–30%). Therefore, for photolysis reactions occurring predominantly at wavelengths <350 nm, adjustment for local conditions using an O(^{1}D)-MDAF is preferred.

The most accurate approach would be to adjust all modelled *j*-values with a species-specific MDAF derivation, or constrain all *j*-values in the model domain to measured values. However this is usually not possible, and use of bandpass filter radiometer measurements are a more accessible method of achieving an adjustment factor to account for local conditions. Measurements of $j(NO_2)$ are simplest, but for some photolysis reactions use of an NO_2-MDAF leads to more error in their adjusted *j*-value than use of an O(^{1}D)-MDAF. However, $j(O^1D)$ filter radiometers require more data processing to account for SZA and ozone column depth. NO_2-MDAF was a very good reference species for HONO and $ClNO_2$ (4 and 13% overall error, respectively), and resulted in overall errors of <31% for the rest of Group 1 and for HCHO-H_2. The maximum error determined from the application of NO_2-MDAF was 91%, within a factor of 2, which may still be acceptable to larger scale models.

Photolysis rate constants are fundamental to atmospheric chemistry mechanisms and chemical transport models. Errors in these values will propagate through mechanism calculations, and can lead to uncertainty in estimated pollutant concentrations. Further work is required to quantify the impact of utilising MDAF values account for local meteorology in models. However, this study has highlighted the importance for *j*-values to be modelled accurately and verified against local measurements more frequently to ensure confidence in the modelled output. This is particularly critical where these are used to assess public health, and support policy makers in developing mitigation strategies. Utilising MDAF parameterisations will ensure that variation in local conditions are accounted for in model domains, without requiring computationally intensive model approaches to predict them.

Chapter 5

Application of an iodide chemical ionisation mass spectrometer for the simultaneous measurement of multiple NO_y species

NOTE: *The work in this study was limited due to the Covid-19 pandemic and associated restrictions, so should be understood as a partially complete study. Limitations and further work for this study are discussed.*

I ran the CIMS at Auchencorth Moss, processed and examined the data with help from my supervisors, Dr M.M. Twigg, Dr C.F. Braban and Professor M.R. Heal. I was assisted for the transport and deployment of the CIMS at Auchencorth Moss by Dr C.F. Braban, N. Mullinger, Dr M.M. Twigg, Dr M.R. Jones, I. Simmons, D. Harvey and S.R. Leeson (UK Centre for Ecology & Hydrology). The contents of this chapter was written by me with subsequent input from my supervisors.

5.1 Introduction

Oxidised reactive nitrogen (NO_y) species are important for understanding atmospheric chemistry and assessing local air quality. NO_y species can contribute to the long-range transport of pollution, act as chemical reservoirs of pollutants, influence formation of secondary pollutants, and provide sinks of atmospheric nitrogen. Ultimately this can have significant effects on both human and environmental health (e.g. respiratory and cardiovascular problems; eutrophication and nitrification).

Chemical ionisation mass spectrometry (CIMS) has been widely used to measure NO_y species in both ground-level (Osthoff et al., 2008; Thornton et al., 2010; Furgeson et al., 2011; Veres et al., 2015; Sommariva et al., 2018; McNamara et al., 2020) and airborne (Le Breton et al., 2014a; Lee et al., 2018) studies, or in both locations simultaneously (Bannan et al., 2017; Jeong et al., 2019). Chemical ionisation is favoured as it is a "soft" ionisation technique in which there is minimal fragmentation of each parent ion generated. Target molecules from each analyte are therefore measured at fewer mass-to-charge ratios (m/z) and the choice of reagent ion gives selectivity to the target molecules measured (see Table 1 of Huey, 2007). Iodide is unreactive with many atmospheric species (Huey et al., 1995), thus providing the desired selectivity to the targeted NO_y species.

Peroxyacetyl nitrate (PAN; $CH_3C(O)O_2NO_2$) is a secondary pollutant, formed through the thermal equilibrium (R5.1) between the peroxyacetyl radical (PA; $CH_3C(O)O_2$) and nitrogen dioxide (NO_2),

$$\mathrm{CH_3C(O)O_2 + NO_2 + M \rightleftharpoons CH_3C(O)O_2NO_2 + M} \qquad \text{(R5.1)}$$

where the PA radical is generated through the oxidation of volatile organic compounds (VOCs) such as isoprene, methyl glyoxal and acetaldehyde (Sillman, 2002; Fischer et al., 2014; Yuan et al., 2018). The stability of PAN at low temperatures (up to 6

months atmospheric lifetime in the lower stratosphere; Khan et al., 2017) means it acts as an NO_2 reservoir, and determines the spatial extent of NO_x pollution by contributing to its long-range transport (Singh & Hanst, 1981).

PAN is measured with I^- CIMS by thermal dissociation (heated inlet, 160–180 °C; Slusher et al., 2004) and reaction with I^- to form an acetate ion ($CH_3C(O)O^-$) in R5.2 and R5.3.

$$CH_3C(O)O_2NO_2 + \textit{heat} \longrightarrow CH_3C(O)O_2 + NO_2 \tag{R5.2}$$

$$CH_3C(O)O_2 + I^- \cdot (H_2O)_n \rightleftharpoons CH_3C(O)O^- \cdot (H_2O)_n + IO \tag{R5.3}$$

Measurement of PAN by CIMS demonstrates good agreement with the widely-used benchmark technique of gas chromatography with electron capture detection (GC-ECD; Slusher et al., 2004), but has a faster time resolution.

Nitric acid (HNO_3) is considered an end-point atmospheric NO_y species due to its "sticky" nature giving rise to a relatively high deposition velocity (Jacob, 2000; Hanke et al., 2003; Phillips et al., 2013a). It is mostly formed during the day by the reaction (R5.4) between NO_2 and the hydroxyl radical (OH).

$$NO_2 + OH + M \longrightarrow HNO_3 + M \tag{R5.4}$$

Measurement of HNO_3 with I^- CIMS (R5.5) has been infrequent ($SF_5{}^-$ and $CO_3{}^-$ have also been used as reagent ions; Hanke et al., 2003; Huey, 2007). In this method, HNO_3 is detected as an iodide-adduct at a unique *m/z*, published as 189 (Le Breton et al., 2014a,b; Bannan et al., 2015) and 190 (Le Breton et al., 2012; McNamara et al., 2020).

$$HNO_3 + I^- \cdot H_2O \longrightarrow I^- \cdot HNO_3 + H_2O \tag{R5.5}$$

This CIMS technique for measurements of HNO_3 has yet to be directly compared with

other techniques such as denuder-based methods like the Monitor for AeRosols and Gases in Ambient air (MARGA; Metrohm Applikon, NL; Rumsey et al., 2014; Twigg et al., 2015) or DEnuder for Long-Term Atmospheric sampling (DELTA; Tang et al., 2009, 2018b; UKEAP, 2015). These denuder techniques are known to suffer chemical interference from other NO_y species, such as the influence of heterogeneous hydrolysis of dinitrogen pentoxide (N_2O_5; R5.6) and was estimated to contribute an average of 17% to nocturnal MARGA measurements in the study by Phillips et al. (2013a).

$$\mathrm{N_2O_5 + H_2O\,_{(het)} \longrightarrow 2\,HNO_3} \tag{R5.6}$$

N_2O_5 is formed from the reaction between nitrate radicals (NO_3) and NO_2 (R5.7), which reaches a thermally-sensitive equilibrium within a few minutes under typical atmospheric conditions (Brown et al., 2003; Brown & Stutz, 2012).

$$\mathrm{NO_2 + NO_3 + M \rightleftharpoons N_2O_5 + M} \tag{R5.7}$$

NO_3 plays an important role in the nocturnal atmosphere, but is photochemically labile during daylight hours (Benton et al., 2010). Consequently, N_2O_5 is only formed at night and can act as a nocturnal reservoir of NO_2. Both N_2O_5 and NO_3 can be detected by I^- CIMS at *m/z* 62 (R5.8 and R5.9; Slusher et al., 2004; Le Breton et al., 2014a; Bannan et al., 2015).

$$\mathrm{N_2O_5 + I^- \cdot H_2O \longrightarrow NO_3{}^- + NO_2 + I \cdot H_2O} \tag{R5.8}$$

$$\mathrm{NO_3 + I^- \cdot (H_2O)_{\mathit{n}} \longrightarrow NO_3{}^- \cdot (H_2O)_{\mathit{n}} + I} \tag{R5.9}$$

This technique cannot differentiate between the contribution of N_2O_5 and NO_3, so measurements at this *m/z* are reported as the sum of these two species. To address this interference, Kercher et al. (2009) demonstrate that if a cool (unheated) inlet is utilised, N_2O_5 can be detected selectively as an iodide-adduct (R5.10) at *m/z* 235. However this

measurement introduces other drawbacks, such as a lower sensitivity and a greater influence of water vapour (Wang et al., 2014). This method of ionisation has since been replicated in numerous studies (Tham et al., 2016; Wang et al., 2016, 2017c; Zhou et al., 2018).

$$N_2O_5 + I^- \cdot H_2O \longrightarrow I^- \cdot N_2O_5 + H_2O \quad \text{(R5.10)}$$

N_2O_5 is an intermediate in the formation of nitryl chloride ($ClNO_2$), through its heterogeneous reactions with chloride-containing aerosols (R5.11), such as those derived from sea spray (Finlayson-Pitts et al., 1989), fossil fuel combustion or biomass burning (Ahern et al., 2018).

$$N_2O_{5\,(g)} + Cl^-_{(aq)} \longrightarrow ClNO_{2\,(g)} + {NO_3}^-_{(aq)} \quad \text{(R5.11)}$$

$ClNO_2$ can increase the oxidising capacity of the local atmosphere by the production of chlorine radicals (Cl atom) through its photolysis (R5.12).

$$ClNO_2 + h\nu \longrightarrow Cl + NO_2 \quad \text{(R5.12)}$$

Due to its photolytic efficiency and its formation from N_2O_5, $ClNO_2$ is predominantly a nocturnal species. As such it can act as a nocturnal NO_x reservoir, as it regenerates NO_2 after sunrise. Measurements of $ClNO_2$ in the UK were first made in 2012 (Bannan et al., 2015), and an overview of subsequent published measurements is presented in Table 5.1. These measurements were made using I^- CIMS, and detected as an iodide-adduct at *m/z* 208 (R5.13).

$$ClNO_2 + I^- \cdot H_2O \longrightarrow I^- \cdot ClNO_2 + H_2O \quad \text{(R5.13)}$$

Measurements at *m/z* 208 are specific to $ClNO_2$, but the ionisation efficiency is depen-

Table 5.1: List of $ClNO_2$ field observations made in the UK, including average and maximum concentrations and the published reference (by date of observation and site). *Anonymised site, part of GAUGE study by Palmer et al. (2018).

Location	Site type	Year	Season	[$ClNO_2$] / ppt	Reference
London	Urban background	2012	Summer	Mean: 84 Max: 724	Bannan et al. (2015)
Weybourne Atmospheric Observatory	Rural, coastal (ground)	2013	Spring	Mean: 10.5 Max: 65	Bannan et al. (2017)
Norfolk Coast and North Sea	Airborne	2013	Winter	Max: 95	Bannan et al. (2017)
UK*	Landfill	2014	Summer	Mean: 901 Max: 4075	Bannan et al. (2019)
Manchester	Urban background	2014	Autumn	Mean: 58 Max: 506	Priestley et al. (2018)
Leicester	Urban background	2014	Spring	Median: 110 Max: 274	Sommariva et al. (2018, 2021)
			Summer	Median: 15.4 Max: 74.2	
			Winter	Median: 50.5 Max: 248	
		2015	Autumn	Median: 27.7 Max: 75.6	Sommariva et al. (2018)
		2016	Winter	Median: 139 Max: 733	Sommariva et al. (2018, 2021)
Penlee Point	Semi-rural, coastal	2015	Spring	Mean: <LOD Max: 922	Sommariva et al. (2018)
Weybourne Atmospheric Observatory	Rural, coastal	2015	Summer	Mean: 21.5 Max: 1100	Sommariva et al. (2018)

dent on the relative humidity of the sample (Bannan et al., 2015). Mielke et al. (2011) show that calibrations using dry zero air resulted in a 27% lower response factor than when humidified gases were used. However, Mielke et al. (2011) state that the ambient air sampled during this study was sufficient to make the CIMS response independent of relative humidity (approx. 20-85%). Similarly, Bannan et al. (2015) conclude that CIMS measurements of N_2O_5 and $ClNO_2$ during ClearfLo and a later study at Weybourne Atmospheric Observatory (Bannan et al., 2017) were independent of changes in ambient relative humidity.

The aim of this study was to create an I^- CIMS set-up to simultaneously measure each of these NO_y species (PAN, HNO_3, N_2O_5 and $ClNO_2$), via an inlet switching system. This was tested at a remote field site (Auchencorth Moss, south-east Scotland), where concentrations of each NO_y species were expected to be small. The study had specific targets of:

1. Quantifying the N_2O_5 interference in long-term MARGA measurements of HNO_3 at the site,
2. Contributing measurements of $ClNO_2$ in Scotland to the small but growing database of measurements across the UK (Table 5.1), and
3. Quantifying the production rate of Cl radicals from $ClNO_2$ at the site.

5.2 Methods

5.2.1 CIMS instrument

A Chemical Ionisation Mass Spectrometer (CIMS; THS Instruments LLC, GA, USA) was used to try and make simultaneous real-time measurements of PAN, HNO_3, $ClNO_2$ and N_2O_5. The instrument was similar in set-up to recent literature Slusher et al. (2004) and Bannan et al. (2017) and is split into 3 separate regions (ion-molecule region, colli-

sional dissociation chamber and mass spectrometer regions as presented schematically in Figure 5.1).

Sample air was directed into the CIMS through a modified sample inlet, made primarily from 1/2" O.D. PFA tubing and Teflon fittings. The instrument has two near-identical inlets, one with a heater (170±5 °C), that alternately direct sample flow into the CIMS via a custom-built switching unit. The flow direction was controlled by two 2-way solenoid valves (Red Dragon Valves, UK) which were swapped every 30 minutes so that the CIMS measured a heated and unheated sample every hour. The total distance that sample air travelled through this inlet was minimised as much as possible, in order to reduce surface loss. Sample air entering the CIMS (approximately 2 lpm; controlled by a mass flow controller; MKS Instruments, UK) was ionised in the ion molecule region (IMR) with iodide (I^-) ions, supplied from a 2 ppm flow of CH_3I in N_2 at 0.5 lpm (controlled by mass flow controllers; MKS Instruments, UK), passed over an alpha ion source (^{210}Po). Pressure in the IMR region was maintained at 20±0.2 Torr, by a scroll pump (DISL-100; ULVAC Technologies, Inc., MA, USA) for the duration of the deployment at Auchencorth Moss (Section 5.2.2), but it was not possible to replicate the pressure in subsequent lab assessments (14-17 Torr) due to pressure limitations through to the vacuum region. The reason for this is not known but is thought to be a possible disparity in the manifold set-up, not a difference in the efficiency of the pumps.

Following ionisation, ions then passed through a pinhole on a charged plate into the collisional dissociation chamber (CDC) which is maintained at ∼0.3 Torr (± <0.1%) by use of a molecular drag pump (MDP 5011; Alcatel Vacuum Technology, FR). In the CDC, an octopole ion guide breaks apart weakly bound ion clusters (e.g. hydrated clusters) in order to simplify the resulting spectrum. Ions then passed into the mass spectrometer region. Within this region, the ions first encounter a second octopole ion guide that focuses them into a narrow beam (pressure of 10^{-3} Torr maintained by a turbomolecular pump; TV-81M; Agilent, IT). A quadrupole mass filter with pre- and

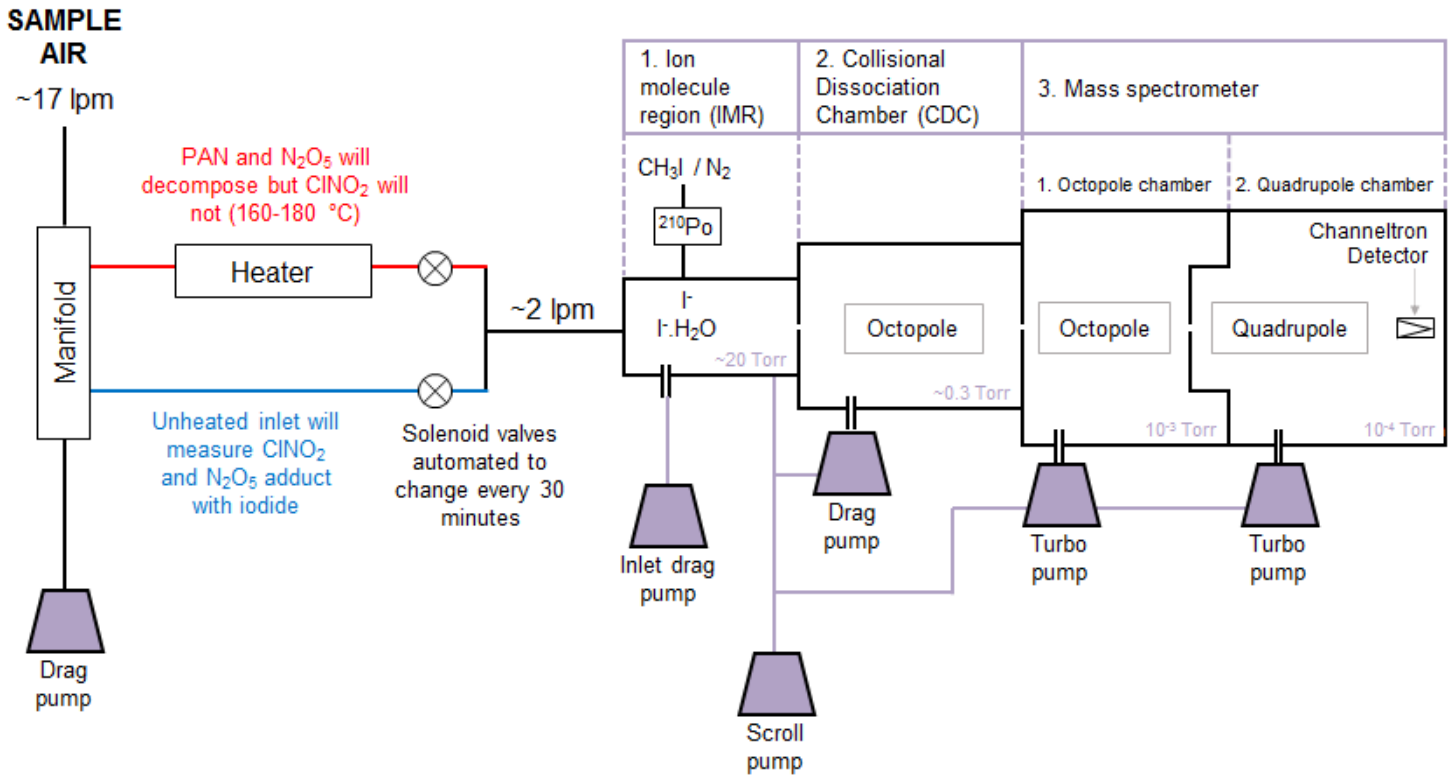

Figure 5.1: Schematic of the chemical ionisation mass spectrometer (CIMS) and inlet set-up designed for measurements at Auchencorth Moss (summer 2019).

post-filters then separated ions by mass. The quadrupole was maintained at a pressure of 10^{-4} Torr by a second turbomolecular pump. Ions were detected using a continuous dynode electron multiplier (Channeltron; Photonis, FR). The applied voltage of the detector was optimised for both reagent ions used in this study, I^- and $I^- \cdot H_2O$ (*m/z* = 127 and 145, respectively; Figure 5.2), to achieve the maximum detector response while preventing excessive degradation of the detector. This was conducted prior to and during the first week of deployment.

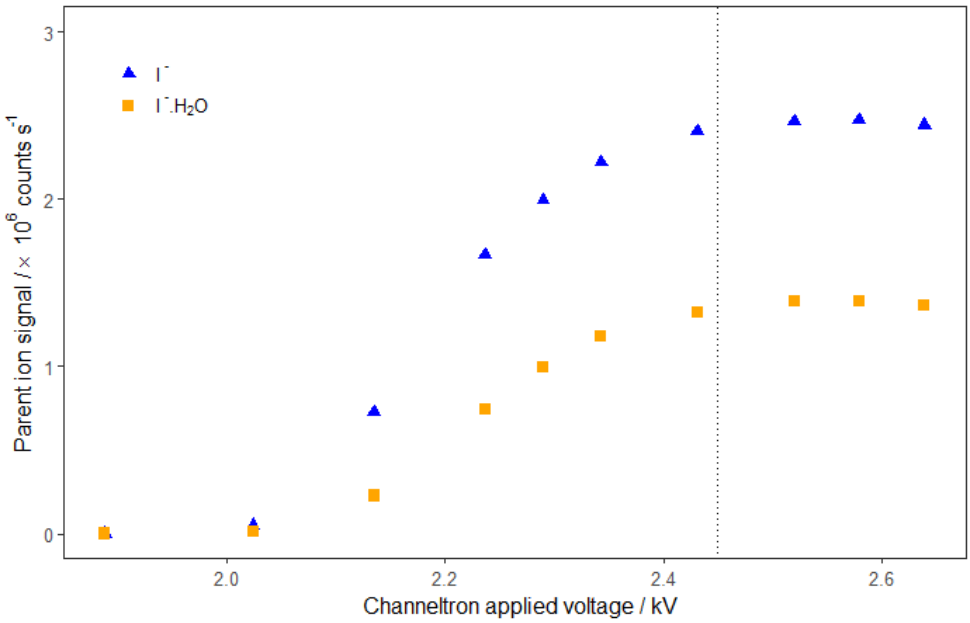

Figure 5.2: Optimisation of applied voltage on the Channeltron electron multiplier detector (Photonis) response for reagent ions used: I^-, *m/z* = 127, blue; $I^- \cdot H_2O$, *m/z* = 145, orange, during the first week of the CIMS deployment at Auchencorth Moss. The vertical dotted line indicates the applied voltage used during this study.

I^- CIMS uses a soft and selective ionisation process due to how unreactive the iodide ion is with atmospheric species (Huey et al., 1995; Slusher et al., 2004). The iodide-water cluster ($I^- \cdot H_2O$) can result in faster ionisations of some species, suggested to be a result of ligand switching via an intermediate cluster ion (Veres et al., 2015), while others are independent of the water cluster population. These include the ionisation of HNO_3, $ClNO_2$ and N_2O_5 through the unheated inlet in this study (Kercher et al., 2009;

Le Breton et al., 2014b), measured at *m/z* of 190, 208 and 235 respectively.

$$HNO_3 + I^- \cdot H_2O \longrightarrow I^- \cdot HNO_3 + H_2O \quad \text{(R5.5, repeated)}$$

$$ClNO_2 + I^- \cdot H_2O \longrightarrow I^- \cdot ClNO_2 + H_2O \quad \text{(R5.13, repeated)}$$

$$N_2O_5 + I^- \cdot H_2O \longrightarrow I^- \cdot N_2O_5 + H_2O \quad \text{(R5.10, repeated)}$$

Within the heated inlet, HNO_3 and $ClNO_2$ are expected to ionise through parallel adduct-forming reactions (R5.5 and R5.13), while PAN and N_2O_5 undergo thermal dissociation in the inlet resulting in different ionisation processes (R5.2 and R5.3; R5.14 and R5.9, respectively) compared to when it sampled with the unheated inlet (Slusher et al., 2004; Phillips et al., 2013b). The acetate ion ($CH_3C(O)O^- \cdot (H_2O)_n$; R5.3) is used to measure PAN at *m/z* = 59, as it has been demonstrated that when a CDC is employed, the most abundant cluster is n = 0 (Slusher et al., 2004). Without a CDC, n = 2 was the most abundant cluster.

$$CH_3C(O)O_2NO_2 + \textit{heat} \longrightarrow CH_3C(O)O_2 + NO_2 \quad \text{(R5.2, repeated)}$$

$$CH_3C(O)O_2 + I^- \cdot (H_2O)_n \rightleftharpoons CH_3C(O)O^- \cdot (H_2O)_n + IO \quad \text{(R5.3, repeated)}$$

$$N_2O_5 + \textit{heat} \longrightarrow NO_2 + NO_3 \quad \text{(R5.14)}$$

$$NO_3 + I^- \cdot (H_2O)_n \longrightarrow {NO_3}^- \cdot (H_2O)_n + I \quad \text{(R5.9, repeated)}$$

N_2O_5 has been shown to react directly with iodide-water clusters to form ${NO_3}^-$ ions (R5.8; *m/z* = 62) using heated inlets at temperatures similar to (Slusher et al., 2004) and lower than (40–50 °C; Le Breton et al., 2014a; Bannan et al., 2015) those used in this study.

$$N_2O_5 + I^- \cdot H_2O \longrightarrow {NO_3}^- + NO_2 + I \cdot H_2O \quad \text{(R5.8, repeated)}$$

${NO_3}^-$ ions resulting from both reactions (R5.8 and R5.9) are measured at *m/z* = 62, and conversion occurs with a 1:1 stoichiometry. Therefore measurements at *m/z* = 62

comprises the sum of N_2O_5 and NO_3 during the night.

In this study, the ratio of the $I^- \cdot H_2O$ ion (*m/z* = 145) to the iodide ion (I^-, *m/z* = 127) ranged from 42–76%, with a mean of 58%. The inlet design ensured that all target species could be measured for at least 30 minutes of every hour at the specified *m/z*. However no precautions were taken to limit potential chemical interference in the measurements, and the magnitude of any interference was to be assessed in the laboratory tests following deployment.

The detector continuously monitored ions at *m/z* = 59 ($CH_3C(O)O^-$), 62 ($NO_3{}^-$), 127 (I^-), 145 ($I^- \cdot H_2O$), 190 ($I^- \cdot HNO_3$), 208 ($I^- \cdot ClNO_2$), 235 ($I^- \cdot N_2O_5$), with a 3 s time resolution. A mass scan took place once every 30 minutes (15 minutes after solenoid valve change; *m/z* 50–250, by 0.1, dwell time 100 ms). A background mass was selected close to the *m/z* of each molecule of interest where no signal was expected, nor observed prior to deployment (*m/z* 65, 194, 214).

With the alternate heated and unheated inlets, the hypothesis was that measurements of each species would not be consistent throughout each measurement cycle. The unheated inlet aimed to measure adducts of iodide and HNO_3, $ClNO_2$ and N_2O_5 (*m/z* 190, 208 and 235, respectively), while the heated inlet was intended to cause thermal dissociation of PAN and N_2O_5, consequently measuring the acetate ion and $NO_3{}^-$ (*m/z* 59 and 62, respectively). As $ClNO_2$ was not observed by thermal dissociation <200 °C by Thaler et al. (2011), it is assumed that $ClNO_2$ is continually measured through both the heated and unheated inlets in this CIMS set-up (Figure 5.1), subject to separate background noise correction in each.

5.2.2 Field study

The CIMS was deployed at Auchencorth Moss (site detailed in Chapter 3 and Twigg et al., 2015) during the summer of 2019 (2 May to 6 August), where it was housed in

an air-conditioned cabin. The inlet was attached to the cabin roof ∼3 m above ground level, in the direction of the predominant prevailing wind at the site (south-west; Figure 5.3). The inlet sampling line faced slightly downward, and was protected by a rain shield. The main sample line drew ambient air from this inlet into the manifold at ∼17 lpm using a piston pump (RP75P SE; Charles Austen Pumps, UK) from 2 to 31 May 2019, and a vacuum pump (VT 4.8, Becker International, DE) from 1 June to 6 August 2019, from which the CIMS inlet drag pump (L-79200-35; Cole Parmer, UK) sampled. IMR pressure was watched closely to ensure it remained at approximately 20 Torr. The length of the inlet prior to the CIMS was 1.5 m, making the total length 2 m.

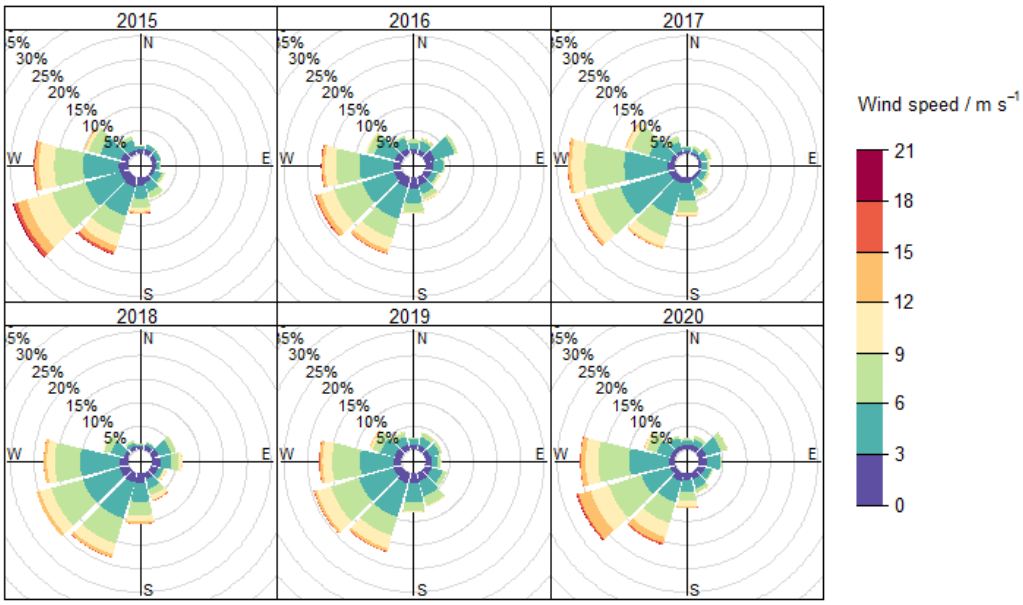

Figure 5.3: Wind roses depicting the annual average frequency of wind speeds arriving at Auchencorth Moss in 30° bins of co-located wind direction measurements, between 2015 and 2020. Wind speed and wind direction measurements were co-located at the site (Coyle et al., 2019), and the underlying time resolution was hourly for both.

5.2.3 Laboratory characterisation and calibration

The CIMS was calibrated for HNO_3 and PAN in the lab following the deployment at Auchencorth Moss, using the same set-up as the field study.

HNO_3

Nitric acid (HNO_3) was calibrated by passing a flow of oxygen-free nitrogen (2.0±0.2 lpm) over a temperature-controlled permeation source (Dynacal Permeation Device; VICI Metronics, WA, USA) to deliver a precise concentration HNO_3 source using a Dynacalibrator (Model 120; also VICI Metronics, henceforth referred to as "Dynacal"). The permeation rate was stabilised with a continuous N_2 flow and a set temperature (30 °C), maintained for at least 48 hours prior to use. Different concentrations were achieved by varying the dilution flow mixed with the flow from the permeation tube, and the flow through the Dynacal, providing the permeation rate was completely stabilised prior to measurements being made. Surface loss of HNO_3 was limited by using only a short section of 1/4" O.D. PFA tubing prior to the manifold, and using Teflon fittings. These known concentrations of HNO_3 were introduced to the sample stream, demonstrated by the schematic in Figure 5.4, and concentrations entering the CIMS were calculated using standard addition methodology. Each concentration was maintained for 1–3 hours, until signal at *m/z* 190 had stabilised.

PAN

The PAN standard was generated from the photolytic reaction of NO in excess acetone (R5.15, R5.16 and R5.1; Flocke et al., 2005; Malley et al., 2016a). A flow of zero air containing acetone was passed through a ∼150 cm^3 photolysis cell, shielded from ambient light and irradiated by UV light (Hg pen lamp, Model 6035; Oriel Instruments, MA, USA) in the presence of O_2, generating the peroxyacetyl (PA) radical. A flow of NO (10 sccm, 1 ppm; BOC, UK) controlled by a mass flow controller (MKS Instruments, UK) was mixed into the gas stream. The NO first oxidised to NO_2, which then reacted with the newly-formed PA radical to generate PAN. The final concentration of PAN was achieved by dilution using a known flow of N_2 (M100B, MKS Instruments, UK), where the conversion efficiency of NO to PAN was assumed to be 93±3% in all

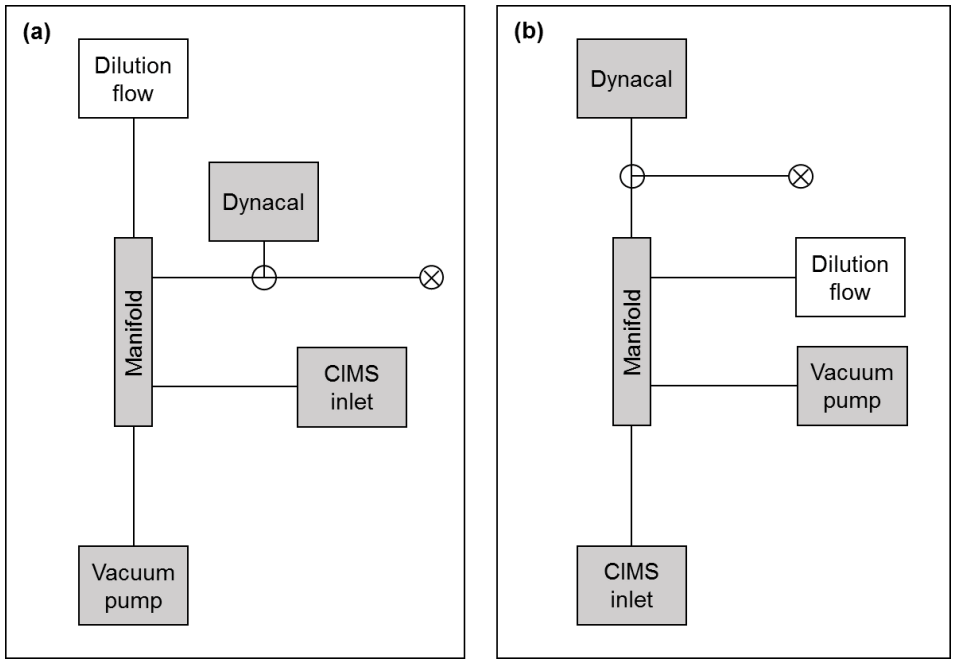

Figure 5.4: Schematics of the set-up used for HNO_3 calibration of the CIMS in the laboratory. The Dynacalibrator labelled 'Dynacal' contains the temperature controlled HNO_3 permeation source. **(a)** Implements the calibration equipment into the setup used at Auchencorth Moss, while **(b)** presents an alternate arrangement where path from Dynacal to CIMS inlet is straight.

calculations (Volz-Thomas et al., 2002; Fischer et al., 2010).

$$CH_3COCH_3 + h\nu \longrightarrow CH_3CO + CH_3 \qquad \text{(R5.15)}$$

$$CH_3CO + O_2 + M \longrightarrow CH_3C(O)O_2 + M \qquad \text{(R5.16)}$$

$$CH_3C(O)O_2 + NO_2 + M \rightleftharpoons CH_3C(O)O_2NO_2 + M \qquad \text{(R5.1, repeated)}$$

N_2O_5 and $ClNO_2$

The set-up for the calibration for N_2O_5 and $ClNO_2$ was also prepared, but due to restrictions following Covid-19 this work could not be completed. The text below describes the set-up which would have been applied to calibrate for N_2O_5 and $ClNO_2$.

Generation of a known N_2O_5 concentration was planned to be in situ via the gaseous reactions between ozone (O_3) and excess nitrogen dioxide (NO_2), and further reaction of the NO_2 with the nitrate radical reaction product (NO_3) (Bertram et al., 2009; Wang

et al., 2016):

$$O_3 + NO_2 \longrightarrow NO_3 + O_2 \quad \text{(R5.17)}$$

$$NO_2 + NO_3 + M \rightleftharpoons N_2O_5 + M \quad \text{(R5.7, repeated)}$$

The O_3 was to be generated from the photolysis of O_2 using an ozone generator (Model 306; 2B Technologies, CO, USA), verified to produce a known O_3 concentration with a calculated uncertainty of 8%. This was to be mixed with excess NO_2 supplied from a cylinder (10 ppm; BOC, UK) in wide diameter PFA tubing for at least 1 minute. The concentration of N_2O_5 would be estimated from the change in NO_2 concentration observed by a Cavity Attenuated Phase Shift (CAPS; Teledyne T500U, CA, USA) NO_2 analyser. This would have then been diluted to the desired concentration with oxygen-free N_2.

$ClNO_2$ would be generated downstream from N_2O_5 by passing the known concentration of N_2O_5 over a slurry of NaCl in ultrapure deionised water (Roberts et al., 2009; Wang et al., 2016; Zhang et al., 2020).

$$N_2O_{5\,(g)} + NaCl_{\,(aq)} \longrightarrow ClNO_{2\,(g)} + NaNO_{3(aq)} \quad \text{(R5.18)}$$

The slurry would be made from 1 g of NaCl ($\geq$99.5%, Sigma Aldrich) in 3 ml of water, quarter filling 1/2" diameter PFA tubing (25 cm length) as in Wang et al. (2016). The conversion efficiency would have been assumed to be unity based on previous studies (Roberts et al., 2009; Wang et al., 2016).

Ionisation of N_2O_5 and $ClNO_2$ has been shown to be more efficient with $I^- \cdot H_2O$ than with I^- (Kercher et al., 2009; Mielke et al., 2011; Wang et al., 2014; Bannan et al., 2015). Ionisation of both species has been demonstrated to increase with relative humidity until a threshold humidity is surpassed, above which ionisation is independent of the relative humidity. To account for this during calibration, a bubbler would be

introduced into the set-up to artificially humidify the sample air and ensure there was enough water vapour in the IMR. Mielke et al. (2011) demonstrate that the ambient air sampled during their study (20–85%; their Supplementary Information) was sufficient to exceed this threshold.

5.3 Results and discussion

5.3.1 Laboratory calibrations

Laboratory calibration of the CIMS were attempted for both HNO_3 and PAN. Unfortunately, calibrations of $ClNO_2$ and N_2O_5 were not trialled due to a restriction of access to the laboratory because of the Covid-19 pandemic and subsequent lockdowns and reduced access. The proposed methods are detailed in this Chapter's methodology.

HNO_3

The HNO_3 calibration was done first for simple practicality, i.e. ease of set-up and availability of the permeation source, as well as its importance in addressing the aims of this work. The "sticky" nature of HNO_3 means the physical loss and deposition on internal surfaces is probable, while its close chemistry with N_2O_5 can cause interference in either measurement.

Hydrolysis of N_2O_5 (R5.6) could cause a loss of N_2O_5 measured (at both *m/z* = 62 and 235 in heated and unheated inlets, respectively), and potentially result in an increase in observed HNO_3 (*m/z* = 190) if the loss was not to internal surfaces.

$$\mathrm{N_2O_5 + H_2O_{\,(het)} \longrightarrow 2\,HNO_3} \qquad \text{(R5.6, repeated)}$$

Wang et al. (2016) demonstrate that use of a nylon filter to semi-selectively remove HNO_3 from the sample gas stream resulted in little change in their measurements of N_2O_5, suggesting negligible/limited production of HNO_3 from N_2O_5 in their set up.

Concentrations achieved during the calibration of HNO_3 ranged between 9–350 µg m^{-3}, presented in Figure 5.5, with the corresponding peaks at *m/z* = 190 for two separate concentrations presented in Figure 5.6b. The challenge during this work was to replicate the IMR pressure used during the field study at Auchencorth Moss, despite using the same set-up. Only pressures between 14–17 Torr were achieved in the laboratory, by varying the inlet flow rate through the manifold, the dilution flow rate mixed with the HNO_3-ladened flow from the Dynacal, and the flow rate through the drag pump connected to the CIMS inlet. The lowest concentration achieved (9 µg m^{-3}) was over 10 times larger than the concentrations reported at Auchencorth Moss during this period by the Monitor for Aerosols and Reactive Gases (MARGA, Metrohm, NL; Figure 5.7).

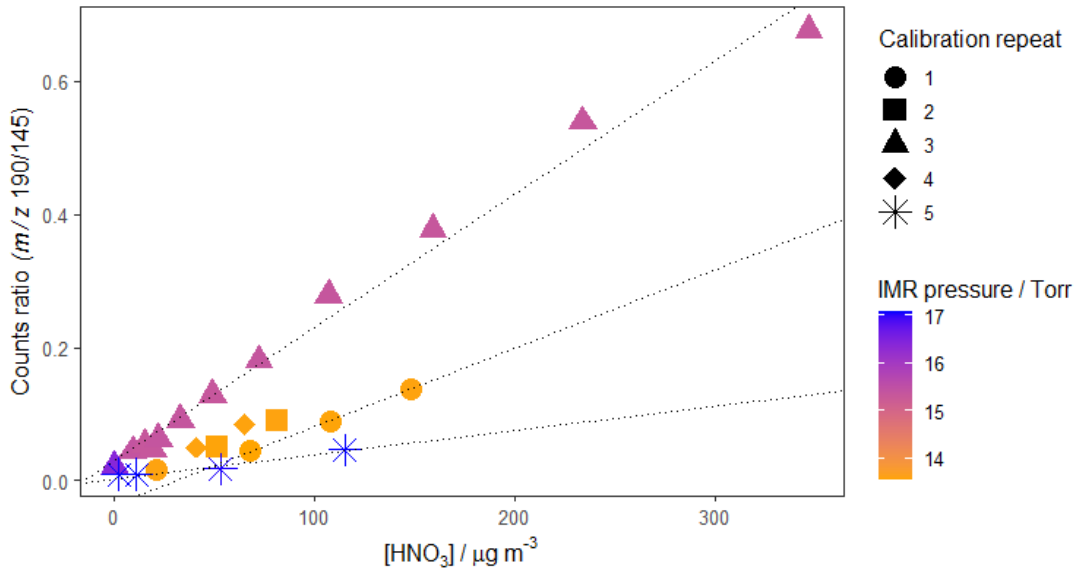

Figure 5.5: Calibration plot of number of counts per second measured at *m/z* 190 against the concentration of HNO_3 generated by a permeation tube. Data points are coloured by the IMR pressure (14-17 Torr). Shapes represent calibration on different days, with a different flow rate through the permeation source. Each change included sufficient time (>1 hour) for the stabilisation of the HNO_3 permeation tube. The three dotted lines represent the linear relationship for each calibration repeat where more than two concentrations were recorded.

HNO_3 was the only species successfully generated and detected by the CIMS, and therefore the only species for which a limit of detection (LOD; 3σ of background signal) could be determined. In the laboratory, the LOD was calculated to be 5 µg m^{-3} for the calibration at approx. 16 Torr IMR pressure. This LOD is higher than concentrations

expected at Auchencorth Moss, but is derived at an IMR pressure lower than maintained during the field study. This difference in IMR pressure affects the ionisation rate within the IMR region due to the frequency of collisions between reagent ions ($I^- \cdot H_2O$) and the analyte (HNO_3). Consequently, a wider range of signals were observed at *m/z* 190 during the field study (approx. 380-8100 counts s^{-1}; around 20 Torr), and were predominantly greater than those observed in the laboratory (approx. 250-2000 counts s^{-1}; around 16 Torr), including at concentrations of HNO_3 up to 115 µg m^{-3}. This difference in pressure affects all potential measurements of HNO_3 made by the CIMS, and therefore means that laboratory calibrations are not applicable to data collected in the field. Figure 5.5 demonstrates that the counts ratio is not directly related to the IMR pressure, suggesting another factor is also involved. The signal observed at *m/z* 190 during the deployment at Auchencorth Moss is discussed further in Section 5.3.2.

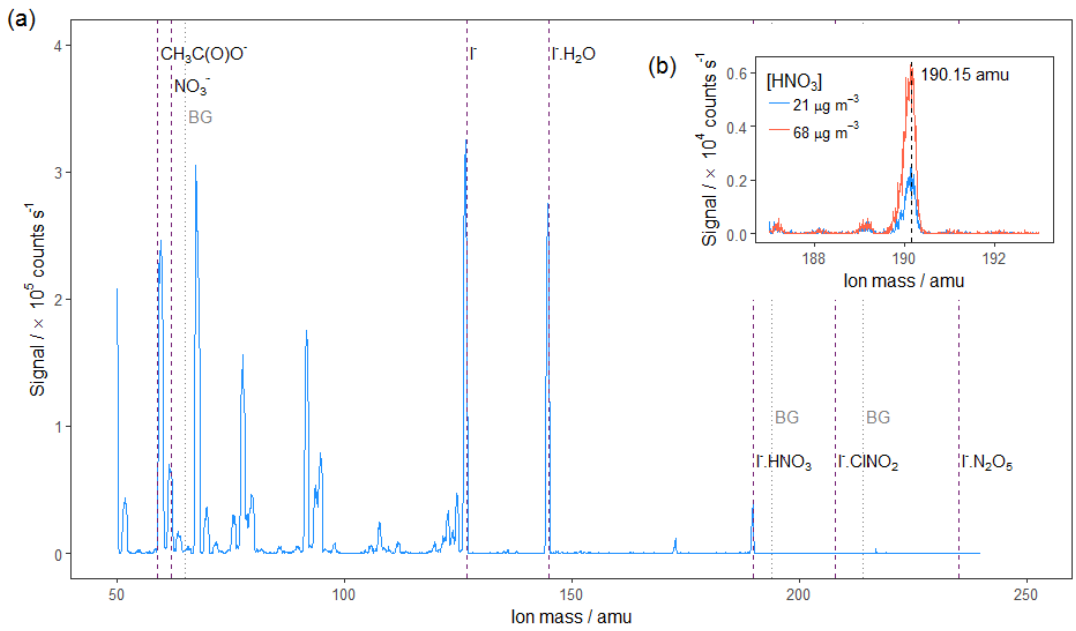

Figure 5.6: **(a)** Example CIMS mass scan taken during the deployment at Auchencorth Moss, between *m/z* 50-250 at a resolution of 0.1 and a dwell time of 500 ms. Vertical dotted lines indicate the signal masses tracked by the CIMS (*m/z* = 59, 62, 127, 145, 190, 208 and 235), and the respective background signals (BG; *m/z* = 65, 194 and 214). **(b, inset)** Expanded scale mass scan of *m/z* 187–193 (by 0.01, dwell time = 500 ms) during the calibration of HNO_3 at two concentrations (21 and 68 µg m^{-3}; blue and red, respectively).

In order to make the calibration applicable to concentrations expected at Auchencorth

Moss, the pressure in the IMR needs to be increased and the instrument's LOD needs to be improved. To improve the pressure, a new set-up is required for calibration, since the variation in dilution flow rates mixed with the HNO_3 flow from the Dynacal was linked to changes in the IMR pressure. The difficulty encountered was balancing the compromise between keeping the length of the inlet short, to minimise HNO_3 loss on inlet surfaces (discussed further in comparison to MARGA; Section 5.3.2), and allowing for sufficient mixing of Dynacal and dilution flows. Figure 5.4a shows the initial set-up, where the calibration equipment was implemented into the field set-up. However this resulted in less signal at *m/z* 190, and no change in counts s^{-1} recorded when concentration was changed. In this set-up, the primary loss of HNO_3 is assumed to be a result of most of the Dynacal flow bypassing the CIMS inlet. The configuration of the set-up was changed to Figure 5.4b to rectify this problem and allow the calibration to take place.

The dilution flow rate was measured in situ so the final concentration could be determined. To achieve the lowest concentrations observed, the dilution flow was increased by opening the adjustable valves which had the most impact on IMR pressure. Future work is required to provide a solution where the dilution can be increased with minimal impact on the IMR pressure. If this is achieved, the LOD can then be improved by further optimising the operation of the CIMS.

PAN

Similarly to HNO_3, the calibration for PAN took place following the deployment at Auchencorth Moss. The generator set-up for PAN (detailed in Section 5.2.3) was plumbed directly into the inlet of the CIMS field set-up (e.g. in Figure 5.1). The excess acetone used to react with a quantified stream of NO is likely also to be photolysed to form the PA radical (R5.15 and R5.16) and measured by the CIMS, thus resulting in a measurement artefact at *m/z* 59.

To separate the signal of PAN from that of the artefacts from the PA radical, the counts s^{-1} recorded through the ambient temperature inlet were subtracted from those recorded using the heated inlet. The difference in signal was attributed to PAN. For this comparison, the inlets were swapped using the two-way solenoid valves used at Auchencorth Moss and allowed to stabilise. However this did not create comparable conditions to calculate this artefact, which was attributed to a potential difference in pressure as a result of the solenoid valve change.

Phillips et al. (2013b) found the cold inlet background to be around 10% of the total signal, but this was attributed to the contribution of peroxyacetic acid (PAA; $CH_3C(O)OOH$; R5.19).

$$CH_3C(O)OOH + I^- \longrightarrow CH_3C(O)O^- + HOI \qquad \text{(R5.19)}$$

Phillips et al. (2013b) suggest that the total signal at *m/z* 59 can be corrected for PAA using inlet heater cycling, as used here, or frequent zeros and NO addition. Moving forward, NO addition will be employed in laboratory characterisation to remove inlet sensitivity to PAN, by loss of the PA radical, and thus determine the contribution of PAA. A CIMS instrument background could be achieved in the laboratory, by using a heated stainless-steel line filled with stainless-steel wool, to remove both PAN and PAA from the analyte gas stream (Flocke et al., 2005; Zheng et al., 2011).

5.3.2 Field study

Due to instrument commitments on other projects, no calibration could be performed prior to instrument deployment. The CIMS signals were briefly optimised prior to deployment, and during the first few days on site once the instrument had been restarted. It was noted that the system was unstable at points during the deployment due to long periods of intermittent electrical noise (see Figure 5.9); however the initial settings were maintained in order to ensure comparability of signals across the study – this was

particularly important given it was not possible to calibrate in the field. An example mass scan during the deployment is presented in Figure 5.6a.

A comparison of the data collected by the heated and unheated inlets is presented in Figure 5.8. Good correlation ($R^2 > 0.85$) is observed for *m/z* 190 and lower, while there is little correlation at mass-to-charge ratios greater than 190. For HNO_3, there is good correlation between inlets for the peak at *m/z* 190 and a distinct lack thereof at the nearby background signal (*m/z* 194).

However, when these hourly average values are compared to co-located measurements of HNO_3 made at Auchencorth Moss by the Monitor for AeRosols and GAses in ambient air (MARGA; Metrohm Applikon, NL; described in Twigg et al., 2015), there is no observed correlation for either the heated or unheated inlet signals (Figure 5.7). As discussed above (Section 5.3.1), measurements from the CIMS are presented in counts s^{-1} due to the issues with the calibration conducted. It is acknowledged that MARGA measurements of HNO_3 also have potential interferences from other NO_y species (Phillips et al., 2013a; Rumsey et al., 2014), and that both instruments will have suffered a different degree of HNO_3 loss due to the set-up of their respective inlets. However, these interferences have not been formally quantified yet, so these measurements are generally accepted but used with caution.

When considering this intercomparison by measurements made during the day and the night, there is no improvement in correlation at either time period, but slightly different patterns. Higher concentrations of HNO_3 are observed by the MARGA during the day, as would be expected from its diurnal cycle (e.g. observed at a similar environment nearby; Ramsay et al., 2018), and so there is more spread in diurnal MARGA measurements, than nocturnal (maximum concentrations of 0.63 and 0.28 µg m^{-3}, respectively). On the contrary, the maximum range of counts s^{-1} observed by the CIMS remains similar (up to 8×10^5 counts s^{-1}). This occurs at the smallest MARGA measurements (<0.1 µg m^{-3}), and could suggest that there is interference in the lowest concentrations

recorded. However reaching such a conclusion from this study would require further investigation, as both this CIMS set-up and the MARGA have unquantified interferences (see below and Section 1.5.2). An alternative explanation is that the measurements recorded by the CIMS are at or below its detection limit, as evidenced by the absence of diurnal variation which would be expected for HNO_3 at Auchencorth Moss, and is observed with the MARGA.

There is a high possibility that there are interactions between HNO_3 and the internal surfaces of the inlet. Potential for interaction was minimised by using the shortest possible lengths of tubing with a large internal diameter (1/2") to provide a smaller surface area to volume ratio to the analyte. This set-up resulted in an inlet residence time of approximately 2.6 s for HNO_3 and the other species measured by the CIMS. In comparison, HNO_3 has a significantly shorter residence time of approximately 0.3 s in the MARGA. Loss of HNO_3 to internal surfaces is therefore more probable in the CIMS. Another factor contributing to interaction with surfaces is the inlet design of the CIMS, which sampled from the analyte gas stream at an almost 90° angle (Figure 5.1). This resulted in a turbulent disruption from the otherwise laminar flow of the inlet, and cause more interactions with internal surfaces and the potential for loss of HNO_3. Since very low concentrations of HNO_3 are expected at Auchencorth Moss, the surface loss of HNO_3 could be a major negative interference, and therefore resulting in unrepresentative recorded measurements. As concentrations of HNO_3 at Auchencorth Moss are low (<2 $\mu g\, m^{-3}$ all year) and both instruments suffer from unquantified interferences, achieving a good correlation from this instrument intercomparison is difficult (Figure 5.7).

Measurements made at *m/z* 59 and 62 for $CH_3C(O)O^-$ (to measure PAN) and NO_3^- (to measure the sum of NO_3 and N_2O_5), respectively, also demonstrate good correlation between inlets (Figure 5.8). This was not expected, as the proposed measurement of PAN requires thermal dissociation to the PA radical prior to ionisation. The back-

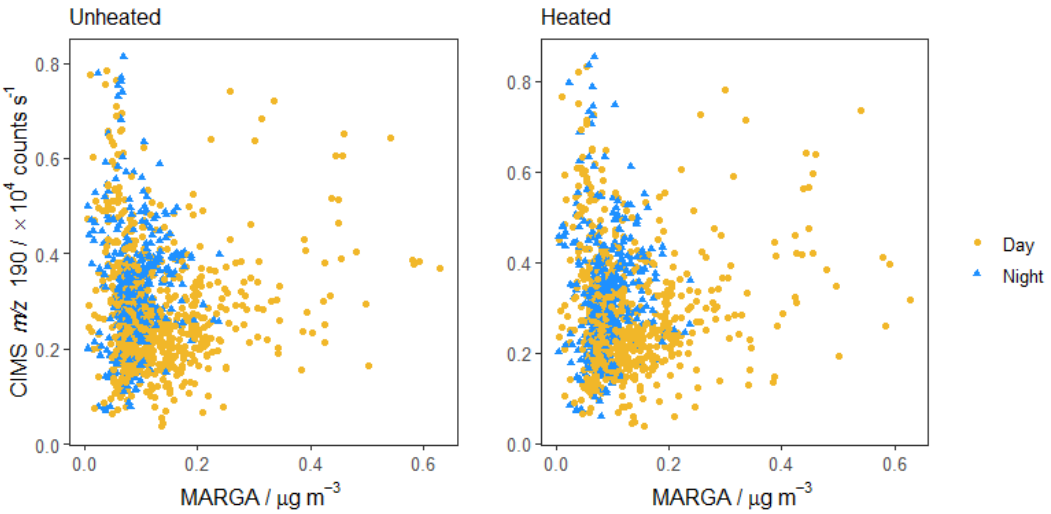

Figure 5.7: Comparison of counts recorded by the CIMS to measure HNO_3 (*m/z* 190) with co-located MARGA measurements at Auchencorth Moss. **(Left)** presents data collected during sampling with the unheated inlet while **(right)** with the heated inlet. All measurements are hourly averages. The colour and shape of points represents measurements made during the day (yellow, circle) or the night (blue, triangle).

ground signal selected for this region (*m/z* 65; see Figure 5.6a) also demonstrates good correlation between signals measured with the heated and unheated inlets (Figure 5.8), compared to the background signals at *m/z* 194 and 214. The background signals at higher mass-to-charge ratios (194 and 214) suggest a more representative background measurement due to the distinct lack of correlation between the two inlets during the same hour ($R^2 \leq 0.1$). This suggests that either *m/z* 65 may not represent a true background signal for this region of the spectra at Auchencorth Moss, or a result of a higher background signal at the lower *m/z* of the spectrum, reflected in the higher counts s^{-1} reported. In order to ascertain this, an instrumental background should have been performed while the CIMS was deployed, to quantify any signal above this. For example, using the heated stainless-steel inlet described in Section 5.3.1. PAN has been measured previously at Auchencorth Moss using GC-ECD (McFadyen & Cape, 2005; Malley et al., 2016a), based on which 15-minute averaged concentrations up to 1.5 ppb are anticipated at similar times of the year.

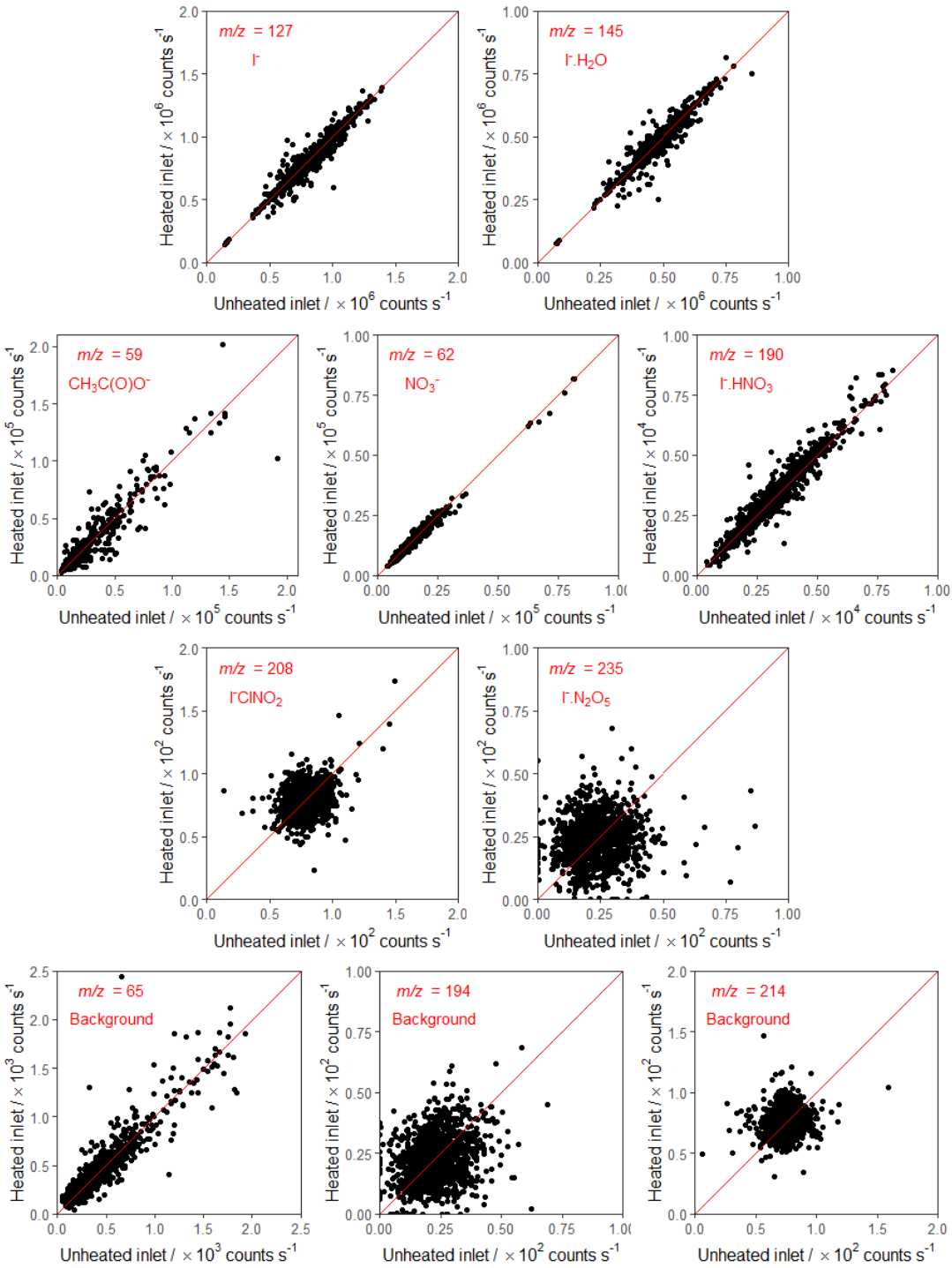

Figure 5.8: Direct comparison of hourly average measurements made during the field study via the heated and unheated inlets, at each of the masses tracked. These include I^- (*m/z* 127), $I^- \cdot H_2O$ (*m/z* 145), $CH_3C(O)O^-$ (PAN; *m/z* 59), NO_3^- (*m/z* 62), $I^- \cdot HNO_3$ (*m/z* 190), $I^- \cdot ClNO_2$ (*m/z* 208) and $I^- \cdot N_2O_5$ (*m/z* 235), as well as the background signals selected (*m/z* 65, 194 and 214). Red lines in each plot illustrate the 1:1 relationships. Note axis scales vary between each subplot.

This drop in the background signal can also be evidenced by the difference in magnitude of observed counts for $ClNO_2$ (*m/z* 208) compared with N_2O_5 (*m/z* 235). A large majority of counts collected for $ClNO_2$ were between 50–100 counts s^{-1}, while those collected for the $I^- \cdot N_2O_5$ adduct were <50 counts s^{-1}. Both masses show no correlation between the two inlets, likely a result of very low sensitivity in this part of the spectrum, coupled with low expected concentrations. Based on summertime measurements of $ClNO_2$ at another rural UK site (Weybourne Atmospheric Observatory; Sommariva et al., 2018), concentrations of $ClNO_2$ <100 ppt are expected at Auchencorth Moss. It could be that the cold inlet did not measure N_2O_5 (at *m/z* 235), and all N_2O_5 measured in this study is actually reported at *m/z* 62. However, it is evident that no $ClNO_2$ nor N_2O_5 was measured during the field study as signals at the respective masses were not visible above the background noise in this CIMS. This can be seen for $I^- \cdot ClNO_2$ in Figure 5.9.

Intermittent noise

Periods of intermittent noise occurred at random intervals during the field study (see example in Figure 5.9). It was initially thought to be a result of the solenoid valve switching causing an abrupt change in pressure within the CIMS. However, this was not evident in practice and the noise did not occur consistently or in correlation with inlet changes. The choice of pump for the sample inlet through the manifold was evaluated, due to the potential instability in pressure resulting from using the piston pump. This was swapped with a vacuum pump, which has a much more consistent pressure flow. However, this did not resolve the issue.

When triggered, a malfunctioning pressure sensor in the mass spectrometer (3rd section of the CIMS; Figure 5.1) perpetuated the period of intermittent noise. Once the sensor reported a value which breached a pressure threshold, a safety mechanism kicked in and switched off the detector. Although the detector restarted once the pressure reported fell below the threshold value again, it took approximately 60 seconds for the

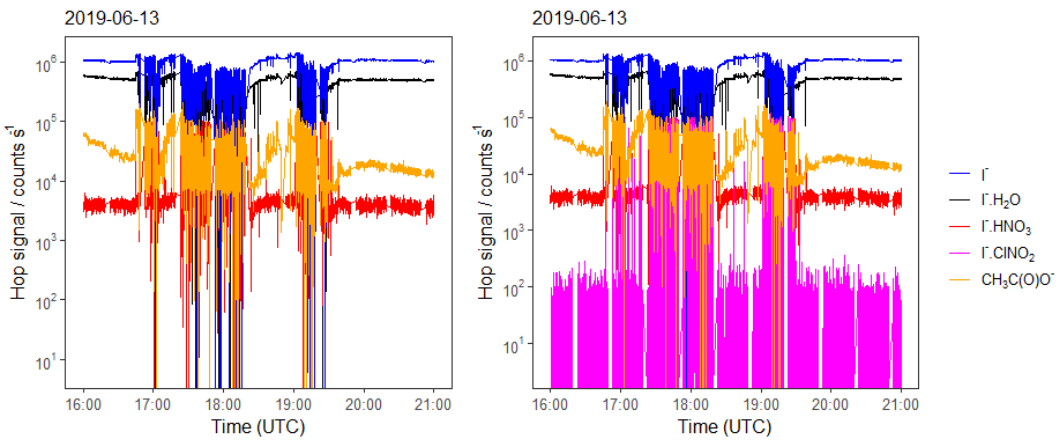

Figure 5.9: Example of intermittent noise recorded in the CIMS on 13 June 2019. Counts per second are presented for I^- (m/z 127, blue), $I^- \cdot H_2O$ (*m/z* 145, black), $CH_3C(O)O^-$ (*m/z* 59, orange), $I^- \cdot HNO_3$ (*m/z* 190, red), $I^- \cdot ClNO_2$ (*m/z* 208, magenta).

detector to restabilise. The sensor used to measure this pressure reported a substantial amount of noise, so when pressure became near the safety threshold, the detector was repeatedly switched on and off (approximately every few seconds) resulting in repeated measurements of much lower signals before there was chance to properly stabilise.

5.4 Conclusions

As evidenced by the theory and surrounding literature, the instruments and method are appropriate for measurement of the intended NO_y species (PAN, HNO_3, N_2O_5 and $ClNO_2$). However, the specific instrument set-up used for this study yielded a limit of detection too high to measure any of the target species.

Calibration was quasi-successful for HNO_3, but yielded an incompatible conversion factor (from counts s^{-1} to $\mu g\, m^{-3}$) due to the difference in pressure in the ion molecule region (IMR; approximately 14-17 Torr during calibration compared with 20±0.2 Torr at Auchencorth Moss), affecting the ionisation efficiency and thus the counts s^{-1} recorded in each location. HNO_3 was detected at concentrations $\geq 9\, \mu g\, m^{-3}$ during laboratory calibrations, but the inability to replicate the higher IMR pressure and reach HNO_3

concentrations as low as expected at Auchencorth Moss meant the calibrations performed were not applicable to field data measured. Similarly, no correlation was observed between co-located HNO_3 measurements made by a MARGA, and the counts s^{-1} (*m/z* = 190) recorded by the CIMS. This did not improve when data were separated by measurements made during the day and at night. This lack of difference between day and night is attributed to the CIMS, as the range of counts s^{-1} observed during the day and the night are the same, compared to the differing concentrations reported by the MARGA (maximum of 0.63 and 0.28 $\mu g\, m^{-3}$, respectively). HNO_3 losses are likely to have occurred to the CIMS inlet, however it was not possible in the time to quantify these losses.

The CIMS instrument background signal was particularly high at low *m/z* values, and decreased with increasing mass-to-charge ratios. As a result, measurement for PAN was inconclusive due to unsuccessfully quantifying the CIMS background signal at *m/z* 59, or interference from species like peroxyacetic acid (PAA). These should be accounted for using heated stainless-steel wool to remove PAN and PAA from the sample stream, and periodic introduction of NO to the analyte gas stream to selectively remove PAN. Signals recorded for $ClNO_2$ and N_2O_5 were subject to much lower sensitivity at their higher *m/z* values (208 and 235, respectively), and were therefore not observed above the background noise.

Overall, the CIMS inlet constructed did not perform as anticipated due to differences in IMR pressure, and long periods of intermittent noise during the field study. If more time and resources were available, the inlet would be reconstructed to reduce residence time and turbulence of the sample air. The two 2-way solenoid valves would also be replaced with a single 3-way solenoid valve in order to stabilise the inlet and IMR pressure throughout the measurement period. Further work would also include optimisation of the CIMS to detect and calibrate $ClNO_2$ and N_2O_5.

Chapter 6

Conclusions

6.1 Overview of thesis results

This research investigated long-term measurements of atmospheric trace gas species and actinic flux at multiple sites across the UK, including the two UK European Monitoring and Evaluation Programme (EMEP) "supersites". In Chapter 2 the relocation of the southern UK supersite was analysed with the aim of establishing whether the concentrations of a number of key atmospheric components at the new site continued to be representative of the wider area, in-line with EMEP site requirements. In Chapters 3 and 4 the benefit of capturing the variation in local meteorological conditions using radiometers for modelling photolysis rate constants accurately was established. Finally the work in Chapter 5 investigated quantification of the possible chemical interference in currently accepted oxidised reactive nitrogen (NO_y) measurements. The findings of these strands of research are briefly summarised again here.

The southern UK EMEP supersite was demonstrated to remain representative of the south England rural background air for concentrations of particulate matter (PM_{10} and $PM_{2.5}$), sulphur dioxide (SO_2) and ozone (O_3) despite the relocation from Harwell to Chilbolton Observatory. This was achieved by using a meteorological normalisation technique on concatenated time series of concentrations from the two sites. Concen-

trations of nitrogen oxides (NO_x) and ammonia (NH_3) exhibited a clear step change in their time series, with elevated concentrations following the relocation to Chilbolton Observatory. NO_x concentrations increased by a factor of approximately 1.6, driven by increased contribution from sources east of the site, including the M3 motorway and Greater London. NH_3 concentrations increased considerably, by a factor of 3. This is attributed to the close proximity of mixed farmland, in particular a strong source to the south-west of the site.

The effect of variation in local meteorological conditions on measured photolysis rate constants was investigated with respect to time-of-year, site (across the UK), direction (2-π or 4-π sr inlet optics), and photodissociation reaction route, through the derivation of species specific measurement driven adjustment factors (MDAF) for the rate constants relative to their modelled cloud-free estimations.

MDAF values were shown to decrease cloud-free model estimates of $j(NO_2)$ by 45-51% across the UK, but less for photodissociation reactions which occur at shorter wavelengths, e.g. approximately 20% for $j(O^1D)$. Including upwelling radiation in the derivation of MDAF values (4-π sr field of view) typically led to good agreement (<6%) with downwelling-only (2-π sr) MDAF derivations at Auchencorth Moss. The exception to this occurred during periods of snow cover, where the increased surface albedo resulted in total derived MDAF values reducing modelled $j(NO_2)$ by 36% less than downwelling-only MDAF.

Separate derivation of MDAF values for 12 photolysis reactions demonstrated the importance of considering the action spectra of each species of interest. The magnitude of MDAF values derived for each photolysis reaction was found to be driven more by the capacity to photodissociate at longer wavelengths in the action spectra, than any absorptions in the UVB region. As such, using an $O(^1D)$-MDAF reference adjustment factor resulted in less overall error than an NO_2-MDAF, except for species which photodissociate considerably at wavelengths longer than 350 nm. However, even adjusting

the cloud free j-values using an NO_2-MDAF reference yielded j-values for all 12 reactions which are considered to be within a factor of 2 of those measured, which may be acceptable for larger-scale models.

This work has demonstrated the advantage of having available long-term radiometer measurements of photolysis rate constants. 4-π sr optical inlets would be most appropriate for local high-detail measurements, or where surface albedo is regularly high, while spectral radiometer measurements would be most appropriate for long-term deployment where more general model validation or adjustment is required to account for local conditions. If the existing long-term measurements could be standardised and archived for use, it would consequently have immense value in supporting atmospheric chemistry measurement and modelling. Such measurements of j-values could be used directly within models to constrain the relevant j-values, or derive a metric like MDAF to scale modelled j-values to account for local conditions, without requiring computationally intensive approaches to estimate them accurately.

An iodide chemical ionisation mass spectrometer (CIMS) was used to attempt to quantify the interference of dinitrogen pentoxide (N_2O_5) hydrolysis in nitric acid (HNO_3) measurements made by the Monitor for AeRosols and GAses (MARGA, Metrohm, NL) stationed at Auchencorth Moss. Methods were also developed for the CIMS in an attempt to capture additional measurements of other NO_y species at the site during the same deployment (e.g. peroxyacetyl nitrate, PAN, $CH_3C(O)O_2NO_2$ and nitryl chloride, $ClNO_2$). The concentrations were expected to be low in this rural environment and the preliminary results showed that this was indeed the case, with concentrations below the instrument's present LOD. As a result, no conclusion could be made on the potential interference of NO_y species in the reported concentrations of HNO_3 from the MARGA.

6.2 Implications and limitations

6.2.1 Trace gas concentrations

Long-term measurements of trace gases are particularly important in assessing changes in atmospheric composition and local air quality at a given site and for the wider area represented by that site. Long-term data provides a wealth of information which can be used to validate model predictions, to develop and evaluate mitigation strategies and to track the response of atmospheric composition to implemented policy changes or to other influences, e.g. climate change (Tørseth et al., 2012; Pope & Wu, 2014). The extended duration of these time series are particularly important for disentangling trends in pollutant concentrations from interannual variation.

Studies using meteorological normalisation take this a step further, by "removing" the potential time (season, day-of-week, hour etc) and meteorological influences (temperature, relative humidity, etc) on pollutant concentrations, to examine trends in atmospheric composition at individual sites associated with policy changes (Grange & Carslaw, 2019; Vu et al., 2019). This study demonstrates the successful application of this technique to assess a site relocation on a time series, which may need to be more frequently undertaken in the future where nearby development may necessitate the relocation of, or land-use change near, current rural background sites (e.g. Latif et al., 2014). With regards to the Chilbolton Observatory, this analysis highlights the disruption in the long-term time series of NH_3 due to the proximity of nearby farmland and stronger influences of more distant NO_x sources (Donnelly et al., 2011). These step changes need to be considered in future analysis, such as regional long-term trends in pollutant concentrations (e.g. across the EMEP network), which require the rural background sites to be representative of the wider area in which they are located, and not directly influenced by a local source.

Measurements of pollutant concentrations should be accurate and free of interferences,

or use a quantified correction. Within a monitoring network, this means that measurements are required to be made using a standardised methodology. The MARGA is an established measurement at Auchencorth Moss, and has been measuring gaseous HNO_3 at the site for over a decade. MARGA measurements of HNO_3 have been demonstrated to have nocturnal interferences from N_2O_5 (Phillips et al., 2013a), while low-cost denuder alternatives require correction factors for numerous NO_y species (DELTAs; Tang et al., 2018b). A study using a similar set-up to Auchencorth Moss reported that HNO_3 was around 50% less than a standard filter method for sampling HNO_3 (Makkonen et al., 2014), though both methods are known to suffer from artefacts.

Nitryl chloride measurements have been made sporadically across the south of the UK (Bannan et al., 2015; Priestley et al., 2018; Sommariva et al., 2018), and this PhD research aimed to contribute measurements from a north UK site at Auchencorth Moss, and to assess its importance with respect to local chemistry.

Unfortunately, this study was not completed due to substantial time constraints and challenges in the operational performance of the instrument. Little time was available prior to and following the deployment of the CIMS with the inlet switching system at Auchencorth Moss, due to its deployment overseas, a 6-month internship, and then Covid-19 restrictions (around 12 months). Access to the laboratory and the opportunity for collaborative work was severely limited. Overall, the inlet switching system used for multi-species quantification in the CIMS did not perform as anticipated, due to the difference in ion-molecule region (IMR) pressure and long periods of intermittent noise during the field study. Laboratory calibration was semi-successful for HNO_3, but yielded an incompatible conversion factor (from counts s^{-1} to $\mu g\, m^{-3}$) and did not reach expected concentrations at Auchencorth Moss (over 10 times larger). For PAN, the calibration was inconclusive due to unsuccessful quantification of the background signal, or potential interferences from acetone or peroxyacetic acid (PAA).

6.2.2 Actinic flux and *j*-values

The research presented in this thesis can improve the accuracy of atmospheric chemistry and air quality models in two main areas:

1) Models estimating *j*-values

Models used for UK policy development, such as the ADMS model, feature an approximated photochemistry scheme, including only $j(NO_2)$ in the two-step photostationary state reactions (photolysis of NO_2 and oxidation of NO by O_3; Environment Agency, 2007). In this case, $j(NO_2)$ is determined from solar radiation (in $W\,m^{-2}$), calculated by a meteorology input module considering solar elevation (via latitude, time-of-day and day-of-year) and cloud amount (in oktas, default = 5 oktas) at nearest grid point (CERC, 2017a,b).

Many studies utilise chemistry mechanisms like the Master Chemical to determine *j*-values. These are calculated as a function of solar zenith angle (SZA) using a parameterisation derived for each species of interest (Saunders et al., 2003; Sommariva et al., 2020). The parameterisations are created by optimising the generic parameterisation to fit a clear-sky estimate from a two-stream isotropic scattering model (Jenkin et al., 1997), which calculates *j*-values using molecule-specific parameters (absorption cross section and quantum yield).

In these cases, the presented measurement driven adjustment factor (MDAF) would be a suitable way to quickly and easily scale *j*-values to account for local meteorology, and adjust chemical mechanisms (e.g. within a box model) for these conditions. Using UK based sites it was demonstrate that adjustment factors derived for $j(NO_2)$ (NO_2-MDAF) decrease the clear-sky estimates of $j(NO_2)$ by an average of 45-51%. Where upwelling measurements were also considered, NO_2-MDAF values agreed within <6% of those accounting for only downwelling. However when surface albedo increased due to snow cover, this value reduced by 36%, meaning the clear-sky estimates of $j(NO_2)$

decreased by approximately 9-15% on these occasions. For photolysis reactions which occur at shorter wavelengths (i.e. do not photodissociate at wavelengths >350 nm), the adjustment factors did not decrease j-values by as much ($j(O^1D)$ decreased 20% when a $O(^1D)$-MDAF was applied).

This work emphasised the importance in the choice of reference species for MDAF derivation, suggesting specific MDAF values should be used for each photolysis reaction. However, as this is not usually possible, NO_2-MDAF and $O(^1D)$-MDAF values were assessed as reference adjustment factors. Use of $O(^1D)$-MDAF to adjust all j-values resulted in less overall error for the reactions considered, but it was recognised that $j(O^1D)$ measurements require more data processing to account for SZA and ozone column depth, so may not be practical. Measurements of $j(NO_2)$ are more straightforward, and the resulting NO_2-MDAF values were best for species which photodissociate at wavelengths >350 nm, but were within a factor of 2 for all photolysis reactions considered, which could still be within acceptable error for coarser-scale models.

2) Approximating the local meteorology, particularly clouds

Validation of atmospheric chemistry and air quality models often exclude or simplify estimations of meteorological variables (e.g. cloud cover and aerosols) which influence photochemistry. There is little systematic validation of modelled j-values in cloudy conditions beyond initial conception or single site, in comparison to frequent validations of modelled trace gas concentrations against measurements.

Often chemical mechanisms (e.g. the Master Chemical Mechanism, MCM; Regional Atmospheric Chemistry Mechanism, RACM; and the Regional Acid Deposition Model chemical mechanism) pre-calculate j-values for clear skies, and ignore the presence of clouds. These calculations are approximated: MCM determines j-values as a function of SZA, while RADM and RACM create a look-up table based on evenly spaced increments in latitude, altitude and time which can be interpolated. Following this, the

approximated clear-sky j-values can be adjusted using a metric like MDAF based on local measured j-values, or the model defined cloud cover (e.g. in CMAQ; Roselle et al., 1999).

Model definitions of cloud cover can be highly variable due to the computational cost of accurately capturing these changeable conditions. The EMEP model, like many, creates an average cloud fraction over each layer, where cloud particles are evenly distributed through the layer and properties are uniform (Simpson et al., 2012). The j-values are calculated and compiled into look-up tables (of 10° latitude and 1° SZA resolution at each model height), for 3 separate conditions: clear sky, light cloud and dense cloud. The model then interpolates between these according to the cloudiness (as a percentage) of the meteorological input data. This is typical of atmospheric chemical transport models (CTMs), which construct meteorological conditions with highly variable columns but much more homogeneous horizontal layers within each grid box (Stamnes et al., 1988; Wild et al., 2000; Prather, 2015). These are not a reflection of the spatio-temporal variability of clouds, particularly in north-west Europe.

The horizontal variability can be improved by sub-grid estimations with fractionally cloudy atmospheres; however in these cases knowledge of cloud overlap is required. To do this, the horizontal layer within a grid box can be subdivided into independent column atmospheres (ICAs) that describe the cloud environment of that sub-grid column. However, this can quickly increase the number of radiative transfer calculations and become too costly to compute (Feng et al., 2004). The Fast-J algorithm reduces this cost in CTMs (Wild et al., 2000), but is still limited by assuming average conditions within each grid box. A quadrature method using Fast-JX expands on this (Neu et al., 2007) and considers the sub-grid distribution of clouds, and is used by the Met Office's Unified Model (MetUM) UKCA module (Telford et al., 2013; O'Connor et al., 2014).

Chapters 3 and 4 discuss a measurement-based alternative, examined at 4 distinct UK

sites, to account for local cloud conditions using ground-based radiometer measurements. As discussed above, the magnitude of the adjustment of clear-sky modelled j-values was subject to the location of measurements at high time resolution, the photolysis reaction and direction considered (downwelling-only, or including upwelling) when deriving MDAF values. Application of an MDAF metric would negate the requirement for such intensive cloud approximations when calculating photolysis rate constants. Furthermore, it would be invaluable to have accessible standardised measurements of photolysis rate constants or actinic flux, as proposed by this PhD study (Section 6.3), for more frequent verification of these model estimates.

Limitations

The main limitations for these Chapters are the lack of standardisation between UK measurements used in Chapter 3, either by a field intercomparison (such as the calibration of the 4-π filter radiometer at Auchencorth Moss in Chapter 3; AU-FR), or against traceable laboratory standards. This was a consequence of individual organisation's ownership of data and maintenance of the instrument collecting it. This also meant that the 2-π filter radiometer at Cardington (CA-FR; Chapter 3) could not be verified, despite the larger observed $j(NO_2)$ compared to Auchencorth Moss and Manchester.

6.3 Future work

Overcoming CIMS study limitations

Initially, future work for the CIMS study (Chapter 5) would be to try to resolve the issues encountered prior to, and during, the deployment at Auchencorth Moss. This includes re-evaluating the inlet switching mechanism with the aims of reducing the inlet residence time of the sample gas to limit interaction with inlet walls, by shortening the total length of the inlet, and stabilising the inlet and ion molecule region (IMR) pressure through alternations between the heated and unheated inlets. The suggestion

for the latter would be to use a 3-way solenoid valve to divert flow from the manifold, rather than the two 2-way solenoid valves that were used, which stop and resume the flow through each inlet every 30 minutes. To resolve the issue of intermittent noise, identified as the triggering of precautionary safety mechanisms which switch off the detector, the pressure sensor used in the mass spectrometer region of the CIMS should be replaced.

The background concentrations of PAN require further characterisation, which requires comparable conditions between the heated and unheated samples. If this is achieved by the use of a 3-way solenoid valve, the signal (at *m/z* 59) measured using the unheated inlet can be subtracted from that using the heated inlet to estimate the signal from PAN. Furthermore, a zero can be measured in the laboratory by using a heated stainless-steel line filled with steel wool to remove both PAN and PAA.

The calibration of $ClNO_2$ and N_2O_5 should be completed as described in Section 5.2.3 for the expected concentrations at Auchencorth Moss, as well as determining the CIMS limit of detection (LOD) for these species. Work is required to lower the detection limit of this system for $ClNO_2$, N_2O_5 and HNO_3. For the former, it is evidenced in Chapter 5 that no $ClNO_2$ nor N_2O_5 were measured during the field study as the signals at the respective masses (*m/z* 208 and 235) were not visible above the background noise in this system. For HNO_3, the LOD was calculated to be $5\,\mu g\,m^{-3}$ at an IMR pressure lower than that measured during the field study. This needs to be reassessed at a comparable IMR pressure, and likely lowered to measure the concentrations expected at Auchencorth Moss ($<2\,\mu g\,m^{-3}$).

If successful, the culmination of this work would be a future deployment of the CIMS at Auchencorth Moss with the same original aims of multi-species quantification in a rural background atmosphere, and individual targets of quantifying the potential interference from N_2O_5 in measurements of HNO_3 by MARGA at this site, and providing the first measurements of $ClNO_2$ at the site.

Model parameterisation of photochemistry and the impact of applying the MDAF approach

Within Chapter 4 only $p(\mathrm{OH})_{\mathrm{O_3}}$ was estimated at Chilbolton Observatory to illustrate the impact of NO_2-MDAF and O(^{1}D)-MDAF derivations on subsequent calculations. Further study would implement these measurements into a local high-resolution model, to quantify the extent to which this impacts predicted pollutant concentrations, particularly those of photolytic interest (e.g. O_3, HO_x radicals and NO_2). Ideally this should be examined for a range of widely used models (e.g. EMEP, CMAQ, and ADMS) and chemical mechanisms (e.g. MCM, RACM, RADM) to identify where it has the greatest influence, and would therefore be most useful. Investigations could include a similar analysis as Sections 4.3.3 and 4.3.3, to evaluate the impact of MDAF values derived for reference species that have previously been utilised (e.g. Sörgel et al., 2011; Elshorbany et al., 2012; Xue et al., 2020 and Lew et al., 2020), compared to reaction-specific MDAF values. Assessments of the use of MDAF compared to different cloud estimation methods in terms of model outputs and computational cost would be equally valuable. This would be critical to investigating where modelled pollutant concentrations could be improved, particularly where models support policy-makers in formulating mitigation actions, and provide further evidence to highlight the importance of validating photolysis rate constants.

Radiometer data accessibility and availability

Existing measurements of *j*-values, either by filter or spectral radiometer, are confined to specific studies or campaigns. Some exist as long-term deployments, already integrated into existing suites of measurements maintained by local field teams (e.g. Auchencorth Moss, Manchester Air Quality Supersite and Cardington in Chapter 3, as well as at least 4 across the European Research Infrastructure for the observation of Aerosol, Clouds and Trace Gases (ACTRIS, www.actris.eu). However, these measure-

ments are not formally compared, nor methodology standardised, nor data made readily available for use.

Creating a standardised network of existing radiometer measurements would be beneficial for implementing the ideas from this research. Available radiometer measurements could be used for model validation more regularly, both across the spatial extent of a model domain, and with respect to time. Implementation of these measurements in metrics like MDAF can be used to streamline processes to accurately account for conditions at a local site at a high time resolution, and circumvent the need for computationally intensive modelling of highly variable local meteorological conditions (e.g. cloud cover and aerosols). These measures will lead to more accurate modelling of photolysis rate constants, and consequently could lead to improved predictions of pollutant concentrations. This can help to improve our understanding of the role of local photochemistry, which in turn provides improvements in policy-based assessments of public health and environmental risks.

Future deployment of radiometers in a network should be incorporated into already established sites as another co-located measurement. This would be recommended for sites where measurements are already used to validate modelled pollutant concentrations, for logistical reasons (e.g. cost, access, site management) and to provide a more complete view of the local atmosphere. It would be beneficial to investigate urban locations, where physical features such as the urban topography and range of surface albedos of nearby materials could significantly influence actinic flux at the site. Such measurements would be less applicable for a wider area, due to the inhomogeneity in environment (e.g. either side of the same street). Urban radiometer measurements could also be used to assess the influence of photolysis on roadside profiles of NO_2, and ascertain whether measurements of NO_2 at a specific roadside site (1-5 m from the kerb) are significantly influenced by photolysis, particularly in air quality management areas where reported concentrations are critical. Where roadside measurements

are used in quantifying public exposure to air pollution, specific local measurements like this would reduce uncertainty in model estimates that arise from estimated local conditions, by using measurements representative of that site.

References

Aas, W., Tsyro, S., Bieber, E., Bergström, R., Ceburnis, D., Ellermann, T., Fagerli, H., Frölich, M., Gehrig, R., Spindler, G., Vana, M., & Yttri, K. E. (2012). Lessons learnt from the first EMEP intensive measurement periods. *Atmos. Chem. Phys.*, 12, 8073–8094.

Abdalmogith, S. S. & Harrison, R. M. (2006). An analysis of spatial and temporal properties of daily sulfate, nitrate and chloride concentrations at UK urban and rural sites. *J. Environ. Monit.*, 8(7), 691–699.

Acker, K. & Möller, D. (2007). Atmospheric variation of nitrous acid at different sites in Europe. *Environ. Chem.*, 4(4), 242–255.

Ahern, A. T., Goldberger, L., Jahl, L., Thornton, J., & Sullivan, R. C. (2018). Production of N_2O_5 and $ClNO_2$ through Nocturnal Processing of Biomass-Burning Aerosol. *Environ. Sci. Technol.*, 52, 550–559.

Alam, M. S., Crilley, L. R., Lee, J. D., Kramer, L. J., Pfrang, C., Vázquez-Moreno, M., Ródenas, M., Muñoz, A., & Bloss, W. J. (2020). Interference from alkenes in chemiluminescent NO_x measurements. *Atmos. Meas. Tech.*, 13, 5977–5991.

Alicke, B., Geyer, A., Hofzumahaus, A., Holland, F., Konrad, S., Pätz, H. W., Schäfer, J., Stutz, J., Volz-Thomas, A., & Platt, U. (2003). OH formation by HONO photolysis during the BERLIOZ experiment. *J. Geophys. Res.*, 108, 8247.

AQEG (2004). *Nitrogen Dioxide in the United Kingdom*. Technical report, available at: https://uk-air.defra.gov.uk/assets/documents/reports/aqeg/nd-summary.pdf.

AQEG (2009). *Ozone in the United Kingdom*. Technical report, available at: https://uk-air.defra.gov.uk/assets/documents/reports/aqeg/aqeg-ozone-report.pdf.

AQEG (2015). *Evidential Value of Defra Air Quality Compliance Monitoring*. Technical report, available at: https://uk-air.defra.gov.uk/assets/documents/reports/cat11/1509290925_DEF-PB14312_Evidential_value_of_Defra_air_quality_compliance_monitoring.pdf.

Atkinson, R., Baulch, D. L., Cox, R. A., Crowley, J. N., Hampson, R. F., Hynes, R. G., Jenkin, M. E., Rossi, M. J., & Troe, J. (2004). Evaluated kinetic and photochemical data for atmospheric chemistry: Volume I - gas phase reactions of O_x, HO_x, NO_x and SO_x species. *Atmos. Chem. Phys.*, 4(6), 1461–1738.

Atkinson, R., Baulch, D. L., Cox, R. A., Crowley, J. N., Hampson, R. F., Hynes, R. G., Jenkin, M. E., Rossi, M. J., & Troe, J. (2007). Evaluated kinetic and photochemical data for atmospheric chemistry: Volume III - gas phase reactions of inorganic halogens. *Atmos. Chem. Phys.*, 7, 981–1191.

Ayers, J. D. & Simpson, W. R. (2006). Measurements of N_2O_5 near Fairbanks, Alaska. *J. Geophys. Res.: Atmos.*, 111(14), D14309.

Bahe, F. C., Schurath, U., & Becker, K. H. (1980). The frequency of NO_2 photolysis at ground level, as recorded by a continuous actinometer. *Atmos. Environ.*, 14, 711–718.

Bais, A. F., Madronich, S., Crawford, J., Hall, S. R., Mayer, B., van Weele, M., Lenoble, J., Calvert, J. G., Cantrell, C. A., Shetter, R. E., Hofzumahaus, A., Koepke, P., Monks, P. S., Frost, G., McKenzie, R., Krotkov, N., Kylling, A., Swartz, W. H., Lloyd, S., Pfister, G., Martin, T. J., Roeth, E.-P., Griffioen, E., Ruggaber, A., Krol,

M., Kraus, A., Edwards, G. D., Mueller, M., Lefer, B. L., Johnston, P., Schwander, H., Flittner, D., Gardiner, B. G., Barrick, J., & Schmitt, R. (2003). International Photolysis Frequency Measurement and Model Intercomparison (IPMMI): Spectral actinic solar flux measurements and modeling. *J. Geophys. Res.: Atmos.*, 108, 8543.

Balis, D. S., Zerefos, C. S., Kourtidis, K., Bais, A. F., Hofzumahaus, A., Kraus, A., Schmitt, R., Blumthaler, M., & Gobbi, G. P. (2002). Measurements and modeling of photolysis rates during the Photochemical Activity and Ultraviolet Radiation (PAUR) II campaign. *J. Geophys. Res.: Atmos.*, 107(D18), 8138.

Bannan, T. J., Bacak, A., Le Breton, M., Flynn, M., Ouyang, B., McLeod, M., Jones, R., Malkin, T. L., Whalley, L. K., Heard, D. E., Bandy, B., Khan, M. A. H., Shallcross, D. E., & Percival, C. J. (2017). Ground and Airborne U.K. Measurements of Nitryl Chloride: An Investigation of the Role of Cl Atom Oxidation at Weybourne Atmospheric Observatory. *J. Geophys. Res.: Atmos.*, 122, 11,154–11,165.

Bannan, T. J., Booth, A. M., Bacak, A., Muller, J. B. A., Leather, K. E., Le Breton, M., Jones, B., Young, D., Coe, H., Allan, J., Visser, S., Slowik, J. G., Furger, M., Prévôt, A. S. H., Lee, J., Dunmore, R. E., Hopkins, J. R., Hamilton, J. F., Lewis, A. C., Whalley, L. K., Sharp, T., Stone, D., Heard, D. E., Fleming, Z. L., Leigh, R., Shallcross, D. E., & Percival, C. J. (2015). The first UK measurements of nitryl chloride using a chemical ionization mass spectrometer in central London in the summer of 2012, and an investigation of the role of Cl atom oxidation. *J. Geophys. Res.: Atmos.*, 120(11), 5638–5657.

Bannan, T. J., Khan, M. A. H., Le Breton, M., Priestley, M., Worrall, S. D., Bacak, A., Marsden, N. A., Lowe, D., Pitt, J., Allen, G., Topping, D., Coe, H., McFiggans, G., Shallcross, D. E., & Percival, C. J. (2019). A Large Source of Atomic Chlorine From $ClNO_2$ Photolysis at a U.K. Landfill Site. *Geophys. Res. Lett.*, 46(14), 8508–8516.

Barnard, J. C., Chapman, E. G., Fast, J. D., Schmelzer, J. R., Slusser, J. R., & Shetter,

R. E. (2004). An evaluation of the FAST-J photolysis algorithm for predicting nitrogen dioxide photolysis rates under clear and cloudy sky conditions. *Atmos. Environ.*, 38, 3393–3403.

Beirle, S., Boersma, K. F., Platt, U., Lawrence, M. G., & Wagner, T. (2011). Megacity Emissions and Lifetimes of Nitrogen Oxides Probed from Space. *Science*, 333, 1737–1739.

Benton, A. K., Langridge, J. M., Ball, S. M., Bloss, W. J., Dall 'osto, M., Nemitz, E., Harrison, R. M., & Jones, R. L. (2010). Night-time chemistry above London: measurements of NO_3 and N_2O_5 from the BT Tower. *Atmos. Chem. Phys.*, 10, 9781–9795.

Bernard, F., Cazaunau, M., Grosselin, B., Zhou, B., Zheng, J., Liang, P., Zhang, Y., Ye, X., Daële, V., Mu, Y., Zhang, R., Chen, J., & Mellouki, A. (2016). Measurements of nitrous acid (HONO) in urban area of Shanghai, China. *Environ. Sci. Pollut. Res.*, 23(6), 5818–5829.

Bertram, T. H., Thornton, J. A., & Riedel, T. P. (2009). An experimental technique for the direct measurement of N_2O_5 reactivity on ambient particles. *Atmos. Meas. Tech.*, 2, 231–242.

Bohn, B., Corlett, G. K., Gillmann, M., Sanghavi, S., Stange, G., Tensing, E., Vrekoussis, M., Bloss, W. J., Clapp, L. J., Kortner, M., Dorn, H.-P., Monks, P. S., Platt, U., Plass-Dülmer, C., Mihalopoulos, N., Heard, D. E., Clemitshaw, K. C., Meixner, F. X., Prevot, A. S. H., & Schmitt, R. (2008). Photolysis frequency measurement techniques: Results of a comparison within the ACCENT project. *Atmos. Chem. Phys.*, 8, 5373–5391.

Bohn, B., Heard, D. E., Mihalopoulos, N., Plass-Dülmer, C., Schmitt, R., & Whalley, L. K. (2016). Characterisation and improvement of $j(O^1D)$ filter radiometers. *Atmos. Meas. Tech.*, 9, 3455–3466.

Bohn, B., Kraus, A., Müller, M., & Hofzumahaus, A. (2004). Measurement of atmospheric $O_3 \longrightarrow O(^1D)$ photolysis frequencies using filterradiometry. *J. Geophys. Res.: Atmos.*, 109, D10S90.

Bohn, B., Rohrer, F., Brauers, T., & Wahner, A. (2005). Actinometric measurements of NO_2 photolysis frequencies in the atmosphere simulation chamber SAPHIR. *Atmos. Chem. Phys.*, 5, 493–503.

Bohnenstengel, S. I., Belcher, S. E., Aiken, A., Allan, J. D., Allen, G., Bacak, A., Bannan, T. J., Barlow, J. F., Beddows, D. C. S., Bloss, W. J., Booth, A. M., Chemel, C., Coceal, O., Di Marco, C. F., Dubey, M. K., Faloon, K. H., Flemiming, Z. L., Furger, M., Gietl, J. K., Graves, R. R., Green, D. C., Grimmond, C. S. B., Halios, C. H., Hamilton, J. F., Harrison, R. M., Heal, M. R., Heard, D. E., Helfter, C., Herndon, S. C., Holmes, R. E., Hopkins, J. R., Jones, A. M., Kelly, F. J., Kotthaus, S., Langford, B., Lee, J. D., Leigh, R. J., Lewis, A. C., Lidster, R. T., Lopez-Hilfiker, F. D., McQuaid, J. B., Mohr, C., Monks, P. S., Nemitz, E., Ng, N. L., Percival, C. J., Prévôt, A. S. H., Ricketts, H. M. A., Sokhi, R., Stone, D., Thornton, J. A., Tremper, A. H., Valach, A. C., Visser, S., Whalley, L. K., Williams, L. R., Xu, L., Young, D. E., & Zotter, P. (2015). Meteorology, air quality, and health in London: The ClearfLo project. *Bull. Am. Meteorol. Soc.*, 96, 779–804.

Bongartz, A., Kames, J., & Schurath, U. (1994). Experimental Determination of HONO Mass Accommodation Coefficients Using Two Different Techniques. *J. Atmos. Chem.*, 18, 149–169.

Bongartz, A., Kames, J., Welter, F., & Schurath, U. (1991). Near-UV Absorption Cross Sections and Trans/Cis Equilibrium of Nitrous Acid. *J. Phys. Chem.*, 95, 1076–1082.

Brown, S. & Stutz, J. (2012). Nighttime radical observations and chemistry. *Chem. Soc. Rev.*, 41(41), 6405–6447.

Brown, S. S., Dibb, J. E., Stark, H., Aldener, M., Vozella, M., Whitlow, S., Williams,

E. J., Lerner, B. M., Jakoubek, R., Middlebrook, A. M., DeGouw, J. A., Warneke, C., Goldan, P. D., Kuster, W. C., Angevine, W. M., Sueper, D. T., Quinn, P. K., Bates, T. S., Meagher, J. F., Fehsenfeld, F. C., & Ravishankara, A. R. (2004). Nighttime removal of NO_x in the summer marine boundary layer. *Geophys. Res. Lett.*, 31(7), 2–6.

Brown, S. S., Stark, H., & Ravishankara, A. R. (2003). Applicability of the steady state approximation to the interpretation of atmospheric observations of NO_3 and N_2O_5. *J. Geophys. Res.: Atmos.*, 108(D17), 4539–4547.

Brown, S. S., Thornton, J. A., Keene, W. C., Pszenny, A. A. P., Sive, B. C., Dubé, W. P., Wagner, N. L., Young, C. J., Riedel, T. P., Roberts, J. M., Vandenboer, T. C., Bahreini, R., Öztürk, F., Middlebrook, A. M., Kim, S., Hübler, G., & Wolfe, D. E. (2013). Nitrogen, Aerosol Composition, and Halogens on a Tall Tower (NACHTT): Overview of a wintertime air chemistry field study in the front range urban corridor of Colorado. *J. Geophys. Res.: Atmos.*, 118, 8067–8085.

Brunekreef, B. & Holgate, S. T. (2002). Air pollution and health. *Lancet*, 360, 1233–1242.

Burkholder, J. B., Abbatt, J. P. D., Cappa, C., Dibble, T. S., Kolb, C. E., Orkin, V. L., Wilmouth, D. M., Sander, S. P., Barker, J. R., Crounse, J. D., Huie, R. E., Kurylo, M. J., Percival, C. J., & Wine, P. H. (2019). Chemical Kinetics and Photochemical Data for Use in Atmospheric Studies, Evaluation Number 19. JPL Publication 19-5, Pasadena, CA.

Burkholder, J. B., Talukdar, R. K., & Ravishankara, A. R. (1994). Temperature dependence of the $ClONO_2$ UV absorption spectrum. *Geophys. Res. Lett.*, 21(7), 585–588.

Burkholder, J. B., Talukdar, R. K., Ravishankara, A. R., & Solomon, S. (1993). Temperature Dependence of the HNO_3 UV Absorption Cross Sections. *J. Geophys. Res.*, 98, 22937–22948.

Cantrell, C. A., Calvert, J. G., Bais, A., Shetter, R. E., Lefer, B. L., & Edwards, G. D. (2003). Overview and conclusions of the International Photolysis Frequency Measurement and Modeling Intercomparison (IPMMI) study. *J. Geophys. Res.: Atmos.*, 108(16).

Cape, J. N. (2009). *Operation of EMEP 'supersites' in the United Kingdom: Annual Report for 2007*. Technical report, available at: http://nora.nerc.ac.uk/id/eprint/8660/, Edinburgh, UK.

Carslaw, D. C. (2015). *deweather*: An R Package to Remove Meteorological Variation from Air Quality Data. available at: https://github.com/davidcarslaw/deweather.

Carslaw, D. C. (2017). *worldmet*: Import Surface Meteorological Data from NOAA Integrated Surface Database (ISD). available at: http://github.com/davidcarslaw/worldmet.

Carslaw, D. C. & Ropkins, K. (2012). Openair - An R package for air quality data analysis. *Environ. Modelling Softw.*, 27-28, 52–61.

Carslaw, D. C. & Taylor, P. J. (2009). Analysis of air pollution data at a mixed source location using boosted regression trees. *Atmos. Environ.*, 43(22-23), 3563–3570.

Caudill, T. R., Flittner, D. E., Herman, B. M., Torres, O., & McPeters, R. D. (1997). Evaluation of the pseudo-spherical approximation for backscattered ultraviolet radiances and ozone retrieval. *J. Geophys. Res.: Atmos.*, 102, 3881–3890.

CEDA (2021). Centre for Environmental Data Analysis: Chilbolton Atmospheric Observatory (CAO). available at: https://catalogue.ceda.ac.uk/uuid/0d60dd064b6449b09f5c7fd4c41bd693.

CERC (2017a). Cambridge Environmental Research Consultants, Technical specifications: NO_x Chemistry Model in ADMS 5 (P18/02J/17). available at: https://www.

cerc.co.uk/environmental-software/assets/data/doc_techspec/P18_02.pdf, last accessed: 20 May 2021.

CERC (2017b). Cambridge Environmental Research Consultants, Technical specifications: The Met Input Module (P05/01S/17). available at: http://www.cerc.co.uk/environmental-software/assets/data/doc_techspec/P05_01S.pdf, last accessed: 20 May 2021.

CFARR (2003). Science and Technology Facilities Council; Chilbolton Facility for Atmospheric and Radio Research; Natural Environment Research Council; Wrench, C.L.: Chilbolton Facility for Atmospheric and Radio Research; Meteorological Sensor Data, Chilbolton Site. available at: http://catalogue.ceda.ac.uk/uuid/45b25a7c531563f4422afcaeea0f07a7, last accessed: 27 February 2018.

Chen, C.-H., Chen, T.-F., Huang, S.-P., & Chang, K.-H. (2021). Comparison of the RADM2 and RACM chemical mechanisms in O_3 simulations: effect of the photolysis rate constant. *Sci. Rep.*, 11, 5024.

Chen, J. & Hoek, G. (2020). Long-term exposure to PM and all-cause and cause-specific mortality: A systematic review and meta-analysis. *Environ. Int.*, 143.

Chen, Y., Wang, W., & Zhu, L. (2000). Wavelength-dependent photolysis of methylglyoxal in the 290-440 nm region. *J. Phys. Chem. A*, 104, 11126–11131.

Claeys, M., Graham, B., Vas, G., Wang, W., Vermeylen, R., Pashynska, V., Cafmeyer, J., Guyon, P., Andreae, M. O., Artaxo, P., & Maenhaut, W. (2004). Formation of Secondary Organic Aerosols Through Photooxidation of Isoprene. *Science*, 303, 1173–1176.

COMEAP (2018). *Associations of long-term average concentrations of nitrogen dioxide with mortality: A report by the Committee on the Medical Effects of Air Pollution*. Technical report, available at: https://assets.publishing.service.gov.

uk/government/uploads/system/uploads/attachment_data/file/734799/COMEAP_NO2_Report.pdf.

Coyle, M., Cape, J. N., Flechard, C., Fowler, D., Helfter, C., Jones, M., Kentisbeer, J., Leeson, S. R., Leith, I. D., Mullinger, N., Nemitz, E., Roberts, E., Simmons, I., Storeton-West, R., Twigg, M., & van Dijk, N. (2019). Meteorological measurements at Auchencorth Moss from 1995 to 2016. *Geosci. Data J.*, 6, 16–29.

Crowley, J. N., Pouvesle, N., Phillips, G. J., Axinte, R., Fischer, H., Petäjä, T., Nölscher, A., Williams, J., Hens, K., Harder, H., Martinez-Harder, M., Novelli, A., Kubistin, D., Bohn, B., & Lelieveld, J. (2018). Insights into HO_x and RO_x chemistry in the boreal forest via measurement of peroxyacetic acid, peroxyacetic nitric anhydride (PAN) and hydrogen peroxide. *Atmos. Chem. Phys.*, 18, 13457–13479.

Cyrys, J., Eeftens, M., Heinrich, J., Ampe, C., Armengaud, A., Beelen, R., Bellander, T., Beregszaszi, T., Birk, M., Cesaroni, G., Cirach, M., de Hoogh, K., De Nazelle, A., de Vocht, F., Declercq, C., Dėdelė, A., Dimakopoulou, K., Eriksen, K., Galassi, C., Graulevičienė, R., Grivas, G., Gruzieva, O., Hagenbjörk Gustafsson, A., Hoffmann, B., Iakovides, M., Ineichen, A., Krämer, U., Lanki, T., Lozano, P., Madsen, C., Meliefste, K., Modig, L., Mölter, A., Mosler, G., Nieuwenhuijsen, M., Nonnemacher, M., Oldenwening, M., Peters, A., Pontet, S., Probst-Hensch, N., Quass, U., Raaschou-Nielsen, O., Ranzi, A., Sugiri, D., Stephanou, E. G., Taimisto, P., Tsai, M.-Y., Vaskövi, É., Villani, S., Wang, M., Brunekreef, B., & Hoek, G. (2012). Variation of NO_2 and NO_x concentrations between and within 36 European study areas: Results from the ESCAPE study. *Atmos. Environ.*, 62, 374–390.

Dammers, E., Schaap, M., Haaima, M., Palm, M., Kruit, R. J. W., Volten, H., Hensen, A., Swart, D., & Erisman, J. W. (2017). Measuring atmospheric ammonia with remote sensing campaign: Part 1 - Characterisation of vertical ammonia concentration profile in the centre of The Netherlands. *Atmos. Environ.*, 169, 97–112.

Defra (2015). *Air Pollution in the UK 2014*. Technical report, available at: http://uk-air.defra.gov.uk/library/annualreport/viewonline?year=2014_issue_1.

Defra (2016). *Air Pollution in the UK 2015*. Technical report, available at: https://uk-air.defra.gov.uk/assets/documents/annualreport/air_pollution_uk_2015_issue_1.pdf.

Defra (2017). *Air Pollution in the UK 2016*. Technical report, available at: https://uk-air.defra.gov.uk/assets/documents/annualreport/air_pollution_uk_2016_issue_1.pdf.

Defra (2018a). Department for Environment Food and Rural Affairs - UK AIR: Site Information for Auchencorth Moss. available at: https://uk-air.defra.gov.uk/networks/site-info?site_id=ACTH, last accessed: 18 January 2018.

Defra (2018b). Department for Environment Food and Rural Affairs: Black Carbon Network. available at: https://uk-air.defra.gov.uk/networks/network-info?view=ukbsn, last accessed: 15 June 2018.

Defra (2018c). Department for Environment Food and Rural Affairs: Interactive Monitoring Networks Map. available at: https://uk-air.defra.gov.uk/interactive-map, last accessed: 15 June 2018.

Defra (2018). Department for Environment Food and Rural Affairs: UK-AIR Air Quality Library. available at: https://uk-air.defra.gov.uk/library/reports?section_id=13, last accessed: 18 January 2018.

Defra (2021a). Department for Environment, Food and Rural Affairs - UK AIR: Air Quality Management Areas (AQMAs). available at: https://uk-air.defra.gov.uk/aqma/, last accessed: 24 May 2021.

Defra (2021b). Department for Environment, Food and Rural Affairs - UK AIR: Data

Selector. available at: https://uk-air.defra.gov.uk/data/data_selector, last accessed: 15 April 2021.

Defra (2021c). Department for Environment, Food and Rural Affairs - UK AIR: Site Information for Chilbolton Observatory. available at: https://uk-air.defra.gov.uk/networks/site-info?site_id=CHBO, last accessed: 10 January 2021.

Defra (2021d). Department for Environment Food and Rural Affairs: Air modelling for Defra. available at: https://uk-air.defra.gov.uk/research/air-quality-modelling?view=modelling, last accessed: 29 May 2021.

Defra (2021e). Department for Environment Food and Rural Affairs: Automatic Urban and Rural Network (AURN). available at: https://uk-air.defra.gov.uk/networks/network-info?view=aurn, last accessed: 10 January 2021.

DeMore, W. B., Sander, S. P., Golden, D. M., Hampson, R. F., Kurylo, M. J., Howard, C. J., Ravishankara, A. R., Kolb, C. E., & Molina, M. J. (1997). Chemical Kinetics and Photochemical Data for Use in Stratospheric Modeling, Evaluation Number 12. JPL Publication 97-4, Pasadena, CA.

DeMore, W. B., Sander, S. P., Howard, C. J., Ravishankara, A. R., Golden, D. M., Kolb, C. E., Hampson, R. F., Kurylo, M. J., & Molina, M. J. (1994). Chemical Kinetics and Photochemical Data for Use in Stratospheric Modeling, Evaluation Number 11. JPL Publication 94-26, Pasadena, CA.

Dollard, G. J., Jones, B. M. R., & Davies, T. J. (1991). Measurements of gaseous hydrogen peroxide and PAN in rural southern England. *Atmos. Environ., Part A*, 25A(9), 2039–2053.

Donnelly, A., Misstear, B., & Broderick, B. (2011). Application of nonparametric regression methods to study the relationship between NO_2 concentrations and local wind direction and speed at background sites. *Sci. Total Environ.*, 409, 1134–1144.

Dusanter, S., Vimal, D., Stevens, P. S., Volkamer, R., Molina, L. T., Baker, A., Meinardi, S., Blake, D., Sheehy, P., Merten, A., Zhang, R., Zheng, J., Fortner, E. C., Junkermann, W., Dubey, M., Rahn, T., Eichinger, B., Lewandowski, P., Prueger, J., & Holder, H. (2009). Measurement of OH and HO_2 concentrations during MCMA-2006 field campaign - Part 2: Model comparison and radical budget. *Atmos. Chem. Phys.*, 9, 6655–6675.

Edwards, G. D. & Monks, P. S. (2003). Performance of a single-monochromator diode array spectroradiometer for the determination of actinic flux and atmospheric photolysis frequencies. *J. Geophys. Res.: Atmos.*, 108, 8546–8558.

Elith, J., Leathwick, J. R., & Hastie, T. (2008). A working guide to boosted regression trees. *J. of Anim. Ecol.*, 77(4), 802–813.

Elshorbany, Y. F., Kleffmann, J., Hofzumahaus, A., Kurtenbach, R., Wiesen, P., Brauers, T., Bohn, B., Dorn, H.-P., Fuchs, H., Holland, F., Rohrer, F., Tillmann, R., Wegener, R., Wahner, A., Kanaya, Y., Yoshino, A., Nishida, S., Kajii, Y., Martinez, M., Kubistin, D., Harder, H., Lelieveld, J., Elste, T., Plass-Dülmer, C., Stange, G., Berresheim, H., & Schurath, U. (2012). HO_x budgets during HOxComp: A case study of HO_x chemistry under NO_x-limited conditions. *J. Geophys. Res.: Atmos.*, 117, D03307.

Elshorbany, Y. F., Kurtenbach, R., Wiesen, P., Lissi, E., Rubio, M., Villena, G., Gramsch, E., Rickard, A. R., Pilling, M. J., & Kleffmann, J. (2009). Oxidation capacity of the city air of Santiago, Chile. *Atmos. Chem. Phys.*, 9, 2257–2273.

Elterman, L. (1968). *UV, visible, and IR attenuation for altitudes to 50 km. Air Force Cambridge Research Laboratories (AFCRL)*. Technical report, Cambridge, MA.

EMEP (2007). *Manual for Sampling and Chemical Analysis*. Technical report, Norwegian Institute for Air Research, Kjellar.

EMEP (2014). *Manual for Sampling and Chemical Analysis*. Technical report, available at: www.nilu.no/projects/ccc/manual/index.html, EMEP/CCC Report 1/2014.

EMEP (2020a). *Data Report 2018: Particulate matter, carbonaceous and inorganic compounds*. Technical report, available at: https://projects.nilu.no/ccc/reports/cccr1-2020_Data_report_2018.pdf, Kjeller, Norway, EMEP/CCC Report 1/2020.

EMEP (2020b). *Ozone measurements 2018*. Technical report, available at: https://projects.nilu.no/ccc/reports/cccr2-2020_Ozone.pdf, Kjeller, Norway, EMEP/CCC Report 2/2020.

EMEP MSC-W (2020). Open Source EMEP/MSC-W model rv4.36 (202011). available at: https://doi.org/10.5281/zenodo.4230110, last accessed: 2 June 2021.

Environment Agency (2007). *Review of methods for NO to NO_2 conversion in plumes at short ranges*. Technical report, Environment Agency, available at: https://assets.publishing.service.gov.uk/government/uploads/system/uploads/attachment_data/file/290985/scho0907bnhi-e-e.pdf.

European Council (2008). *Directive 2008/50/EC of the European Parliament and of the Council of 21 May 2008 on ambient air quality and cleaner air for Europe*. Brussels, Belgium.

EuroPhen (2020). European Phenology Camera Network. available at: http://european-webcam-network.net/, last accessed: 1 April 2020.

Fagerli, H. & Aas, W. (2008). Trends of nitrogen in air and precipitation: Model results and observations at EMEP sites in Europe, 1980-2003. *Environ. Pollut.*, 154, 448–461.

Feng, Y., Penner, J. E., Sillman, S., & Liu, X. (2004). Effects of cloud overlap in photochemical models. *J. Geophys. Res.: Atmos.*, 109, D04310.

Finlayson-Pitts, B. J., Ezell, M. J., & Pitts Jr, J. N. (1989). Formation of chemically active chlorine compounds by reactions of atmospheric NaCl particles with gaseous N_2O_5 and $ClONO_2$.

Finlayson-Pitts, B. J. & Pitts Jr., J. N. (1999). *Chemistry of the Upper and Lower Atmosphere: Theory, Experiments, and Applications*. Academic Press, San Diego, CA, USA.

Fischer, E. V., Jacob, D. J., Yantosca, R. M., Sulprizio, M. P., Millet, D. B., Mao, J., Paulot, F., Singh, H. B., Roiger, A., Ries, L., Talbot, R. W., Dzepina, K., & Pandey Deolal, S. (2014). Atmospheric peroxyacetyl nitrate (PAN): A global budget and source attribution. *Atmos. Chem. Phys.*, 14(5), 2679–2698.

Fischer, E. V., Jaffe, D. A., Reidmiller, D. R., & Jaeglé, L. (2010). Meteorological controls on observed peroxyacetyl nitrate at Mount Bachelor during the spring of 2008. *J. Geophys. Res.: Atmos.*, 115(3), 1–18.

Flechard, C. R. & Fowler, D. (1998). Atmospheric ammonia at a moorland site. I: The meteorological control of ambient ammonia concentrations and the influence of local sources. *Q. J. R. Meteorol. Soc.*, 124, 733–757.

Flemming, J., Stern, R., & Yamartino, R. J. (2005). A new air quality regime classification scheme for O_3, NO_2, SO_2 and PM_{10} observations sites. *Atmos. Environ.*, 39, 6121–6129.

Flocke, F. M., Weinheimer, A. J., Swanson, A. L., Roberts, J. M., Schmitt, R., & Shertz, S. (2005). On the measurement of PANs by gas chromatography and electron capture detection. *J. Atmos. Chem.*, 52(1), 19–43.

Friedman, J. H. (2002). Stochastic gradient boosting. *Comput. Stat. Data Anal.*, 38(4), 367–378.

Furgeson, A., Mielke, L. H., Paul, D., & Osthoff, H. D. (2011). A photochemical source of peroxypropionic and peroxyisobutanoic nitric anhydride. *Atmos. Environ.*, 45, 5025–5032.

Furlan, A., Haeberli, M. A., & Robert Huber, J. (2000). The 248 nm Photodissociation of $ClNO_2$ Studied by Photofragment Translational Energy Spectroscopy. *J. Phys. Chem. A*, 104, 10392–10397.

Galvin, J. F. P. & McGhee, J. (2005). Meteorology at Benson, Oxfordshire. *Weather*, 60, 319–325.

Gardner, E. P., Sperry, P. D., & Calvert, J. G. (1987). Primary Quantum Yields of NO_2 Photodissociation. *J. Geophys. Res.: Atmos.*, 92(D6), 6642–6652.

Gerasopoulos, E., Kazadzis, S., Vrekoussis, M., Kouvarakis, G., Liakakou, E., Kouremeti, N., Giannadaki, D., Kanakidou, M., Bohn, B., & Mihalopoulos, N. (2012). Factors affecting O_3 and NO_2 photolysis frequencies measured in the eastern Mediterranean during the five-year period 2002-2006. *J. Geophys. Res.: Atmos.*, 117(22), 1–14.

Gerboles, M., Lagler, F., Rembges, D., & Brun, C. (2003). Assessment of uncertainty of NO_2 measurements by the chemiluminescence method and discussion of the quality objective of the NO_2 European Directive. *J. Environ. Monit.*, 5, 529–540.

Ghosh, B., Papanastasiou, D. K., Talukdar, R. K., Roberts, J. M., & Burkholder, J. B. (2012). Nitryl Chloride ($ClNO_2$): UV/Vis Absorption Spectrum between 210 and 296 K and $O(^3P)$ Quantum Yield at 193 and 248 nm. *J. Phys. Chem. A*, 116(24), 5796–5805.

Ghosh, D. & Sarkar, U. (2016). Analysis of the photochemical production of ozone using Tropospheric Ultraviolet-Visible (TUV) Radiation Model in an Asian megacity. *Air Qual., Atmos. Health*, 9, 367–377.

Goliff, W. S., Stockwell, W. R., & Lawson, C. V. (2013). The regional atmospheric chemistry mechanism, version 2. *Atmos. Environ.*, 68, 174–185.

Google Earth (2021). Satellite imagery of the United Kingdom (2021). available at: https://earth.google.com/web, last accessed: 6 May 2021.

Govender, P. & Sivakumar, V. (2020). Application of k-means and hierarchical clustering techniques for analysis of air pollution: A review (1980–2019). *Atmos. Pollut. Res.*, 11, 40–56.

Grange, S. K. & Carslaw, D. C. (2019). Using meteorological normalisation to detect interventions in air quality time series. *Sci. Total Environ.*, 653, 578–588.

Grange, S. K., Carslaw, D. C., Lewis, A. C., Boleti, E., & Hueglin, C. (2018). Random forest meteorological normalisation models for Swiss PM_{10} trend analysis. *Atmos. Chem. Phys.*, 18, 6223–6239.

Hall, S. R., Ullmann, K., Prather, M. J., Flynn, C. M., Murray, L. T., Fiore, A. M., Correa, G., Strode, S. A., Steenrod, S. D., Lamarque, J.-F., Guth, J., Josse, B., Flemming, J., Huijnen, V., Abraham, N. L., & Archibald, A. T. (2018). Cloud impacts on photochemistry: building a climatology of photolysis rates from the Atmospheric Tomography mission. *Atmos. Chem. Phys.*, 18, 16809–16828.

Hanke, M., Umann, B., Uecker, J., Arnold, F., & Bunz, H. (2003). Atmospheric measurements of gas-phase HNO_3 and SO_2 using chemical ionization mass spectrometry during the MINATROC field campaign 2000 on Monte Cimone. *Atmos. Chem. Phys.*, 3(2), 417–436.

Harrison, R. M., Peak, J. D., & Collins, G. M. (1996). Tropospheric cycle of nitrous acid. *J. Geophys. Res.: Atmos.*, 101, 14429–14439.

Heard, D. (2006). *Analytical Techniques for Atmospheric Measurement*. Blackwell Publishing, Hoboken, NJ, USA.

Heard, D. E., Carpenter, L. J., Creasey, D. J., Hopkins, J. R., Lee, J. D., Lewis, A. C., Pilling, M. J., Seakins, P. W., Carslaw, N., & Emmerson, K. M. (2004). High levels of the hydroxyl radical in the winter urban troposphere. *J. Geophys. Res.: Atmos.*, 31, L18112.

Hofzumahaus, A., Kraus, A., Kylling, A., & Zerefos, C. S. (2002). Solar actinic radiation (280-420 nm) in the cloud-free troposphere between ground and 12 km altitude: Measurements and model results. *J. Geophys. Res.: Atmos.*, 107(D18).

Holland, F., Hofzumahaus, A., Schäfer, J., Kraus, A., & Pätz, H.-W. (2003). Measurements of OH and HO_2 radical concentrations and photolysis frequencies during BERLIOZ. *J. Geophys. Res.: Atmos.*, 108(D4), 8246.

Hollaway, M., Wild, O., Yang, T., Sun, Y., Xu, W., Xie, C., Whalley, L., Slater, E., Heard, D., & Liu, D. (2019). Photochemical impacts of haze pollution in an urban environment. *Atmos. Chem. Phys.*, 19, 9699–9714.

Horowitz, A. & Calvert, J. G. (1978). Wavelength dependence of the quantum efficiencies of the primary processes in formaldehyde photolysis at 25 °C. *Int. J. Chem. Kinet.*, 10(8), 805–819.

Horowitz, A. & Calvert, J. G. (1982). Wavelength dependence of the primary processes in acetaldehyde photolysis. *J. Phys. Chem.*, 86(16), 3105–3114.

Huey, L. G. (2007). Measurement of trace atmospheric species by chemical ionization mass spectrometry: speciation of reactive nitrogen and future directions. *Mass Spectrom. Rev.*, 26, 166–184.

Huey, L. G., Hanson, D. R., & Howard, C. J. (1995). Reactions of SF_6^- and I^- with Atmospheric Trace Gases. *J. Phys. Chem.*, 99, 5001–5008.

Huntingford, C., Marsh, T., Scaife, A. A., Kendon, E. J., Hannaford, J., Kay, A. L., Lockwood, M., Prudhomme, C., Reynard, N. S., Parry, S., Lowe, J. A., Screen, J. A.,

Ward, H. C., Roberts, M., Stott, P. A., Bell, V. A., Bailey, M., Jenkins, A., Legg, T., Otto, F. E., Massey, N., Schaller, N., Slingo, J., & Allen, M. R. (2014). Potential influences on the United Kingdom's floods of winter 2013/14. *Nat. Clim. Change*, 4, 769–777.

Illies, A. J. & Takacs, G. A. (1976). Gas phase ultra-violet photoabsorption cross-sections for nitrosyl chloride and nitryl chloride. *J. Photochem.*, 6, 35–42.

Iversen, T. (1993). Modelled and measured transboundary acidifying pollution in Europe - verification and trends. *Atmos. Environ.*, 27A(6), 889–920.

Jacob, D. J. (1999). *Introduction to Atmospheric Chemistry*. Princeton University Press, Princeton, NJ, USA.

Jacob, D. J. (2000). Heterogeneous chemistry and tropospheric ozone. *Atmos. Environ.*, 34, 2131–2159.

Jenkin, M. E., Saunders, S. M., & Pilling, M. J. (1997). The tropospheric degradation of volatile organic compounds: A protocol for mechanism development. *Atmos. Environ.*, 31(1), 81–104.

Jeong, D., Seco, R., Gu, D., Lee, Y., Nault, B. A., Knote, C. J., Mcgee, T., Sullivan, J. T., Jimenez, J. L., Campuzano-Jost, P., Blake, D. R., Sanchez, D., Guenther, A. B., Tanner, D., Huey, L. G., Long, R., Anderson, B. E., Hall, S. R., Ullmann, K., Shin, H.-j., Herndon, S. C., Lee, Y., Kim, D., Ahn, J., & Kim, S. (2019). Integration of airborne and ground observations of nitryl chloride in the Seoul metropolitan area and the implications on regional oxidation capacity during KORUS-AQ 2016. *Atmos. Chem. Phys.*, 19, 12,779–12,795.

Joly, M. & Peuch, V. H. (2012). Objective classification of air quality monitoring sites over Europe. *Atmos. Environ.*, 47, 111–123.

Jung, J., Lee, J., Kim, B., & Oh, S. (2017). Seasonal variations in the NO_2 artifact from chemiluminescence measurements with a molybdenum converter at a suburban site in Korea (downwind of the Asian continental outflow) during 2015–2016. *Atmos. Environ.*, 165, 290–300.

Junkermann, W., Platt, U., & Volz-Thomas, A. (1989). A photoelectric detector for the measurement of photolysis frequencies of ozone and other atmospheric molecules. *J. Atmos. Chem.*, 8, 203–227.

Kanaya, Y., Cao, R., Akimoto, H., Fukuda, M., Komazaki, Y., Yokouchi, Y., Koike, M., Tanimoto, H., Takegawa, N., & Kondo, Y. (2007). Urban photochemistry in central Tokyo: 1. Observed and modeled OH and HO_2 radical concentrations during the winter and summer of 2004. *J. Geophys. Res.: Atmos.*, 112, D21312.

Kanaya, Y., Kajii, Y., & Akimoto, H. (2003). Solar actinic flux and photolysis frequency determinations by radiometers and a radiative transfer model at Rishiri Island: comparisons, cloud effects, and detection of an aerosol plume from Russian forest fires. *Atmos. Environ.*, 37, 2463–2475.

Kenagy, H. S., Lin, C., Wu, H., & Heal, M. R. (2016). Greater nitrogen dioxide concentrations at child versus adult breathing heights close to urban main road kerbside. *Air Qual., Atmos. Health*, 9, 589–595.

Kercher, J. P., Riedel, T. P., & Thornton, J. A. (2009). Chlorine activation by N_2O_5: simultaneous, in situ detection of $ClNO_2$ and N_2O_5 by chemical ionization mass spectrometry. *Atmos. Meas. Tech.*, 2, 193–204.

Khan, A. H., Cooke, M. C., Utembe, S. R., Archibald, A. T., Derwent, R. G., Jenkin, M. E., Leather, K. E., Percival, C. J., & Shallcross, D. E. (2017). Global Budget and Distribution of Peroxyacetyl Nitrate (PAN) for Present and Preindustrial Scenarios. *Int. J. Earth Environ. Sci.*, 2, 130.

Kleffmann, J. (2005). Daytime formation of nitrous acid: A major source of OH radicals in a forest. *Geophys. Res. Lett.*, 32(5), L05818.

Kleffmann, J. (2007). Daytime sources of nitrous acid (HONO) in the atmospheric boundary layer. *ChemPhysChem*, 8, 1137–1144.

Kleffmann, J., Lozer, J. C., Wiesen, P., Kern, C., Trick, S., Volkamer, R., Rodenas, M., & Wirtz, K. (2006). Intercomparison of the DOAS and LOPAP techniques for the detection of nitrous acid (HONO). *Atmos. Environ.*, 40, 3640–3652.

Kracht, O., Santiago, J.-L., Martin, F., Piersanti, A., Cremona, G., Righini, G., Vitali, L., Delaney, K., Basu, B., Ghosh, B., Spangl, W., Brendle, C., Latikka, J., Kousa, A., Pärjälä, E., Meretoja, M., Malherbe, L., Letinois, L., Beauchamp, M., Lenartz, F., Hutsemekers, V., Nguyen, L., Hoogerbrugge, R., Eneroth, K., Silvergren, S., Hooybergs, H., Viaene, P., Maiheu, B., Janssen, S., Roet, D., & Gerboles, M. (2017). *Spatial representativeness of air quality monitoring sites: Outcomes of the FAIRMODE/AQUILA intercomparison exercise (EUR - Scientific and Technical Research Reports)*. Technical report, available at: https://publications.jrc.ec.europa.eu/repository/handle/JRC108791, Publications Office of the European Union.

Kramer, L. J., Crilley, L. R., Adams, T. J., Ball, S. M., Pope, F. D., & Bloss, W. J. (2020). Nitrous acid (HONO) emissions under real-world driving conditions from vehicles in a UK road tunnel. *Atmos. Chem. Phys.*, 20, 5231–5248.

Kraus, A. & Hofzumahaus, A. (1998). Field Measurements of Atmospheric Photolysis Frequencies for O_3, NO_2, HCHO, CH_3CHO, H_2O_2 and HONO by UV Spectroradiometry. *J. Atmos. Chem.*, 31, 161–180.

Kuhlbusch, T. A. J., Quincey, P., Fuller, G., Kelly, F., Mudway, I., Viana, M., Querol, X., Alastuey, A., Katsouyanni, K., Weijers, E., Borowiak, A., Gehrig, R., Hueglin, C., Bruckmann, P., Favez, O., Sciare, J., Hoffmann, B., EspenYttri, K., Tørseth, K.,

Sager, U., Asbach, C., & Quass, U. (2014). New Directions: The future of European urban air quality monitoring. *Atmos. Environ.*, 87, 258–260.

Kylling, A., Stamnes, K., & Tsay, S.-C. (1995). A Reliable and Efficient Two-Stream Algorithm for Spherical Radiative Transfer: Documentation of Accuracy in Realistic Layered Media. *J. Atmos. Chem.*, 21, 115–150.

Kylling, A., Webb, A. R., Bais, A. F., Blumthaler, M., Schmitt, R., Thiel, S., Kazantzidis, A., Kift, R., Misslbeck, M., Schallhart, B., Schreder, J., Topaloglou, C., Kazadzis, S., & Rimmer, J. (2003). Actinic flux determination from measurements of irradiance. *J. Geophys. Res.: Atmos.*, 108(D16), 4506–4516.

Ladd, D. & Rumi, E. (2021). NASA AERONET (AErosol RObotic NETwork): Chilbolton. available at: https://aeronet.gsfc.nasa.gov/cgi-bin/data_display_aod_v3?site=Chilbolton&nachal=2&level=3&place_code=10, last accessed: 20 March 2021.

LaFranchi, B. W., Wolfe, G. M., Thornton, J. A., Harrold, S. A., Browne, E. C., Min, K. E., Wooldridge, P. J., Gilman, J. B., Kuster, W. C., Goldan, P. D., de Gouw, J. A., McKay, M., Goldstein, A. H., Ren, X., Mao, J., & Cohen, R. C. (2009). Closing the peroxy acetyl nitrate budget: observations of acyl peroxy nitrates (PAN, PPN, and MPAN) during BEARPEX 2007. *Atmos. Chem. Phys.*, 9, 7623–7641.

Lantz, K. O., Shetter, R. E., Cantrell, C. A., Flocke, S. J., Calvert, J. G., & Madronich, S. (1996). Theoretical, actinometric, and radiometric determinations of the photolysis rate coefficient of NO_2 during the Mauna Loa Observatory Photochemistry Experiment 2. *J. Geophys. Res.: Atmos.*, 101, 14613–14629.

Larason, T. C. & Cromer, C. L. (2001). Sources of error in UV radiation measurements. *J. Res. Natl. Inst. Stand. Technol.*, 106(4), 649–656.

Latif, M. T., Dominick, D., Ahamad, F., Khan, M. F., Juneng, L., Hamzah, F. M., &

Nadzir, M. S. M. (2014). Long term assessment of air quality from a background station on the Malaysian Peninsula. *Sci. Total Environ.*, 482-483, 336–348.

Le Breton, M., Bacak, A., Muller, J. B. A., Bannan, T. J., Kennedy, O., Ouyang, B., Xiao, P., Ephane, S., Bauguitte, J.-B., Shallcross, D. E., Jones, R. L., Daniels, M. J. S., Ball, S. M., & Percival, C. J. (2014a). The first airborne comparison of N_2O_5 measurements over the UK using a CIMS and BBCEAS during the RONOCO campaign. *Anal. Methods*, 6, 9731–9743.

Le Breton, M., Bacak, A., Muller, J. B. A., Xiao, P., Shallcross, B. M. A., Batt, R., Cooke, M. C., Shallcross, D. E., Bauguitte, S. J.-B., & Percival, C. J. (2014b). Simultaneous airborne nitric acid and formic acid measurements using a chemical ionization mass spectrometer around the UK: Analysis of primary and secondary production pathways. *Atmos. Environ.*, 83, 166–175.

Le Breton, M., McGillen, M. R., Muller, J. B. A., Bacak, A., Shallcross, D. E., Xiao, P., Huey, L. G., Tanner, D., Coe, H., & Percival, C. J. (2012). Airborne observations of formic acid using a chemical ionization mass spectrometer. *Atmos. Meas. Tech.*, 5, 3029–3039.

Lee, B. H., Lopez-Hilfiker, F. D., Veres, P. R., McDuffie, E. E., Fibiger, D. L., Sparks, T. L., Ebben, C. J., Green, J. R., Schroder, J. C., Campuzano-Jost, P., Iyer, S., D'Ambro, E. L., Schobesberger, S., Brown, S. S., Wooldridge, P. J., Cohen, R. C., Fiddler, M. N., Bililign, S., Jimenez, J. L., Kurtén, T., Weinheimer, A. J., Jaegle, L., & Thornton, J. A. (2018). Flight Deployment of a High-Resolution Time-of-Flight Chemical Ionization Mass Spectrometer: Observations of Reactive Halogen and Nitrogen Oxide Species. *J. Geophys. Res.: Atmos.*, 123(14), 7670–7686.

Lee, J. D., Whalley, L. K., Heard, D. E., Stone, D., Dunmore, R. E., Hamilton, J. F., Young, D. E., Allan, J. D., Laufs, S., & Kleffmann, J. (2016). Detailed budget anal-

ysis of HONO in central London reveals a missing daytime source. *Atmos. Chem. Phys.*, 16, 2747–2764.

Lee-Taylor, J. & Madronich, S. (2002). Calculation of actinic fluxes with a coupled atmosphere-snow radiative transfer model. *J. Geophys. Res.: Atmos.*, 107(24).

Levy, H. (1972). Photochemistry of the lower troposphere. *Planet. Space Sci.*, 20, 919–935.

Lew, M. M., Rickly, P. S., Bottorff, B. P., Sklaveniti, S., Léonardis, T., Locoge, N., Dusanter, S., Kundu, S., Wood, E., & Stevens, P. S. (2020). OH and HO_2 radical chemistry in a midlatitude forest: Measurements and model comparisons. *Atmos. Chem. Phys.*, 20, 9209–9230.

Li, X., Brauers, T., Häseler, R., Bohn, B., Fuchs, H., Hofzumahaus, A., Holland, F., Lou, S., Lu, K. D., Rohrer, F., Hu, M., Zeng, L. M., Zhang, Y. H., Garland, R. M., Su, H., Nowak, A., Wiedensohler, A., Takegawa, N., Shao, M., & Wahner, A. (2012). Exploring the atmospheric chemistry of nitrous acid (HONO) at a rural site in Southern China. *Atmos. Chem. Phys.*, 12(3), 1497–1513.

Lin, W., Zhu, T., Song, Y., Zou, H., Tang, M., Tang, X., & Hu, J. (2008). Photolysis of surface O_3 and production potential of OH radicals in the atmosphere over the Tibetan Plateau. *J. Geophys. Res.: Atmos.*, 113, D02309.

Lu, K., Fuchs, H., Hofzumahaus, A., Tan, Z., Wang, H., Zhang, L., Schmitt, S. H., Rohrer, F., Bohn, B., Broch, S., Dong, H., Gkatzelis, G. I., Hohaus, T., Holland, F., Li, X., Liu, Y., Liu, Y., Ma, X., Novelli, A., Schlag, P., Shao, M., Wu, Y., Wu, Z., Zeng, L., Hu, M., Kiendler-Scharr, A., Wahner, A., & Zhang, Y. (2019). Fast Photochemistry in Wintertime Haze: Consequences for Pollution Mitigation Strategies. *Environ. Sci. Technol.*, 53, 10676–10684.

Madronich, S. (1987). Photodissociation in the Atmosphere: 1. Actinic Flux and the Effects of Ground Reflections and Clouds. *J. Geophys. Res.*, 92, 9740–9752.

Madronich, S. (1993). The Atmosphere and UV-B Radiation at Ground Level. In A. R. Young (Ed.), *Environmental UV Photobiology*. Plenum Press, New York, NY, USA.

Makar, P. A., Moran, M. D., Zheng, Q., Cousineau, S., Sassi, M., Duhamel, A., Besner, M., Davignon, D., Crevier, L.-P., & Bouchet, V. S. (2009). *Atmos. Chem. Phys.*, 9, 7183–7212.

Makkonen, U., Virkkula, A., Hellén, H., Hemmilä, M., Sund, J., Äijälä, M., Ehn, M., Junninen, H., Keronen, P., Petäjä, T., Worsnop, D., Kulmala, M., & Hakola, H. (2014). Semi-continuous gas and inorganic aerosol measurements at a boreal forest site: seasonal and diurnal cycles of NH_3, HONO and HNO_3. *Boreal Environ. Res.*, 19, 311–328.

Makkonen, U., Virkkula, A., Mäntykenttä, J., Hakola, H., Keronen, P., Vakkari, V., & Aalto, P. P. (2012). Semi-continuous gas and inorganic aerosol measurements at a Finnish urban site: Comparisons with filters, nitrogen in aerosol and gas phases, and aerosol acidity. *Atmos. Chem. Phys.*, 12, 5617–5631.

Malley, C. S., Braban, C. F., & Heal, M. R. (2014). The application of hierarchical cluster analysis and non-negative matrix factorization to European atmospheric monitoring site classification. *Atmos. Res.*, 138, 30–40.

Malley, C. S., Cape, J. N., Jones, M. R., Leeson, S. R., Coyle, M., Braban, C. F., Heal, M. R., & Twigg, M. M. (2016a). Regional and hemispheric influences on measured spring peroxyacetyl nitrate (PAN) mixing ratios at the Auchencorth UK EMEP supersite. *Atmos. Res.*, 174-175, 135–141.

Malley, C. S., Heal, M. R., & Braban, C. F. (2016b). Insights from a chronology of the development of atmospheric composition monitoring networks since the 1800s. *Atmosphere*, 7(12), 160.

Mao, H., Wang, W.-C., Liang, X.-Z., & Talbot, R. W. (2003). Global and seasonal vari-

ations of O_3 and NO_2 photodissociation rate coefficients. *J. Geophys. Res.: Atmos.*, 108(7).

Martín, F., Santiago, J. L., Kracht, O., García, L., & Gerboles, M. (2015). *FAIRMODE Spatial representativeness feasibility study*. Technical report, available at: https://ec.europa.eu/jrc/en/publication/fairmode-spatial-representativeness-feasibility-study, Publications Office of the European Union.

Martinez, R. D., Buitrago, A. A., Howell, N. W., Hearn, C. H., & Joens, J. A. (1992). The near U.V. absorption spectra of several aliphatic aldehydes and ketones at 300 K. *Atmos. Environ., Part A*, 26A(5), 785–792.

Matsumi, Y., Comes, F. J., Hancock, G., Hofzumahaus, A., Hynes, A. J., Kawasaki, M., & Ravishankara, A. R. (2002). Quantum yields for production of $O(^1D)$ in the ultraviolet photolysis of ozone: Recommendation based on evaluation of laboratory data. *J. Geophys. Res.: Atmos.*, 107, 4024.

McFadyen, G. G. & Cape, J. N. (2005). Peroxyacetyl nitrate in eastern Scotland. *Sci. Total Environ.*, 337, 213–222.

McGregor, J. & Price, J. (2018). Met Office Meteorological Research Unit Cardington: Met Office surface measurements from Cardington, Bedfordshire Version 1 (2006 to present). Centre for Environmental Data Analysis, available at: https://catalogue.ceda.ac.uk/uuid/20923d5a6a194340a94dcf4feda018a6, last accessed: 3 March 2021.

McKenzie, R., Johnston, P., Hofzumahaus, A., Kraus, A., Mandronich, S., Cantrell, C., Calvert, J., & Shetter, R. (2002). Relationship between photolysis frequencies derived from spectroscopic measurements of actinic fluxes and irradiances during the IPMMI campaign. *J. Geophys. Res.: Atmos.*, 107(D5), 4042.

McNamara, S. M., Kolesar, K. R., Wang, S., Kirpes, R. M., May, N. W., Gunsch, M. J., Cook, R. D., Fuentes, J. D., Hornbrook, R. S., Apel, E. C., China, S., Laskin, A., &

Pratt, K. A. (2020). Observation of Road Salt Aerosol Driving Inland Wintertime Atmospheric Chlorine Chemistry. *ACS Cent. Sci.*, 6, 684–694.

Meller, R. & Moortgat, G. K. (2000). Temperature dependence of the absorption cross sections of formaldehyde between 223 and 323 K in the wavelength range 225-375 nm. *J. Geophys. Res.: Atmos.*, 105(D6), 7089–7101.

Meller, R., Raber, W., Crowley, J. N., Jenkin, M. E., & Moortgat, G. K. (1991). The UV-visible absorption spectrum of methylglyoxal. *J. Photochem. Photobiol., A*, 62(2), 163–171.

Mérienne, M. F., Jenouvrier, A., & Coquart, B. (1995). The NO_2 Absorption Spectrum. I: Absorption Cross-Sections at Ambient Temperature in the 300-500 nm Region. *J. Atmos. Chem.*, 20, 281–297.

Met Office (2021). The UK land observation network. available at: https://www.metoffice.gov.uk/weather/guides/observations/uk-observations-network, last accessed: 24 April 2021.

Meyrahn, H., Moortgat, G. K., & Warneck, P. (1982). presented at the XVth Informal Conference on Photochemistry, in. Stanford Research Institute, Stanford, California.

Michalsky, J. J. & Kiedron, P. W. (2008). Comparison of UV-RSS spectral measurements and TUV model runs for clear skies for the May 2003 ARM aerosol intensive observation period. *Atmos. Chem. Phys.*, 8, 1813–1821.

Michoud, V., Colomb, A., Borbon, A., Miet, K., Beekmann, M., Camredon, M., Aumont, B., Perrier, S., Zapf, P., Siour, G., Ait-Helal, W., Afif, C., Kukui, A., Furger, M., Dupont, J. C., Haeffelin, M., & Doussin, J. F. (2014). Study of the unknown HONO daytime source at a European suburban site during the MEGAPOLI summer and winter field campaigns. *Atmos. Chem. Phys.*, 14, 2805–2822.

Mielke, L. H., Furgeson, A., & Osthoff, H. D. (2011). Observation of $ClNO_2$ in a Mid-Continental Urban Environment. *Environ. Sci. Technol.*, 45, 8889–8896.

Misselbrook, T. H., Van Der Weerden, T. J., Pain, B. F., Jarvis, S. C., Chambers, B. J., Smith, K. A., Phillips, V. R., & Demmers, T. G. M. (2000). Ammonia emission factors for UK agriculture. *Atmos. Environ.*, 34, 871–880.

Molina, L. T. & Molina, M. J. (1981). UV absorption cross sections of HO_2NO_2 vapour. *J. Photochem.*, 15, 97–108.

Molina, L. T. & Molina, M. J. (1986). Absolute Absorption Cross Sections of Ozone in the 185- to 350-nm Wavelength Range. *J. Geophys. Res.*, 91(D13), 14,501–14,508.

Monks, P. S. (2005). Gas-phase radical chemistry in the troposphere. *Chem. Soc. Rev.*, 34(5), 376–395.

Monks, P. S., Rickard, A. R., Hall, S. L., & Richards, N. A. D. (2004). Attenuation of spectal actinic flux and photolysis frequencies at the surface through homogenous cloud fields. *J. Geophys. Res.: Atmos.*, 109, D17606.

Moortgat, G. K., Seiler, W., & Warneck, P. (1983). Photodissociation of HCHO in air: CO and H_2 quantum yields at 220 and 300 K. *J. Chem. Phys.*, 78, 1185–1190.

Moxim, W. J., Levy II, H., & Kasibhatla, P. (1996). Simulated global tropospheric PAN: Its transport and impact on NO_x. *J. Geophys. Res.: Atmos.*, 101(D7), 12621–12638.

NCAR (2019). National Centre for Atmospheric Research (NCAR) Tropospheric Ultraviolet and Visible (TUV) Radiation Model v5.3. available at: https://www2.acom.ucar.edu/modeling/tropospheric-ultraviolet-and-visible-tuv-radiation-model, last accessed: 28 May 2021.

Neu, J. L., Prather, M. J., & Penner, J. E. (2007). Global atmospheric chemistry: Integrating over fractional cloud cover. *J. Geophys. Res.: Atmos.*, 112, D11306.

NOAA (2020). National Oceanic and Atmospheric Administration - Integrated Surface Database (NOAA-ISD). available at: https://www.ncdc.noaa.gov/isd, last accessed: 1 December 2020.

NOAA ESRL (2021). National Oceanic and Atmospheric Administration Earth System Research Laboratory Global Monitoring Devision (NOAA-ESRL-GMD) OMI Satellite Level 3e daily averaged ozone data gridded at 0.25 x 0.25 degrees. available at: https://www.esrl.noaa.gov/gmd/grad/neubrew/SatO3DataTimeSeries.jsp, last accessed: 20 March 2021.

O'Connor, F. M., Johnson, C. E., Morgenstern, O., Abraham, N. L., Braesicke, P., Dalvi, M., Folberth, G. A., Sanderson, M. G., Telford, P. J., Voulgarakis, A., Young, P. J., Zeng, G., Collins, W. J., & Pyle, J. A. (2014). Evaluation of the new UKCA climate-composition model – Part 2: The Troposphere. *Geosci. Model Dev.*, 7, 41–91.

Orellano, P., Reynoso, J., Quaranta, N., Bardach, A., & Ciapponi, A. (2020). Short-term exposure to particulate matter (PM_{10} and $PM_{2.5}$), nitrogen dioxide (NO_2), and ozone (O_3) and all-cause and cause-specific mortality: Systematic review and meta-analysis. *Environ. Int.*, 142, 105876.

Osthoff, H. D., Roberts, J. M., Ravishankara, A. R., Williams, E. J., Lerner, B. M., Sommariva, R., Bates, T. S., Coffman, D., Quinn, P. K., Dibb, J. E., Stark, H., Burkholder, J. B., Talukdar, R. K., Meagher, J., Fehsenfeld, F. C., & Brown, S. S. (2008). High levels of nitryl chloride in the polluted subtropical marine boundary layer. *Nat. Geosci.*, 1, 324–328.

Oswald, R., Behrendt, T., Ermel, M., Wu, D., Su, H., Cheng, Y., Breuninger, C., Moravek, A., Mougin, E., Delon, C., Loubet, B., Pommerening-Röser, A., Sörgel, M., Pöschl, U., Hoffmann, T., Andreae, M. O., Meixner, F. X., & Trebs, I. (2013).

HONO Emissions from Soil Bacteria as a Major Source of Atmospheric Reactive Nitrogen. *Science*, 341(1233-1235).

Palmer, P. I., O'Doherty, S., Allen, G., Bower, K., Bösch, H., Chipperfield, M. P., Connors, S., Dhomse, S., Feng, L., Finch, D. P., Gallagher, M. W., Gloor, E., Gonzi, S., Harris, N. R. P., Helfter, C., Humpage, N., Kerridge, B., Knappett, D., Jones, R. L., Le Breton, M., Lunt, M. F., Manning, A. J., Matthiesen, S., Muller, J. B. A., Mullinger, N., Nemitz, E., O'Shea, S., Parker, R. J., Percival, C. J., Pitt, J., Riddick, S. N., Rigby, M., Sembhi, H., Siddans, R., Skelton, R. L., Smith, P., Sonderfeld, H., Stanley, K., Stavert, A. R., Wenger, A., White, E., Wilson, C., & Young, D. (2018). A measurement-based verification framework for UK greenhouse gas emissions: An overview of the Greenhouse gAs Uk and Global Emissions (GAUGE) project. *Atmos. Chem. Phys.*, 18, 11753–11777.

Phillips, G. J., Makkonen, U., Schuster, G., Sobanski, N., Hakola, H., & Crowley, J. N. (2013a). The detection of nocturnal N_2O_5 as HNO_3 by alkali-and aqueous-denuder techniques. *Atmos. Meas. Tech.*, 6, 231–237.

Phillips, G. J., Pouvesle, N., Thieser, J., Schuster, G., Axinte, R., Fischer, H., Williams, J., Lelieveld, J., & Crowley, J. N. (2013b). Peroxyacetyl nitrate (PAN) and peroxyacetic acid (PAA) measurements by iodide chemical ionisation mass spectrometry: first analysis of results in the boreal forest and implications for the measurement of PAN fluxes. *Atmos. Chem. Phys.*, 13, 1129–1139.

Phillips, G. J., Tang, M. J., Thieser, J., Brickwedde, B., Schuster, G., Bohn, B., Lelieveld, J., & Crowley, J. N. (2012). Significant concentrations of nitryl chloride observed in rural continental Europe associated with the influence of sea salt chloride and anthropogenic emissions. *Geophys. Res. Lett.*, 39(10), 1–5.

Pope, R. & Wu, J. (2014). A multi-objective assessment of an air quality monitoring

network using environmental, economic and social indicators and GIS-based models. *J. Air Waste Manage. Assoc.*, 64(6), 721–737.

Pope, R. J., Arnold, S. R., Chipperfield, M. P., Latter, B. G., Siddans, R., & Kerridge, B. J. (2018). Widespread changes in UK air quality observed from space. *Atmos. Sci. Lett.*, 19, e817.

Prather, M. J. (2015). Photolysis rates in correlated overlapping cloud fields: Cloud-J 7.3c. *Geosci. Model Dev.*, 8, 2587–2595.

Priestley, M., Le Breton, M., Bannan, T. J., Worrall, S. D., Bacak, A., Smedley, A. R. D., Reyes-Villegas, E., Mehra, A., Allan, J., Webb, A. R., Shallcross, D. E., Coe, H., & Percival, C. J. (2018). Observations of organic and inorganic chlorinated compounds and their contribution to chlorine radical concentrations in an urban environment in Northern Europe during the wintertime. *Atmos. Chem. Phys.*, 18, 13481–12493.

Prinn, R. G. (2003). The Cleansing Capacity of the Atmosphere. *Annu. Rev. Environ. Resour.*, 28, 29–57.

R Core Team (2020). R: A language and environment for statistical computing. available at: https://www.r-project.org/.

Ramsay, R., Di Marco, C. F., Heal, M. R., Twigg, M. M., Cowan, N., Jones, M. R., Leeson, S. R., Bloss, W. J., Kramer, L. J., Crilley, L., Sörgel, M., Andreae, M., & Nemitz, E. (2018). Surface – atmosphere exchange of water – soluble gases and aerosols above agricultural grassland pre– and postfertilisation. *Atmos. Chem. Phys.*, 18, 16,953–16,978.

Reed, C., Evans, M. J., Di Carlo, P., Lee, J. D., & Carpenter, L. J. (2016). Interferences in photolytic NO_2 measurements: Explanation for an apparent missing oxidant? *Atmos. Chem. Phys.*, 16, 4707–4724.

Ren, Y., Stieger, B., Spindler, G., Grosselin, B., Mellouki, A., Tuch, T., Wiedensohler, A., & Herrmann, H. (2020). Role of the dew water on the ground surface in HONO distribution: a case measurement in Melpitz. *Atmos. Chem. Phys.*, 20, 13069–13089.

Riedel, T. P., Wolfe, G. M., Danas, K. T., Gilman, J. B., Kuster, W. C., Bon, D. M., Vlasenko, A., Li, S.-M., Williams, E. J., Lerner, B. M., Veres, P. R., Roberts, J. M., Holloway, J. S., Lefer, B., Brown, S. S., & Thornton, J. A. (2014). An MCM modeling study of nitryl chloride ($ClNO_2$) impacts on oxidation, ozone production and nitrogen oxide partitioning in polluted continental outflow. *Atmos. Chem. Phys.*, 14(8), 3789–3800.

Roberts, J. M., Osthoff, H. D., Brown, S. S., Ravishankara, A. R., Coffman, D., Quinn, P., & Bates, T. (2009). Laboratory studies of products of N_2O_5 uptake on Cl^- containing substrates. *Geophys. Res. Lett.*, 36, L20808.

Robinson, N. H., Newton, H. M., Allan, J. D., Irwin, M., Hamilton, J. F., Flynn, M., Bower, K. N., Williams, P. I., Mills, G., Reeves, C. E., McFiggans, G., & Coe, H. (2011). Source attribution of Bornean air masses by back trajectory analysis during the OP3 project. *Atmos. Chem. Phys.*, 11, 9605–9630.

Roehl, C. M., Orlando, J. J., Tyndall, G. S., Shetter, R. E., Vázquez, G. J., Cantrell, C. A., & Calvert, J. G. (1994). Temperature Dependence of the Quantum Yields for the Photolysis of NO_2 near the Dissociation Limit. *J. Phys. Chem.*, 98, 7837–7843.

Roselle, S. J., Schere, K. L., Pleim, J. E., & Hanna, A. F. (1999). Photolysis Rates for CMAQ in Science Algorithms of the EPA Models-3 Community Multiscale Air Quality (CMAQ) Modeling System. available at: https://www.cmascenter.org/cmaq/science_documentation/.

RoTAP (2012). *Review of Transboundary Air Pollution (RoTAP): Acidification, Eutrophication, Ground Level Ozone and Heavy Metals in the UK*. Technical report, available at: http://www.rotap.ceh.ac.uk/.

Rumsey, I. C., Cowen, K. A., Walker, J. T., Kelly, T. J., Hanft, E. A., Mishoe, K., Rogers, C., Proost, R., Beachley, G. M., Lear, G., Frelink, T., & Otjes, R. P. (2014). An assessment of the performance of the Monitor for AeRosols and GAses in ambient air (MARGA): a semi-continuous method for soluble compounds. *Atmos. Chem. Phys.*, 14, 5639–5658.

Ryan, R. G., Rhodes, S., Tully, M., Wilson, S., Jones, N., Frieß, U., & Schofield, R. (2018). Daytime HONO, NO_2 and aerosol distributions from MAX-DOAS observations in Melbourne. *Atmos. Chem. Phys.*, 18, 13969–13985.

Ryu, Y.-H., Hodzic, A., Descombes, G., Hall, S., Minnis, P., Spangenberg, D., Ullmann, K., & Madronich, S. (2017). Improved modeling of cloudy-sky actinic flux using satellite cloud retrievals. *Geophys. Res. Lett.*, 44, 1592–1600.

Sander, S. P., Friedl, R. R., Barker, J. R., Golden, D. M., Kurylo, M. J., Wine, P. H., Abbatt, J. P. D., Burkholder, J. B., Kolb, C. E., Moortgat, G. K., Huie, R. E., & Orkin, V. L. (2011). Chemical Kinetics and Photochemical Data for Use in Atmospheric Studies, Evaluation Number 17. JPL Publication 10-6, Pasadena, CA.

Sarwar, G., Simon, H., Xing, J., & Mathur, R. (2014). Importance of tropospheric $ClNO_2$ chemistry across the Northern Hemisphere. *Geophys. Res. Lett.*, 41(11), 4050–4058.

Sather, M. E., Mathew, J., Nguyen, N., Lay, J., Golod, G., Vet, R., Cotie, J., Hertel, T., Aaboe, E., Callison, R., Adam, J., Keese, D., Freise, J., Hathcoat, A., Sakizzie, B., King, M., Lee, C., Oliva, S., San Miguel, G., Crow, L., & Geasland, F. (2008). Baseline ambient gaseous ammonia concentrations in the Four Corners area and eastern Oklahoma, USA. *J. Environ. Monit.*, 10(11), 1319–1325.

Saunders, S. M., Jenkin, M. E., Derwent, R. G., & Pilling, M. J. (2003). Protocol for the development of the Master Chemical Mechanism, MCM v3 (Part A): tropospheric

degradation of non-aromatic volatile organic compounds. *Atmos. Chem. Phys.*, 3, 161–180.

Schade, N. H., Macke, A., Sandmann, H., & Stick, C. (2007). Enhanced solar global irradiance during cloudy sky conditions. *Meteorol. Z.*, 16, 295–303.

Shetter, R. E., Davidson, J. A., Cantrell, C. A., Burzynski, Jr., N. J., & Calvert, J. G. (1988). Temperature Dependence of the Atmospheric Photolysis Rate Coefficient for NO_2. *J. Geophys. Res.: Atmos.*, 93(D6), 7,113–7,118.

Shetter, R. E., Junkermann, W., Swartz, W. H., Frost, G. J., Crawford, J. H., Lefer, B. L., Barrick, J. D., Hall, S. R., Hofzumahaus, A., Bais, A., Calvert, J. G., Cantrell, C. A., Madronich, S., Müller, M., Kraus, A., Monks, P. S., Edwards, G. D., McKenzie, R., Johnston, P., Schmitt, R., Griffioen, E., Krol, M., Kylling, A., Dickerson, R. R., Lloyd, S. A., Martin, T., Gardiner, B., Mayer, B., Pfister, G., Röth, E. P., Koepke, P., Ruggaber, A., Schwander, H., & van Weele, M. (2003). Photolysis frequency of NO_2: Measurement and modeling during the International Photolysis Frequency Measurement and Modeling Intercomparison (IPMMI). *J. Geophys. Res.: Atmos.*, 108, 8544.

Shetter, R. E., McDaniel, A. H., Cantrell, C. A., Madronich, S., & Calvert, J. G. (1992). Actinometer and Eppley radiometer measurements of the NO_2 photolysis rate coefficient during the Mauna Loa Observatory photochemistry experiment. *J. Geophys. Res.*, 97(D10), 10349.

Shi, X., Ge, Y., Zheng, J., Ma, Y., Ren, X., & Zhang, Y. (2020). Budget of nitrous acid and its impacts on atmospheric oxidative capacity at an urban site in the central Yangtze River Delta region of China. *Atmos. Environ.*, 238, 117725.

Shi, Z., Vu, T., Kotthaus, S., Harrison, R. M., Grimmond, S., Yue, S., Zhu, T., Lee, J., Han, Y., Demuzere, M., Dunmore, R. E., Ren, L., Liu, D., Wang, Y., Wild, O., Allan, J., Joe Acton, W., Barlow, J., Barratt, B., Beddows, D., Bloss, W. J., Calzolai,

G., Carruthers, D., Carslaw, D. C., Chan, Q., Chatzidiakou, L., Chen, Y., Crilley, L., Coe, H., Dai, T., Doherty, R., Duan, F., Fu, P., Ge, B., Ge, M., Guan, D., Hamilton, J. F., He, K., Heal, M., Heard, D., Nicholas Hewitt, C., Hollaway, M., Hu, M., Ji, D., Jiang, X., Jones, R., Kalberer, M., Kelly, F. J., Kramer, L., Langford, B., Lin, C., Lewis, A. C., Li, J., Li, W., Liu, H., Liu, J., Loh, M., Lu, K., Lucarelli, F., Mann, G., McFiggans, G., Miller, M. R., Mills, G., Monk, P., Nemitz, E., O'Connor, F., Ouyang, B., Palmer, P. I., Percival, C., Popoola, O., Reeves, C., Rickard, A. R., Shao, L., Shi, G., Spracklen, D., Stevenson, D., Sun, Y., Sun, Z., Tao, S., Tong, S., Wang, Q., Wang, W., Wang, X., Wang, X., Wang, Z., Wei, L., Whalley, L., Wu, X., Wu, Z., Xie, P., Yang, F., Zhang, Q., Zhang, Y., Zhang, Y., & Zheng, M. (2019). Introduction to the special issue "In-depth study of air pollution sources and processes within Beijing and its surrounding region (APHH-Beijing)". *Atmos. Chem. Phys.*, 19, 7519–7546.

Sillman, S. (2002). Chapter 12 The relation between ozone, NO_x and hydrocarbons in urban and polluted rural environments. *Dev. Environ. Sci.*, 1, 339–385.

Simpson, D., Benedictow, A., Berge, H., Bergström, R., Emberson, L. D., Fagerli, H., Flechard, C. R., Hayman, G. D., Gauss, M., Jonson, J. E., Jenkin, M. E., Nyúri, A., Richter, C., Semeena, V. S., Tsyro, S., Tuovinen, J.-P., Valdebenito, Á., & Wind, P. (2012). The EMEP MSC-W chemical transport model - technical description. *Atmos. Chem. Phys.*, 12, 7825–7865.

Singh, H. B. & Hanst, P. L. (1981). Peroxyacetyl nitrate (PAN) in the unpolluted atmosphere: An important reservoir for nitrogen oxides. *Geophys. Res. Lett.*, 8(8), 941–944.

Slusher, D. L., Huey, L. G., Tanner, D. J., Flocke, F. M., & Roberts, J. M. (2004). A thermal dissociation–chemical ionization mass spectrometry (TD-CIMS) technique for the simultaneous measurement of peroxyacyl nitrates and dinitrogen pentoxide. *J. Geophys. Res.*, 109, D19315.

Smith, G. D., Molina, L. T., & Molina, M. J. (2002). Measurement of radical quantum yields from formaldehyde photolysis between 269 and 339 nm. *J. Phys. Chem. A*, 106, 1233–1240.

Sommariva, R., Cox, S., Martin, C., Borońska, K., Young, J., Jimack, P. K., Pilling, M. J., Matthaios, V. N., Nelson, B. S., Newland, M. J., Panagi, M., Bloss, W. J., Monks, P. S., & Rickard, A. R. (2020). AtChem (version 1), an open-source box model for the Master Chemical Mechanism. *Geosci. Model Dev.*, 13(1), 169–183.

Sommariva, R., Crilley, L. R., Ball, S. M., Cordell, R. L., Hollis, L. D. J., Bloss, W. J., & Monks, P. S. (2021). Enhanced wintertime oxidation of VOCs via sustained radical sources in the urban atmosphere. *Environ. Pollut.*, 274, 116563.

Sommariva, R., Hollis, L. D. J., Sherwen, T., Baker, A. R., Ball, S. M., Bandy, B. J., Bell, T. G., Chowdhury, M. N., Cordell, R. L., Evans, M. J., Lee, J. D., Reed, C., Reeves, C. E., Roberts, J. M., Yang, M., & Monks, P. S. (2018). Seasonal and geographical variability of nitryl chloride and its precursors in Northern Europe. *Atmos. Sci. Lett.*, 19, 1–10.

Sörgel, M., Regelin, E., Bozem, H., Diesch, J. M., Drewnick, F., Fischer, H., Harder, H., Held, A., Hosaynali-Beygi, Z., Martinez, M., & Zetzsch, C. (2011). Quantification of the unknown HONO daytime source and its relation to NO_2. *Atmos. Chem. Phys.*, 11, 10433–10447.

Søvde, O. A., Prather, M. J., Isaksen, I. S. A., Berntsen, T. K., Stordal, F., Zhu, X., Holmes, C. D., & Hsu, J. (2012). The chemical transport model Oslo CTM3. *Geosci. Model Dev.*, 5, 1441–1469.

Spangl, W., Schneider, J., Moosmann, L., & Nagi, C. (2007). *Representativeness and classification of air quality monitoring stations, Umweltbundesamt Report*. Technical report, available at: https://www.umweltbundesamt.at/fileadmin/site/publikationen/rep0121.pdf.

Spataro, F. & Ianniello, A. (2014). Sources of atmospheric nitrous acid: State of the science, current research needs, and future prospects. *J. Air Waste Manage. Assoc.*, 64(11), 1232–1250.

Staffelbach, T. A., Orlando, J. J., Tyndall, G. S., & Calvert, J. G. (1995). The UV-visible absorption spectrum and photolysis quantum yields of methlyglyoxal. *J. Geophys. Res.: Atmos.*, 100(D7), 14,189–14,198.

Stamnes, K., Tsay, S.-C., Wiscombe, W., & Jayaweera, K. (1988). Numerically stable algorithm for discrete-ordinate-method radiative transfer in multiple scattering and emitting layered media. *Appl. Opt.*, 27(12), 2502–2509.

Steinbacher, M., Zellweger, C., Schwarzenbach, B., Bugmann, S., Buchmann, B., Ordóñez, C., Prevot, A. S. H., & Hueglin, C. (2007). Nitrogen oxide measurements at rural sites in Switzerland: Bias of conventional measurement techniques. *J. Geophys. Res.: Atmos.*, 112, D11307.

Stemmler, K., Ndour, M., Elshorbany, Y., Kleffmann, J., DÁnna, B., George, C., Bohn, B., & Ammann, M. (2007). Light induced conversion of nitrogen dioxide into nitrous acid on submicron humic acid aerosol. *Atmos. Chem. Phys.*, 7, 4237–4248.

Stieger, B., Spindler, G., Fahlbusch, B., Müller, K., Grüner, A., Poulain, L., Thöni, L., Seitler, E., Wallasch, &. M., Herrmann, H., Chem, J. A., & De, H. (2018). Measurements of PM_{10} ions and trace gases with the online system MARGA at the research station Melpitz in Germany – A five-year study. *J. Atmos. Chem.*, 75, 33–70.

Stockwell, W. R., Kirchner, F., Kuhn, M., & Seefeld, S. (1997). A new mechanism for regional atmospheric chemistry modeling. *J. Geophys. Res.: Atmos.*, 102(D22), 25,847–25,879.

Stockwell, W. R., Middleton, P., Chang, J. S., & Tang, X. (1990). The Second Generation Regional Acid Deposition Model Chemical Mechanism for Regional Air Quality Modeling. *J. Geophys. Res.: Atmos.*, 95(D10), 16,343–16,367.

Stone, D., Evans, M. J., Commane, R., Ingham, T., Floquet, C. F. A., McQuaid, J. B., Brookes, D. M., Monks, P. S., Purvis, R., Hamilton, J. F., Hopkins, J., Lee, J., Lewis, A. C., Stewart, D., Murphy, J. G., Mills, G., Oram, D., Reeves, C. E., & Heard, D. E. (2010). HO_x observations over West Africa during AMMA: Impact of isoprene and NO_x. *Atmos. Chem. Phys.*, 10, 9415–9429.

Stone, D., Whalley, L. K., & Heard, D. E. (2012). Tropospheric OH and HO_2 radicals: Field measurements and model comparisons. *Chem. Soc. Rev.*, 41, 6348–6404.

Su, H., Cheng, Y., Oswald, R., Behrendt, T., Trebs, I., Meixner, F., Andreae, M., Cheng, P., Zhang, Y., & Poschl, U. (2011). Soil Nitrite as a Source of Atmospheric HONO and OH Radicals. *Science*, 333, 1215–1172.

Sutton, M. A. & Fowler, D. (2002). Introduction: Fluxes and impacts of atmospheric ammonia on national, landscape and farm scales. *Environ. Pollut.*, 119, 7–8.

Sutton, M. A., Howard, C. M., Erisman, J. W., Billen, G., Bleeker, A., Grennfelt, P., van Grinsven, H., & Grizzetti, B. (2011). *European Nitrogen Assessment: Sources, Effects and Policy Perspectives*. Cambridge University Press, Cambridge, UK.

Sutton, M. A., Reis, S., & Baker, S. M. H. (2009). *Atmospheric Ammonia: Detecting emission changes and environmental impacts*. Springer, Dordrecht, Netherlands.

Tan, Z., Rohrer, F., Lu, K., Ma, X., Bohn, B., Broch, S., Dong, H., Fuchs, H., Gkatzelis, G. I., Hofzumahaus, A., Holland, F., Li, X., Liu, Y., Liu, Y., Novelli, A., Shao, M., Wang, H., Wu, Y., Zeng, L., Hu, M., Kiendler-Scharr, A., Wahner, A., & Zhang, Y. (2018). Wintertime photochemistry in Beijing: Observations of RO_x radical concentrations in the North China Plain during the BEST-ONE campaign. *Atmos. Chem. Phys.*, 18, 12391–12411.

Tang, Y. S., Braban, C. F., Dragosits, U., Dore, A. J., Simmons, I., Dijk, N. V., Poskitt, J., Dos, G., Pereira, S., Keenan, P. O., Conolly, C., Vincent, K., Smith, R. I., Heal,

M. R., & Sutton, M. A. (2018a). Drivers for spatial, temporal and long-term trends in atmospheric ammonia and ammonium in the UK. *Atmos. Chem. Phys.*, 18, 705–733.

Tang, Y. S., Braban, C. F., Dragosits, U., Simmons, I., Leaver, D., van Dijk, N., Poskitt, J., Thacker, S., Patel, M., Carter, H., Pereira, M. G., Keenan, P. O., Lawlor, A., Conolly, C., Vincent, K., Heal, M. R., & Sutton, M. A. (2018b). Acid gases and aerosol measurements in the UK (1999-2015): regional distributions and trends. *Atmos. Chem. Phys.*, 18, 16293–16324.

Tang, Y. S., Simmons, I., Van Dijk, N., Di Marco, C. F., Nemitz, E., Dä Mmgen, U., Gilke, K., Djuricic, V., Vidic, S., Gliha, Z., Borovecki, D., Mitosinkova, M., Hanssen, J. E., Uggerud, T. H., Sanz, M. J., Sanz, P., Chorda, J. V., Flechard, C. R., Fauvel, Y., Ferm, M., Perrino, C., & Sutton, M. A. (2009). European scale application of atmospheric reactive nitrogen measurements in a low-cost approach to infer dry deposition fluxes. *Agric., Ecosyst. Environ.*, 133, 183–195.

Telford, P. J., Abraham, N. L., Archibald, A. T., Braesicke, P., Dalvi, M., Morgenstern, O., O'Connor, F. M., Richards, N. A. D., & Pyle, J. A. (2013). Implementation of the Fast-JX Photolysis scheme (v6.4) into the UKCA component of the MetUM chemistry-climate model (v7.3). *Geosci. Model Dev.*, 6, 161–177.

Telling, S., Eaton, S., & Stevenson, K. (2009). *Site Operators Manual: Automatic Urban and Rural Network*. Technical report, Defra and the Devolved Administrations, available at: https://uk-air.defra.gov.uk/assets/documents/reports/empire/lsoman/Section_A.pdf.

Thaler, R. D., Mielke, L. H., & Osthoff, H. D. (2011). Quantification of Nitryl Chloride at Part Per Trillion Mixing Ratios by Thermal Dissociation Cavity Ring-Down Spectroscopy. *Anal. Chem.*, 83, 2761–2766.

Tham, Y. J., Wang, Z., Li, Q., Yun, H., Wang, W., Wang, X., Xue, L., Lu, K., Ma, N., Bohn, B., Li, X., Kecorius, S., Größ, J., Shao, M., Wiedensohler, A., Zhang,

Y., & Wang, T. (2016). Significant concentrations of nitryl chloride sustained in the morning: Investigations of the causes and impacts on ozone production in a polluted region of northern China. *Atmos. Chem. Phys.*, 16, 14959–14977.

Thiel, S., Ammannato, L., Bais, A., Bandy, B., Blumthaler, M., Bohn, B., Engelsen, O., Gobbi, G. P., Gröbner, J., Jäkel, E., Junkermann, W., Kazadzis, S., Kift, R., Kjeldstad, B., Kouremeti, N., Kylling, A., Mayer, B., Monks, P. S., Reeves, C. E., Schallhart, B., Scheirer, R., Schmidt, S., Schmitt, R., Schreder, J., Silbernagl, R., Topaloglou, C., Thorseth, T. M., Webb, A. R., Wendisch, M., & Werle, P. (2008). Influence of clouds on the spectral actinic flux density in the lower troposphere (INSPECTRO): Overview of the field campaigns. *Atmos. Chem. Phys.*, 8, 1789–1812.

Thornton, J. A., Kercher, J. P., Riedel, T. P., Wagner, N. L., Cozic, J., Holloway, J. S., Dubé, W. P., Wolfe, G. M., Quinn, P. K., Middlebrook, A. M., Alexander, B., & Brown, S. S. (2010). A large atomic chlorine source inferred from mid-continental reactive nitrogen chemistry. *Nature*, 464, 271–274.

Tie, X., Madronich, S., Walters, S., Zhang, R., Rasch, P., & Collins, W. (2003). Effect of clouds on photolysis and oxidants in the troposphere. *J. Geophys. Res.: Atmos.*, 108(D20), 4642.

Topaloglou, C., Kazadzis, S., Bais, A. F., Blumthaler, M., Schallhart, B., & Balis, D. (2005). NO_2 and HCHO photolysis frequencies from irradiance measurements in Thessaloniki, Greece. *Atmos. Chem. Phys.*, 5, 1645–1653.

Tørseth, K., Aas, W., Breivik, K., Fjaeraa, A. M., Fiebig, M., Hjellbrekke, A. G., Myhre, C. L., Solberg, S., & Yttri, K. E. (2012). Introduction to the European Monitoring and Evaluation Programme (EMEP) and observed atmospheric composition change during 1972–2009. *Atmos. Chem. Phys.*, 12, 5447–5481.

Trebs, I., Bohn, B., Ammann, C., Rummel, U., Blumthaler, M., Königstedt, R.,

Meixner, F. X., Fan, S., & Andreae, M. O. (2009). Relationship between the NO_2 photolysis frequency and the solar global irradiance. *Atmos. Meas. Tech.*, 2, 725–739.

Troe, J. (2000). Are Primary Quantum Yields of NO_2 Photolysis at $\lambda \leq 398$ nm Smaller than Unity? *Z. Phys. Chem.*, 214, 573–581.

Twigg, M., Ilyinskaya, E., Beccaceci, S., Green, D., Jones, M., Langford, B., Leeson, S., Lingard, J., Pereira, G., Carter, H., Poskitt, J., Richter, A., Ritchie, S., Simmons, I., Smith, R., Sim Tang, Y., Van Dijk, N., Vincent, K., Nemitz, E., Vieno, M., & Braban, C. (2016). Impacts of the 2014-2015 Holuhraun eruption on the UK atmosphere. *Atmos. Chem. Phys.*, 16(17), 11415–11431.

Twigg, M. M., Di Marco, C. F., Leeson, S., Van Dijk, N., Jones, M. R., Leith, I. D., Morrison, E., Coyle, M., Proost, R., Peeters, A. N. M., Lemon, E., Frelink, T., Braban, C. F., Nemitz, E., & Cape, J. N. (2015). Water soluble aerosols and gases at a UK background site – Part 1: Controls of $PM_{2.5}$ and PM_{10} aerosol composition. *Atmos. Chem. Phys.*, 15, 8131–8145.

UKCEH (2017). Coyle, M., Roberts, E., Jones, M., Leeson, S., Mullinger, N., Simmons, I., Van Dijk, N., Kentisbeer, J., Leith, I., Storton-West, R., Flechard, C., Twigg, M., Helfter, C., Fowler, D. and Nemitz, E.: Auchencorth Moss Atmospheric Observatory (AU): Annual half-hourly meteorology since 1995, Near Edinburgh, UK. available at: https://catalogue.ceda.ac.uk/uuid/8e6cbb111cfd41a19c92aadcb2d040fd, last accessed: 26 March 2020.

UKEAP (2015). *UK Eutrophying and Acidifying Atmospheric Pollutants (UKEAP) Annual Report 2015*. Technical report, available at: http://nora.nerc.ac.uk/id/eprint/520602/, Department for Environment Food and Rural Affairs (Defra), Didcot, UK.

UNECE (2004a). *Handbook for the 1979 Convention on Long-Range Transboundary Air Pollution and its Protocols*. Technical report, ECE/EB.AIR/85. United Nations Economic Commissions for Europe, Geneva, Switzerland.

UNECE (2004b). *The EMEP Monitoring Strategy and measurement programme 2004-2009*. Technical report, EB.AIR/GE.1/2004/5. United Nations Economic Commissions for Europe, Geneva, Switzerland.

UNECE (2012). 1999 Protocol to Abate Acidification, Eutrophication and Ground-level Ozone (Gothenburg Protocol). available at: https://unece.org/gothenburg-protocol, last accessed 27 May 2021.

van Oss, R. F. & Spurr, R. J. D. (2002). Fast and accurate 4 and 6 stream linearized discrete ordinate radiative transfer models for ozone profile retrieval. *J. Quant. Spectrosc. Radiat. Transfer*, 75, 177–220.

Vandaele, A. C., Hermans, C., Simon, P. C., Carleer, M., Colin, R., Fally, S., Mérienne, M. F., Jenouvrier, A., & Coquart, B. (1998). Measurements of the NO_2 absorption cross-section from 42.000 cm^{-1} to 10.000 cm^{-1} (238-1000 nm) at 220 K and 294 K. *J. Quant. Spectrosc. Radiat. Transfer*, 59, 171–184.

Veres, P. R., Roberts, J. M., Wild, R. J., Edwards, P. M., Brown, S. S., Bates, T. S., Quinn, P. K., Johnson, J. E., Zamora, R. J., & de Gouw, J. (2015). Peroxynitric acid (HO_2NO_2) measurements during the UBWOS 2013 and 2014 studies using iodide ion chemical ionization mass spectrometry. *Atmos. Chem. Phys.*, 15(14), 8101–8114.

Vestreng, V., Myhre, G., Fagerli, H., Reis, S., & Tarrasón, L. (2007). Twenty-five years of continuous sulphur dioxide emission reduction in Europe. *Atmos. Chem. Phys.*, 7, 3663–3681.

Vicedo-Cabrera, A. M., Sera, F., Liu, C., Armstrong, B., Milojevic, A., Guo, Y., Tong, S., Lavigne, E., Kyselý, J., Urban, A., Orru, H., Indermitte, E., Pascal, M., Huber, V., Schneider, A., Katsouyanni, K., Samoli, E., Stafoggia, M., Scortichini, M., Hashizume, M., Honda, Y., Ng, C. F. S., Hurtado-Diaz, M., Cruz, J., Silva, S., Madureira, J., Scovronick, N., Garland, R. M., Kim, H., Tobias, A., Íñiguez, C., Forsberg, B., Åström, C., Ragettli, M. S., Röösli, M., Guo, Y.-L. L., Chen, B.-Y.,

Zanobetti, A., Schwartz, J., Bell, M. L., Kan, H., & Gasparrini, A. (2020). Short term association between ozone and mortality: global two stage time series study in 406 locations in 20 countries. *BMJ*, 368, m108.

Vieno, M., Dore, A. J., Bealey, W. J., Stevenson, D. S., & Sutton, M. A. (2010). The importance of source configuration in quantifying footprints of regional atmospheric sulphur deposition. *Sci. Total Environ.*, 408, 985–995.

Vieno, M., Heal, M. R., Hallsworth, S., Famulari, D., Doherty, R. M., Dore, A. J., Tang, Y. S., Braban, C. F., Leaver, D., Sutton, M. A., & Reis, S. (2014). The role of long-range transport and domestic emissions in determining atmospheric secondary inorganic particle concentrations across the UK. *Atmos. Chem. Phys.*, 14, 8435–8447.

Vieno, M., Heal, M. R., Twigg, M. M., MacKenzie, I. A., Braban, C. F., Lingard, J. J. N., Ritchie, S., Beck, R. C., Móring, A., Ots, R., Di Marco, C. F., Nemitz, E., Sutton, M. A., & Reis, S. (2016a). The UK particulate matter air pollution episode of March–April 2014: more than Saharan dust. *Environ. Res. Lett.*, 11, 044004.

Vieno, M., Heal, M. R., Williams, M. L., Carnell, E. J., Nemitz, E., Stedman, J. R., & Reis, S. (2016b). The sensitivities of emissions reductions for the mitigation of UK $PM_{2.5}$. *Atmos. Chem. Phys.*, 16, 265–276.

Villena, G., Bejan, I., Kurtenbach, R., Wiesen, P., & Kleffmann, J. (2012). Interferences of commercial NO_2 instruments in the urban atmosphere and in a smog chamber. *Atmos. Meas. Tech.*, 5, 149–159.

Villena, G., Wiesen, P., Cantrell, C. A., Flocke, F., Fried, A., Hall, S. R., Hornbrook, R. S., Knapp, D., Kosciuch, E., Mauldin III, R. L., McGrath, J. A., Montzka, D., Richter, D., Ullmann, K., Walega, J., Weibring, P., Weinheimer, A., Staebler, R. M., Liao, J., Huey, L. G., & Kleffmann, J. (2011). Nitrous acid (HONO) during polar

spring in Barrow, Alaska: A net source of OH radicals? *J. Geophys. Res.: Atmos.*, 116, D00R07.

Vogt, E., Dragosits, U., Braban, C. F., Theobald, M. R., Dore, A. J., van Dijk, N., Tang, Y. S., McDonald, C., Murray, S., Rees, R. M., & Sutton, M. A. (2013). Heterogeneity of atmospheric ammonia at the landscape scale and consequences for environmental impact assessment. *Environ. Pollut.*, 179, 120–131.

Volz-Thomas, A., Lerner, A., Pätz, H.-W., Schultz, M., Mckenna, D. S., Schmitt, R., Madronich, S., & Röth, E. P. (1996). Airborne measurements of the photolysis frequency of NO_2. *J. Geophys. Res.: Atmos.*, 101, 18613–18627.

Volz-Thomas, A., Xueref, I., & Schmitt, R. (2002). An automatic gas chromatograph and calibration system for ambient measurements of PAN and PPN. *Environ. Sci. Pollut. Res.*

von Clarmann, T. & Johansson, S. (2018). Chlorine nitrate in the atmosphere. *Atmos. Chem. Phys.*, 18, 15363–15386.

Voulgarakis, A., Savage, N. H., Wild, O., Carver, G. D., Clemitshaw, K. C., & Pyle, J. A. (2009). Upgrading photolysis in the p-TOMCAT CTM: model evaluation and assessment of the role of clouds. *Geosci. Model Dev.*, 2, 59–72.

Vu, T. V., Shi, Z., Cheng, J., Zhang, Q., He, K., Wang, S., & Harrison, R. (2019). Assessing the impact of clean air action on air quality trends in Beijing using a machine learning technique. *Atmos. Chem. Phys.*, 19, 11303–11314.

Walker, H. L., Heal, M. R., Braban, C. F., Ritchie, S., Conolly, C., Sanocka, A., Dragosits, U., & Twigg, M. M. (2019). Changing supersites: assessing the impact of the southern UK EMEP supersite relocation on measured atmospheric composition. *Environ. Res. Commun.*, 1, 041001.

Wallace, J. M. & Hobbs, P. V. (2006). *Atmospheric Science: An Introductory Survey, 2nd Edition*. Academic Press, Cambridge, MA, USA.

Wang, H., Lu, K., Tan, Z., Sun, K., Li, X., Hu, M., Shao, M., Zeng, L., Zhu, T., & Zhang, Y. (2017a). Model simulation of NO_3, N_2O_5 and $ClNO_2$ at a rural site in Beijing during CAREBeijing-2006. *Atmos. Res.*, 196, 97–107.

Wang, J., Zhang, X., Guo, J., Wang, Z., & Zhang, M. (2017b). Observation of nitrous acid (HONO) in Beijing, China: Seasonal variation, nocturnal formation and daytime budget. *Sci. Total Environ.*, 587-588, 350–359.

Wang, T., Tham, Y. J., Xue, L., Li, Q., Zha, Q., Wang, Z., Poon, S. C. N., Dubé, W. P., Blake, D. R., Louie, P. K. K., Luk, C. W. Y., Tsui, W., & Brown, S. S. (2016). Observations of nitryl chloride and modeling its source and effect on ozone in the planetary boundary layer of southern China. *J. Geophys. Res.: Atmos.*, 121, 2476–2489.

Wang, W., Li, X., Shao, M., Hu, M., Zeng, L., Wu, Y., & Tan, T. (2019). The impact of aerosols on photolysis frequencies and ozone production in Beijing during the 4-year period 2012-2015. *Atmos. Chem. Phys.*, 19, 9413–9429.

Wang, X., Wang, H., Xue, L., Wang, T., Wang, L., Gu, R., Wang, W., Tham, Y. J., Wang, Z., Yang, L., Chen, J., & Wang, W. (2017c). Observations of N_2O_5 and $ClNO_2$ at a polluted urban surface site in North China: High N_2O_5 uptake coefficients and low $ClNO_2$ product yields. *Atmos. Environ.*, 156, 125–134.

Wang, X., Wang, T., Yan, C., Tham, Y. J., Xue, L., Xu, Z., & Zha, Q. (2014). Large daytime signals of N_2O_5 and NO_3 inferred at 62 amu in a TD-CIMS: chemical interference or a real atmospheric phenomenon? *Atmos. Meas. Tech.*, 7, 1–12.

Webb, A. R., Bais, A. F., Blumthaler, M., Gobbi, G.-P., Kylling, A., Schmitt, R., Thiel, S., Barnaba, F., Danielsen, T., Junkermann, W., Kazantzidis, A., Kelly, P., Kift, R.,

Liberti, G. L., Misslbeck, M., Schallhart, B., Schreder, J., & Topaloglou, C. (2002a). Measuring Spectral Actinic Flux and Irradiance: Experimental Results from the Actinic Flux Determination from Measurements of Irradiance (ADMIRA) Project. *J Atmos. Ocean Technol.*, 19(7), 1049–1062.

Webb, A. R., Kift, R., Thiel, S., & Blumthaler, M. (2002b). An empirical method for the conversion of spectral UV irradiance measurements to actinic flux data. *Atmos. Environ.*, 36, 4397–4404.

Whalley, L., Stone, D., Dunmore, R., Hamilton, J., Hopkins, J. R., Lee, J. D., Lewis, A. C., Williams, P., Kleffmann, J., Laufs, S., Woodward-Massey, R., & Heard, D. E. (2018). Understanding in situ ozone production in the summertime through radical observations and modelling studies during the Clean air for London project (ClearfLo). *Atmos. Chem. Phys.*, 18, 2547–2571.

WHO (2006). *Air quality guidelines for particulate matter, ozone, nitrogen dioxide and sulfur dioxide, global update 2005: summary of risk assessment*. Technical report, available at: http://whqlibdoc.who.int/hq/2006/WHO_SDE_PHE_OEH_06.02_eng.pdf?ua=1, World Health Organisation, World Health Organisation.

WHO (2013a). *Health Effects of Particulate Matter: Policy implications for countries in eastern Europe, Caucasus and central Asia*. Technical report, available at: https://www.euro.who.int/__data/assets/pdf_file/0006/189051/Health-effects-of-particulate-matter-final-Eng.pdf, World Health Organisation.

WHO (2013b). *Review of evidence on health aspects of air pollution – REVIHAAP Project*. Technical report, available at: http://www.euro.who.int/__data/assets/pdf_file/0004/193108/REVIHAAP-Final-technical-report-final-version.pdf, World Health Organisation.

Wild, O., Zhu, X., & Prather, M. J. (2000). Fast-J: Accurate Simulation of In- and

Below-Cloud Photolysis in Tropospheric Chemical Models. *J. Atmos. Chem.*, 37, 245–282.

Wilson, S. R. (2015). Characterisation of $J(O^1D)$ at Cape Grim 2000–2005. *Atmos. Chem. Phys.*, 15(13), 7337–7349.

Xu, W., Kuang, Y., Zhao, C., Tao, J., Zhao, G., Bian, Y., Yang, W., Yu, Y., Shen, C., Liang, L., Zhang, G., Lin, W., & Xu, X. (2019). NH_3-promoted hydrolysis of NO_2 induces explosive growth in HONO. *Atmos. Chem. Phys.*, 19, 10557–10570.

Xu, Z., Wang, T., Xue, L., Louie, P. K., Luk, C. W., Gao, J., Wang, S., Chai, F., & Wang, W. (2013). Evaluating the uncertainties of thermal catalytic conversion in measuring atmospheric nitrogen dioxide at four differently polluted sites in China. *Atmos. Environ.*, 76, 221–226.

Xue, C., Zhang, C., Ye, C., Liu, P., Catoire, V., Krysztofiak, G., Chen, H., Ren, Y., Zhao, X., Wang, J., Zhang, F., Zhang, C., Zhang, J., An, J., Wang, T., Chen, J., Kleffmann, J., Mellouki, A., & Mu, Y. (2020). HONO Budget and Its Role in Nitrate Formation in the Rural North China Plain. *Environ. Sci. Technol.*, 54, 11048–11057.

Ye, C., Gao, H., Zhang, N., & Zhou, X. (2016). Photolysis of Nitric Acid and Nitrate on Natural and Artificial Surfaces. *Environ. Sci. Technol.*, 50, 3530–3536.

Young, C. J., Washenfelder, R. A., Edwards, P. M., Parrish, D. D., Gilman, J. B., Kuster, W. C., Mielke, L. H., Osthoff, H. D., Tsai, C., Pikelnaya, O., Stutz, J., Veres, P. R., Roberts, J. M., Griffith, S., Dusanter, S., Stevens, P. S., Flynn, J., Grossberg, N., Lefer, B., Holloway, J. S., Peischl, J., Ryerson, T. B., Atlas, E. L., Blake, D. R., & Brown, S. S. (2014). Chlorine as a primary radical: evaluation of methods to understand its role in initiation of oxidative cycles. *Atmos. Chem. Phys.*, 14, 3427–3440.

Young, C. J., Washenfelder, R. A., Roberts, J. M., Mielke, L. H., Osthoff, H. D., Tsai, C., Pikelnaya, O., Stutz, J., Veres, P. R., Cochran, A. K., Vandenboer, T. C., Flynn, J.,

Grossberg, N., Haman, C. L., Lefer, B., Stark, H., Graus, M., De Gouw, J., Gilman, J. B., Kuster, W. C., & Brown, S. S. (2012). Vertically resolved measurements of nighttime radical reservoirs in Los Angeles and their contribution to the urban radical budget. *Environ. Sci. Technol.*, 46, 10965–10973.

Yuan, J., Ling, Z., Wang, Z., Lu, X., Fan, S., He, Z., Guo, H., Wang, X., & Wang, N. (2018). PAN-precursor relationship and process analysis of PAN variations in the Pearl River Delta region. *Atmosphere*, 9, 372.

Zhang, G., Xia, L., Zang, K., Xu, W., Zhang, F., Liang, L., Yao, B., Lin, W., & Mu, Y. (2020). The abundance and inter-relationship of atmospheric peroxyacetyl nitrate (PAN), peroxypropionyl nitrate (PPN), O_3, and NO_y during the wintertime in Beijing, China. *Sci. Total Environ.*, 718, 137388.

Zhao, S., Hu, B., Liu, H., Du, C., Xia, X., & Wang, Y. (2021). The influence of aerosols on the NO_2 photolysis rate in a suburban site in North China. *Sci. Total Environ.*, 767.

Zheng, W., Flocke, F. M., Tyndall, G. S., Swanson, A., Orlando, J. J., Roberts, J. M., Huey, L. G., & Tanner, D. J. (2011). Characterization of a thermal decomposition chemical ionization mass spectrometer for the measurement of peroxy acyl nitrates (PANs) in the atmosphere. *Atmos. Chem. Phys.*, 11, 6529–6547.

Zhou, W., Zhao, J., Ouyang, B., Mehra, A., Xu, W., Wang, Y., Bannan, T. J., Worrall, S. D., Priestley, M., Bacak, A., Chen, Q., Xie, C., Wang, Q., Wang, J., Du, W., Zhang, Y., Ge, X., Ye, P., Lee, J. D., Fu, P., Wang, Z., Worsnop, D., Jones, R., Percival, C. J., Coe, H., & Sun, Y. (2018). Production of N_2O_5 and $ClNO_2$ in summer in urban Beijing, China. *Atmos. Chem. Phys.*, 18, 11581–11597.

Appendices

Supplementary information – Chapter 2

S1. Meteorological consistency between measurement sites and periods

Meteorology is an important variable influencing local air pollutant concentrations. For example, prolonged changes in frequency and direction of cyclonic and anticyclonic conditions can give rise to variability in wind direction and speed. Therefore, to assess the spatial and temporal consistency of the meteorology between Harwell and Chilbolton, meteorological data for Harwell (2014-15) and Chilbolton (2016-17) were compared with 2010-17 mean measured meteorology at Benson, south Oxfordshire (lat: 51.620°, lon: −1.099°, altitude: 63 m). This site is located on open, relatively flat land approximately 18 km south-east of Oxford and 20 km north-west of Reading (Galvin & McGhee, 2005). The time series of meteorological data that underpins Figure S3 is shown as an overview for the entire concatenated time series (2014-17 daily average), and a month of raw hourly measurements in Figure S2. The time series show similar magnitudes and trends in temperature, wind speed and relative humidity at all three sites. The summary of long-term mean ambient temperature and its variability (represented by standard deviation of annual hourly values) given in Table S1 confirms these to be similar between the two years at Harwell and Chilbolton Observatory, and to the long-term averages at Benson. Mean wind speed was somewhat lower at Harwell in 2014 and 2015 compared both Chilbolton in 2016 and 2017 and the Benson long-term average, but in all cases variability was large. Rainfall was notably higher in 2014 ($\sim$1.3 times as much as 2015 and 2016), primarily falling in January and February. Both months exceeded 180% of the 1981-2010 monthly averages for southern England (Huntingford et al., 2014).

S2. *deweather* model description

To remove as much as possible the influence of meteorological variability on the interpretation of the pollutant time series on analysing the datasets, the *deweather* function (Carslaw, 2015) was implemented on concatenated Harwell and Chilbolton Observatory datasets. The objective was to examine for evidence of a step change in the concentrations coincident with the change in location. The *deweather* function uses a boosted regression trees approach to build a predictive model for air pollutant concentrations from a set of predictor variables (wind speed and direction, ambient temperature and pressure, relative humidity, hour-of-day, day-of-week, day-of-year and week of year), also allowing for non-linear relationships and complex interactions between the variables (Carslaw & Taylor, 2009). Models are built using a stochastic process, with a random subset of data taken to fit each new regression tree, resulting in reduced variance in the final model (Friedman, 2002). A consequence is that a slightly different model is produced with each run (Elith et al., 2008), so in this work a set of 10 identically-built models were performed for each pollutant time series "deweathered".

Figures and Tables

Table S1: Annual mean ± standard deviation of measured meteorological data (hourly) at Harwell, Chilbolton Observatory and Benson.

	Harwell 2014	Harwell 2015	Chilbolton 2016	Chilbolton 2017	Benson 2014-2017
Temperature / °C	11.2 ± 5.3	10.3 ± 5.0	10.5 ± 6.1	10.7 ± 5.9	10.3 ± 6.3
Wind speed / km h^{-1}	11.3 ± 6.4	12.2 ± 6.8	13.2 ± 8.0	13.6 ± 7.9	14.0 ± 8.5
Total annual rainfall / mm	1507	963	1139	1255	NA

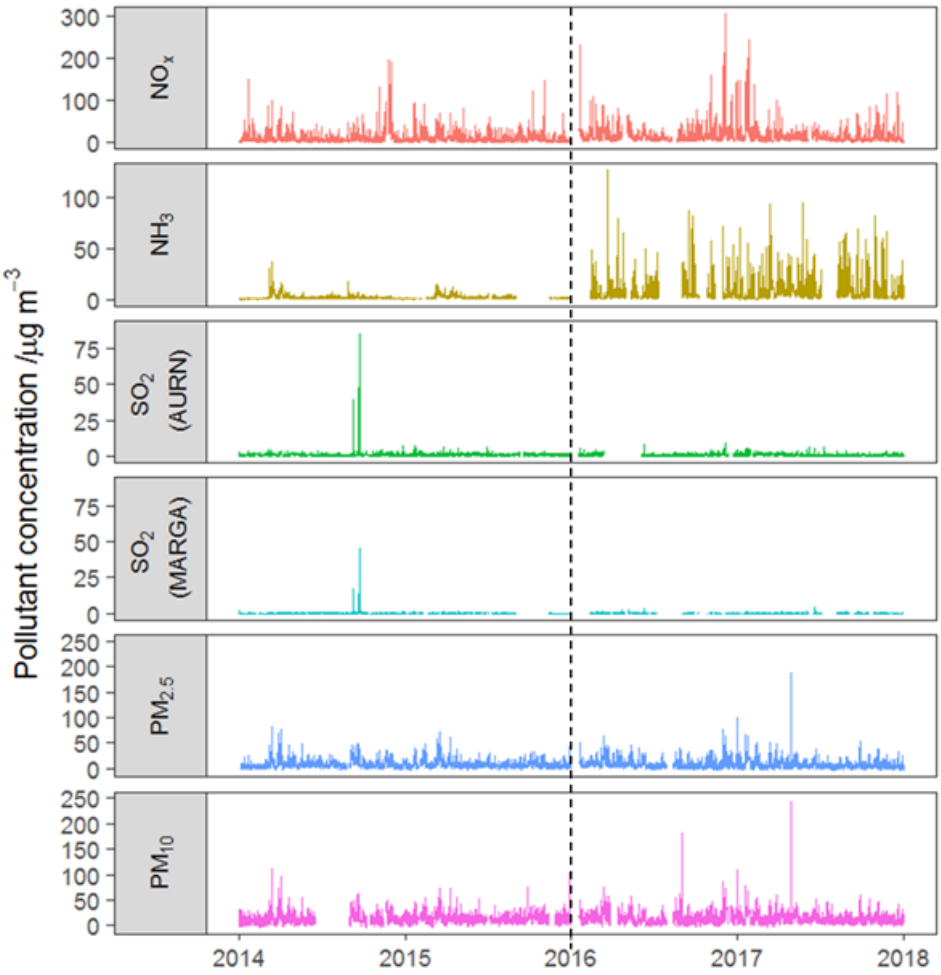

Figure S1: Concatenated time series of hourly average concentrations of NO_x, NH_3, SO_2, $PM_{2.5}$ and PM_{10} (recorded by the AURN and MARGA), from Harwell (2014-15) and Chilbolton (2016-17). All measured data acquired from UK-Air (Defra, 2021e). The cessation of operations at Harwell is depicted by the vertical dotted line.

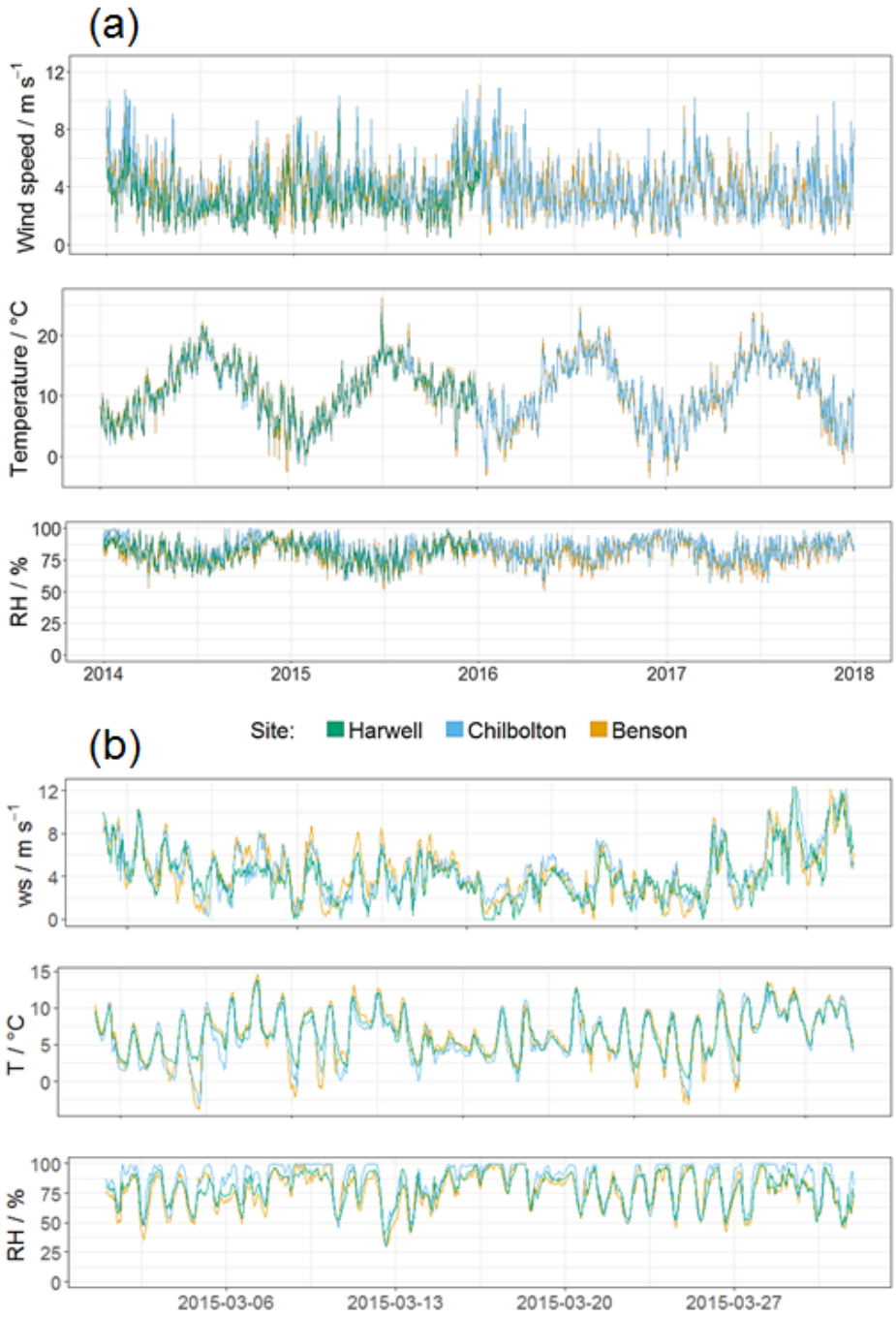

Figure S2: Comparison of measured meteorological parameters between sites in southern England. Measurements of wind speed (ws), ambient temperature (T) and relative humidity (RH) are presented for Benson (orange), Chilbolton (blue) and Harwell (green). Harwell is only represented for two years as meteorological measurements ceased with the site closure on 31 December 2015. (a) Comparison of daily averages for the two years pre- and post- site relocation (2014-2017). (b) Illustrative of comparison of the raw hourly data used in the *deweather* model runs (March 2015).

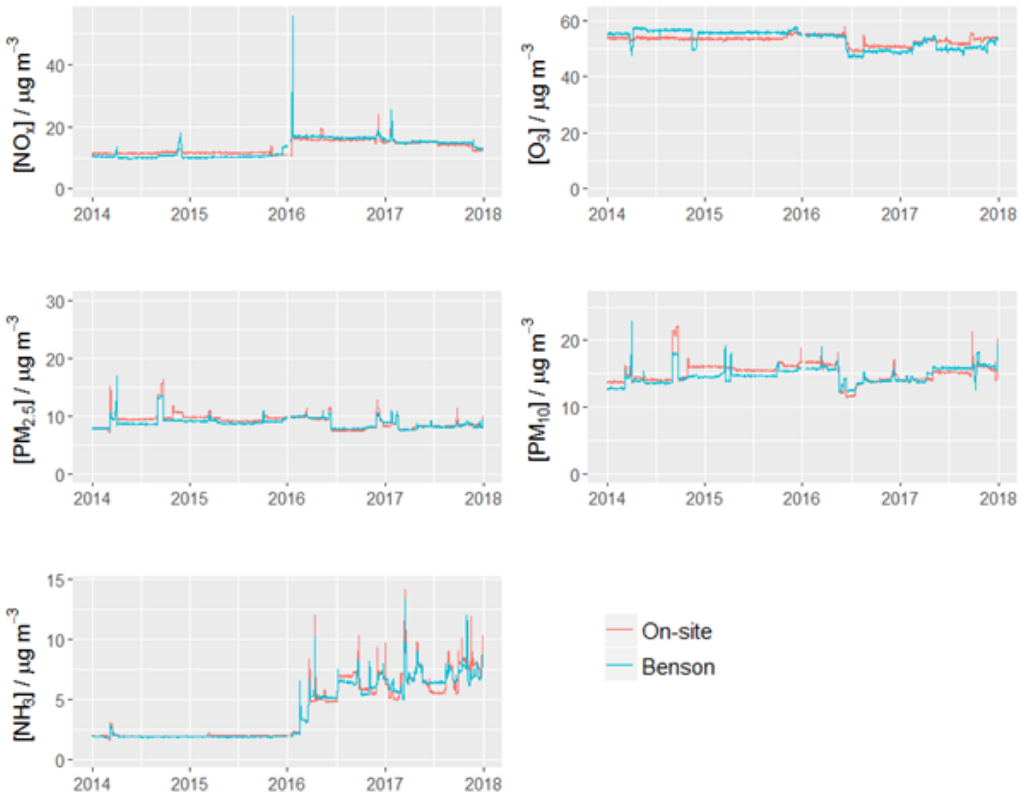

Figure S3: Comparison between *deweather* model (Carslaw, 2015) outputs of predicted concentrations of NO_x, O_3, $PM_{2.5}$, PM_{10} and NH_3 for different sources of meteorological data. Shown in blue are predicted *deweather* concentrations using measurements of wind speed, wind direction, air temperature, relative humidity and pressure from Benson (2014-2017). Shown in red are the concentrations using the same methodology but with a concatenated time series of the meteorological parameters measured on-site at Harwell (2014-15) and Chilbolton (2016-17).

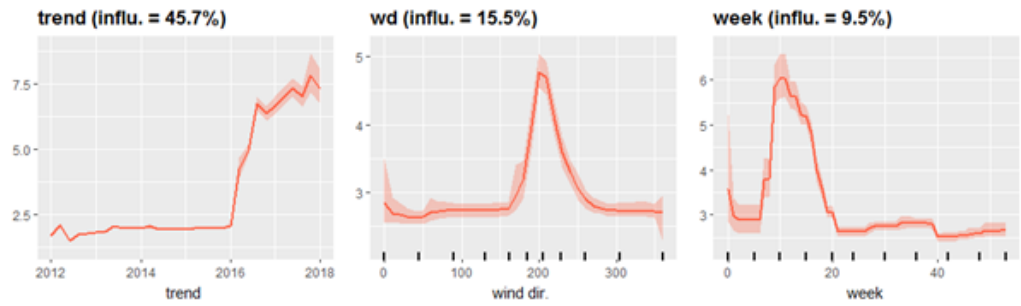

Figure S4: Covariates of largest relative importance for one *deweather* model run (Carslaw, 2015) of the NH_3 time series using meteorology measured on-site ('trend' is a proxy for year, 'wd' is wind direction and 'week' is week-of-year). Plots show predicted NH_3 concentrations ($\mu g\, m^{-3}$) against these variables, when all other covariates are held at their mean level. The percentage value in the plot title is the relative importance of the covariate for the model run.

Table S2: Mean percentage relative importance ($\pm$ 1σ) of all covariates used in the 10 identical repeat *deweather* model runs for the NH_3 and NO_x time series. These results are used as a quantitative representation of the stability of each variable's influence on predicted concentrations.

Covariate name	Mean relative importance %		$\pm$ 1σ %	
	NH_3	NO_x	NH_3	NO_x
trend (proxy for year)	45.5	18.4	0.6	0.6
wind direction	15.5	19.1	0.6	0.7
week-of-year	9.3	9.8	0.4	0.3
ambient temperature	6.4	18.7	0.3	0.6
weekday	6.2	7.2	0.3	0.3
wind speed	6.0	10.4	0.5	0.5
relative humidity	4.5	6.4	0.2	0.3
ambient pressure	3.6	5.9	0.2	0.3
hour-of-day	3.1	4.0	0.3	0.2

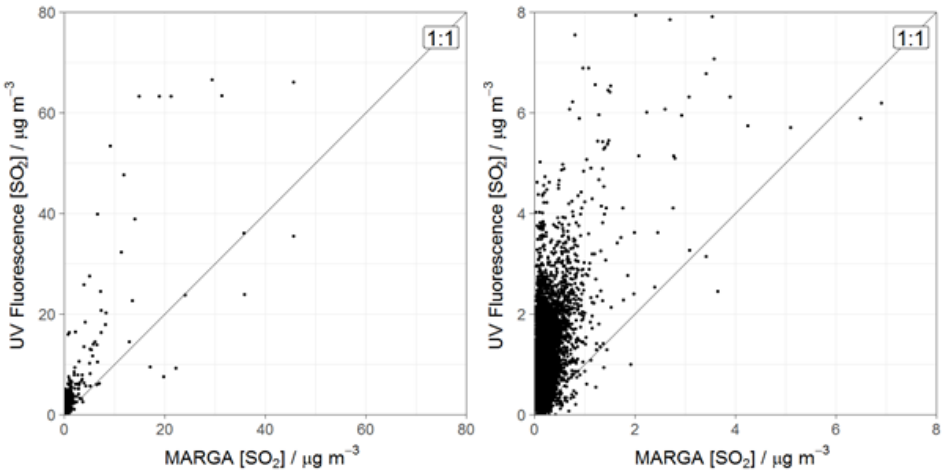

Figure S5: Scatter plot of hourly SO_2 concentrations measured by the MARGA and by UV fluorescence (AURN data). Both instruments had high data capture at Harwell (70-98%, see Table 2.1) but lower data capture at Chilbolton (58-64%, Table 2.1). The left plot includes all data from 2014-2017, whilst the right plot shows a smaller range of concentrations in order to visualise normal ambient concentrations.

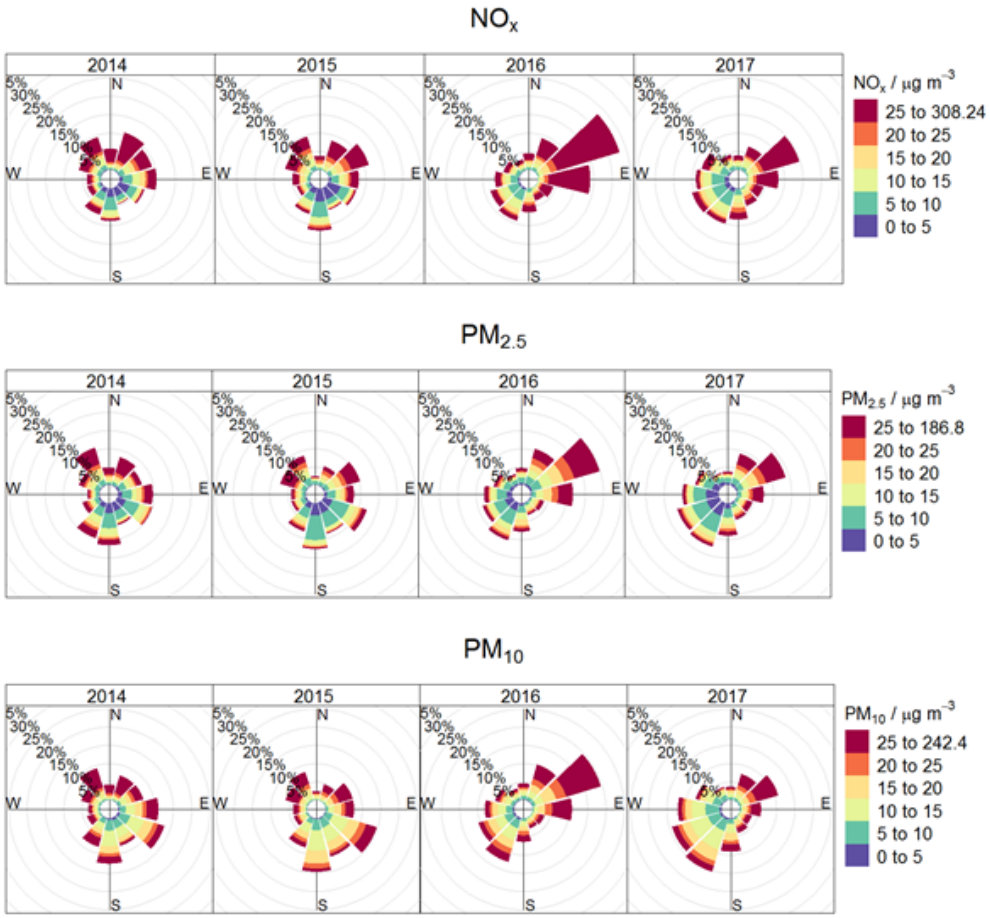

Figure S6: Pollution wind roses detailing the contribution of the 5 µg m^{-3} concentration bins in each wind sector to the annual mean NO_x, $PM_{2.5}$ and PM_{10} concentrations at Harwell in 2014 and 2015, and at Chilbolton in 2016 and 2017. Wind direction and AURN measurements were co-located at each site, and the underlying time resolution was hourly for both.

Table S3: Annual mean concentrations of hourly $PM_{2.5}$ measurements for easterly (0°−180°) and westerly (181°−360°) wind directions. The remaining percentage of data (% NA) includes hours where $PM_{2.5}$ concentration or wind direction were not recorded.

	Mean $PM_{2.5}$ concentration / µg m^{-3}		Percentage of annual wind / %		
Site and year	Westerly	Easterly	Westerly	Easterly	NA
Harwell 2014	10.8	8.0	38	58	4
Harwell 2015	9.6	8.1	33	54	12
Chilbolton 2016	6.8	13.2	54	37	9
Chilbolton 2017	5.4	12.5	71	27	2

Supplementary information – Chapter 4

S3. Calculation of overall error in Table 4.4

The overall error used when directly comparing X-MDAF derived for each photolysis reaction to the reference MDAF value (NO_2-MDAF and O(^{1}D)-MDAF) is calculated as the sum in quadrature of the relative standard deviation (RSD) of the hourly X-MDAF values for the full dataset,

$$\text{RSD} = \frac{\sigma}{\overline{x}}$$

where $\overline{x}$ and σ are the mean and standard deviation of the derived X-MDAF values, respectively, and the percentage difference between the mean X-MDAF/NO_2-MDAF or X-MDAF/O(^{1}D)-MDAF value and unity, in the following equation:

$$\text{Overall error (\%)} = \left(\sqrt{\text{RSD}^2 + \left(\frac{(\overline{x} - 1)}{1} \right)^2} \right) \times 100$$

Here $\overline{x}$ is the relevant mean X-MDAF/NO_2-MDAF or X-MDAF/O(^{1}D)-MDAF value calculated across the full dataset, and unity represents what each ratio would be if the reference MDAF value (NO_2 or O(^{1}D)) was a perfect substitute for X-MDAF.

S4. Calculation of $p(\text{OH})_{\text{O}_3}$ at Chilbolton Observatory

The rate of OH radical production from the photolysis of ozone (O_3) is calculated using the following equations:

$$p(\text{OH})_{\text{O}_3} = 2 \times f \times j(\text{O}^1\text{D}) \times [\text{O}_3]$$

$$f = \frac{k_{\text{H}_2\text{O}}[\text{H}_2\text{O}]}{k_{\text{N}_2}[\text{N}_2] + k_{\text{O}_2}[\text{O}_2] + k_{\text{H}_2\text{O}}[\text{H}_2\text{O}]}$$

In these equations, $j(O^1D)$ is the photolysis rate constant for O_3, and f is the fraction of $O(^1D)$ atoms that react with water vapour to form OH, as opposed to their quenched removal by N_2 and O_2 molecules. Rate constants for the individual reactions between $O(^1D)$ and H_2O, N_2 and O_2 (k_{H_2O}, k_{N_2} and k_{O_2}, respectively) were taken from Atkinson et al. (2004). Temperature dependence was included for the rate constants of the quenching reactions but not for k_{H_2O}, as the latter is stated to be independent of temperature in the range 200-350 K (Atkinson et al., 2004). Local relative humidity and temperature measurements (Vaisala HMP155A humidity and temperature probe) were used to derive absolute H_2O concentrations, and hourly concentrations of ground-level O_3 measured at Chilbolton Observatory were downloaded directly from UK-AIR (Defra, 2021b). For the study period at Chilbolton Observatory, the mean $\pm$ sd fraction f was 4.7$\pm$1%.

Figures

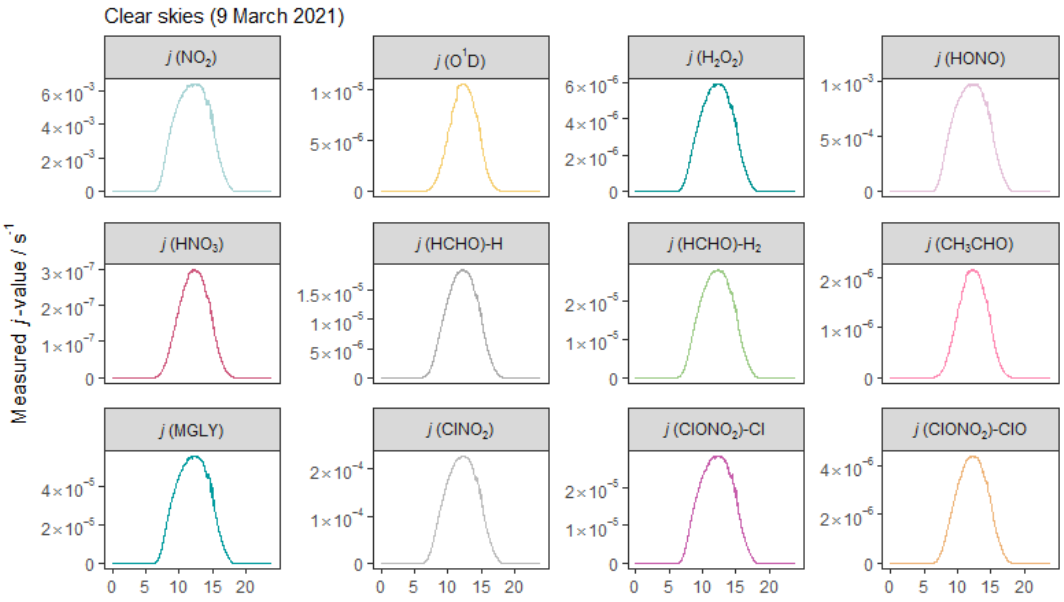

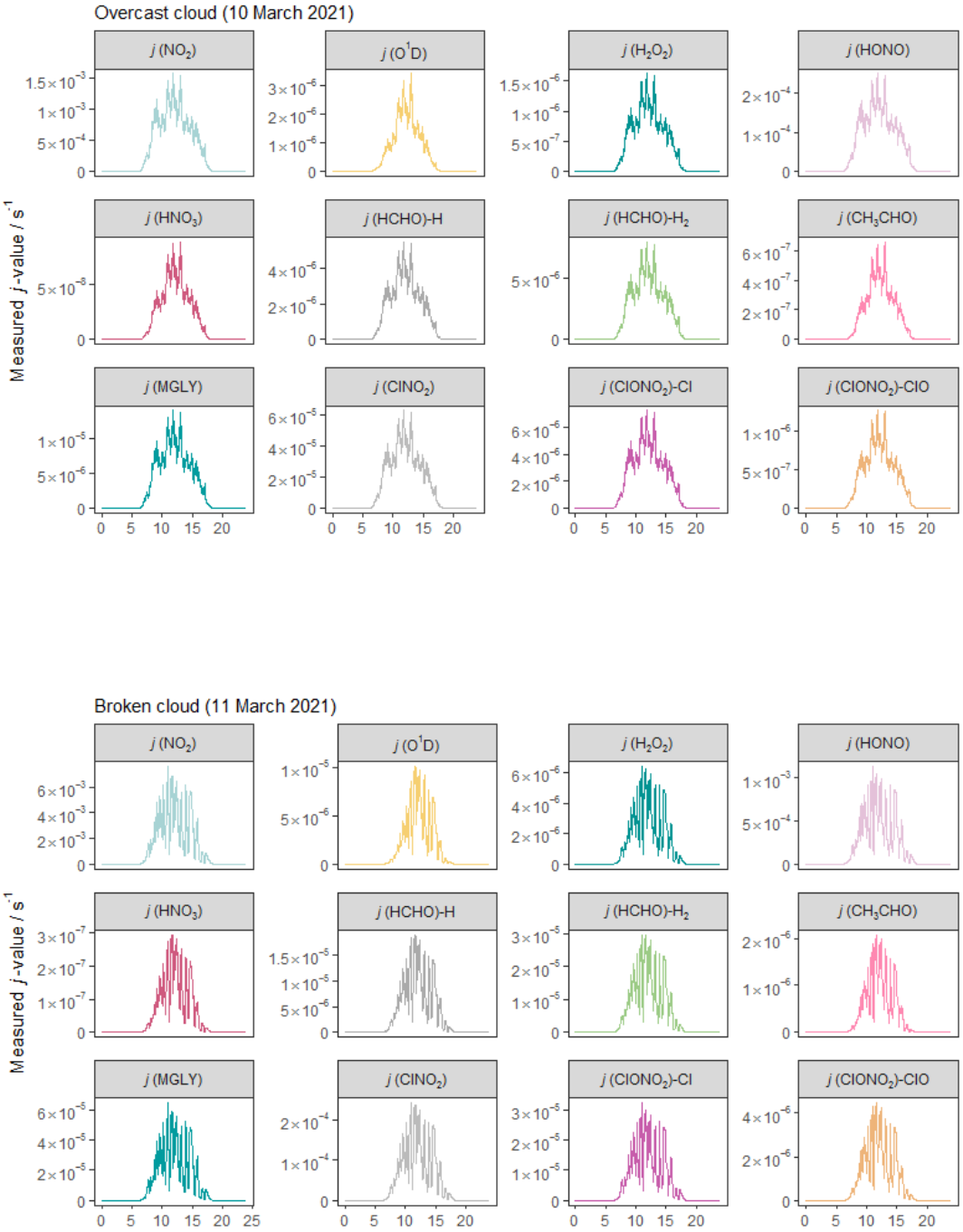

Figure S7: Diurnal cycles of photodissociation rate constants (j-values) for each species investigated at Chilbolton Observatory, using 1 minute scans of actinic flux made by a spectral radiometer (Ocean Optics QE65000), and processed using absorption cross-section and quantum yield values in Table 4.1. The first set of panels show the j-values on the clearest day of the study (9 March 2021); the second and third set of panels show the j-values on two cloudy days near this: one overcast (10 March 2021) and one of continuous broken cloud (11 March 2021). Note the vertical axis scales for each photolysis reaction vary between the three days.

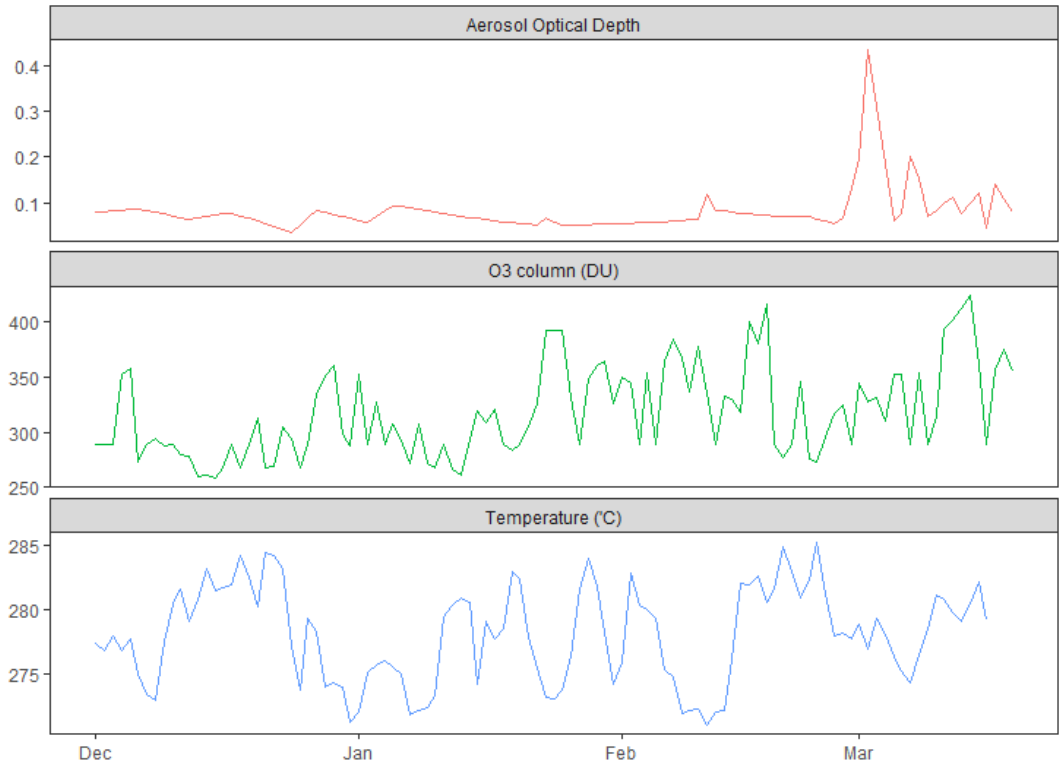

Figure S8: Time series of daily mean temperature, aerosol optical depth (AOD) and ozone column used in the TUV model input. Temperature data is measured on site by a Viasala HMP155. AOD is measured at Chilbolton Observatory by a Cimel sun photometer and downloaded from the AERONET network (https://aeronet.gsfc.nasa.gov/new_web/aerosols.html). Ozone column measurements derive from the NOAA Ozone Monitoring Instrument (OMI) on the NASA Aura satellite, and downloaded from the online archive (https://www.esrl.noaa.gov/gmd/grad/neubrew/SatO3DataTimeSeries.jsp).

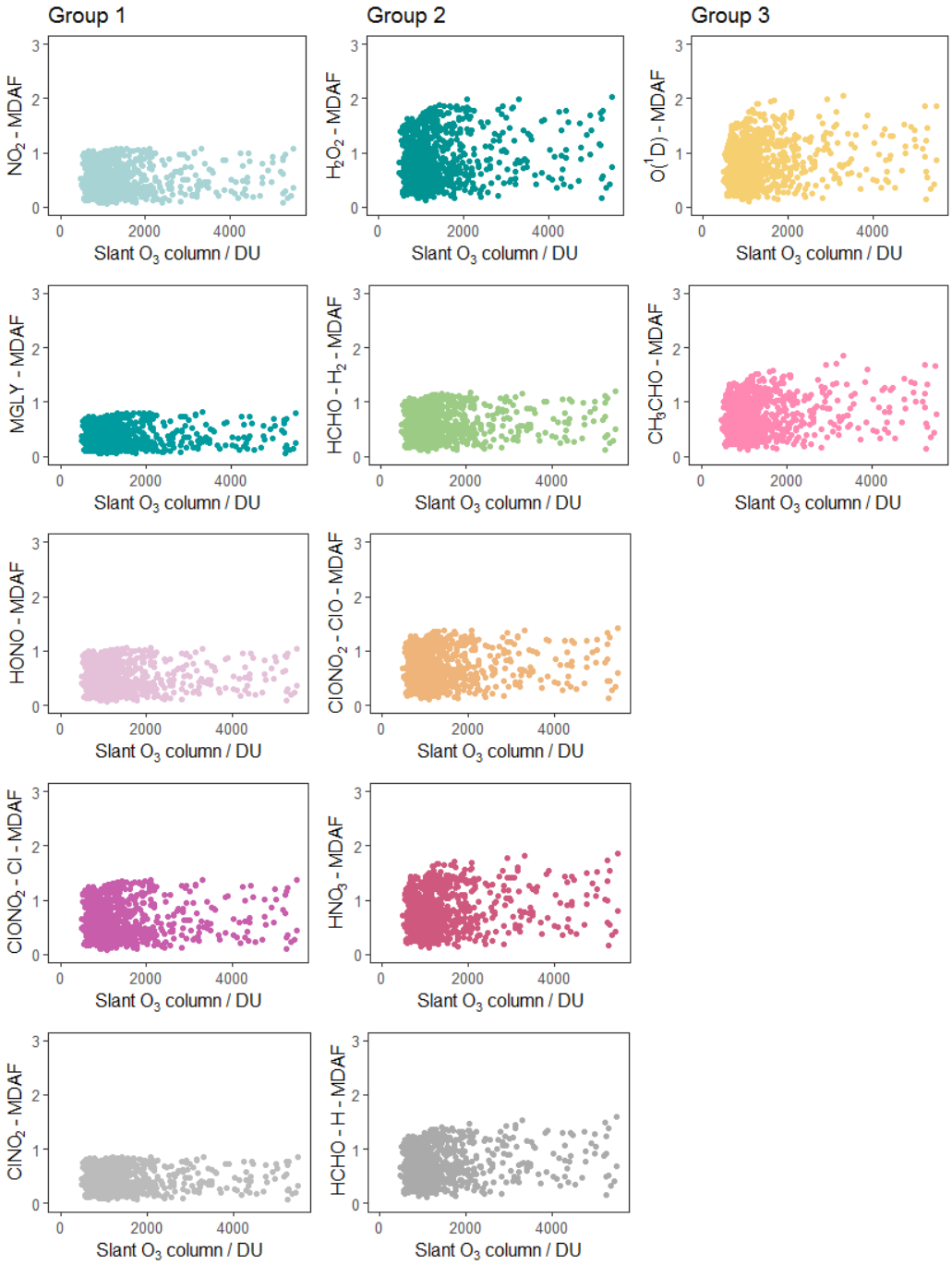

Figure S9: MDAF values derived for each photolysis reaction against slant ozone column, calculated as O_3 column in DU divided by cos(SZA). Plots are presented in columns corresponding to the three groups of photolysis reactions obtained from the hierarchical clustering of MDAF time series described in the main paper.

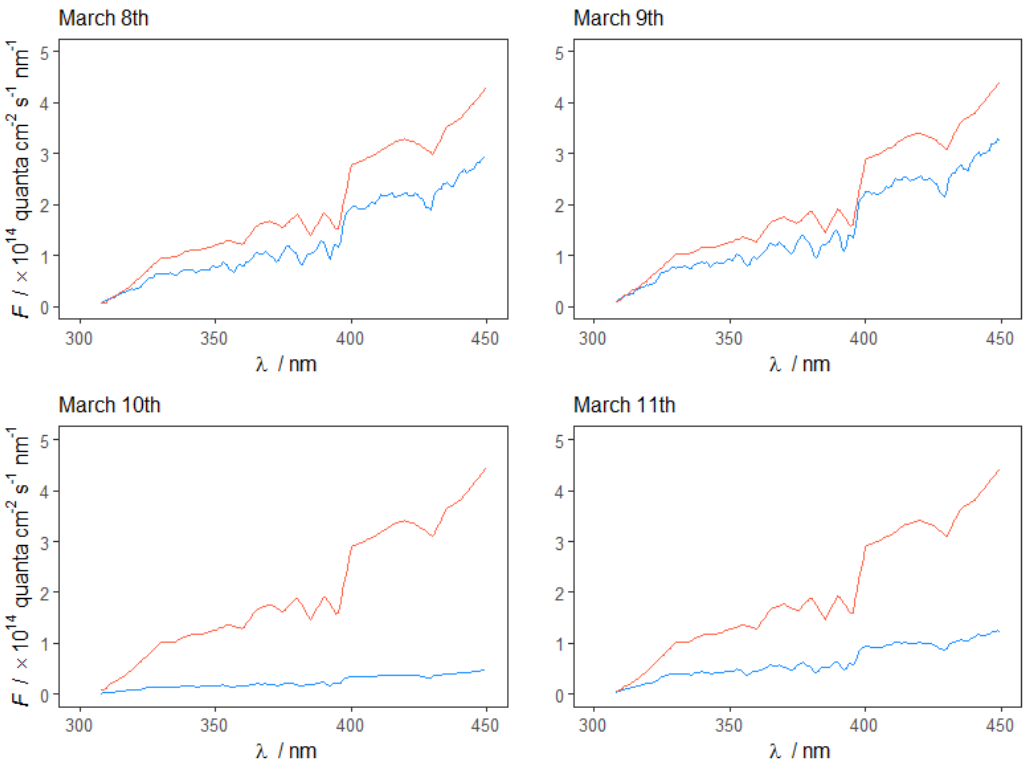

Figure S10: Actinic flux spectra measured at Chilbolton Observatory using the spectral radiometer (blue) and modelled for cloud-free conditions using the TUV radiative transfer model (v5.3; red) at a solar zenith angle (SZA) of ∼55°. Panels show this comparison for a clear-sky day (9 March 2021), an overcast day (10 March 2021) and two days of different intermittent cloud conditions (8 and 11 March 2021).

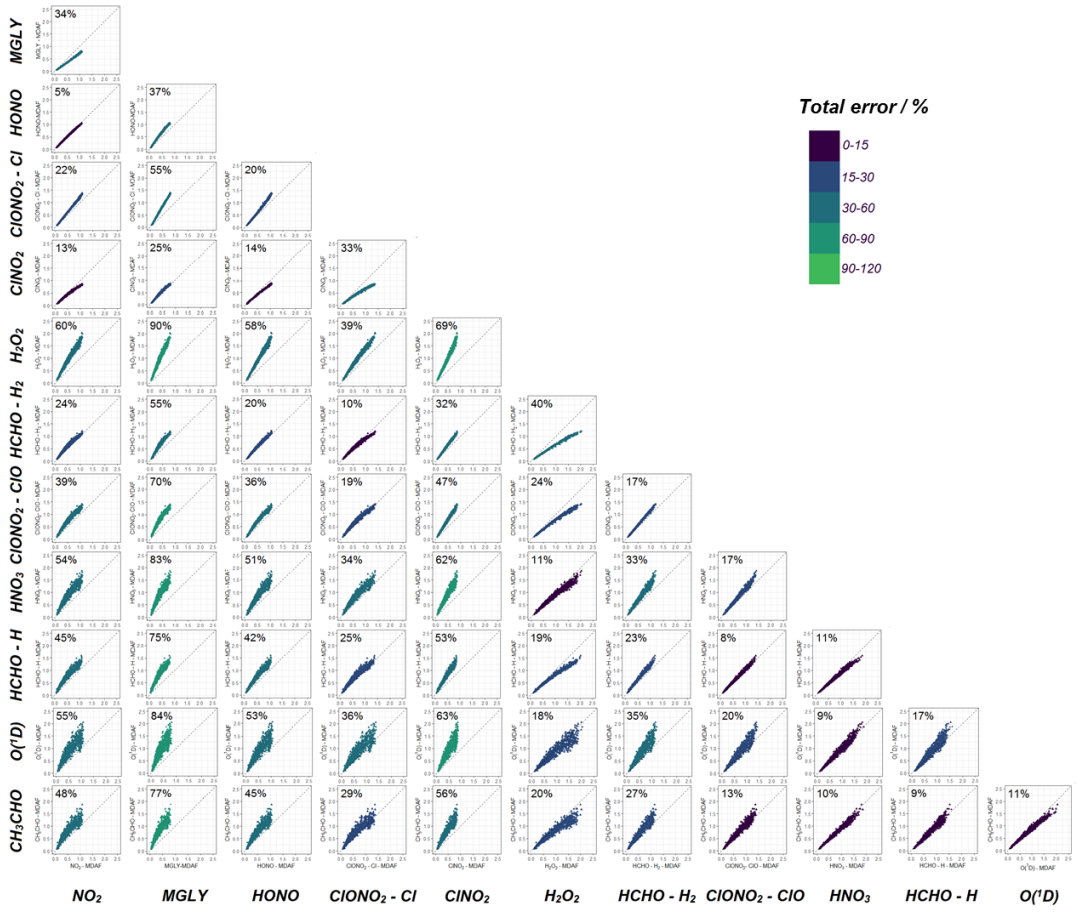

Figure S11: Correlation plot of measurement-driven adjustment factors (MDAFs) derived for all photolysis reactions included in this study. The 1:1 lines are depicted in grey, and the percentage annotations depict the total error, calculated as the sum in quadrature of the relative standard deviation (spread of data) and the absolute percentage difference between using X-MDAF in place of Y-MDAF (distance from 1:1). Plot points are coloured by bins of total error.